ADVANCED MR NEUROIMAGING IN EARLY STAGE PRESENILE DEMENTIA

Geavanceerde MR beeldvorming van de hersenen
in het vroege stadium van preseniele dementie

Rebecca Steketee

ADVANCED MR NEUROIMAGING IN EARLY STAGE PRESENILE DEMENTIA

Geavanceerde MR beeldvorming van de hersenen
in het vroege stadium van preseniele dementie

Proefschrift

ter verkrijging van de graad van doctor aan de
Erasmus Universiteit Rotterdam
op gezag van de
rector magnificus

prof.dr. H.A.P. Pols

en volgens het besluit van het College voor Promoties.

De openbare verdediging zal plaatsvinden op
vrijdag 5 februari 2016 om 9.30 uur.

door

Rebecca Martinetta Elisabeth Steketee
geboren te Leiden

Cover design: Rebecca Steketee
Photo cover: Gaby Jongenelen fotografie
Thesis layout: Ton Everaers
Printing: Print Partners Ipskamp

ISBN:

Erasmus University Rotterdam

PROMOTIECOMMISSIE

Promotoren:
Prof.dr. A. van der Lugt
Prof.dr. J.C. van Swieten

Overige leden:
Prof.dr. W.M. van der Flier
Prof.dr. S.A.R.B. Rombouts
Prof.dr. M.A. Frens

Copromotor:
Dr. M. Smits

TABLE OF CONTENTS

Chapter 1

General Introduction

Dementia poses an increasing challenge for public health with an estimated number of patients of 35.6 million world-wide in 2010; moreover, the number of patients is expected to double every 20 years [1]. In the Netherlands, over 260,000 people suffer from dementia, of which approximately 12,000 people are affected before the age of 65 years, i.e. presenile dementia. Alzheimer's disease (AD) is the most common underlying cause of dementia, both at older and younger age, and characterized by a gradual onset and progressive impairment of memory, language, and visuospatial functions [2]. Frontotemporal dementia (FTD) is more prevalent among the younger population [3] and manifests with a spectrum of clinical syndromes. The behavioral variant of frontotemporal dementia (bvFTD) is most common and usually presents with disinhibition, apathy, loss of empathy, perseverative behavior and/or hyperorality [4]. A subset of FTD as well as AD patients presents with language dysfunction as primary clinical feature, and is classified as having primary progressive aphasia (PPA) [5].

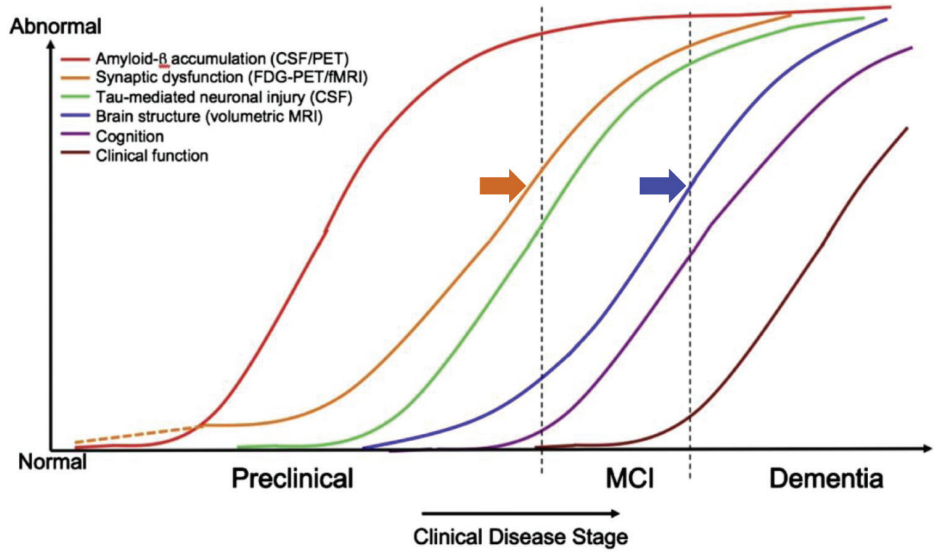

Figure 1: Hypothetical model of dynamic biomarkers of dementia. Of note is that advanced imaging techniques (orange) are more sensitive to early changes, such as synaptic dysfunction, while structural MRI (blue) detects brain changes in the later stage, when abnormalities are more severe. Reprinted with permission of Elsevier from Jack et al., 2010 [11], as adapted by Sperling et al., 2011 [13]. Arrows added.

Early and accurate diagnosis is of utmost importance in these younger patients, as progression is more rapid in presenile dementia [6]. Furthermore, AD and FTD have different implications with respect to heritability, disease progression and life expectancy [7,8]. Besides facilitating proper and tailored care, early diagnosis will provide most benefit from the future therapies delaying disease progression.

Unfortunately, to establish the underlying cause of presenile dementia in the early stage proves to be difficult. First, younger dementia patients often initially present with atypical symptoms. For instance, presenile AD more often has a non-amnestic presentation than late onset AD [9]. Second, cognitive dysfunction in younger patients more frequently has a non-neurological cause but may nevertheless resemble a neurodegenerative disorder [10]. Diagnosis in patients with PPA is particularly difficult, as the underlying pathology can either be AD or FTD [5]. Often, the etiology underlying presenile dementia can be diagnosed only in later stages, when clinical symptoms have become distinctive, which is obviously a missed opportunity for possible intervention and care.

Structural magnetic resonance imaging (MRI) of the brain may support diagnosis of the underlying neurodegenerative disease by showing specific patterns of atrophy, but these are often absent or unspecific at the early stage [11,12]. Imaging biomarkers are therefore not included as core diagnostic criteria for AD or FTD. As neuronal injury has to be substantial to be detected as abnormality on structural imaging, advanced MR neuroimaging techniques may be more sensitive to neurodegenerative processes in an earlier stage [13] (Figure 1). Specifically, alterations in brain morphology as detected with structural MRI in later stages are preceded by changes in (synaptic) function that can be captured using functional MR techniques, such as resting state functional MRI (rs-fMRI) and arterial spin labeling (ASL) MRI. Rs-fMRI measures spontaneous fluctuations of brain activation by acquiring functional MRI data when a participant is at rest. By assessing which brain regions are simultaneously active, rs-fMRI allows us to map functional connections in the brain (Figure 2A). Such functional networks are robust over time and people, but also show alterations as a result of neurodegeneration. Importantly, these alterations are evident before atrophy occurs.

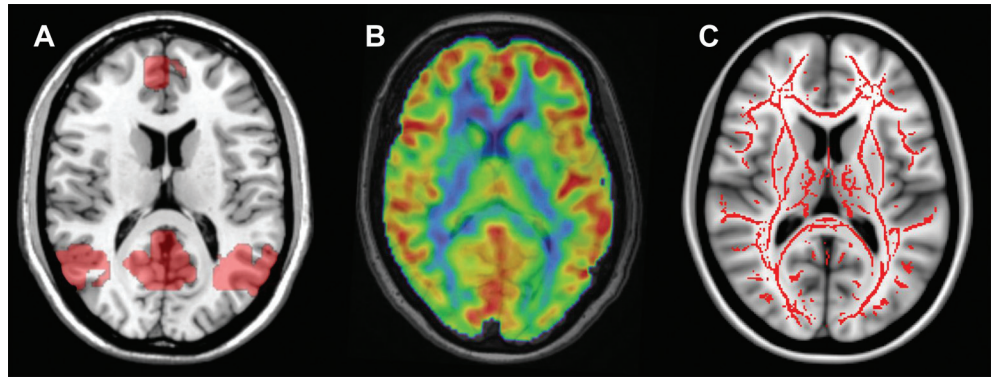

Figure 2: Advanced MR neuroimaging applications A) Functionally connected brain regions in a group of healthy older participants as identified by resting state fMRI; B) Cerebral blood flow (CBF, in ml/100g gray matter/min) in a healthy elderly participant as measured with ASL MRI; C) White matter microstructure in a group of healthy older participants as measured with diffusion tensor MR imaging.

Another way to image synaptic dysfunction is by using ASL-MRI, which quantitatively measures brain perfusion (Figure 2B). Brain perfusion is tightly coupled to metabolism, which is traditionally visualized by fluorodeoxyglucose-positron

emission tomography (FDG-PET). FDG-PET can detect regional changes in neuronal metabolism that precede structural damage in dementia, but has limited availability and relatively high costs. ASL-MRI has therefore been proposed as an alternative [14]. Besides being non-invasive, it can easily be added to routine diagnostic MRI protocols, which makes it attractive for clinical practice. However, despite being a quantitative technique, there is extensive variability between ASL data acquired on MR scanners of different vendors, as each vendor provides their own particular ASL implementation. Such variability needs to be assessed and accounted for before ASL can be (clinically) implemented on a large scale.

In addition to changes in brain function, (macro)structural changes as a result of neurodegenerative disease are preceded by microstructural changes in the white matter of the brain. These changes can be detected by using diffusion tensor imaging (DTI), which is sensitive to the diffusion of water. By measuring changes in the direction and magnitude of water diffusion, microstructural changes of white matter can be assessed before atrophy or white matter lesions are present (Figure 2C). In addition, this information can be used to reconstruct white matter trajectories, and thus to visualize anatomical connections in the brain, i.e. structural connectivity.

In conclusion, there are several advanced MR imaging techniques, namely rs-fMRI, ASL and DTI, that may aid in diagnosing presenile dementia at an earlier stage. In this thesis, I investigate whether these advanced MR neuroimaging measures can serve as early neuropathological markers of presenile dementia.

In **Section 2,** I describe the early brain changes found in presenile AD and FTD using ASL and DTI. In **Chapter 2.1** I investigate the added value of ASL relative to structural gray matter MR imaging in the computer aided classification of presenile dementia patients versus healthy controls. In **Chapter 2.2** I extend these findings to investigating the contribution of ASL to early differential diagnosis of early AD and FTD. In **Chapter 2.3** I describe the regional associations between gray and white matter abnormalities in AD and bvFTD using structural imaging, ASL and DTI.

In **Section 3** I focus on a subset of patients that present with the characteristic behavioral features of bvFTD but who do not show abnormalities on routine structural imaging, or cognitive or functional decline. These patients are referred to as phenocopy FTD (phFTD) patients. Although previous studies report no abnormalities on conventional imaging, I show that there are structural and perfusion changes (**Chapter 3.1**) as well as changes in functional networks and white matter microstructure (**Chapter 3.2**) in these patients.

It should be noted that inclusion of FTD patients in clinical studies is particularly hard, as it is a rare disorder, even in a tertiary referral center like ours. Additionally inclusion and exclusion criteria have to be applied very strictly to ensure well defined samples, leading to modest bvFTD and phFTD sample sizes.

As Section 2 and 3 illustrate the value of ASL as a clinical imaging tool, exploring its wider application – including but not limited to dementia – may be beneficial. However, as mentioned above, despite being a quantitative technique, not every

ASL implementation provides the same information as a result of vendor specific implementation. In **Section 4** I report to which extent the implementation of similar sequences by two different vendors affect ASL perfusion data in several experimental designs. In **Chapter 4.1**, I assess whether baseline perfusion measurements are reproducible when acquired with sequences from different vendors. In **Chapter 4.2** I focus on imaging brain activation using ASL (functional ASL, fASL). I investigate the sensitivity of both sequences to detect task related brain activation, as well as their reproducibility in quantifying that activation. Finally in **Chapter 4.3**, I study the reproducibility of pharmacological ASL (phASL), by comparing a caffeine induced perfusion decrease between the sequences.

In **Section 5**, I discuss the main findings, their clinical implications and methodological considerations. Finally, I suggest future directions for research on advanced MR imaging in dementia.

REFERENCES

1. Prince M, Bryce R, Albanese E, Wimo A, Ribeiro W, Ferri CP. The global prevalence of dementia: a systematic review and metaanalysis. Alzheimers Dement. 2013;9: 63-75.e2.
2. McKhann GM, Knopman DS, Chertkow H, Hyman BT, Jack CR,Jr, Kawas CH, et al. The diagnosis of dementia due to Alzheimer's disease: recommendations from the National Institute on Aging-Alzheimer's Association workgroups on diagnostic guidelines for Alzheimer's disease. Alzheimers Dement. 2011;7: 263-269.
3. van der Flier, W. M., Scheltens P. Epidemiology and risk factors of dementia. J Neurol Neurosurg Psychiatr. 2005;76 Suppl 5: v2-7.
4. Rascovsky K, Hodges JR, Knopman D, Mendez MF, Kramer JH, Neuhaus J, et al. Sensitivity of revised diagnostic criteria for the behavioural variant of frontotemporal dementia. Brain. 2011;134: 2456-2477.
5. Gorno-Tempini ML, Hillis AE, Weintraub S, Kertesz A, Mendez M, Cappa SF, et al. Classification of primary progressive aphasia and its variants. Neurology. 2011;76: 1006-1014.
6. Koedam EL, Pijnenburg YA, Deeg DJ, Baak MM, van der Vlies, A. E., Scheltens P, et al. Early-onset dementia is associated with higher mortality. Dement Geriatr Cogn Disord. 2008;26: 147-152.
7. Rascovsky K, Salmon DP, Hansen LA, Galasko D. Distinct cognitive profiles and rates of decline on the Mattis Dementia Rating Scale in autopsy-confirmed frontotemporal dementia and Alzheimer's disease. J Int Neuropsychol Soc. 2008;14: 373-383.
8. Roberson ED, Hesse JH, Rose KD, Slama H, Johnson JK, Yaffe K, et al. Frontotemporal dementia progresses to death faster than Alzheimer disease. Neurology. 2005;65: 719-725.
9. Koedam EL, Lauffer V, van der Vlies AE, van der Flier WM, Scheltens P, Pijnenburg YA. Early-versus late-onset Alzheimer's disease: more than age alone. J Alzheimers Dis. 2010;19: 1401-1408.
10. Rossor MN, Fox NC, Mummery CJ, Schott JM, Warren JD. The diagnosis of young-onset dementia. Lancet Neurol. 2010;9: 793-806.
11. Jack CR,Jr, Knopman DS, Jagust WJ, Shaw LM, Aisen PS, Weiner MW, et al. Hypothetical model of dynamic biomarkers of the Alzheimer's pathological cascade. Lancet Neurol. 2010;9: 119-128.
12. Frisoni GB, Fox NC, Jack CR,Jr, Scheltens P, Thompson PM. The clinical use of structural MRI in Alzheimer disease. Nat Rev Neurol. 2010;6: 67-77.
13. Sperling RA, Aisen PS, Beckett LA, Bennett DA, Craft S, Fagan AM, et al. Toward defining the preclinical stages of Alzheimer's disease: recommendations from the National Institute on Aging-Alzheimer's Association workgroups on diagnostic guidelines for Alzheimer's disease. Alzheimers Dement. 2011;7: 280-292.
14. McMahon PM, Araki SS, Sandberg EA, Neumann PJ, Gazelle GS. Cost-effectiveness of PET in the diagnosis of Alzheimer disease. Radiology. 2003;228: 515-522.

Chapter 2

Advanced MR neuroimaging in early-stage presenile dementia

Chapter 2.1

Diagnostic classification of arterial spin labeling and structural MRI in presenile early-stage dementia

Esther E. Bron
Rebecca M.E. Steketee
Gavin C. Houston
Ruth A. Oliver
Hakim C. Achterberg
Marco Loog
John C. van Swieten
Alexander Hammers
Wiro J. Niessen
Marion Smits
Stefan Klein

Hum Brain Mapp. 2014;35:4916-31.

ABSTRACT

Because hypoperfusion of brain tissue precedes atrophy in dementia, the detection of dementia may be advanced by the use of perfusion information. Such information can be obtained non-invasively with arterial spin labeling (ASL), a relatively new MR technique quantifying cerebral blood flow (CBF). Using ASL and structural MRI, we evaluated diagnostic classification in 32 prospectively included presenile early-stage dementia patients and 32 healthy controls. Patients were suspected of Alzheimer's disease or frontotemporal dementia. Classification was based on CBF as perfusion marker, gray matter (GM) volume as atrophy marker, and their combination. These markers were each examined using six feature extraction methods: a voxel-wise method and a region of interest (ROI)-wise approach using five ROI-sets in the GM. These ROI-sets ranged in number from 72 brain regions to a single ROI for the entire supratentorial brain. Classification was performed with a linear support vector machine classifier (SVM). For validation of the classification method on the basis of GM features, a reference dataset from the Alzheimer's Disease Neuroimaging Initiative (ADNI) database was used consisting of AD patients and healthy controls. In our early-stage dementia population, the voxelwise feature-extraction approach achieved more accurate results (area under the curve (AUC) range=86-91%) than all other approaches (AUC=57-84%). Used in isolation, CBF quantified with ASL was a good diagnostic marker for dementia. However, our findings indicated only little added diagnostic value when combining ASL with the structural MRI data (AUC=91%) which did not significantly improve over accuracy of structural MRI atrophy marker by itself.

INTRODUCTION

The growing prevalence of dementia is an increasing health problem [1]. Early and accurate diagnosis is beneficial for patient care, aiding the planning of care and living arrangements, and preserving function and independence for as long as possible [2,3]. In addition, an early and accurate diagnosis increases research opportunities into understanding the disease process and into the development of treatments. However, early-stage diagnosis can be very difficult, as clinical symptoms and the loss of brain tissue, atrophy, may not yet be marked. To aid the diagnosis of dementia, machine-learning techniques applied to imaging and associated data are of interest. These techniques may improve diagnosis of individual patients, since they are trained on group differences which may not be noted from qualitative visual inspection of brain imaging data. The machine-learning techniques use labeled data to train a classifier to categorize two groups (e.g. patients and controls) based on features derived from brain imaging or other data. Several studies demonstrated the successful classification of dementia based on atrophy derived from structural MRI using such machine-learning methods, (e.g. [4-13]).

Because hypoperfusion of brain tissue precedes atrophy in dementia [14,15], early diagnosis may be advanced by the use of perfusion information. Such information can be obtained with ASL, an MRI technique which measures brain perfusion noninvasively, i.e. without the need for injecting contrast media [16,17]. ASL uses inversion labeling of arterial blood to quantify the CBF.

Although previous studies have indicated that perfusion information may be valuable for diagnosing early-stage dementia [18-20], to the best of our knowledge only three studies have applied machine-learning techniques to ASL data showing the diagnostic value of ASL for Alzheimer's disease (AD) using linear discriminant analysis [21], for frontotemporal dementia (FTD) using logistic regression methods [22], and for mild cognitive impairment using regression preceded by local linear embedding [23].

In this work, we studied the value of CBF as quantified with ASL for differentiation of dementia patients from healthy controls using machine-learning techniques. This was studied on a patient group consisting of presenile (disease onset <65 years), early-stage dementia patients suspected of AD or FTD and a matched control group (Group I). For comparison of the structural-MRI-based classifications with previous work (e.g. [4-13]), we also included a reference dataset from the Alzheimer's Disease Neuroimaging Initiative (ADNI) database (Group II). We evaluated several linear SVM classification methods. Two aspects of the classification model were examined: 1) the type of data, and 2) the feature-extraction approach. For the first aspect, we included three groups of data in the analysis: CBF as perfusion marker on its own, gray matter (GM) volume as an atrophy marker, obtained from high-resolution structural T1-weighted (T1w) MRI, and their combination. CBF and GM features were combined using four methods: feature concatenation, feature multiplication, and classifier combination using both the product rule and the mean rule [24]. For the second aspect regarding feature extraction, we examined the two main approaches that were used in previously published dementia-classification papers: voxel-wise (e.g. [8]) and ROI-wise feature extraction (e.g. [10]).

MATERIALS AND METHODS

Participants

Group I consisted of participants from the Iris study, which was approved by the review board at our institution. Informed consent was obtained from all participants. For this group, 32 presenile patients with early-stage dementia (17 male, age = 62.8±4.1 years) were recruited from the outpatient clinic. As presenile dementia is defined by the age at disease onset (<65 years), this does not exclude a 69-year-old patient to suffer from a presenile form of dementia. Therefore, we considered patients in the age range of 45-70 years and with a Mini Mental State Examination (MMSE) score ≥ 20 for inclusion. Exclusion criteria were normal pressure hydrocephalus, Huntington's disease, cerebral vascular disease, psychiatric disease, alcohol abuse, brain tumor, epilepsy or encephalitis. All patients underwent neurological and neuropsychological examination as part of their routine diagnostic work up, and diagnosis of dementia was established in a multidisciplinary clinical meeting on the basis of neurological, neuropsychological and conventional-imaging criteria. Patients who were subsequently suspected of having either AD [25-27] or FTD [28] were asked to participate in this study. The participating patients had a MMSE score of 26.6±2.9 (mean ± standard deviation) out of 30. This indicated that cognitive function was not yet much impaired, and confirmed that dementia was still at an early stage. Based on patient history and neuropsychological testing, every patient was assigned a provisional diagnostic label in the multidisciplinary meeting. These labels were probable AD (n=8), possible AD (n=3), AD/FTD (n=9), possible FTD (n=8), and probable FTD (n=3). We additionally included 32 age-matched healthy controls (18 male, age = 62.0±4.4 years). Control subjects had no history of neurological or psychiatric disease and did not have contraindications for MRI. An MMSE score was obtained from 23 of the controls, which was 29.0±1.0 on average.

Group II consisted of participants from the ADNI and was used as reference dataset for validation of the pipeline for classification based on GM features**.** This group was included to enable comparison with results from previous papers. The ADNI was launched in 2003 by the National Institute on Aging, the National Institute of Biomedical Imaging and Bioengineering, the Food and Drug Administration, private pharmaceutical companies and non-profit organizations, as a $60 million, 5-year public-private partnership. The primary goal of ADNI has been to test whether serial MRI, PET, other biological markers, and clinical and neuropsychological assessment can be combined to measure the progression of mild cognitive impairment (MCI) and early AD. The ADNI cohort used in this paper is adopted from the study of Cuingnet et al. [11], from which we selected the AD patient group and the elderly control group. The inclusion criteria for participants were defined in the ADNI GO protocol (http://www.adni-info.org/Scientists/Pdfs/ADNI_Go_Protocol.pdf). The patient group consisted of 137 patients (67 male, age = 76.0±7.3 years, MMSE = 23.2±2.0)), and the control group of 162 participants (76 male, age = 76.3±5.4 years, MMSE = 29.2±1.0).

MR imaging

For Group I, images were acquired on a 3T MR scanner (Discovery MR750, GE Healthcare, Milwaukee, WI, USA) using a dedicated 8-channel brain coil. For each participant, a T1w image and a pseudo-continuous ASL image [29,30] were acquired. T1w images were acquired with a 3D inversion recovery (IR) fast spoiled gradient-recalled echo (FSPGR) sequence with the following parameters: inversion time (TI) = 450 ms, repetition time (TR) = 7.9 ms, and echo time (TE) = 3.1 ms. These T1w images had a resolution of 0.94x0.94 mm in the sagittal plane and a slice thickness of 1.0 mm. For ten of the controls, T1w images were acquired axially with a resolution of 0.94x0.94x0.8 mm and acquisition parameters of TI=450 ms, TR=6.1 ms, and TE=2.1 ms. Acquisition time was around 4 minutes. The ASL data were acquired with a post-labeling delay time of 1.53 s using background suppression. 3D acquisition was performed with an interleaved stack of spiral readouts using 512 sampling points on 8 spirals, resulting in an isotropic 3.3 mm resolution in a 24 cm field of view. Other imaging parameters were: TR=4.6 s, TE=10.5 ms, number of excitations = 3, labeling pulse duration =1.45 s. The reconstructed voxel size was 1.9x1.9x4 mm. For the ASL data, the acquisition time was 4:30 minutes.

For Group II, T1w imaging data were acquired at 1.5T. Acquisition had been performed according to the ADNI acquisition protocol [31].

Image Processing

Probabilistic tissue segmentations were obtained for white matter (WM), gray matter (GM) and cerebrospinal fluid (CSF) on the T1w image using the unified tissue segmentation method [32] of SPM8 (Statistical Parametric Mapping, London, UK). To minimize errors in the image processing, visual inspections of the tissue maps were performed after specific image processing steps. The tissue segmentation procedures did not compensate for white matter lesions and infarcts, but this was not necessary as patients with a history of cerebrovascular accidents (CVA) or CVA reported in their MRI examination were excluded from our study. Accordingly, since the study population was quite young and vascular dementia patients were not included, only few white matter lesions were present.

For Group I, ASL imaging data consisted of a difference image (ΔA) and a control image (A_0) [33]. To obtain an indication of the image quality, we estimated the signal-to-noise ratio (SNR) of the ΔA images of five randomly chosen patients and five controls. SNR was defined as,

$$\mathrm{SNR}_{\Delta A} = \frac{\mu_{\Delta A}}{\sigma_{noise}} \qquad [1]$$

in which $\mu_{\Delta A}$ is the mean ΔA in a small ROI in the brain, and σ_{noise} is the standard deviation of the signal in a small ROI in the background. For the patients the SNR was 20.3 ± 7.7 (mean ± std), and for the controls 27.0 ± 5.4. Figure 1A shows an example ΔA scan for a patient with SNR=24.4.

For each subject, T1w images were rigidly registered to the A_0 images using Elastix registration software [34] by maximizing mutual information [35] within a mask. For the T1w images, a dilated brain mask obtained with the brain extraction tool (BET) [36] was used, and for the A_0 image, voxels with zero intensity, outside the brain, were masked out. All registrations were visually checked. Tissue maps and brain masks were transformed to ASL space accordingly. In the ASL space, ΔA and A_0 were corrected for partial volume effects using local linear regression based on the tissue probability maps using a 3D kernel of 3x3x3 voxels [37,38]. CBF maps were quantified using the single-compartment model by Buxton et al. [33] as implemented by the scanner manufacturer. Figure 1B shows the partial volume corrected CBF map which corresponds to the ΔA image in Figure 1A. After quantification, CBF maps were transformed to T1w space. In the analysis only the CBF in the GM was used, as cortical CBF is of primary interest in the disease processes studied here. In addition, quantification of CBF with ASL in WM is less reliable than in GM [39].

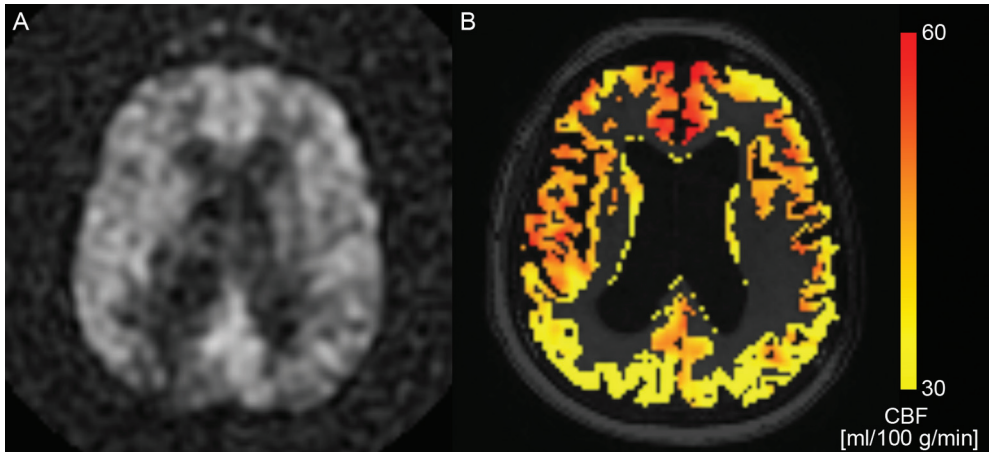

Figure 1: A) ASL difference scan (ΔA) of a dementia patient (SNR=24.4), and B) the corresponding CBF map in the GM after partial volume correction in color overlay. The background image in B) is the T1-weighted image.

For partial volume correction of the ASL images and for estimation of intracranial volume, a brain mask was required for each subject. This brain mask was constructed using a multi-atlas segmentation approach. We performed brain extraction [36] on the T1w images associated with a set of 30 atlases [40,41], checked the brain extractions visually, and adjusted extraction parameters if needed. The extracted brains were transformed to each subject's T1w image and the labels were fused, resulting in a brain mask for each subject. The multi-atlas segmentation approach is explained in more detail the next section.

Common template space and individual regions-of-interest (ROIs)

For each subject, we defined two image spaces which refer to the coordinate systems of the subject's ASL and T1w scan respectively: an ASL-space (Ω_{ASL}) and a T1w-space (Ω_{T1w}). Additionally, a common template space ($\Omega_{Template}$) was defined on the basis of the T1w images of all subjects. For registration of images, the following notation is used: a transformation $\boldsymbol{T}$ is applied to an image (moving image, M) to optimally fit another image (fixed image, F). The deformed moving image can be written as $M(\boldsymbol{T})$. Figure 2 illustrates the image spaces and the transformations between them.

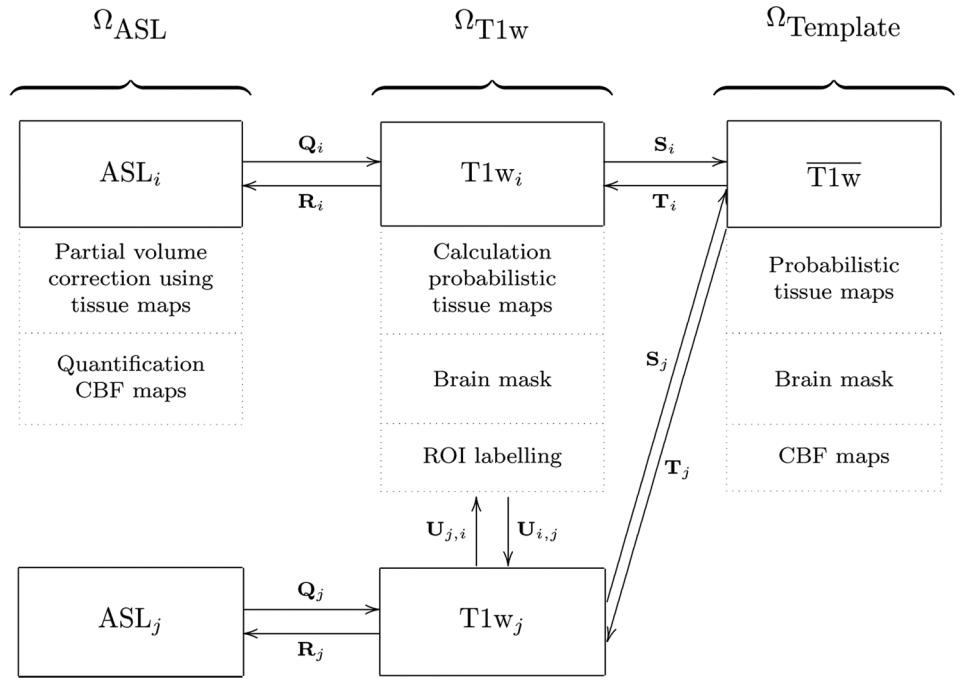

Figure 2: Image spaces including processed images in these spaces: ASL space (Ω_{ASL}), T1w space (Ω_{T1w}) and the template space ($\Omega_{Template}$). Transformations between the image spaces are indicated by **Q**, **R**, **S**, **T**, and **U**. The arrows are pointing from the fixed to the moving domain. Different subjects are represented by *i* and *j*. From all $T1w_j$, a template space image (1) is calculated. In each image space, the dotted boxes represent the processed images.

The template space ($\Omega_{Template}$) was constructed based on the T1w images of all subjects using a procedure that avoids bias towards any of the individual T1w images [42]. In this approach, the coordinate transformations from the template space to the subject's T1w space ($\boldsymbol{T}_i$: $\Omega_{Template} \rightarrow \Omega_{T1w,i}$) were derived from pairwise image registrations. For computation of $\boldsymbol{T}_i$, the T1w image of an individual subject ($T1w_i$) was registered to all other subjects' images ($T1w_j$) using $T1w_i$ as the fixed

image. This resulted in a set of transformations $\boldsymbol{U}_{i,j}$: $\Omega_{T1wi} \rightarrow \Omega_{T1wj}$. By averaging the transformations $\boldsymbol{U}_{i,j}$, the transformation $\boldsymbol{S}_i$: $\Omega_{T1wi} \rightarrow \Omega_{Template}$ was calculated:

$$S_i(x) = \frac{1}{N} \sum_{(j=1)}^{N} U_{i,j}(x) \qquad [2]$$

The transformation $\boldsymbol{T}_i$ was calculated as an inversion of $\boldsymbol{S}_i$: $\boldsymbol{T}i = \boldsymbol{S}_i^{-1}$. Note that the identity transformation $\boldsymbol{U}_{i,i}$ is also included in [2]. The pairwise registrations were performed using a similarity, affine, and non-rigid B-spline transformation model consecutively. A similarity transformation is a rigid transformation including isotropic scaling. The non-rigid B-spline registration used a three-level multi-resolution framework with isotropic control-point spacing of 24, 12, and 6 mm in the three resolutions respectively. A T1w template image was created by averaging the deformed individual T1w images. This template was thresholded and dilated to create a dilated brain mask for this population. To prevent background information in the T1w images from influencing the process, the complete pairwise registration procedure was repeated masking the $T1w_i$ images with these dilated brain masks in Ω_{T1wi}. To check if subjects were properly registered to the template space, the final T1w template image was visually inspected. Processed images (P_i) were transformed to template space using $P_i(\boldsymbol{T}_i)$ for the brain masks and tissue maps, and using $P_i(\boldsymbol{R}_i(\boldsymbol{T}_i))$ for the CBF maps with $\boldsymbol{R}_i$: $\Omega_{T1wi} \rightarrow \Omega_{ASLi}$. We defined a common GM mask in template space by combining the GM segmentations of all subjects using majority vote. The voxel-wise CBF features included only voxels within this common GM mask.

Five sets of ROIs in the gray matter were constructed for every subject individually in T1w space (Ω_{T1w}) differing in the number and size of ROIs (Figure 3): A) regional labeling of the supratentorial brain (*region*; 72 features), B) selection of brain regions affected by AD or FTD based on the literature (*selection*; 28 features; [43-55], C) brain lobes (*lobe*; occipital, temporal, parietal, frontal lobes and central structures in both hemispheres; 10 features), D) hemispheres (*hemisphere*; 2 features), and E) the total gray matter in the entire supratentorial brain (*brain*; 1 feature). The ROI-sets were constructed using a multi-atlas segmentation procedure. Thirty labeled T1w images containing 83 ROIs each [40,41] were used as atlas images. The atlas images were registered to the subject's T1w image using a rigid, affine, and non-rigid B-spline transformation model consecutively. A rigid transformation model was used instead of the similarity transformation model that was used in the template space registrations. The rigid model was used because the similarity transformation failed here, probably due to the cropping around the brain which had been performed in the atlas images to remove most non-brain tissue. Registration was performed by maximization of mutual information [35] within dilated brain masks [36]. For initialization, the dilated brain masks were rigidly registered. For non-rigid registration, the same multi-resolution settings were used as in the template-space construction. The subjects' T1w images were corrected for inhomogeneities to improve registrations [56]. Labels were fused using a majority voting algorithm [57]. All final region segmentations were visually inspected. The brain stem, corpus callosum, third ventricle, lateral ventricles, cerebellum, and substantia nigra were excluded. For construction of the *lobe*, *hemisphere* and

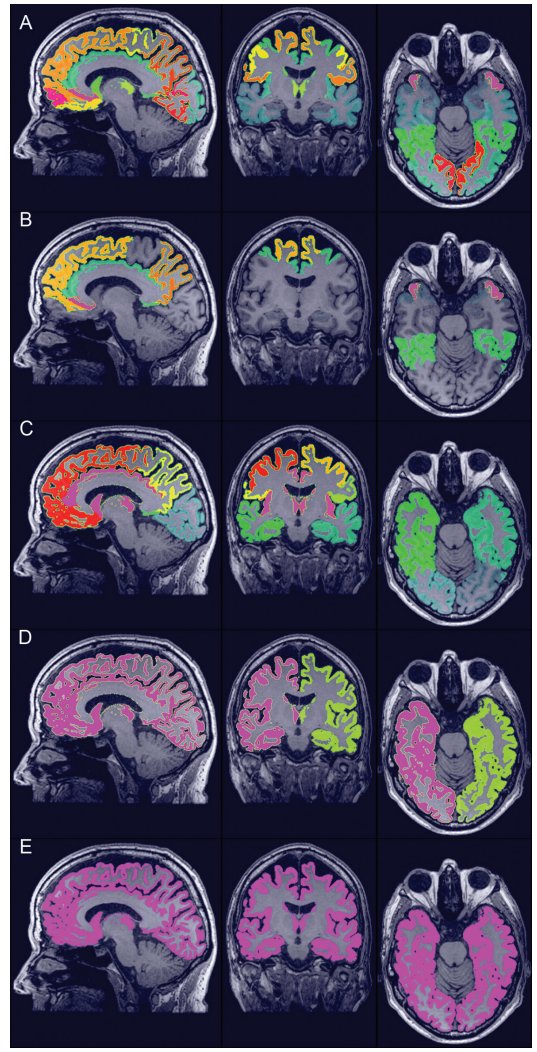

Figure 3: The five ROI-sets for ROI-wise feature extraction of the gray matter: A) *region* (72 features), B) *selection* (28 features), C) *lobe* (10 features), D) *hemisphere* (2 features), and E) *brain* (1 feature).

brain GM ROIs, the regions were fused in the original atlas images before transformation to Ω_{T1w}.

Classification methods

We evaluated two aspects of dementia classification, which are discussed in this section: 1) the type of data, and 2) the method used to extract features. For the first aspect, classifications were performed using three types of data: CBF values quantified with ASL, GM volumes derived from the T1w images, and their combination. Four combination strategies were explored. In the first strategy, the feature vectors for CBF and GM were concatenated into one large feature vector, which was used to train the classifier (*[CBF GM]*, feature concatenation). In the second strategy, we multiplied the CBF and GM features element-wise (*CBF * GM*, feature multiplication). In the third and fourth strategy, two separate SVM models for CBF and GM were combined by respectively the product rule: $(\omega(CBF) * \omega(GM))$ and the mean rule: $\left(\frac{1}{2}(\omega(CBF) + \omega(GM))\right)$ [24]. In these approaches, the combined classifier was obtained by multiplication or averaging of the posterior class probabilities (ω) of the single modality classifiers and by renormalizing the posterior probabilities. As an SVM does not naturally output posterior probabilities, these were obtained from the distance between the sample and the classifier by applying a logistic function [58]. For the second aspect, six methods were used to extract features from the data: a voxel-wise method (*voxel*) and a ROI-wise approach using the five previously defined ROI-sets (*region*, *selection*, *lobe*, *hemisphere*, and *brain*). These methods were applied in turn to the T1w data, ASL data and combined data. Voxel-wise features were defined as CBF intensities and GM probabilistic segmentations in the template space ($\Omega_{Template}$) [8,11]. For the CBF

features, only voxels within the common GM mask were included. For the GM segmentations, we performed a modulation step, i.e. multiplication by the Jacobian determinant of the deformation field (Figure 2, transformation $\boldsymbol{T}_j$), to take account of compression and expansion [59]. This modulation step ensures that the overall GM volume was not changed by the transformation to template space. The ROI-wise features were calculated in subject T1w space (Ω_{T1w}) for the five ROI-sets. The CBF features were defined as the mean CBF intensity in the GM, and the GM features as the GM volume obtained from the probabilistic GM maps [10,11]. To correct for head size, the GM features were divided by intracranial volume. All features were normalized to have zero mean and unit variance.

Analysis and statistics

For classification, linear SVM classifiers [60] were applied using the LibSVM software package [61]. Classification performance was quantified by the AUC. The SVM C-parameter was optimized using grid search on the training set with LOO cross-validation.

On Group I, the SVM classifiers were trained and tested using both LOO cross-validation and iterated four-fold cross-validation. LOO cross-validation was used for calculation of classification performance because it uses the maximum number of available data for training of the classifier, resulting in the best possible classifier using those data and features. In four-fold cross-validation, on the other hand, only a part of the available training data is used, which allows for calculation of the standard deviations on the AUC. These standard deviations provide an indication of the robustness of the classifier, i.e. the dependence of the performance on the sampling of training and test sets. For the iterated four-fold cross-validation, classification was performed iteratively on four groups, each consisting of eight patients and eight control subjects, using repeatedly three groups for training and one group for testing. The total number of iterations was 50. To assess whether ASL improved the performance of the classifications relative to those based on structural GM features only, we performed McNemar's binomial exact test.

For detection of features associated with group differences using the SVM classifier, we calculated statistical significance maps (p-maps). Using permutation testing, a null distribution for the features was obtained using 5000 permutations [62,63]. The p-maps were calculated for every feature extraction method on both the CBF and GM data. We used a p-value threshold of α=0.05 and we did not correct for multiple comparisons, as permutation testing has a low false positive detection rate [64]. Voxel-wise p-maps were visually inspected to identify clusters of significant voxels.

On Group II, we evaluated the classifications based on GM features. Instead of cross-validation, separate training and test sets were used for classification. The participants were randomly split into two groups of the same size, a training set and a test set, while preserving the age and sex distribution [11]. All post-processing and classification methods were identical to those of group I, except for the construction of the template space which is for group II only based on the

training set. In Cuingnet et al. [11], classification results are presented as the highest sum of sensitivity and specificity. For comparison, we also included this measure for Group II.

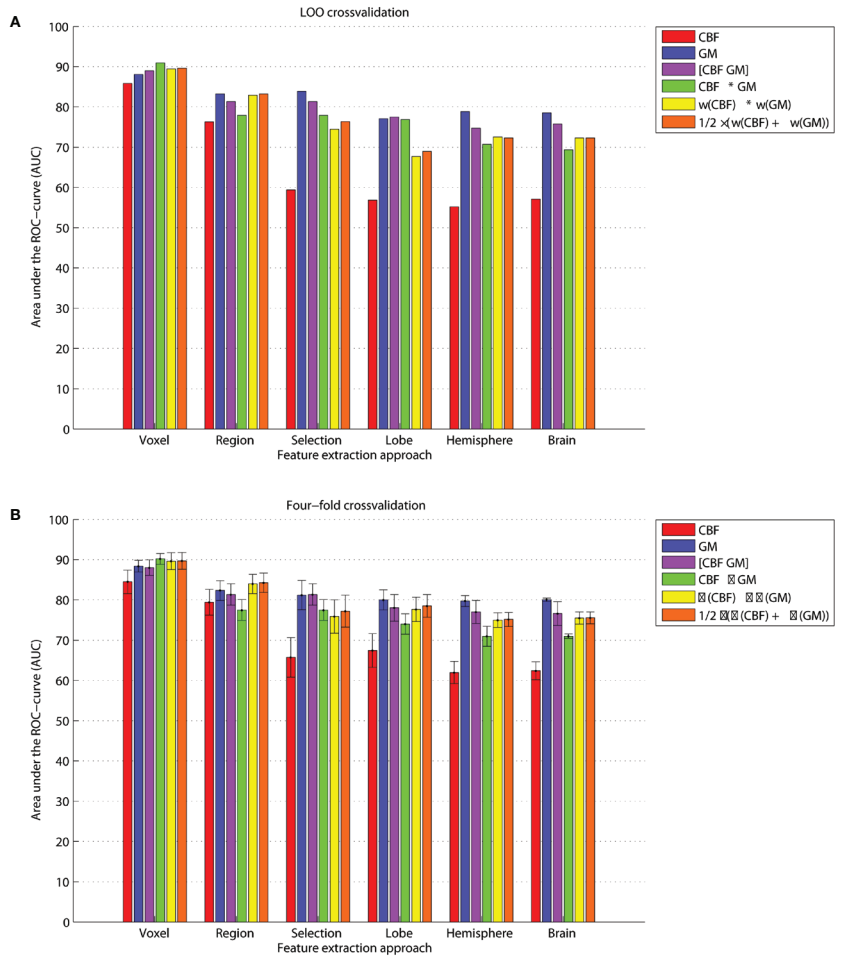

Figure 4: Classification performances quantified by the area under the ROC-curve (AUC) determined using (a) leave-one-out and (b) four-fold cross-validation. For the four-fold cross-validation, the bars represent mean AUC and the standard deviations are shown as error bars. Features were extracted using two approaches: voxel-wise and ROI-wise using 5 **GM** ROI-sets (*region*, *selection*, *lobe*, *hemisphere* and *brain*). We included *CBF* data, *GM* data, and their combination using 1) feature concatenation (*[CBF GM]*), 2) feature multiplication (*CBF * GM*), 3) the product rule $\left(\omega(CBF) * \omega(GM)\right)$, and 4) the mean rule: $\left(\frac{1}{2}\left(\omega(CBF) + \omega(GM)\right)\right)$

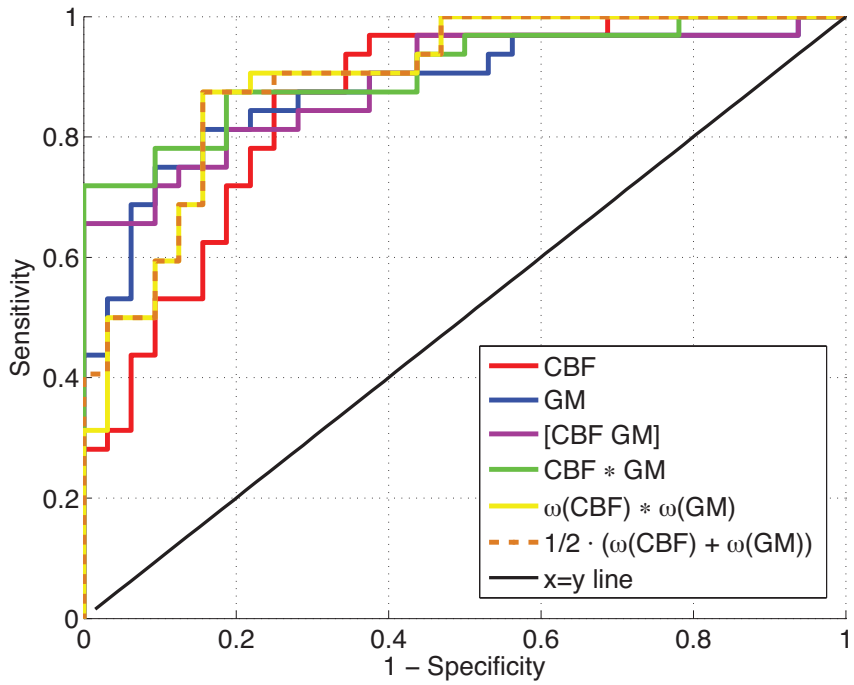

Figure 5: Receiver operator characteristic (ROC) curves for the voxel-wise classifications using LOO cross-validation: based on CBF features, GM features, and the combination of both using feature concatenation (*[CBF GM]*), feature multiplication (*CBF * GM*), the product rule $(\omega(CBF) * \omega(GM))$, and 4) the mean rule $\left(\frac{1}{2}(\omega(CBF) + \omega(GM))\right)$

RESULTS

Group I

Figure 4 shows the classification results for a) the LOO cross-validation, and b) the iterated four-fold cross-validation. The voxelwise feature-extraction approach (AUC range=86-91%) resulted in higher performance than all other approaches (AUC range=57-84%). CBF and GM single modality classifications performed similarly in the voxel-wise approach, but in the ROI-wise approaches the AUC for the CBF classification declined with decreasing feature numbers.

For the voxel-wise method, the combination of CBF and GM data (AUC range=89-91%) performed somewhat better than classification based on a single modality (AUC=86-88%) as can be appreciated from the ROC-curves shown in Figure 5. For the other approaches, the GM classification performed best (AUC range=77-84%) and this was not improved by adding the CBF data (AUC range=73-83%). In the voxel-wise approach, the feature multiplication method had a slightly higher performance than the other approaches, but overall the performances of the four combination methods were similar. For the region-wise meth-

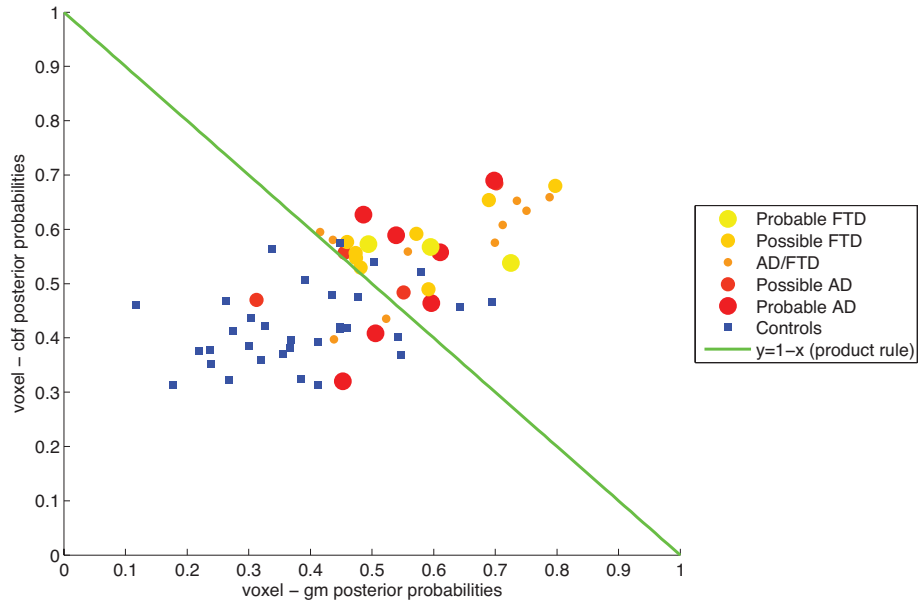

Figure 6: Scatter plot of the posterior probabilities for the voxel-wise classifications based on GM features (x-axis) and CBF features (y-axis). Patients are represented by dots colored and sized according to the assigned provisional diagnostic label. Controls are represented by blue squares. The green line (y=1-x) shows the decision boundary for the product rule and mean rule combination methods (for a threshold of 0.5 on the combined posterior probability).

od, combination of CBF and GM by the product and mean combination methods (AUC=83%) performed better than feature concatenation or multiplication (AUC range=78-81%), while in the other ROI-wise approaches with fewer ROIs, feature concatenation was the best performing combination method.

The McNemar tests showed no significant differences between the performance of the voxel-wise classification based on GM features and the other voxel-wise classifications: CBF (p=0.38), the mean rule (p=0.38), and the other combination methods (all p=1.0).

Generally, the mean classification performances for the iterated four-fold cross-validation were similar to those obtained with LOO cross-validation (Figure 4b). The standard deviations, indicated by the error bars in Figure 4b, showed that the classifications had a relatively small variance and were rather robust.

Posterior probabilities for the voxel-wise classifications are shown in Figure 6 and do not indicate that the type of dementia influences the success for patients of being correctly classified, as AD and FTD patients cannot be clearly separated in the plot. It should be noted that the classifiers were not trained for this specific differentiation.

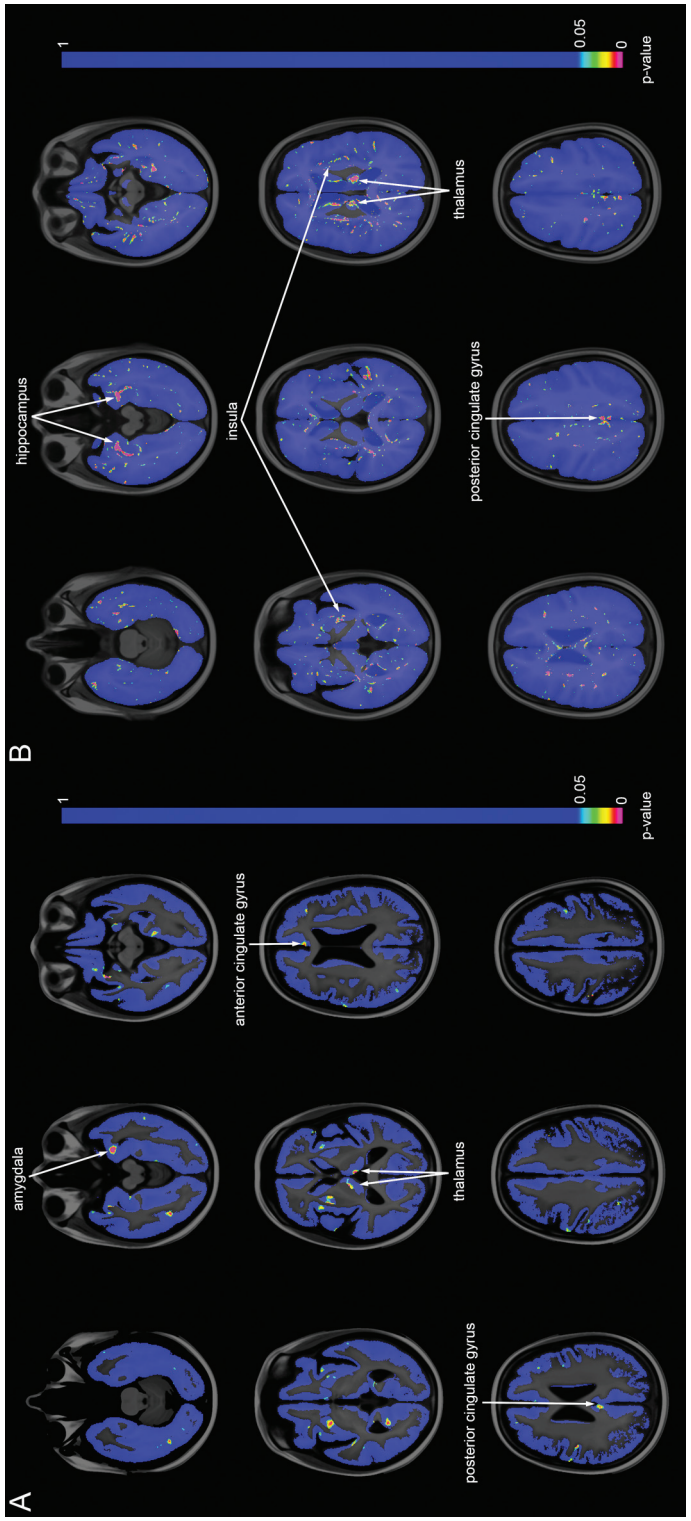

Figure 7: Statistical significance maps (p-maps) for the voxel-wise classifications: A) CBF, B) GM. Non-blue voxels are significantly different (p<0.05) between patient and control groups based on SVM classification.

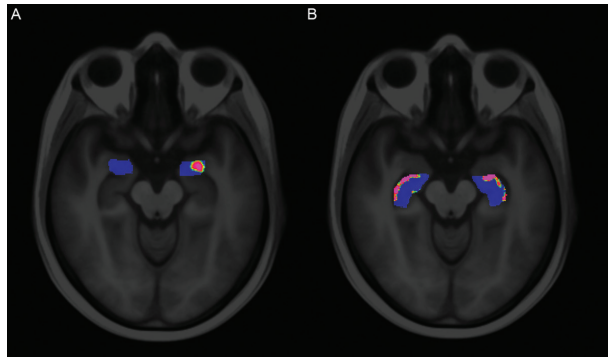

Figure 8: Voxel-wise p-maps A) within the amygdala for CBF, and B) within the hippocampus for GM. These two regions showed the highest percentage of significant voxels. The regions were based on the region labeling in template space. Non-blue voxels are significantly different (p<0.05).

P-maps for the voxel-wise classifications are shown in Figure 7. For CBF (Figure 7a), several clusters of significantly different voxels were observed, located mainly in the thalamus, amygdala, and anterior and posterior cingulate gyrus. For GM (Figure 7b), clusters of significantly different voxels were seen in the hippocampus, insula, posterior cingulate gyrus and thalamus. We also observed significantly different voxels in regions with a low GM probability, around the ventricles and corpus callosum. Table 1 lists all regions with visually observed clusters of

Table 1: Regions with clusters of significant voxels in the p-maps

CBF	GM
Amygdala (left > right)	Hippocampus (bilateral)
Cingulate gyrus, anterior part (left)	Insula (bilateral)
Cingulate gyrus, posterior part (right)	Cingulate gyrus, posterior part (bilateral)
Thalamus (bilateral)	Thalamus (bilateral)
Postcentral gyrus (right > left)	Medial temporal gyrus (bilateral)
Inferior frontal gyrus (bilateral)	Inferior temporal gyrus (bilateral)
Putamen (right > left)	Lingual gyrus (bilateral)
Insula (left)	Superior frontal gyrus (bilateral)
Medial frontal gyrus (bilateral)	
Superior frontal gyrus (left)	
Caudate nucleus (left)	
Occipital gyrus (left)	
Gyrus parahippocampalis (bilateral)	
Medial temporal gyrus (bilateral)	

significantly different voxels in the p-map. Within these regions, as defined by Hammers et al. [41] and Gousias et al. [40], only a small percentage of voxels was significantly different. For CBF, the highest percentage of significantly different voxels was observed in the amygdala (20%), and for GM in the hippocampus (18%), see Figure 8.

In the supplementary materials, the p-values for the *region* classification are listed. For CBF, two significantly different regions were found, and for GM one region. For CBF, one of the significantly different regions was also clearly found in the voxel-wise p-maps. However, for GM this correspondence was less clear since the only significantly different ROI (right Subgenual anterior cingulate gyrus) was not shown in the voxel-wise p-map. The regions with the most clear clusters of significantly different voxels in the voxel-wise p-map **(**hippocampus, insula and thalamus) were not found to be significantly different in the region-wise approach. In the *selection* and *lobe* ROI-wise approaches , two significantly different ROIs were found for both CBF (*selection*: superior parietal gyrus left and pre-subgenual anterior cingulate gyrus right; *lobe*: occipital lobe left and frontal lobe right) and GM (*selection*: subgenual anterior cingulate gyrus right and pre-subgenual anterior cingulate gyrus left; *lobe*: temporal lobe left and right). For *hemisphere* and *brain*, no significant ROIs were found.

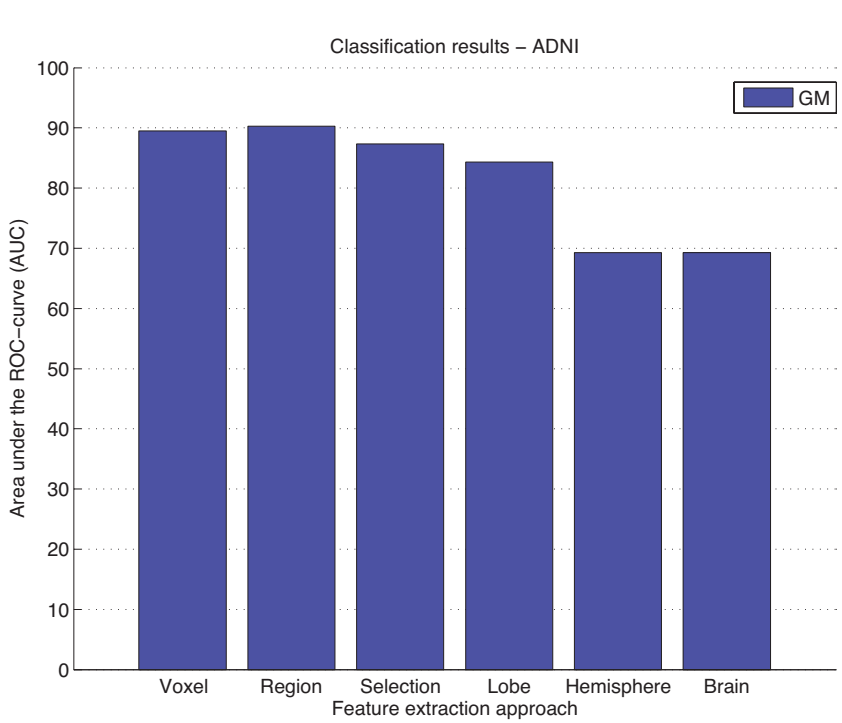

Figure 9: Classification performances for the ADNI data quantified by the area under the ROC-curve (AUC). GM features were extracted using two approaches: voxel-wise, and ROI-wise using 5 **GM** ROI sets (region, selection, lobe, hemisphere, and brain).

Group II

Classification performances based on GM features for the ADNI reference data are shown in Figure 9. For both voxel- and ROI-wise approaches, we obtained an AUC of about 90%. For the voxel-wise method, the performance reported by Cuingnet et al. [11] was somewhat higher than what we found (Table 2). For the region-wise method, performances were similar: we obtained a slightly higher sum of sensitivity and specificity, and Cuingnet et al. [11] obtained a slightly higher AUC.

Table 2: Classification performance on the ADNI reference data for the voxel- and region-wise approaches compared to the performances on the same data reported by Cuingnet et al. [11]. The method Voxel-Direct-D-gm is similar to our voxel-wise method, using modulated GM maps, and the method Voxel-Atlas-D-gm is similar to our method region, using features for a set of ROIs. Performance measures were area under the ROC curve (AUC), sensitivity (Sens.), specificity (Spec.), and the sum of sensitivity and specificity (Sum).

Study	Method	AUC (%)	Sens. (%)	Spec. (%)	Sum
This study	*voxel*	89	85	79	165
Cuingnet et al.	Voxel-Direct-D-gm	95	81	95	176
This study	*region*	90	83	90	172
Cuingnet et al.	Voxel-Atlas-D-gm	92	78	91	169

DISCUSSION

We evaluated different approaches for classification of early-stage presenile dementia patients and controls. These approaches included different types of MRI data, and both voxel-wise and ROI-wise methods for feature extraction. In this section we first discuss the classification performances on Group I. Second, the added value of ASL for diagnosis of dementia is discussed. Finally, we discuss the validation of methods using the reference dataset of Group II.

Classification performance

The voxel-wise classification methods showed a high diagnostic performance with an AUC of up to 91% for early-stage presenile dementia (Group I). We can consider this a high accuracy for this patient population, because the patients were still at an early stage of the disease, when both clinical symptomatology and GM atrophy are known to be less pronounced than at more advanced stages of the disease. Additionally, our patient population was relatively young, since we only included presenile dementia patients. The group was also rather heterogeneous,

as patients were included when they were suspected of suffering from either AD or FTD, in which different regions of the brain are affected. In AD, hypoperfusion and atrophy are expected mainly in the medial temporal and parietal lobes, while in FTD this is mainly seen in the frontal and temporal lobes [65]. Such heterogeneity of affected brain regions makes the classification of dementia more difficult. Due to these issues, diagnostic performance in this group may be expected to be lower than that in homogeneous patient populations at more advanced stages of disease. However, one can also argue that a young patient group and therefore also a young control group, may have positively influenced the diagnostic performance as the younger control group is not so much affected by age-related atrophy and might therefore be better distinguishable. For Group I, cross-validation was used for estimating classifier performance. This technique is frequently used and mainly applied when a relatively small amount of data is available (for classification of dementia). The voxel-wise methods overall provided higher performance than the ROI-based techniques, which indicates that important diagnostic information was lost by averaging over the ROIs. This is illustrated by the p-maps obtained with permutation testing (Figure 7-Figure 8: Voxel-wise p-maps A) within the amygdala for CBF, and B) within the hippocampus for GM. These two regions showed the highest percentage of significant voxels. The regions were based on the region labeling in template space. Non-blue voxels are significantly different ($p<0.05$).), which showed that the voxel-wise classifiers mainly rely on small clusters of voxels within the anatomically defined regions used here. These clusters only maximally covered 20% of the voxels within such a region. Therefore, we can assume that the used anatomical region labeling was not optimal for the ROI-wise classifications, as the regions may have been too large to be sensitive to information from a small proportion of significantly different voxels.

For the voxel-wise and *region* methods, the feature concatenation method was outperformed by the other combination methods, possibly due to the large number of features relative to the small amount of data. However, for the other ROI-wise approaches, feature concatenation was the best performing combination methods. The relatively small standard deviations obtained with the four-fold cross-validation indicated that the classifications were rather robust.

When using one feature only, i.e. whole brain measures, ROI-wise methods for GM still gave a relatively good performance (AUC=73%). However for CBF, the classification performance declined with decreasing number of features. Especially remarkable was the reduction in AUC for CBF after selection of 28 dementia-related brain regions. For the GM classifications, we did not find this dramatic decrease in performance. This might be due to the fact that the regions were selected on the basis of the literature reporting either focal atrophy or hypoperfusion/hypometabolism. Such regions may not coincide, particularly not in the early stage of dementia. For instance, in fluoro-deoxyglucose positron emission tomography (FDG-PET) studies no significant hypoperfusion is found in specific brain regions which are known to have volume loss in AD, for example the hippocampus [66,67], or vice versa. For assessing the diagnostic performance of CBF classification methods, the *selection* classification may have reduced performance because certain regions may have been included that only exhibited atrophy but not perfusion changes.

Using the p-maps, we visualized which features were significant for classification. For CBF, we mainly found clusters of significantly different voxels in the amygdala, thalamus and cingulate gyrus, corresponding to findings from the literature on AD reporting hypoperfusion in the cingulate gyrus and prefrontal cortex. Hypoperfusion in the parietal lobe is also reported, but was not found here [19]. For GM, significantly different voxels were found in the hippocampus, insula, thalamus and cingulate gyrus, corresponding to the literature [68-70]. GM p-maps were mostly symmetrical, showing similar clusters of significantly different voxels bilaterally, whereas CBF p-maps where more asymmetrical. Some asymmetry is expected particularly in FTD patients [71]. Cuingnet et al. [11] did not calculate p-maps, but evaluated the optimal margin hyperplane (w-map), which provides qualitative information on the classifiers showing regions in which atrophy increased the likelihood of being classified as AD. These regions were the medial temporal lobe (including hippocampus), thalamus, posterior cingulate gyrus, inferior and middle temporal gyri, posterior middle frontal gyrus, and fusiform gyrus. This corresponds well to our p-maps as we found the same regions except the last two. In addition, we detected clusters of significantly different voxels in the insula.

Because in AD and FTD different brain regions are affected, atrophy and hypoperfusion information could be used to make a differential diagnosis. A future aim of this work is to perform a multi-class classification to distinguish the two groups of patients. One year after inclusion, follow-up information will be used to establish a definitive diagnosis which is needed for the multi-class classification.

A minor limitation of this work is that a different T1-weighted protocol was used for 10 of the control subjects. We believe that the impact of this is minor, because the used sequences are very similar, both are near isotropic with a resolution ≤ 1mm, and both sequences allow for good differentiation between white and gray matter.

The added value of ASL

CBF-based classification yielded high diagnostic performance for the voxelwise and region-wise approaches with AUCs of 87% and 76%, respectively. For the voxel-wise classification, this was similar to the diagnostic performance based on GM features ($p=0.38$, McNemar's test). This indicates that CBF quantified with ASL is a good diagnostic marker for early-stage dementia, in concordance with previous studies [18-20].

Although CBF may be a good diagnostic marker by itself, our results showed no added value over atrophy markers based on structural MRI. The four different combination methods - feature concatenation, feature multiplication, the product rule, and the mean rule - showed a slight improvement in AUC for the voxel-wise approaches, but the McNemar tests showed no significant increase in diagnostic performance by using any methods ($p\geq0.38$). For ASL to add value, other combination methods than these four may need to be explored to more efficiently com-

bine the CBF and GM features. In addition, one should note that the limited added value of ASL over structural MRI found in this work may be partly attributed to the specific methodology used, both in ASL acquisition and analysis. A potential confounder in this study is the arterial transit time (ATT), which could conceivably be different between patient and control group. However, we expect these differences to be small, since on the one hand patients with cerebral vascular disease were excluded and on the other hand the patients and control groups were age-matched. We compared our results to those of three previously published papers or abstracts studying the added value of ASL for the diagnosis of dementia. Du et al. [22] based classification of FTD patients and controls on logistic regression. The mean CBF and GM volume in certain regions in the frontal and parietal lobes were used as features. Performance was evaluated on the training data. Classification based on GM volume only showed no significant separation between the groups, but including CBF yielded an AUC of 80% ($p<0.01$). The second study by Dashjamts et al. [21] performed linear discriminant analysis to discriminate between AD patients and controls using LOO cross-validation. Features were defined for the whole brain as the normalized CBF intensities and the GM segmentation in DARTEL template space [72]. For the GM features no modulation step was performed. The number of features was reduced using a VBM approach, which performs voxel-wise t-tests at different significance levels. The classification AUCs were 78% for GM, 89% for CBF, and 92% for the combination of both using concatenation. These findings are similar to our results, except for the AUC for GM, which in their study was lower than our results and lower than the values reported by Cuingnet et al. [11] and Klöppel et al. [8]. The classifiers may have been overtrained since the feature reduction was performed on the complete set and since optimal significance levels for the classification on both CBF and GM were selected using the labels of the test data. The third study, an abstract by Schuff et al. [23], studied the classification of early MCI using local linear embedding and logistic regressions. Features were defined as the mean CBF or tissue volume for a set of ROIs. The accuracies of the classification were 67% based on the volume features, 58% based on CBF, and 71% for the combination of both.

These studies on classification using ASL [21-23] conclude that ASL improves the classification of dementia over structural MRI. Although in our dataset we also observed a small increase in performance by combining CBF and GM, we could not conclude that this significantly improves classification, as classifications on the basis of GM features alone already had a high performance. For early-stage dementia lower performances were expected, as for instance Klöppel et al. [8] reported a GM-based classification accuracy of 81.1% in a mild AD group (age $\leq$ 80 years, MMSE range = 20-30). The relatively high performances for the GM-based classifications we found here may be attributed to the presenile patient and control population, as addressed in the previous section. We therefore assume that the added value of ASL in this study was limited by the relatively high performance of the classifications based on structural MRI.

In addition, the small samples sizes of each of these studies may hinder a reliable comparison. Similar to the studies mentioned above, we used a relatively small dataset (32 patients/32 controls; Du et al.: 21 FTD/24 AD/25 controls [22]; Dashjamts et al.: 23 AD/23 controls [21]; Schuff et al.: 7 AD/44 early MCI/17 MCI/29 controls [23]). To our knowledge, the added value of ASL for classification of dementia has not been assessed with larger sample size studies, but for further verification of our conclusion larger sample size studies would be preferred.

Comparison with related work

The GM image-processing and classification methods were evaluated on an AD patient group and a healthy control group from the ADNI database (Group II) to enable comparison with related work. The classification performances we obtained were generally comparable (Table 2) to those of Cuingnet et al. [11], from which the subject groups were adopted. However, some performance differences could be observed, which we think may be largely attributed to three differences in the methodology. The first difference is in the *region* approach, in which we used 72 regions constructed with multi-atlas registration, whereas the Voxel-Atlas-D-gm of Cuingnet et al. [11] uses 119 regions from a single atlas [73]. Although our atlas contains fewer ROIs, which could impact the performance either positively, as fewer features reduce the risk of overtraining, or negatively, as fewer features contain less information, we chose this atlas because multi-atlas-based segmentation is more accurate and robust than single-atlas-based segmentation [57]. Second, the data used for template-space construction differs. We based the template space for Group II on the training data only, whereas Cuingnet's Voxel-Direct-D-gm method uses the complete set. Our approach requires less computation time which is practical for clinical use, but may perform slightly worse as the testing subjects are not included in the template space. Third, we used a different method for template-space construction. Cuingnet et al. uses the DARTEL algorithm [72] which differs from our method in three main ways: 1) DARTEL iteratively maps the scans to their average, instead of using the pairwise registrations of our approach; 2) DARTEL uses tissue segmentations instead of directly registering T1w images; and 3) DARTEL uses a large-deformation diffeomorphic algorithm, while our approach uses a small-deformation parametric (B-spline) transformation model assuming small deformations. Although the methods use different approaches, both aim to find the group mean image.

Although some steps in our method differed from the method of Cuingnet et al. [11], classification performances on the same dataset were very similar, indicating that our methodology is valid and providing context for our findings in the presenile early-stage dementia patients (Group I).

Conclusion

Of the different classification methods, voxel-wise classifications provided the best classification performance for early-stage presenile dementia and controls with an AUC of about 91%. This can be considered a high diagnostic accuracy in this presenile patient population in the very early stage of either of two different types of dementia.

Although CBF quantified with ASL was found to be a good diagnostic marker of dementia, with similar diagnostic accuracy as GM in the voxel-based classifications, its added value over structural MRI was not significant.

REFERENCES

1. Alzheimer's Association. 2011 Alzheimer's disease facts and figures. Alzheimers Dement. 2011;7: 208-244.
2. Paquerault S. Battle against Alzheimer's disease: the scope and potential value of magnetic resonance imaging biomarkers. Acad Radiol. 2012;19: 509-511.
3. Prince M, Bryce R, Albanese E, Wimo A, Ribeiro W, Ferri CP. The global prevalence of dementia: a systematic review and metaanalysis. Alzheimer Dement. 2013;9: 63-75. e2.
4. Davatzikos C, Fan Y, Wu X, Shen D, Resnick SM. Detection of prodromal Alzheimer's disease via pattern classification of magnetic resonance imaging. Neurobiol Aging. 2008;29: 514-523.
5. Duchesne S, Caroli A, Geroldi C, Barillot C, Frisoni GB, Collins DL. MRI-based automated computer classification of probable AD versus normal controls. IEEE Trans Med Imaging. 2008;27: 509-520.
6. Fan Y, Batmanghelich N, Clark CM, Davatzikos C, Alzheimer's Disease Neuroimaging Initiative. Spatial patterns of brain atrophy in MCI patients, identified via high-dimensional pattern classification, predict subsequent cognitive decline. Neuroimage. 2008;39: 1731-1743.
7. Fan Y, Resnick SM, Wu X, Davatzikos C. Structural and functional biomarkers of prodromal Alzheimer's disease: a high-dimensional pattern classification study. Neuroimage. 2008;41: 277-285.
8. Kloppel S, Stonnington CM, Chu C, Draganski B, Scahill RI, Rohrer JD, et al. Automatic classification of MR scans in Alzheimer's disease. Brain. 2008;131: 681-689.
9. Vemuri P, Gunter JL, Senjem ML, Whitwell JL, Kantarci K, Knopman DS, et al. Alzheimer's disease diagnosis in individual subjects using structural MR images: validation studies. Neuroimage. 2008;39: 1186-1197.
10. Magnin B, Mesrob L, Kinkingnehun S, Pelegrini-Issac M, Colliot O, Sarazin M, et al. Support vector machine-based classification of Alzheimer's disease from whole-brain anatomical MRI. Neuroradiology. 2009;51: 73-83.
11. Cuingnet R, Gerardin E, Tessieras J, Auzias G, Lehericy S, Habert MO, et al. Automatic classification of patients with Alzheimer's disease from structural MRI: a comparison of ten methods using the ADNI database. Neuroimage. 2011;56: 766-781.
12. Wolz R, Julkunen V, Koikkalainen J, Niskanen E, Zhang DP, Rueckert D, et al. Multi-method analysis of MRI images in early diagnostics of Alzheimer's disease. PLoS One. 2011;6: e25446.
13. Koikkalainen J, Polonen H, Mattila J, van Gils M, Soininen H, Lotjonen J, et al. Improved classification of Alzheimer's disease data via removal of nuisance variability. PLoS One. 2012;7: e31112.
14. Jack CR,Jr, Knopman DS, Jagust WJ, Shaw LM, Aisen PS, Weiner MW, et al. Hypothetical model of dynamic biomarkers of the Alzheimer's pathological cascade. Lancet Neurol. 2010;9: 119-128.
15. Sperling RA, Aisen PS, Beckett LA, Bennett DA, Craft S, Fagan AM, et al. Toward defining the preclinical stages of Alzheimer's disease: recommendations from the National Institute on Aging-Alzheimer's Association workgroups on diagnostic guidelines for Alzheimer's disease. Alzheimers Dement. 2011;7: 280-292.
16. Detre JA, Leigh JS, Williams DS, Koretsky AP. Perfusion imaging. Magn Reson Med. 1992;23: 37-45.
17. Williams DS, Detre JA, Leigh JS, Koretsky AP. Magnetic resonance imaging of perfusion using spin inversion of arterial water. Proc Natl Acad Sci U S A. 1992;89: 212-216.
18. Wang Z, Das SR, Xie SX, Arnold SE, Detre JA, Wolk DA. Arterial spin labeled MRI in prodromal Alzheimer's disease: A multi-site study. Neuroimage: Clinical. 2013;2: 630-636.

19. Wolk DA, Detre JA. Arterial spin labeling MRI: an emerging biomarker for Alzheimer's disease and other neurodegenerative conditions. Curr Opin Neurol. 2012;25: 421-428.
20. Binnewijzend MA, Kuijer JP, Benedictus MR, van der Flier WM, Wink AM, Wattjes MP, et al. Cerebral blood flow measured with 3D pseudocontinuous arterial spin-labeling MR imaging in Alzheimer disease and mild cognitive impairment: a marker for disease severity. Radiology. 2013;267: 221-230.
21. Dashjamts T, Yoshiura T, Hiwatashi A, Yamashita K, Monji A, Ohyagi Y, et al. Simultaneous arterial spin labeling cerebral blood flow and morphological assessments for detection of Alzheimer's disease. Acad Radiol. 2011;18: 1492-1499.
22. Du AT, Jahng GH, Hayasaka S, Kramer JH, Rosen HJ, Gorno-Tempini ML, et al. Hypoperfusion in frontotemporal dementia and Alzheimer disease by arterial spin labeling MRI. Neurology. 2006;67: 1215-1220.
23. Schuff N, Liu X, Weiner MW. Regional abnormalities of cerebral blood flow in early mild cognitive impairment: Insights from the ASL-MRI study of ADNI. ISMRM Scient Worksh Perf MRI. 2012. p 5500.
24. Tax DMJ, Van Breukelen M, Duin RPW, Kittler J. Combining multiple classifiers by averaging or by multiplying? Pattern Recogn. 2000;33: 1475-1485.
25. Dubois B, Feldman HH, Jacova C, Cummings JL, Dekosky ST, Barberger-Gateau P, et al. Revising the definition of Alzheimer's disease: a new lexicon. Lancet Neurol. 2010;9: 1118-1127.
26. Dubois B, Feldman HH, Jacova C, Dekosky ST, Barberger-Gateau P, Cummings J, et al. Research criteria for the diagnosis of Alzheimer's disease: revising the NINCDS-ADRDA criteria. Lancet Neurol. 2007;6: 734-746.
27. McKhann GM, Knopman DS, Chertkow H, Hyman BT, Jack CR,Jr, Kawas CH, et al. The diagnosis of dementia due to Alzheimer's disease: recommendations from the National Institute on Aging-Alzheimer's Association workgroups on diagnostic guidelines for Alzheimer's disease. Alzheimers Dement. 2011;7: 263-269.
28. Rascovsky K, Hodges JR, Knopman D, Mendez MF, Kramer JH, Neuhaus J, et al. Sensitivity of revised diagnostic criteria for the behavioural variant of frontotemporal dementia. Brain. 2011;134: 2456-2477.
29. Dai W, Garcia D, de Bazelaire C, Alsop DC. Continuous flow-driven inversion for arterial spin labeling using pulsed radio frequency and gradient fields. Magn Reson Med. 2008;60: 1488-1497.
30. Wu WC, Fernandez-Seara M, Detre JA, Wehrli FW, Wang J. A theoretical and experimental investigation of the tagging efficiency of pseudocontinuous arterial spin labeling. Magn Reson Med. 2007;58: 1020-1027.
31. Jack CR,Jr, Bernstein MA, Fox NC, Thompson P, Alexander G, Harvey D, et al. The Alzheimer's Disease Neuroimaging Initiative (ADNI): MRI methods. J Magn Reson Imaging. 2008;27: 685-691.
32. Ashburner J, Friston KJ. Unified segmentation. Neuroimage. 2005;26: 839-851.
33. Buxton RB, Frank LR, Wong EC, Siewert B, Warach S, Edelman RR. A general kinetic model for quantitative perfusion imaging with arterial spin labeling. Magn Reson Med. 1998;40: 383-396.
34. Klein S, Staring M, Murphy K, Viergever MA, Pluim JP. Elastix: a Toolbox for Intensity-Based Medical Image Registration. IEEE Trans Med Imaging. 2010;29: 196-205.
35. Thevenaz P, Unser M. Optimization of mutual information for multiresolution image registration. IEEE Trans Image Process. 2000;9: 2083-2099.
36. Smith SM. Fast robust automated brain extraction. Hum Brain Mapp. 2002;17: 143-155.
37. Asllani I, Borogovac A, Brown TR. Regression algorithm correcting for partial volume effects in arterial spin labeling MRI. Magn Reson Med. 2008;60: 1362-1371.

38. Oliver RA, Thomas DL, Golay X. Improved partial volume correction of ASL images using 3D kernels. ISMRM British Chapter. 2012.
39. van Gelderen P, de Zwart JA, Duyn JH. Pittfalls of MRI measurement of white matter perfusion based on arterial spin labeling. Magn Reson Med. 2008;59: 788-795.
40. Gousias IS, Rueckert D, Heckemann RA, Dyet LE, Boardman JP, Edwards AD, et al. Automatic segmentation of brain MRIs of 2-year-olds into 83 regions of interest. Neuroimage. 2008;40: 672-684.
41. Hammers A, Allom R, Koepp MJ, Free SL, Myers R, Lemieux L, et al. Three-dimensional maximum probability atlas of the human brain, with particular reference to the temporal lobe. Hum Brain Mapp. 2003;19: 224-247.
42. Seghers D, D'Agostino E, Maes F, Vandermeulen D, Suetens P. Construction of a brain template from MR images using state-of-the-art registration and segmentation techniques. Proc Intl Conf Med Image Comput Comp Ass Intervent. 2004: 696-703.
43. Foster NL, Wang AY, Tasdizen T, Fletcher PT, Hoffman JM, Koeppe RA. Realizing the potential of positron emission tomography with 18F-fluorodeoxyglucose to improve the treatment of Alzheimer's disease. Alzheimers Dement. 2008;4: S29-36.
44. Fukuyama H, Ogawa M, Yamauchi H, Yamaguchi S, Kimura J, Yonekura Y, et al. Altered cerebral energy metabolism in Alzheimer's disease: a PET study. J Nucl Med. 1994;35: 1-6.
45. Herholz K, Carter SF, Jones M. Positron emission tomography imaging in dementia. Br J Radiol. 2007;80 Spec No 2: S160-7.
46. Ishii K, Sasaki M, Matsui M, Sakamoto S, Yamaji S, Hayashi N, et al. A diagnostic method for suspected Alzheimer's disease using H(2)15O positron emission tomography perfusion Z score. Neuroradiology. 2000;42: 787-794.
47. Ishii K, Sakamoto S, Sasaki M, Kitagaki H, Yamaji S, Hashimoto M, et al. Cerebral glucose metabolism in patients with frontotemporal dementia. J Nucl Med. 1998;39: 1875-1878.
48. Ishii K, Sasaki M, Kitagaki H, Yamaji S, Sakamoto S, Matsuda K, et al. Reduction of cerebellar glucose metabolism in advanced Alzheimer's disease. J Nucl Med. 1997;38: 925-928.
49. Ishii K, Sasaki M, Yamaji S, Sakamoto S, Kitagaki H, Mori E. Demonstration of decreased posterior cingulate perfusion in mild Alzheimer's disease by means of H215O positron emission tomography. Eur J Nucl Med. 1997;24: 670-673.
50. Ishii K, Kitagaki H, Kono M, Mori E. Decreased medial temporal oxygen metabolism in Alzheimer's disease shown by PET. J Nucl Med. 1996;37: 1159-1165.
51. Johannsen P, Jakobsen J, Gjedde A. Statistical maps of cerebral blood flow deficits in Alzheimer's disease. Eur J Neurol. 2000;7: 385-392.
52. Minoshima S, Giordani B, Berent S, Frey KA, Foster NL, Kuhl DE. Metabolic reduction in the posterior cingulate cortex in very early Alzheimer's disease. Ann Neurol. 1997;42: 85-94.
53. Santens P, De Bleecker J, Goethals P, Strijckmans K, Lemahieu I, Slegers G, et al. Differential regional cerebral uptake of (18)F-fluoro-2-deoxy-D-glucose in Alzheimer's disease and frontotemporal dementia at initial diagnosis. Eur Neurol. 2001;45: 19-27.
54. Scarmeas N, Habeck CG, Zarahn E, Anderson KE, Park A, Hilton J, et al. Covariance PET patterns in early Alzheimer's disease and subjects with cognitive impairment but no dementia: utility in group discrimination and correlations with functional performance. Neuroimage. 2004;23: 35-45.
55. Womack KB, Diaz-Arrastia R, Aizenstein HJ, Arnold SE, Barbas NR, Boeve BF, et al. Temporoparietal hypometabolism in frontotemporal lobar degeneration and associated imaging diagnostic errors. Arch Neurol. 2011;68: 329-337.
56. Tustison NJ, Avants BB, Cook PA, Zheng Y, Egan A, Yushkevich PA, et al. N4ITK: improved N3 bias correction. IEEE Trans Med Imaging. 2010;29: 1310-1320.

57. Heckemann RA, Hajnal JV, Aljabar P, Rueckert D, Hammers A. Automatic anatomical brain MRI segmentation combining label propagation and decision fusion. Neuroimage. 2006;33: 115-126.
58. Duin RP, Tax DM. Classifier conditional posterior probabilities. In: Anonymous Advances in pattern recognition. : Springer; 1998. pp. 611-619.
59. Ashburner J, Friston KJ. Voxel-based morphometry--the methods. Neuroimage. 2000;11: 805-821.
60. Vapnik VN. The nature of statistical learning theory. New York: Springer-Verlag; 1995.
61. Chang C, Lin C. LIBSVM: A library for support vector machines. ACM Trans Intell Syst Technol. 2011;2.
62. Mourao-Miranda J, Bokde AL, Born C, Hampel H, Stetter M. Classifying brain states and determining the discriminating activation patterns: Support Vector Machine on functional MRI data. Neuroimage. 2005;28: 980-995.
63. Wang Z, Childress AR, Wang J, Detre JA. Support vector machine learning-based fMRI data group analysis. Neuroimage. 2007;36: 1139-1151.
64. Gaonkar B, Davatzikos C. Analytic estimation of statistical significance maps for support vector machine based multi-variate image analysis and classification. Neuroimage. 2013;78: 270-283.
65. Hu WT, Wang Z, Lee VM, Trojanowski JQ, Detre JA, Grossman M. Distinct cerebral perfusion patterns in FTLD and AD. Neurology. 2010;75: 881-888.
66. La Joie R, Perrotin A, Barre L, Hommet C, Mezenge F, Ibazizene M, et al. Region-specific hierarchy between atrophy, hypometabolism, and beta-amyloid (Abeta) load in Alzheimer's disease dementia. J Neurosci. 2012;32: 16265-16273.
67. Maldjian JA, Whitlow CT, Alzheimer's Disease Neuroimaging Initiative. Whither the hippocampus? FDG-PET hippocampal hypometabolism in Alzheimer disease revisited. AJNR Am J Neuroradiol. 2012;33: 1975-1982.
68. Chetelat G, Baron JC. Early diagnosis of Alzheimer's disease: contribution of structural neuroimaging. Neuroimage. 2003;18: 525-541.
69. Karas GB, Burton EJ, Rombouts SA, van Schijndel RA, O'Brien JT, Scheltens P, et al. A comprehensive study of gray matter loss in patients with Alzheimer's disease using optimized voxel-based morphometry. Neuroimage. 2003;18: 895-907.
70. Karas GB, Scheltens P, Rombouts SA, Visser PJ, van Schijndel RA, Fox NC, et al. Global and local gray matter loss in mild cognitive impairment and Alzheimer's disease. Neuroimage. 2004;23: 708-716.
71. McKhann GM, Albert MS, Grossman M, Miller B, Dickson D, Trojanowski JQ, et al. Clinical and pathological diagnosis of frontotemporal dementia: report of the Work Group on Frontotemporal Dementia and Pick's Disease. Arch Neurol. 2001;58: 1803-1809.
72. Ashburner J. A fast diffeomorphic image registration algorithm. Neuroimage. 2007;38: 95-113.
73. Tzourio-Mazoyer N, Landeau B, Papathanassiou D, Crivello F, Etard O, Delcroix N, et al. Automated anatomical labeling of activations in SPM using a macroscopic anatomical parcellation of the MNI MRI single-subject brain. Neuroimage. 2002;15: 273-289.

SUPPLEMENTARY MATERIAL

Table 3: P-values obtained with permutation tests for the region-wise classification. Red values are significant (p<0.05, not corrected for multiple comparisons). Italic regions were included in the selection classification.

		CBF		GM	
		left	right	left	right
1	*Hippocampus*	0.63	0.30	0.63	0.62
2	Amygdala	0.13	0.81	0.83	0.59
3	Anterior temporal lobe, medial part	0.80	0.23	0.38	0.79
4	*Anterior temporal lobe, lateral part*	0.18	0.52	0.55	0.15
5	Gyrus parahippocampalis	0.69	0.93	0.75	0.55
6	Superior temporal gyrus, central part	0.90	0.82	0.56	0.49
7	Medial and inferior temporal gyri	0.77	0.92	0.34	0.56
8	Lateral occipitotemporal gyrus	0.89	0.63	0.60	0.55
9	Insula	0.56	0.15	0.23	0.88
10	Lateral remainder of occipital lobe	0.34	0.25	0.88	0.65
11	*Cingulate gyrus, anterior part*	0.46	0.60	0.65	0.51
12	*Cingulate gyrus, posterior part*	0.38	0.57	0.66	0.25
13	*Middle frontal gyrus*	0.74	0.29	0.69	0.85
14	*Posterior temporal lobe*	0.40	0.15	0.69	0.21
15	*Remainder of parietal lobe*	0.53	0.42	0.10	0.52
16	Caudate nucleus	0.68	0.74	0.48	0.72
17	Nucleus accumbens	0.74	0.94	0.09	0.21
18	Putamen	0.07	0.05	0.73	0.64
19	Thalamus	0.28	0.14	0.55	0.82
20	Pallidum	0.83	0.51	0.45	0.87
21	Precentral gyrus	0.37	0.02	0.29	0.33
22	Straight gyrus	0.59	0.77	0.33	0.71
23	Anterior orbital gyrus	0.80	0.59	0.78	0.95
24	*Inferior frontal gyrus*	0.79	0.84	0.47	0.59

25	*Superior frontal gyrus*	0.99	0.33	0.28	0.15
26	Postcentral gyrus	0.14	0.07	0.47	0.38
27	*Superior parietal gyrus*	0.94	0.48	0.91	0.63
28	Lingual gyrus	0.24	0.71	0.97	0.11
29	Cuneus	0.27	0.85	0.43	0.16
30	Medial orbital gyrus	0.81	0.57	0.78	0.79
31	Lateral orbital gyrus	0.36	0.53	0.34	0.12
32	Posterior orbital gyrus	0.91	0.56	0.51	0.60
33	*Subgenual anterior cingulate gyrus*	0.83	0.50	0.91	0.03
34	Subcallosal area	0.07	0.42	0.16	0.80
35	*Pre-subgenual anterior cingulate gyrus*	0.66	0.19	0.23	0.41
36	*Superior temporal gyrus, anterior part*	0.24	0.16	0.59	0.24

Chapter 2.2

Early-stage differentiation between presenile Alzheimer's disease and frontotemporal dementia using arterial spin labeling MRI

Rebecca M.E. Steketee
Esther E. Bron
Rozanna Meijboom
Gavin C. Houston
Stefan Klein
Henk Jan M.M. Mutsaerts
Carolina P. Méndez Orellaña
Frank Jan de Jong
John C. van Swieten
Aad van der Lugt
Marion Smits

Eur Radiol. 2016:26;244-53.

ABSTRACT

Objective To investigate arterial spin labeling (ASL)-MRI for the early diagnosis of and differentiation between the two most common types of presenile dementia: Alzheimer's disease (AD) and frontotemporal dementia (FTD), and for distinguishing age-related from pathological perfusion changes.

Methods 13 AD and 19 FTD patients, and 25 age-matched older and 22 younger controls underwent 3D pseudo-continuous ASL-MRI at 3T. Gray matter (GM) volume and cerebral blood flow (CBF), corrected for partial volume effects, were quantified in the entire supratentorial cortex and in 10 GM regions. Sensitivity, specificity and diagnostic performance were evaluated in regions showing significant CBF differences between patient groups or between patients and older controls.

Results AD compared with FTD patients had hypoperfusion in the posterior cingulate cortex, differentiating these with a diagnostic performance of 74%. Compared to older controls, FTD patients showed hypoperfusion in the anterior cingulate cortex, whereas AD patients showed a more widespread regional hypoperfusion as well as atrophy. Regional atrophy was not different between AD and FTD. Diagnostic performance of ASL to differentiate AD or FTD from controls was good (78-85%). Older controls showed global hypoperfusion compared to young controls.

Conclusion ASL-MRI contributes to early diagnosis of and differentiation between presenile AD and FTD.

INTRODUCTION

Although less prevalent, presenile dementia (age of onset ≤65 years) comprises a substantial subset of dementia patients [1]. Compared to late-onset dementia, it more often has an atypical presentation and more progressive disease course. Early diagnosis of presenile dementia remains difficult as different etiologies are hard to distinguish. Presenile Alzheimer's disease (AD) more often has a non-amnestic presentation than late-onset AD [2]. Additionally, non-neurological causes of cognitive dysfunction are more prevalent in younger patients and may mimic neurodegenerative disorders, particularly obscuring differentiation between psychiatric disease and frontotemporal dementia (FTD) [3]. Another large subset of young patients presents with primary progressive aphasia (PPA), in which the underlying pathology – AD or FTD – is often unclear [4].

Conventional magnetic resonance imaging (MRI) often shows distinctive brain atrophy only in later stages AD and FTD [5]. Early diagnosis requires techniques that detect early brain changes, such as fluorodeoxyglucose-positron emission tomography (FDG-PET). FDG-PET visualizes hypometabolism in temporo-parietal regions, posterior cingulate and precuneus in AD, while FTD affects the prefrontal cortex (PFC), anterior cingulate cortex (ACC) and anterior temporal cortex [6]. Arterial spin labeling (ASL)-MRI, measuring brain perfusion, has been proposed as an alternative as it is noninvasive and easily added to routine diagnostic MRI protocols, whereas FDG-PET has limited availability and relatively high costs [7]. Hypoperfusion measured with ASL is consistent with PET in advanced AD and FTD, indicating that ASL could contribute to differential diagnosis [8,9]. The use of ASL in the earliest stages of dementia is being increasingly studied [10,11], but little is known about ASL findings in the early stage of presenile dementia, when diagnosis is often still uncertain. To reliably assess regional cerebral blood flow (CBF) changes in such patients, we also need to determine normal regional CBF variability, as this is substantial in healthy young adults [12].

The aim of this study was to investigate ASL-MRI for the early diagnosis of and differentiation between the two most common types of presenile dementia: AD and FTD [2]. We also investigated age-related CBF changes to distinguish pathological from physiological changes in – regional – perfusion.

MATERIALS & METHODS

Participants

Newly presenting patients visiting our outpatient memory clinic between January 2011 and September 2013, aged 45 to 70 years, and with a Mini Mental State Examination (MMSE) score ≥ 20 (indicating mild dementia) were prospectively considered for inclusion. All patients underwent neurological and neuropsychological examination as part of their routine diagnostic work up. We consecutively included patients with a diagnosis of possible or probable AD or FTD. In addition, patients were included with PPA in which the underlying etiology can be

either AD or FTD. The reference standard was nosological diagnosis of AD or FTD by consensus according to the McKhann [13] and Rascovsky [14] criteria, or AD or FTD underlying PPA [4]. Diagnosis was established either at baseline (initial visit), or after follow-up when diagnosis at baseline was uncertain, and verified independently by two experienced neurologists. Conventional structural MRI was assessed as part of the diagnostic process and simultaneously assessed for exclusion criteria, ASL-MRI was not. Patients with psychiatric or neurological disorders other than dementia were excluded. Other exclusion criteria were normal pressure hydrocephalus, Huntington's disease, cerebral vascular disease, alcohol abuse, brain tumor, epilepsy or encephalitis.

Healthy young (18 to 40 years) and older (45 to 70 years) controls were recruited through advertisement, and older controls also from the patient peers. Data from these young participants were previously reported in a reproducibility study of ASL [15]. Both control groups were matched for gender, and older controls for age with the patients. A researcher screened all participants, who were included only when there was no history of neurological or psychiatric disease, and no contraindications for MRI. Older controls were administered the MMSE to assess global cognitive functioning.

The study was approved by the local medical ethics committee. All participants gave written informed consent.

Image acquisition

All participants were scanned at 3T (Discovery MR750 system, GE Healthcare, USA). Perfusion was measured with state-of-the-art [16] whole brain 3D pseudo-continuous ASL (p-CASL) (background-suppressed, post-labeling delay 1525ms, labeling duration 1450ms, echo time (TE) 10.5ms, repetition time (TR) 4632ms, interleaved FSE stack-of-spiral readout of 512 sampling points on 8 spirals, isotropic resolution 3.3mm in a field of view (FOV) of 240mm, 36 axial slices, number of excitations 3, acquisition time 4.29 min). The labeling plane was positioned 9 cm below the anterior commissure-posterior commissure line. A high resolution 3D fast spoiled gradient-echo T1-weighted (T1w) image (FOV 240 mm, TR/TE/inversion time 7.9/3.06/450ms, ASSET factor 2, matrix 240*240, and slice thickness 1mm, acquisition time 4.41 min) was acquired for anatomical reference.

Image data processing

The data were processed according to methods described previously [17] to obtain partial volume effect corrected CBF values from gray matter (GM) only.

Tissue segmentation

Gray matter (GM), white matter and cerebrospinal fluid maps were obtained from the T1w image using the unified tissue segmentation method [18] of SPM8 (Statistical Parametric Mapping, London, UK). GM volumes were computed from the GM map. CBF was analyzed in GM only.

ASL post-processing

The ASL imaging dataset consisted of two images, a perfusion-weighted image (PWI) and a proton density image (PD), that were required for CBF calculation [16]. CBF maps from representative patients are shown in Figure 1. The GM map derived from the T1w image was rigidly registered with the PD image for each participant (Elastix registration software [19]). Then GM maps were transformed to ASL image space to enable partial volume (PV) correction. PV effects were corrected in PWI and PD images using local linear regression within a 3D kernel based on tissue maps [20]. The PV-corrected ASL images were quantified as CBF maps using the single-compartment model [16] as implemented by the scanner manufacturer. Finally CBF maps were transformed to T1w image space for further analysis.

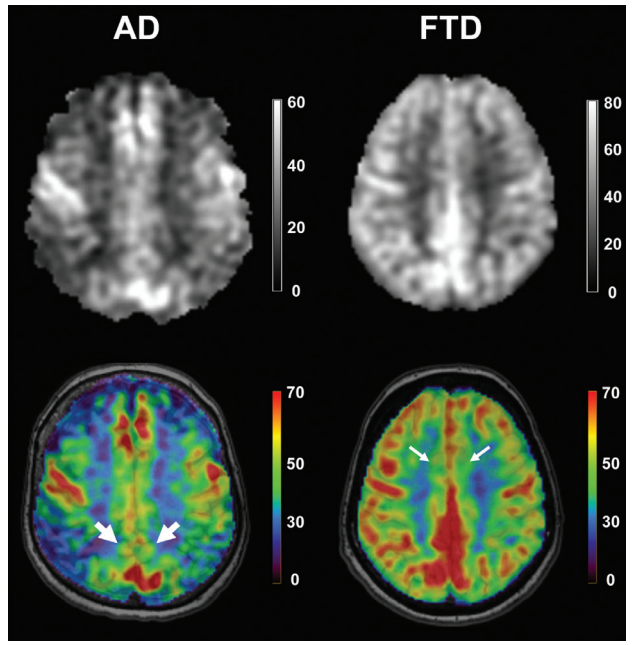

Figure 1: Cerebral blood flow (CBF in ml/100g GM/min) maps for a representative AD (left column) and FTD patient (right column). The top row shows their skull-stripped CBF map, the bottom row shows their color-coded CBF maps overlaid on the structural T1w images. Prominent hypoperfusion in the PCC (thick arrows) in AD compared to FTD. Also note the global and more extensive hypoperfusion in AD compared to the focal hypoperfusion in the ACC in FTD (thin arrows).
CBF: cerebral blood flow; AD: Alzheimer's disease; FTD: frontotemporal dementia; T1w: T1 weighted; PCC: posterior cingulate cortex; ACC: anterior cingulate cortex.

ROI labeling

For each participant, regions of interest (ROIs) were defined using a multi-atlas approach. This involved the registration of 30 labeled T1w images, each containing 83 ROIs [21,22], to the participants' T1w images. The labels of the 30 atlas images were fused using a majority voting algorithm to obtain a final ROI labeling

[23]. Registration to the participants' nonuniformity corrected T1w images [24] were performed with a rigid, affine, and non-rigid B-spline transformation model consecutively. For this registration, both the participants' and the labeled T1w images were masked using the Brain Extraction Tool [25].

Region selection

CBF was assessed per participant globally in the entire supratentorial cortex, and regionally in 10 predefined cortical regions relevant for dementia, based on previously reported PET-findings in AD and FTD [26-28] (Table 1). Mean GM CBF and volumes in these regions were extracted for the left and right hemisphere separately and subsequently reported as an average of the bilateral regions. GM volumes were reported as percentage of the total intracranial volume (% ICV).

Data analysis

Gender differences across patient and control groups were examined using chi-square tests ($p<0.05$). One-way analysis of variance (ANOVA) with Bonferroni correction ($p<0.05$) was used to examine age and MMSE differences across AD and FTD patients and older controls; and to compare global and regional GM CBF and volume across the patient and control groups. Variation within and between groups was visualized with a boxplot.

Sensitivity and specificity of regional CBF were evaluated for both patient groups using Receiver Operating Characteristic (ROC) analysis. We examined regions known to be affected in dementia that showed significant differences between FTD or AD patients and older controls. Regions that showed significant differences ($p<0.05$, Bonferroni corrected) between FTD and AD patients and controls in the one-way ANOVA were selected to investigate their performance in differentiating the groups. Diagnostic performance was expressed by areas under the curve (AUC) with 95% confidence intervals. For the regions with the highest AUCs, optimal cut-off points were determined to discriminate between the examined groups by locating the cut-off point where the distance from maximum sensitivity and specificity was minimal. Distance was calculated for each observed cut-off point using the equation: $distance = \sqrt{[(1 - \text{sensitivity})^2 + (1 - \text{specificity})^2]}$. Based on these cut-off points, false positives (FPs) and false negatives (FNs) were determined to explore whether age, gender, MMSE or PPA variant affected misclassification.

Statistical analyses were performed in IBM SPSS Statistics, version 20.0 (New York, USA).

Table 1: selected regions of interest (ROIs)

	ROI (literature)	Anatomical region [21,22]
Regions affected	Medial temporal lobe (MTL)	Hippocampus Gyri parahippocampalis et ambiens
	Remainder of temporal lobe	Anterior temporal lobe, medial part Anterior temporal lobe, lateral part Superior temporal gyrus, central part Medial and inferior temporal gyri Posterior temporal lobe Superior temporal gyrus
	Precuneus	Superior parietal gyrus
	Posterior cingulate cortex (PCC)	Cingulate gyrus, posterior part
	Thalamus	Thalamus
	Anterior cingulate cortex (ACC)	Cingulate gyrus, anterior (supragenual) part Subgenual anterior cingulate gyrus Presubgenual anterior cingulate gyrus
	Medial prefrontal cortex (medial PFC)	Straight gyrus (gyrus rectus) Superior frontal gyrus Medial orbital gyrus Posterior orbital gyrus
Regions initially unaffected	Precentral gyrus	Precentral gyrus
	Occipital lobe	Lateral remainder of occipital lobe
	Calcarine cortex	Lingual gyrus Cuneus

Reported regions were matched as closely as possible to our anatomically defined ROIs [21,22].

RESULTS

Participant characteristics

100 participants were included in our study: 53 dementia patients, 22 healthy young adult and 25 healthy older participants (Table 2). Post hoc, 21 of the 53 included patients were excluded due to diagnoses other than AD or FTD during follow-up (7), lack of progression (4), low data quality (4), or because of incomplete imaging data (6). Median follow-up was 1.2 years (range 2 weeks – 2.8 years).

Table 2: Participant characteristics

	AD	FTD	Older controls	Young controls
N (male, female)	13 (8, 5)	19 (11, 8)	25 (13, 12)	22 (9, 13)
Mean age ± SD in years	62.2 ± 5.46	63.0 ± 4.46	60.9 ± 5.85	22.1 ± 2.12
Mean MMSE ± SD	25.3 ± 2.29	25.8 ± 3.88	29.2 ± 0.98[a]	N/A
Probable cause of dementia	11 AD 2 PPA-AD	8 FTD 11 PPA-FTD	N/A	N/A

[a] based on 24 healthy participants' scores
AD: Alzheimer's disease; FTD: frontotemporal dementia; MMSE: Mini Mental State Examination; N/A: not available or applicable; PPA: primary progressive aphasia; SD: standard deviation.

Gender was not different across groups (χ^2 (3, n=79) = 1.822, p>.05). Age was not different between AD and FTD patients and older controls (F(2,54) = 0.886, p>.05). MMSE was different across the patient groups and older controls (F(2,53) = 13.476, p<.05): both patient groups had lower scores compared to older controls, but not compared to each other (Table 2). Due to language deficits, two patients with PPA had MMSE scores of <20. Their full neuropsychological examination indicated only moderate impairment in all cognitive domains except for language, affecting the MMSE score. Their data were therefore retained in the analysis.

Global perfusion and volume changes

Mean CBF of the supratentorial cortex (Table 3, Figure 2) was not different between AD and FTD. Compared with older controls, global perfusion was lower in AD, but not in FTD. Older controls showed lower global perfusion than young controls. Mean GM volume was not different between AD and FTD, but was lower in both AD and FTD compared to controls (Table 3).

Regional perfusion and volume changes

Changes related to dementia

Of the regions affected by dementia, the PCC showed lower CBF in AD than FTD (Table 3, Figure 2). Compared to older controls, CBF was lower in all these regions in AD, but only in the ACC in FTD. GM volume was not different between AD and FTD, but was lower in AD compared to controls in all regions affected in

Table 3: Mean GM CBF and volume (standard deviations) for AD and FTD patients, and older and young controls.

		AD	FTD	Older controls (OC)	Young controls (YC)	P-values		
						AD vs. OC	FTD vs. OC	FTD vs. AD
Total GM	CBF	32.6 (8.79)	37.4 (6.91)	42.0 (7.90)	60.7 (7.86)	*.005*	.372	.542
	Volume	31.7 (4.01)	31.0 (3.23)	35.7 (2.38)	43.1 (1.35)	*<.0005*	*<.0005*	1.000
Regions affected in dementia								
MTL	CBF	33.0 (5.69)	36.2 (7.10)	38.4 (5.10)	49.0 (5.31)	*.048*	1.000	.762
	Volume	0.17 (0.02)	0.15 (0.03)	0.20 (0.02)	0.19 (0.01)	*.001*	*<.0005*	.122
Temporal lobe	CBF	33.9 (8.25)	37.3 (6.78)	42.7 (6.15)	55.5 (7.74)	*.003*	.094	1.000
	Volume	0.54 (0.08)	0.50 (0.08)	0.62 (0.04)	0.72 (0.03)	*<.0005*	*<.0005*	.367
Precuneus	CBF	27.0 (7.30)	35.3 (8.73)	39.5 (10.2)	58.2 (8.33)	*.001*	.751	.074
	Volume	1.10 (0.13)	1.12 (0.14)	1.25 (0.10)	1.48 (0.11)	*.006*	*.008*	1.000
PCC	CBF	40.1 (11.5)	49.6 (9.40)	55.8 (9.78)	73.4 (8.41)	*<.0005*	.223	*.048*
	Volume	0.28 (0.06)	0.29 (0.04)	0.33 (0.04)	0.41 (0.03)	*.003*	*.046*	1.000
Thalamus	CBF	32.4 (8.27)	36.4 (8.59)	42.5 (8.36)	56.6 (7.45)	*.004*	.105	1.000
	Volume	0.15 (0.02)	0.18 (0.03)	0.18 (0.01)	0.25 (0.03)	*.037*	1.000	.122
ACC	CBF	42.6 (10.9)	43.0 (7.04)	50.9 (7.55)	70.3 (9.01)	*.033*	*.018*	1.000
	Volume	0.13 (0.03)	0.12 (0.03)	0.14 (0.02)	0.19 (0.02)	.691	*.005*	.978

Medial PFC	CBF	37.6 (10.8)	39.9 (7.99)	46.0 (7.55)	71.5 (8.79)	*.033*	.136	1.000
	Volume	0.52 (0.08)	0.46 (0.09)	0.57 (0.05)	0.71 (0.04)	.153	*<.0005*	.130
Regions initially unaffected in dementia								
Precentral gyrus	CBF	35.0 (11.1)	38.2 (6.57)	40.8 (9.48)	62.5 (8.01)	.320	1.000	1.000
	Volume	0.90 (0.14)	0.86 (0.08)	0.92 (0.09)	1.06 (0.09)	1.000	.371	1.000
Occipital lobe	CBF	26.1 (7.48)	32.5 (8.63)	36.2 (8.64)	48.6 (7.93)	*.004*	.880	.213
	Volume	1.35 (0.20)	1.45 (0.17)	1.52 (0.15)	1.85 (0.16)	*.022*	1.000	.508
Calcarine cortex	CBF	34.2 (7.79)	41.4 (6.91)	42.5 (9.65)	54.8 (7.24)	*.021*	1.000	.094
	Volume	0.42 (0.05)	0.45 (0.04)	0.46 (0.05)	0.53 (0.05)	*.017*	1.000	.237

Mean GM CBF (ml/100g GM/min) and volume (% intracranial volume) in ROIs in FTD and AD patients and older and young controls. P-values printed in italics indicate significant differences ($p<0.05$, Bonferroni corrected). As differences between young controls and all other groups were significant in all ROIs (except for MTL volume, please see text), p-values of these comparisons are not shown.
ACC: anterior cingulate cortex; AD: Alzheimer's disease; CBF = cerebral blood flow; FTD: frontotemporal dementia; GM: gray matter; MTL: medial temporal lobe; PCC: posterior cingulate cortex; PFC: prefrontal cortex

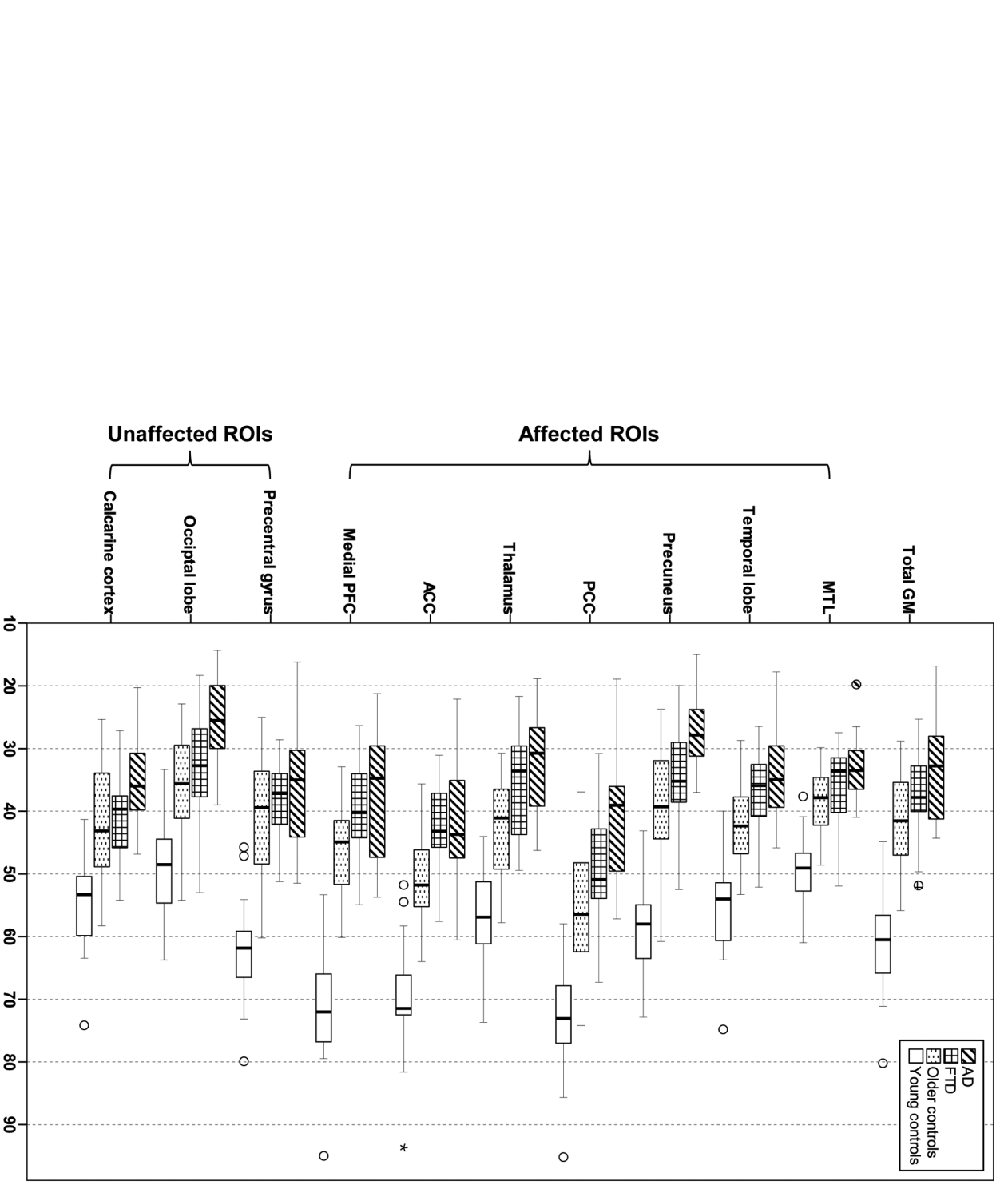

Figure 2: Regional cerebral blood flow (CBF in ml/100g GM/min) in FTD and AD patients and older and young controls. The central box represents values from lower to upper quartile (25-75 percentile), the middle line represents the median, and vertical bars extend from minimum to maximum values. Markers outside the bars indicate extreme values (sphere: value ≥ 1.5 x interquartile range (IQR); asterisk: value ≥ 3 x IQR.
ACC: anterior cingulate cortex; AD: Alzheimer's disease; CBF: cerebral blood flow; FTD: frontotemporal dementia; GM: gray matter; MTL: medial temporal lobe; PCC: posterior cingulate cortex; PFC: prefrontal cortex; ROI: region of interest.

dementia except the ACC and medial PFC. FTD had lower volumes in all regions except the thalamus (Table 3).

Of the regions initially unaffected by dementia, CBF in and volume of the precentral gyrus showed differences neither between AD and FTD nor between each of the patient groups and older controls. Mean CBF and GM volume in the occipital lobe and calcarine cortex was lower in AD than in older controls, but did not differ between FTD and controls.

Age-related changes

Mean CBF in all ROIs was lower in older than in young controls (Table 3, Figure 2). Mean GM volumes (Table 3) were lower in all ROIs except the medial temporal lobe (MTL) (Table 3). In both control groups, CBF was relatively highest in the PCC and lowest in the occipital lobe.

Diagnostic performance of ASL in dementia

CBF was lower in AD than FTD in the PCC (Table 3), in which ROC analysis yielded an AUC of 0.741 (Table 4). The optimal cut-off point differentiated AD from FTD with 69% sensitivity and 68% specificity (Figure 3A).

As all regions showed lower CBF in AD than controls (Table 3), these were all examined (Table 4). The precuneus performed best (AUC: 0.849) and differentiated AD patients from controls with 77% sensitivity and 76% specificity (Figure 3B).

FTD had lower CBF than controls in the ACC (Table 3), in which ROC analysis yielded an AUC of 0.775 and differentiated FTD from controls with 79% sensitivity and 76% specificity (figure 3C).

Overall, misclassification of participants was not explained by age, gender, PPA variant or MMSE, as these variables deviated less than 1 standard deviation in FP and FN cases compared to true positive and negative cases. However, male controls were labeled as diseased more than female controls: in differentiating AD from healthy controls, 5 out of 6 FP cases were male and in differentiating FTD from controls 6 out of 6.

DISCUSSION

The main finding of our study is that ASL-MRI contributes to early differential diagnosis of presenile dementia. Compared to FTD patients, AD patients showed hypoperfusion in the PCC. Differentiation between the patient groups based on this finding had a diagnostic performance of 74%. Compared to age-matched controls, FTD patients showed focal hypoperfusion in the ACC, whereas AD patients showed a more extensive hypoperfusion. These CBF changes discriminated FTD and AD patients well from age-matched controls (diagnostic performances of

Table 4: Diagnostic performance (area under the curve: AUC) of cerebral blood flow in regions significantly different between patients and controls.

	AD vs. FTD			AD vs. OC			FTD vs. OC		
	AUC	95% CI		AUC	95% CI		AUC	95% CI	
		Upper	Lower		Upper	Lower		Upper	lower
MTL	…	…	…	0.760	0.604	0.916	…	…	…
Temporal lobe	…	…	…	0.812	0.666	0.958	…	…	…
Precuneus	…	…	…	0.849	0.729	0.969	…	…	…
PCC	0.741	0.563	0.919	0.837	0.706	0.967	…	…	…
Thalamus	…	…	…	0.797	0.645	0.949	…	…	…
ACC	…	…	…	0.735	0.555	0.916	0.775	0.633	0.916
Medial PFC	…	…	…	0.735	0.554	0.917	…	…	…

ACC: anterior cingulate cortex; AD: Alzheimer's disease; AUC: area under the curve; CI: confidence interval; FTD: frontotemporal dementia; MTL: medial temporal lobe; OC: older controls; PCC: posterior cingulate cortex; PFC: prefrontal cortex. Only regions showing significant differences between groups in the one way-ANOVA are shown.

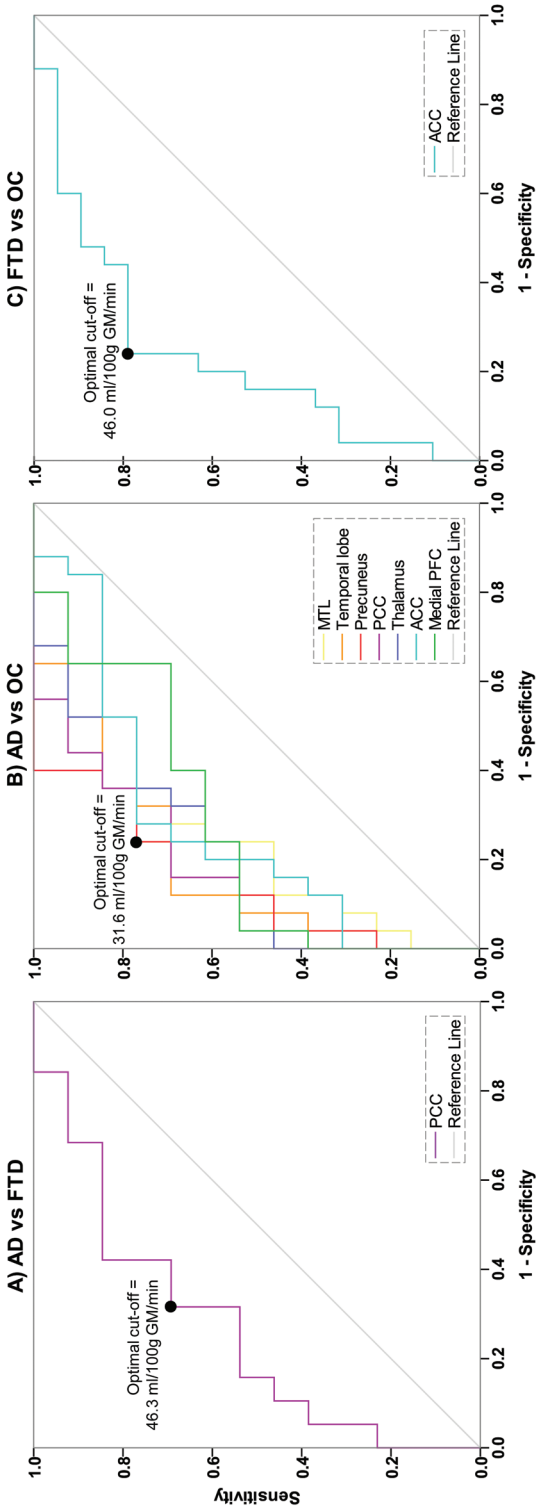

Figure 3: Receiver operating characteristic (ROC) curves and optimal cut-off points and associated sensitivity and specificity for GM CBF in regions of interest that show significant differences between AD and FTD patients (a), AD patients and older controls (b) and FTD patients and older controls (c).
ACC: anterior cingulate cortex; AD: Alzheimer's disease; FTD: frontotemporal dementia; GM: gray matter; MTL: medial temporal lobe; OC: older controls; PCC: posterior cingulate cortex; PFC: prefrontal cortex.

78% and 85% respectively). Finally, we observed that CBF was globally reduced with increased age, which should be distinguished from the pathological hypoperfusion in dementia**.** Atrophy and hypoperfusion corresponded frequently in AD, but not in FTD. Crucially, gray matter volume was not different between AD and FTD, indicating that these cannot be distinguished based on regional atrophy at this stage and in this patient population. This indicates that ASL-MRI provides contributing information for the differential diagnosis.

The observed lower CBF in the PCC in AD than FTD is in agreement with previous studies [8,9,29]. Notably, we found CBF measurement in the PCC performing reasonably (74%) to differentiate presenile AD from FTD, which may thus serve as a diagnostic marker to differentiate these diseases at an early stage. Previous studies reported additional differential regional hypoperfusion in the precuneus and temporo-parietal cortex in AD, and in the ACC and frontal cortex in FTD [8,9,29]. Our AD patients had lower CBF than FTD patients in all regions, including in those typically lower in FTD, which may have obscured differences between the patient groups. Nevertheless, the extensive CBF changes are consistent with literature [30-32], and with the finding that in early FTD the extent of atrophy exceeds that of hypoperfusion, while in AD these are similar [29].

This discrepancy in hypoperfusion may also explain why CBF changes in FTD patients were limited to the ACC. Additional hypoperfusion in FTD has been reported in the temporal lobe, medial PFC, and thalamus [29], whereas hypometabolism on PET is generally limited to frontal regions in early-stage fluent PPA and behavioral-variant FTD (bv-FTD) [33]. The localized ACC hypoperfusion may thus be due to the disease still being at an early stage. Furthermore, focal ACC neuronal loss has been associated with tau pathology [34] which is correlated with both bv-FTD and PPA variants [35], suggesting our FTD sample comprises predominantly patients with tau pathology.

CBF was globally decreased in AD, but of note is that a global CBF decrease does not necessarily indicate dementia. Compared to young controls, older controls also show globally decreased CBF. This is concordant with previous studies [36] and suggests that CBF reduces with aging. To our knowledge, no longitudinal ASL studies exist to verify this, but a longitudinal PET study supports this conclusion [37]. Closer examination of the global CBF changes showed that relative regional differences are generally preserved with age but also with neurodegeneration. For instance, despite the disproportionate widespread hypoperfusion in AD, and being most severely affected in AD and FTD, the PCC and ACC remain among the regions with the highest CBF. This intrinsically high regional CBF may obscure subtle neurodegenerative changes, and thus requires quantitative measurement rather than visual inspection.

This study has some limitations. First, our ROI definition was somewhat different from functionally definition of ROIs by literature. The structural ROIs used here may explain some unexpected findings, such as hypoperfusion in the calcarine cortex in AD. Our structural ROI also included the lingual gyrus and cuneus, which have shown hypoperfusion in AD [30] and may thus have affected this entire region's CBF. Nevertheless, our results are generally consistent with previous findings.

We specifically chose this multi-subject atlas [21,22] because its automated ROI definition is more robust than single-subject atlases. Second, the cross-sectional design does not allow for generalization of results to aging as a process. Still, the results provide insight in physiological CBF changes associated with higher age, compared to pathological CBF changes in higher age with concomitant dementia. Third, our sample is rather heterogeneous, comprising not only patients with AD or FTD phenotype, but also with PPA with AD or FTD as underlying pathology. Patient misclassification seemed not be affected by PPA variant, nor by gender, age, or MMSE. The heterogeneity of our sample on the other hand illustrates precisely the complexity of this patient population and the difficulty inherent to nosological diagnosis as a reference standard: a degree of uncertainty always remains, although it decreases as the disease progresses. Nevertheless, like the majority of *in vivo* dementia studies, our study relies on a reference standard that implies classification by means of best available evidence. In addition, we report group effects which may not necessarily generalize to individual patients. These issues may challenge the diagnostic value of ASL. However, we collected ASL data at a time point in the diagnostic process when diagnosis was not yet definitive. Only after follow-up, diagnosis was established. This shows that with ASL diagnosis can be made earlier than with routine clinical criteria, even at the individual patient level. Future studies should focus on validation of group results for individual diagnosis. Finally, the current results were obtained using a single scanner, while CBF measurement may not be robust across imaging centers. Inter-scanner and inter-vendor differences should be taken into account in patient studies [15] to reliably interpret quantitative CBF changes indicative of dementia and establish cut-off values.

In conclusion, we show that ASL-MRI can contribute to early diagnosis of presenile dementia and differentiate between AD and FTD where structural MRI does not. Hypoperfusion in the precuneus, ACC and PCC may serve as quantitative diagnostic markers for respectively presenile AD, FTD, and their differentiation. Widespread hypoperfusion is seen in early stage presenile AD, but needs to be distinguished from a physiological CBF decrease in the older population. The clinical implementation of ASL should eventually be based on data of multicenter studies. This will help to determine and validate reference values and further improve diagnostic performance of differential diagnosis in early stage presenile dementia.

REFERENCES

1. van der Flier, W. M., Scheltens P. Epidemiology and risk factors of dementia. J Neurol Neurosurg Psychiatr. 2005;76 Suppl 5: v2-7.
2. Koedam EL, Lauffer V, van der Vlies AE, van der Flier WM, Scheltens P, Pijnenburg YA. Early-versus late-onset Alzheimer's disease: more than age alone. J Alzheimers Dis. 2010;19: 1401-1408.
3. Rossor MN, Fox NC, Mummery CJ, Schott JM, Warren JD. The diagnosis of young-onset dementia. Lancet Neurol. 2010;9: 793-806.
4. Gorno-Tempini ML, Hillis AE, Weintraub S, Kertesz A, Mendez M, Cappa SF, et al. Classification of primary progressive aphasia and its variants. Neurology. 2011;76: 1006-1014.
5. Frisoni GB, Fox NC, Jack CR,Jr, Scheltens P, Thompson PM. The clinical use of structural MRI in Alzheimer disease. Nat Rev Neurol. 2010;6: 67-77.
6. Ishii K. PET Approaches for Diagnosis of Dementia. American Journal of Neuroradiology. 2013.
7. McMahon PM, Araki SS, Sandberg EA, Neumann PJ, Gazelle GS. Cost-effectiveness of PET in the diagnosis of Alzheimer disease. Radiology. 2003;228: 515-522.
8. Hu WT, Wang Z, Lee VM, Trojanowski JQ, Detre JA, Grossman M. Distinct cerebral perfusion patterns in FTLD and AD. Neurology. 2010;75: 881-888.
9. Du AT, Jahng GH, Hayasaka S, Kramer JH, Rosen HJ, Gorno-Tempini ML, et al. Hypoperfusion in frontotemporal dementia and Alzheimer disease by arterial spin labeling MRI. Neurology. 2006;67: 1215-1220.
10. Wang Z. Characterizing early Alzheimer's disease and disease progression using hippocampal volume and arterial spin labeling perfusion MRI. J Alzheimers Dis. 2014;42 Suppl 4: S495-502.
11. Wierenga CE, Hays CC, Zlatar ZZ. Cerebral blood flow measured by arterial spin labeling MRI as a preclinical marker of Alzheimer's disease. J Alzheimers Dis. 2014;42 Suppl 4: S411-9.
12. Pfefferbaum A, Chanraud S, Pitel AL, Shankaranarayanan A, Alsop DC, Rohlfing T, et al. Volumetric cerebral perfusion imaging in healthy adults: regional distribution, laterality, and repeatability of pulsed continuous arterial spin labeling (PCASL). Psychiatry Res. 2010;182: 266-73.
13. McKhann GM, Knopman DS, Chertkow H, Hyman BT, Jack CR,Jr, Kawas CH, et al. The diagnosis of dementia due to Alzheimer's disease: recommendations from the National Institute on Aging-Alzheimer's Association workgroups on diagnostic guidelines for Alzheimer's disease. Alzheimers Dement. 2011;7: 263-269.
14. Rascovsky K, Hodges JR, Knopman D, Mendez MF, Kramer JH, Neuhaus J, et al. Sensitivity of revised diagnostic criteria for the behavioural variant of frontotemporal dementia. Brain. 2011;134: 2456-2477.
15. Mutsaerts HJ, Steketee RME, Heijtel DF, Kuijer JP, van Osch MJ, Majoie CB, et al. Inter-vendor reproducibility of pseudo-continuous arterial spin labeling at 3 tesla. PLoS One. 2014;9: e104108.
16. Alsop DC, Detre JA, Golay X, Günther M, Hendrikse J, Hernandez-Garcia L, et al. Recommended implementation of arterial spin-labeled perfusion MRI for clinical applications: A consensus of the ISMRM perfusion study group and the European consortium for ASL in dementia. Magn Reson Med. 2015;73: 102-116.
17. Bron EE, Steketee RME, Houston GC, Oliver RA, Achterberg HC, Loog M, et al. Diagnostic classification of arterial spin labeling and structural MRI in presenile early stage dementia. Hum Brain Mapp. 2014;35: 4916-4931.
18. Ashburner J, Friston KJ. Unified segmentation. Neuroimage. 2005;26: 839-851.
19. Klein S, Staring M, Murphy K, Viergever MA, Pluim JP. Elastix: a Toolbox for Intensity-Based Medical Image Registration. IEEE Trans Med Imaging. 2010;29: 196-205.

20. Asllani I, Borogovac A, Brown TR. Regression algorithm correcting for partial volume effects in arterial spin labeling MRI. Magn Reson Med. 2008;60: 1362-1371.
21. Hammers A, Allom R, Koepp MJ, Free SL, Myers R, Lemieux L, et al. Three-dimensional maximum probability atlas of the human brain, with particular reference to the temporal lobe. Hum Brain Mapp. 2003;19: 224-247.
22. Gousias IS, Rueckert D, Heckemann RA, Dyet LE, Boardman JP, Edwards AD, et al. Automatic segmentation of brain MRIs of 2-year-olds into 83 regions of interest. Neuroimage. 2008;40: 672-684.
23. Heckemann RA, Hajnal JV, Aljabar P, Rueckert D, Hammers A. Automatic anatomical brain MRI segmentation combining label propagation and decision fusion. Neuroimage. 2006;33: 115-126.
24. Tustison NJ, Avants BB, Cook PA, Zheng Y, Egan A, Yushkevich PA, et al. N4ITK: improved N3 bias correction. IEEE Trans Med Imaging. 2010;29: 1310-1320.
25. Smith SM. Fast robust automated brain extraction. Hum Brain Mapp. 2002;17: 143-155.
26. Foster NL, Heidebrink JL, Clark CM, Jagust WJ, Arnold SE, Barbas NR, et al. FDG-PET improves accuracy in distinguishing frontotemporal dementia and Alzheimer's disease. Brain. 2007;130: 2616-2635.
27. Ibach B, Poljansky S, Marienhagen J, Sommer M, Manner P, Hajak G. Contrasting metabolic impairment in frontotemporal degeneration and early onset Alzheimer's disease. Neuroimage. 2004;23: 739-743.
28. Santens P, De Bleecker J, Goethals P, Strijckmans K, Lemahieu I, Slegers G, et al. Differential regional cerebral uptake of (18)F-fluoro-2-deoxy-D-glucose in Alzheimer's disease and frontotemporal dementia at initial diagnosis. Eur Neurol. 2001;45: 19-27.
29. Zhang Y, Schuff N, Ching C, Tosun D, Zhan W, Nezamzadeh M, et al. Joint assessment of structural, perfusion, and diffusion MRI in Alzheimer's disease and frontotemporal dementia. Int J Alzheimers Dis. 2011;2011: 546871.
30. Asllani I, Habeck C, Scarmeas N, Borogovac A, Brown TR, Stern Y. Multivariate and univariate analysis of continuous arterial spin labeling perfusion MRI in Alzheimer's disease. J Cereb Blood Flow Metab. 2008;28: 725-736.
31. Chen Y, Wolk DA, Reddin JS, Korczykowski M, Martinez PM, Musiek ES, et al. Voxel-level comparison of arterial spin-labeled perfusion MRI and FDG-PET in Alzheimer disease. Neurology. 2011;77: 1977-1985.
32. Binnewijzend MA, Kuijer JP, van der Flier WM, Benedictus MR, Moller CM, Pijnenburg YA, et al. Distinct perfusion patterns in Alzheimer's disease, frontotemporal dementia and dementia with Lewy bodies. Eur Radiol. 2014;24: 2326-2333.
33. Diehl J, Grimmer T, Drzezga A, Riemenschneider M, Förstl H, Kurz A. Cerebral metabolic patterns at early stages of frontotemporal dementia and semantic dementia. A PET study. Neurobiol Aging. 2004;25: 1051-1056.
34. Tan RH, Pok K, Wong S, Brooks D, Halliday GM, Kril JJ. The pathogenesis of cingulate atrophy in behavioral variant frontotemporal dementia and Alzheimer's disease. Acta Neuropathol Commun. 2013;1: 30-5960-1-30.
35. Chare L, Hodges JR, Leyton CE, McGinley C, Tan RH, Kril JJ, et al. New criteria for frontotemporal dementia syndromes: clinical and pathological diagnostic implications. J Neurol Neurosurg Psychiatry. 2014;85: 865-870.
36. Chen JJ, Rosas HD, Salat DH. Age-associated reductions in cerebral blood flow are independent from regional atrophy. Neuroimage. 2011;55: 468-478.
37. Thambisetty M, Beason-Held L, An Y, Kraut MA, Resnick SM. APOE epsilon4 genotype and longitudinal changes in cerebral blood flow in normal aging. Arch Neurol. 2010;67: 93-98.

Chapter 2.3

Concurrent white and gray matter degeneration of disease-specific networks in early-stage Alzheimer's disease and behavioral variant frontotemporal dementia

Rebecca M.E. Steketee*
Rozanna Meijboom*
Marius de Groot
Esther E. Bron
Frank Jan de Jong
Aad van der Lugt
John C. van Swieten
Marion Smits
* These authors contributed equally to this work

Submitted

ABSTRACT

In presenile Alzheimer's disease (AD) and behavioral variant frontotemporal dementia (bvFTD), abnormalities of white matter (WM) microstructure, gray matter (GM) volume and GM perfusion are found in disease-specific regions. This study investigates whether these WM and GM abnormalities co-occur on a regional level in the context of a common disease process.

Eleven AD and nine bvFTD patients, and 18 controls underwent structural imaging, diffusion tensor imaging (DTI), and arterial spin labeling (ASL) to assess GM volume, WM fractional anisotropy (FA) and mean diffusivity (MD), and GM cerebral blood flow (CBF) respectively. First, between-group differences were assessed for each measure separately. Second, for WM tracts affected in AD and bvFTD, FA and MD were extracted and correlated with regional mean GM volume and CBF at either end of the WM tract. Subsequently, correlations between WM and GM measures were compared between groups to establish disease-specific differences in regional WM-GM coherence.

Separate structural WM and GM abnormalities were more extensive in bvFTD than in AD, and hypoperfusion was evident in AD but not in bvFTD. Compared with controls, WM-GM coherence was stronger between the cingulum and frontotemporal GM in AD, and temporoparietal GM in bvFTD. Additionally, in AD compared with controls, coherence was stronger between the inferior fronto-occipital fasciculus microstructure and occipital GM perfusion.

In this first study assessing regional WM-GM coherence in AD and bvFTD we show that WM microstructure and GM volume and perfusion measures are coherent. This is particularly strong in regions implicated in AD and bvFTD pathology indicating concurrent degeneration in disease-specific networks. This methodology allows for the detection of incipient abnormalities that go undetected in comparative group analyses.

INTRODUCTION

Alzheimer's disease (AD) and frontotemporal dementia (bvFTD) are two common types of presenile dementia (onset ≤ 65 years) [1]. These diseases are characterized by distinct abnormalities in gray matter (GM) and white matter (WM), as measured with magnetic resonance imaging (MRI) [2-7]. Although regional relationships between GM volume and perfusion have been widely studied in AD and bvFTD [8-15], it is still largely unclear whether and how WM and GM abnormalities are related. One hypothesis is that WM and GM abnormalities develop in a Wallerian-like degenerative manner, in which GM cell death leads to degeneration of WM tracts connecting affected GM regions. Another possible mechanism is that WM degeneration occurs independently from GM volume loss and/or hypoperfusion [16]. However, since both diseases are characterized by specific WM and GM abnormalities, it is conceivable that these abnormalities do not occur in isolation, but that they co-occur in the context of a common disease process. Regional coherence would indicate that abnormalities in local WM and GM occur to a similar degree, and thus reflect regionally concurrent degeneration.

Thus far, relationships between abnormalities in WM microstructure and GM volume have been found to be inconsistent in AD [17-21], whereas in bvFTD WM microstructural abnormalities have been consistently found to exceed GM volume loss [3,22-24]. One study looked at the relationship between WM microstructure, GM volume, and GM perfusion in AD and bvFTD [25], and confirmed that WM microstructure is more severely affected in bvFTD than in AD. Additionally, it confirmed that GM volume loss and WM microstructural abnormalities in bvFTD exceed GM hypoperfusion, whereas in AD the degree of (micro)structural abnormalities and GM hypoperfusion is similar. However, this study did not assess the spatial relationships between WM microstructure and GM measures. This precludes the demonstration of possible regional relationships between WM and GM abnormalities, which is of particular interest given their disease-specific regional distribution.

In this study we aimed to establish whether there is coherence between regional abnormalities of WM microstructure and GM volume and perfusion in AD and in bvFTD. First, we assessed abnormalities of WM microstructure, GM volume and GM perfusion for each measure separately. Second, we correlated WM measures in affected tracts with volume and perfusion in the GM regions at either end of the tract.

MATERIALS AND METHODS

Participants

Patients were recruited at the Alzheimer Centre Southwest Netherlands and included in the analysis if they were clinically diagnosed with AD [26] or bvFTD [27], had an age of 45 to 70 years, and a Mini-Mental State Examination (MMSE, [28]) score of ≥ 20. Patient exclusion criteria were other causes of dementia, other

neurological disorders, psychiatric diagnosis, contraindications for MRI, and expected loss to follow up within 1 year. Healthy age and gender matched controls with an age between 45 and 70 years, and without psychiatric or neurological history, were recruited from patient peers and through advertisement.

Both patients and controls underwent a full neuropsychological assessment evaluating attention and concentration, executive functioning, memory, language, social cognition, and constructive and visuospatial skills and MMSE. The MMSE was assessed in healthy controls after the MRI scan by the researcher. All participants gave written informed consent, and the study was approved by the local medical ethics committee.

Image acquisition

Scanning was performed on a 3-Tesla GE Discovery MR750 system (GE Healthcare, Milwaukee, WI, US).

Diffusion imaging

DTI was acquired with 25 non-collinear directions using a spin echo echo planar imaging (EPI) sequence and with full coverage of the supratentorial brain (echo time (TE) set to minimum with range 81.9ms-90.8ms, repetition time (TR) 7.9ms, voxel size 1.9x1.9x2.5mm^3 with a 240mm field of view (FOV), array spatial sensitivity encoding technique (ASSET) acceleration factor 2, flip angle 90°, maximum b-value 1000 s/mm^2, 3 non-diffusion-weighted volumes, 59 axial slices per volume, total acquisition time 3:50min).

Structural imaging

A high-resolution three-dimensional (3D) inversion recovery fast spoiled gradient echo T1-weighted (T1w) image was acquired for GM volumetric assessment with TE 3.06ms, TR 7.90ms, inversion time 450ms, isotropic voxel size 1mm^3 with a 240mm FOV, ASSET acceleration factor 2, flip angle 12°, 176 sagittal slices, total acquisition time 4:41min.

Perfusion imaging

Perfusion images were acquired using whole brain 3D pseudo-continuous ASL (p-CASL), which is currently the recommended sequence for clinical use [29] (interleaved fast spin-echo stack-of-spiral readout of 512 sampling points on 8 spirals, TE 10.5ms, TR 4632ms, isotropic voxel size 3.3mm^3 with a 240mm FOV, 36 axial slices, number of excitations (NEX) 3, total acquisition time 4:29min; with background suppression, post label delay 1525ms, labeling duration 1450ms). The labeling plane was positioned 9cm below the anterior commissure – posterior commissure line.

Demographical analysis

Using SPSS Statistics, version 20.0 (New York, USA), gender differences across groups were assessed using chi-square tests and age differences using one-way ANOVA, with Bonferroni correction for multiple comparisons. As MMSE was not normally distributed across groups (Shapiro-Wilk test $p<0.05$) a nonparametric Kruskal-Wallis test was used to assess differences between groups, with Dunn-Bonferroni correction for multiple comparisons. Thresholds for significance were set at $p<0.05$.

DTI processing and analysis

Data were analyzed using FMRIB Software Library (FSL5, Oxford, UK) [30-32]. Data were corrected for motion and eddy currents using Eddy Correct and then skull-stripped using BET [33].

Tract-Based Spatial Statistics (TBSS)

Using whole brain TBSS, WM tracts showing fractional anisotropy (FA) abnormalities were identified. First, diffusion tensors were reconstructed using DTIFIT [34], resulting in an FA output image for each participant. Second, FA images were registered using TBSS [35]. TBSS removed brain-end artifacts and end slices in order to exclude FA image outliers. Participant FA images were non-linearly registered to the FMRIB58 FA template, followed by normalization to the Montreal Neurological Institute (MNI) template. The mean of all normalized participant FA images was taken to create a mean FA skeleton, which was then binarized. All participant FA images were projected onto the binary FA skeleton, resulting in an FA value skeleton for each participant.

Group differences in FA were tested using Randomize [36]. Using the General Linear Model (GLM) a one-way ANOVA design with three groups (AD≠bvFTD≠controls) was defined. Six t-contrasts (AD>HC, HC>AD, bvFTD>HC, HC>bvFTD, AD>bvFTD, bvFTD>AD) were constructed to assess post-hoc differences in FA between groups. Nonparametric permutation testing with 5000 permutations and threshold-free cluster enhancement (TFCE, [37]) were applied. Results were family-wise error corrected for multiple comparisons ($p<0.05$).

In order to identify post-hoc t-tests results within the boundaries of the f-test results, common binary masks were created using Fslmaths. First, for the f-test and all t-tests a binary mask was created ($p=0.95$). Second, each t-test binary mask was multiplied with the f-test binary mask, resulting in a common binary mask for every t-test. Last, cluster size ($k\geq50$) was extracted from all t-test common binary masks using Cluster.

Using FSLview, results were visualised and anatomically identified with the implemented JHU White-Matter Tractography Atlas and the JHU ICBM-DTI-81 White-Matter labels. WM tracts showing decreased FA in AD and/or bvFTD in the current study, and known to be associated with cognition were selected for tractography:

anterior thalamic radiation [38,39], cingulum [40], forceps major [39,41] and minor [39,42,43] (representing respectively the splenium and genu of the corpus callosum), inferior fronto-occipital fasciculus [44-46], inferior longitudinal fasciculus [46,47], superior longitudinal fasciculus [47,48] and uncinate fasciculus [40,42,45].

Tractography

From the selected WM tracts, median FA values were extracted. In addition, median values of mean diffusivity (MD) were extracted to obtain a more comprehensive view on how WM measures relate to GM measures. Automated probabilistic tractography (AutoPtx, [49]) was used to apply a tensor fit with DTIFIT [34], followed by a FNIRT registration and a Bedpostx probabilistic model fit for each participant. Then Probtracx was run for all selected WM tracts (Table 1) using default space seed, target, stop and exclusion masks available in AutoPtx [49], resulting in a tract density image for each tract in each participant. Tract density images were normalized by dividing these by the number of tracts included in the image and then thresholded for WM tract segmentation, based on the best-fit segmentation thresholds established by De Groot et al. (2014) (see Supplementary Table 1 for thresholds).

Using FSLstats, FA and MD images were masked with thresholded tract images to acquire median FA and MD values for each tract. Significant effects of age and TE on FA and MD were identified using linear regression and corrected for if necessary.

Structural imaging and ASL processing and analysis

Tissue segmentation

The unified tissue segmentation method [50] of SPM8 (Statistical Parametric Mapping, London, UK) was used to segment the T1w image into GM, WM and cerebrospinal fluid maps. Volume and cerebral blood flow (CBF) were derived from GM only.

ASL post-processing

The ASL dataset consisted of a labeled and a control image. The GM map of each participant was rigidly registered with the ASL control image (Elastix registration software [51]). Subsequently, GM maps were transformed to ASL image space to enable partial volume (PV) correction. Both labeled and control ASL images were corrected for PV effects using local linear regression within a 3D kernel based on tissue maps [52]. Then, CBF was quantified in the PV-corrected ASL images using the single-compartment model [29]. CBF maps were transformed to T1w image space to enable labeling of regions.

ROI labeling

A multi-atlas approach was used to define regions of interest (ROIs) for each participant. The atlas included 30 labeled T1w images, each containing 83 ROIs [53,54]. These atlas images were registered to the participants' T1w images using a rigid, affine, and non-rigid B-spline transformation model consecutively. For this registration, both the participants' and the labeled T1w images were masked (Brain Extraction Tool, [33]) and T1w images were non-uniformity corrected [55]. ROI labels were fused using a majority voting algorithm [56].

Regional GM volume and CBF analysis

GM volume and CBF were analyzed in the global supratentorial brain and in ROIs. The multi-atlas approach parcellated each participant's T1w image into 83 ROIs. The cerebellum, brainstem, pallidum, substantia nigra, ventricles and WM regions were excluded from analysis. The remaining GM ROIs were analyzed at the gyral level, by combining regions smaller than a single gyrus to constitute an entire gyrus (Supplementary Table 2). Regional GM volumes were corrected for head size by normalizing to total intracranial volume (ICV). These are referred to as normalized GM (nGM) volumes and reported as percentage of ICV. CBF was divided by nGM volume to correct for atrophy. Significant effects of age on nGM volume and CBF were identified using linear regression and corrected if necessary.

As nGM volumes and CBF values were not normally distributed across groups (Shapiro-Wilk test $p<0.05$), a nonparametric Kruskal-Wallis test with Dunn-Bonferroni correction for multiple comparisons was used to compare measures from the global supratentorial cortex and the ROIs between groups.

Correlation analyses

Correlation analyses were performed for WM tracts that were affected in both AD and/or bvFTD (Table 1). To determine the cortical regions at either end of the tract (ROI1 and ROI2), tracts were visualized in FSLview using the JHU White-Matter Tractography Atlas overlaid on the MNI 1mm template, and/or the default WM masks available in AutoPtx [49]. For WM tracts that projected to multiple cortical regions, GM measures (nGM volume, CBF) were averaged over all cortical regions included in ROI1 or ROI2. This resulted in six variables per tract: FA, MD, nGM volume in ROI1 and ROI2, and CBF in ROI1 and ROI2 (Figure 1). Correlations between WM measures (FA and MD) and GM measures (nGM and CBF in ROI1 and ROI2) were assessed with Spearman analysis. Correlations exceeding the threshold of $0.6 \leq rho \leq -0.6$ are reported.

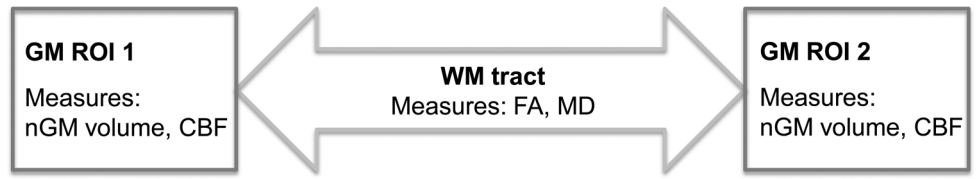

Figure 1: Schematic overview of variables entered into correlation analysis. WM = white matter, FA = fractional anisotropy, MD = mean diffusivity, ROI = region of interest, nGM = normalized gray matter, CBF = cerebral blood flow.

Table 1. Affected WM tracts and GM regions at either end of these tracts, and their abbreviations.

WM tract	Abbr.	Cortical ROI1	Abbr.	Cortical ROI2	Abbr.
Anterior thalamic radiation	ATR	Inferior frontal gyrus	IFG	Hippocampal formation	HF
		Orbitofrontal gyrus	OFG		
Cingulum (cingulate gyrus)	CGc	Subcallosal area		Posterior cingulate cortex	PCC
		Anterior cingulate cortex	ACC	Precuneus	
Cingulum (hippocampus)	CGh	Posterior cingulate cortex	PCC	Hippocampal formation	HF
		Precuneus		Anterior temporal lobe	ATL
Forceps major	FMa	Left lingual gyrus	Occipital	Right lingual gyrus	Occipital
		Left cuneus		Right cuneus	
		Left lateral occipital lobe		Right lateral occipital lobe	
Forceps minor	FMi	Left superior frontal gyrus	SFG	Right superior frontal gyrus	SFG
		Left straight gryus		Right straight gyrus	
		Left orbital frontal gyrus	OFG	Right orbital frontal gyrus	OFG
Inferior fronto-occipital fasciculus	IFOF	Inferior frontal gyrus	IFG	Lingual gyrus	Occipital
		Orbitofrontal gyrus	OFG	Cuneus	
				Lateral occipital lobe	
Inferior longitudinal fasciculus	ILF	Inferior temporal gyrus	ITG	Lingual gyrus	Occipital
		Superior temporal gyrus	STG	Cuneus	
		Anterior temporal lobe	ATL	Lateral occipital lobe	
Superior longitudinal fasciculus	SLF	Precentral gyrus		Inferior temporal gyrus	ITG
		Inferior frontal gyrus	IFG	Posterior temporal lobe	PTL
Uncinate fasciculus	UF	Inferior frontal gyrus	IFG	Superior temporal gyrus	STG
		Orbitofrontal gyrus	OFG	Anterior temporal lobe	ATL

Affected WM tracts and cortical ROIs were analyzed in the left and in the right hemisphere (except for the forceps major and minor). GM metrics were averaged per ROI, resulting in five variables for the correlation analysis: FA of WM tract, GM volume ROI1, CBF ROI1, GM volume ROI2 and CBF ROI2.

Differences between these within-group correlations were subsequently tested for significance using a Fisher's r to z transformation with Bonferroni correction for multiple comparisons. As sample sizes were small, uncorrected significant results are also reported.

WM-GM coherence was considered positive when correlations between FA and GM measures were positive, or when correlations between MD and GM measures were negative. WM-GM coherence was considered negative when correlations between FA and GM measures were negative, or correlations between MD and GM measures were positive.

RESULTS

Participant and disease characteristics

Eleven AD patients, 9 bvFTD patients and 18 healthy controls were included in the study. Gender (χ^2 (2, n=37) = 2.508, p>0.05) and age (F(2,35) = .823, p>0.05) were not different between groups. MMSE differed across groups (H(2) = 19.938, p<0.05), with post hoc analyses indicating that both patient groups had lower MMSE scores compared to controls, but not to each other (Table 2). One AD patient was excluded from the ASL analysis due to low image quality.

Table 2: Participant characteristics

	Healthy controls	bvFTD	AD
N (male)	18 (8)	9 (4)	11 (8)
Mean age ± SD in years	59.8 ± 6.73	62.3 ± 5.68	62.3 ± 5.04
Median MMSE (range)	30 (27-30)	28 (24-30)	25 (22-28)

AD = Alzheimer's disease; bvFTD = behavioral variant frontotemporal dementia; MMSE = Mini Mental State Examination; SD = standard deviation

Separate WM and GM abnormalities

WM abnormalities

AD and bvFTD patients compared with controls showed decreased FA (Figure 2, Supplementary Tables 3-4) in the anterior thalamic radiation, cingulate gyral and hippocampal cingulum, forceps major and minor, inferior fronto-occipital fasciculus, inferior and superior longitudinal fasciculus, and uncinate fasciculus.

In bvFTD patients compared with AD patients, FA was decreased in all the above-mentioned WM tracts (Supplementary Table 5). AD patients did not show regions of decreased FA compared with bvFTD patients.

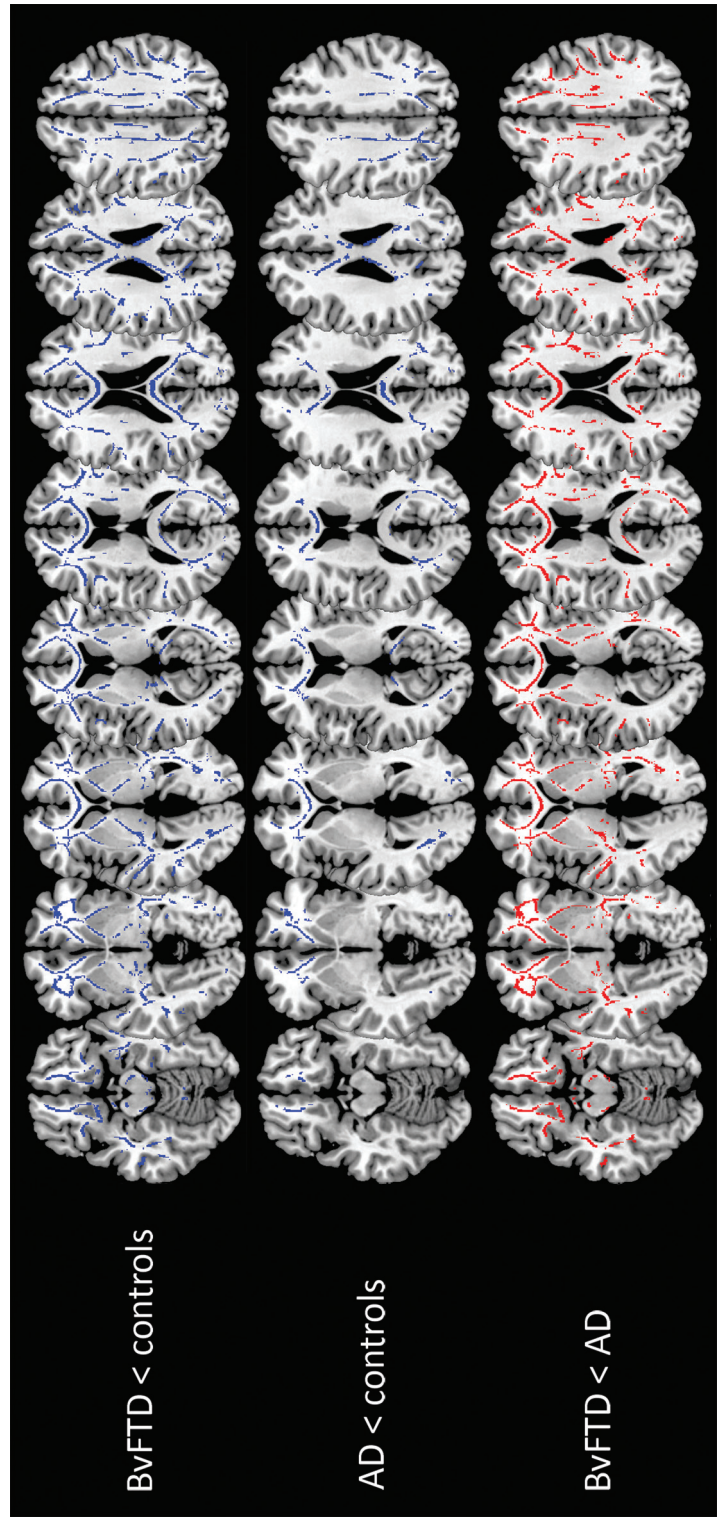

Figure 2. Post-hoc t-test (p<0.05, family-wise error corrected for multiple comparisons; k≥50) white matter FA abnormalities. Decreased FA in comparison with controls for bvFTD (top row) and AD (middle row) is shown in blue and decreased FA in bvFTD in comparison with AD (bottom row) is shown in red.
FA = fractional anisotropy, AD = Alzheimer's disease, BvFTD = behavioral variant frontotemporal dementia.

nGM volume loss

In AD patients compared with controls, nGM volumes were reduced in the bilateral parietal cortex, left temporal cortex, right occipital regions, right thalamus and left nucleus accumbens. In bvFTD patients compared with controls, global supratentorial nGM volume was reduced, as were volumes of the bilateral frontal, temporal and parietal cortices and bilateral basal ganglia. There was more extensive volume loss in the frontal lobe in bvFTD than AD patients (Supplementary Table 6).

GM hypoperfusion

AD patients compared with controls showed reduced CBF (corrected for nGM volume) in the posterior temporal lobe bilaterally, left superior temporal gyrus, bilateral precuneus and left posterior cingulate, and in the lateral remainder of the right occipital lobe. In bvFTD patients, CBF (corrected for nGM volume) was not different from controls. AD patients compared with bvFTD patients showed reduced CBF (corrected for nGM volume) in the bilateral orbitofrontal gyri, right hippocampal formation, left superior and right inferior temporal gyrus, and right fusiform gyrus (Supplementary Table 7).

Correlations between WM and GM measures

Only tracts found to be affected in AD and/or bvFTD (Supplementary Tables 3-5; Table 1) were selected for the correlation analysis.

Within-group WM-GM correlations

Within-group correlations (rho ≥ 0.6) between WM and GM measures are shown in Supplementary Table 8. Both patient groups showed more correlations between WM and GM measures than controls.

Between-group differences in WM-GM correlations

Group differences detected with Fisher Z testing are shown in Table 3. In AD patients compared with controls, strong positive correlations were found between cingulum microstructure and frontal GM perfusion and temporal GM volume, and between inferior fronto-occipital fasciculus microstructure and occipital GM volume and perfusion (Figure 3).

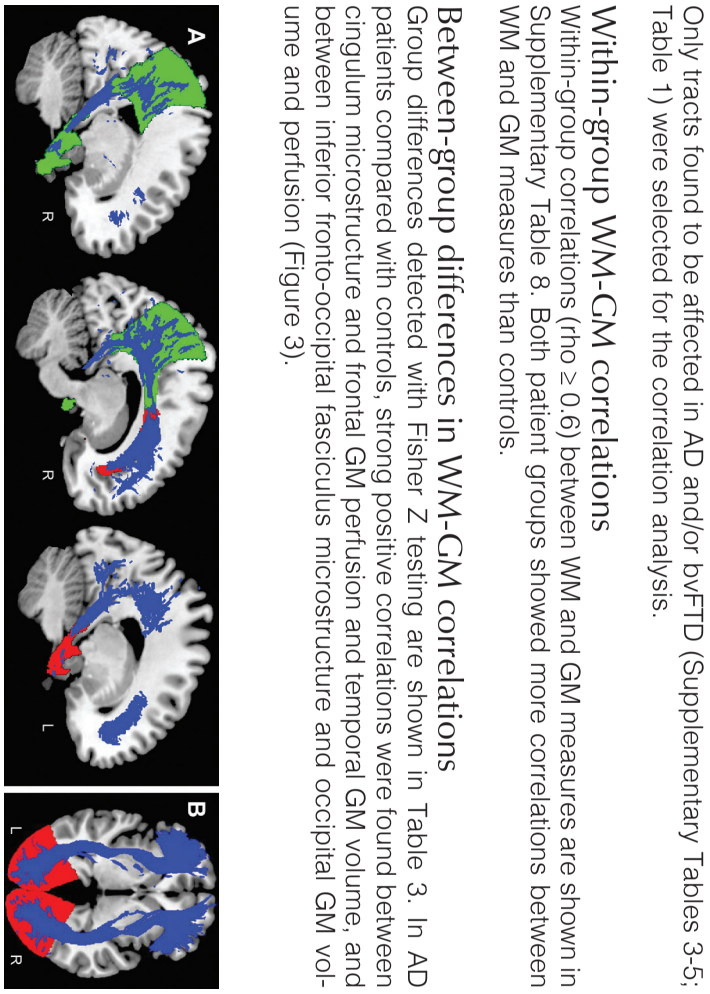

Figure 3. White matter (WM) tracts and gray matter (GM) regions that are correlated in AD and bvFTD. A: Cingulum microstructure (blue) correlated with frontal and temporal GM in AD (red) and temporal and parietal GM in bvFTD (green). B: Inferior fronto-occipital fasciculus microstructure (blue) correlated with occipital GM in AD (red).

Table 3. Between-group differences in regional correlation coefficients for WM tracts and associated GM volume and CBF. Correlations that were significantly different between groups after applying Bonferroni correction for multiple comparisons are printed in italic. The remaining correlations were significant (p<0.05) without correction for multiple comparisons but nevertheless reported because sample sizes were small.

					Correlation coefficient	
WM tract	**WM measure**	**GM region**	**GM measure**	**L/R**	**AD**	**Control**
			Positive WM-GM coherence in AD			
CGC	FA	ACC/subcallosal	CBF	R	0.648	-0.077
CGH	MD	HF/ATL	volume	L	-0.645	0.216
IFOF	FA	Occipital	CBF	R	0.636	-0.104
IFOF	MD	Occipital	CBF	L	-0.748	0.023
IFOF	MD	Occipital	volume	R	-0.137	-0.765
WM tract	**WM measure**	**GM region**	**GM measure**	**L/R**	**BvFTD**	**Control**
			Positive WM-GM coherence in bvFTD			
CGC	MD	Precuneus/PCC	CBF	R	*-0.867*	*-0.178*
CGH	FA	Precuneus/PCC	CBF	R	*0.933*	*-0.003*
CGH	MD	Precuneus/PCC	CBF	R	-0.650	0.323
CGH	MD	HF/ATL	volume	R	-0.767	-0.001

WM tract	WM measure	GM region	GM measure	L/R	BvFTD	AD
Positive WM-GM coherence in bvFTD						
CGH	FA	Precuneus/ PCC	CBF	R	*0.933*	*-0.382*
Negative WM-GM coherence in bvFTD						
UF	MD	OFG/IFG	CBF	L	*0.533*	*-0.624*

WM-GM coherence was considered positive when correlations between FA and GM measures were positive, or when correlations between MD and GM measures were negative. WM-GM coherence was considered negative when correlations between FA and GM measures were negative, or correlations between MD and GM measures were positive.
CGC = cingulum (cingulate gyrus); CGH = cingulum (hippocampal); IFOF = inferior fronto-occipital fasciculus; UF = uncinate fasciculus; OFG = orbitofrontal gyrus; ACC/PCC = anterior/posterior cingulate cortex; HF = hippocampal formation; ATL = anterior temporal lobe; L = left; R = right; CBF = cerebral blood flow; GM = gray matter; WM = white matter; FA = fractional anisotropy; MD = mean diffusivity; AD = Alzheimer's disease; bvFTD = behavioral variant frontotemporal dementia.

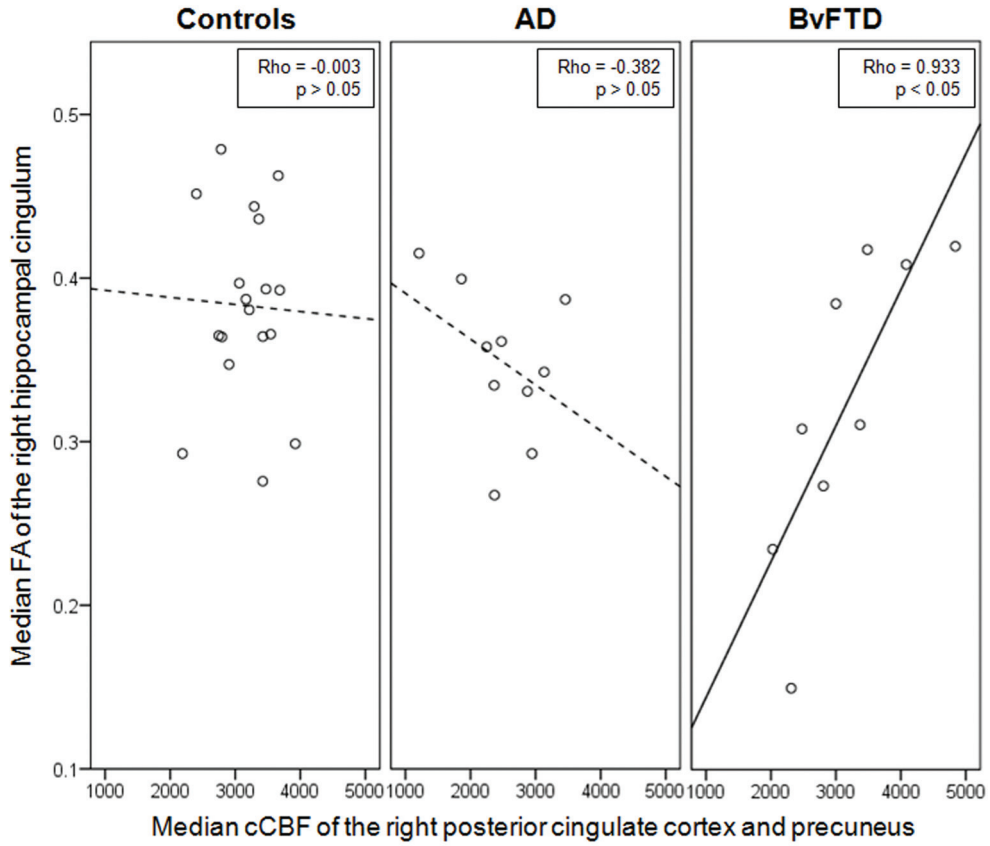

Figure 4. Correlation between median FA of the right hippocampal cingulum and median CBF corrected for GM volume in the right PCC and precuneus in controls, AD, and bvFTD patients. Correlations were significantly different between AD and bvFTD patients. Dashed lines indicate non-significant correlations; solid line indicates significant correlation.
FA = fractional anisotropy, CBF = cerebral blood flow, GM = gray matter, PCC = posterior cingulate cortex, AD = Alzheimer's disease, bvFTD = behavioral variant frontotemporal dementia.

In bvFTD patients compared with controls, strong positive correlations were found between cingulum microstructure and parietal GM perfusion and temporal GM volume.

In bvFTD compared with AD, a strong positive correlation was observed between cingulum microstructure and parietal GM perfusion (Figure 4). Not a stronger, but negative rather than positive correlation was observed between uncinate fasciculus microstructure and frontal GM perfusion.

DISCUSSION

In this study we observed a disease-specific dissociation between structural and perfusion abnormalities with more microstructural WM abnormalities and GM atrophy in bvFTD patients, and more hypoperfusion in AD patients. More importantly, we observed coherence between WM microstructure and GM volume and perfusion in both AD and bvFTD, which was strongly increased compared to controls in regions implicated in AD and bvFTD. We hypothesize that this is due to concurrent degeneration in disease specific networks.

Our findings of WM and GM abnormalities assessed separately are in line with the published literature. Compared to controls, bvFTD showed more extensive structural abnormalities in both WM and GM than AD. In bvFTD, WM abnormalities were observed throughout the entire brain, and GM atrophy in the frontal, temporal, parietal and subcortical regions [2,3,5]. In AD, WM abnormalities were less extensive and found in frontal, parietal and occipital regions and GM atrophy in temporal, parietal, occipital and subcortical regions [2,4,5]. Only AD showed prominent temporal, parietal and occipital hypoperfusion [57], while there was no significant hypoperfusion in bvFTD.

In this study, we took these – known – findings a step further by assessing the coherence between regional WM and GM measures. In the healthy elderly, only a small number of regions showed positive coherence between WM microstructure and GM volume. Coherence between WM microstructure and GM perfusion was even less pronounced. Conversely, patients showed strong coherence in many disease-specific regions. This indicates that WM and GM changes co-occur to a similar degree, and may thus reflect concurrent degeneration of WM and GM. The strong positive coherence between WM and GM measures in patients was particularly prominent between cingulum microstructure and associated temporal GM volume and frontal GM perfusion in AD, and between cingulum microstructure and temporal GM volume and parietal GM perfusion in bvFTD.

The cingulum is central to the Papez circuit, which comprises regions implicated in AD such as the entorhinal cortex, fornix and hippocampal formation. The positive coherence between cingulum microstructure and GM volume of the hippocampal formation and anterior temporal lobe can thus be explained by concurrent anterior medial temporal atrophy and cingulum degeneration. Additionally, we observed coherence between the cingulum and its associated anterior GM regions, which we hypothesize to be related to the posterior to anterior propagation of AD pathology [58]. This propagation is widely believed to result from Wallerian degeneration in which WM pathology is presumably secondary to GM pathology. However, there also is increasing evidence that WM pathology is primary to GM pathology in AD [59]. Our cross-sectional correlational study design does not allow for claims on changes over time, but rather shows evidence of concurrent changes in WM and GM. Instead of AD being primarily a WM or GM disease, we speculate that WM microstructural abnormalities and GM abnormalities are dependent in pathogenesis, as changes of the cingulum microstructure and associated GM regions seem to co-occur. In support of this, individual WM and GM measures in this study showed a similar degree of WM and GM structural abnormalities in AD.

In bvFTD, positive coherence between cingulum microstructure and parietal GM perfusion was not only evident in comparison with controls, but also with AD patients, in whom this regional coherence was absent. On a group level, cingulum microstructure in bvFTD was abnormal but parietal perfusion was not. Nevertheless, the strong positive coherence indicates that as cingulum WM deteriorates, perfusion decreases too, implying incipient parietal perfusion abnormalities, as previously reported in bvFTD [60]. Additionally, higher coherence was observed exclusively in the right hemisphere, consistent with the notion of greater right than left hemisphere involvement in bvFTD [61-63].

It may seem counterintuitive that bvFTD showed high coherence in posterior regions and AD in anterior regions, when relating it to propagation of pathology from anterior to posterior in bvFTD, and from posterior to anterior in AD. Higher coherence may be expected in more severely affected anterior regions in bvFTD and posterior regions in AD. Instead, this study shows coherence between WM and GM measures in the less rather than the more severely affected regions. We postulate that when abnormalities are incipient, WM and GM changes are concurrent, whereas this coherence is lost once abnormalities are advanced. This is in line with previous findings of changes of functional connectivity in the default mode network (DMN). The DMN consists of a frontal and parietal component, connected through the cingulum. In parallel with our findings, in bvFTD functional connectivity is generally found to be higher in the parietal than in the frontal DMN, whereas in AD functional connectivity is found to be lower in the parietal than in the frontal DMN [64]. The coherence we found between the uncinate fasciculus and frontal GM perfusion in AD can be similarly interpreted in the context of the salience network (SN), which has previously shown increased frontal functional connectivity in AD [64].

Additionally, in AD coherence was also observed between inferior fronto-occipital fasciculus microstructure and occipital GM perfusion, but not occipital GM volume. GM abnormalities of the occipital lobe are not consistently implicated in AD pathology [13,57,65] and indeed when we assessed GM measures separately, we found dissimilar perfusion and GM volume abnormalities.

Surprisingly, in bvFTD we observed negative coherence between uncinate fasciculus microstructure and frontal GM perfusion, suggesting diverging WM and GM changes. This may seem remarkable as both uncinate fasciculus WM abnormalities and frontal hypoperfusion have been reported in bvFTD [3,66]. In our study we corrected perfusion for GM volume and showed that perfusion was slightly increased in the frontal GM in bvFTD, albeit non-significantly. Slightly increased perfusion may suggest functional compensation for structural damage in the frontal lobe. It was only seen in the frontal lobe, which is indeed the most severely affected brain region structurally in bvFTD. As we found rather extensive frontal WM and GM volume abnormalities, we suspect that the slightly increased perfusion may be the final stage of a compensatory process, just prior to the occurrence of hypoperfusion.

Overall, our findings demonstrate that the concurrent changes in WM and GM adhere to the disease-specific distribution of abnormalities, generally propagat-

ing from posterior to anterior regions in AD and from anterior to posterior regions in bvFTD. It is of interest that the correlational methodology appears to be sensitive to incipient abnormalities that are not (yet) evident as differences between groups.

This study knows some limitations. First, our patient group sizes were relatively small. To correct for the sensitivity of small samples to outliers, we used non-parametric testing which is generally more stringent and thus carries the risk of false negative results. A potentially larger problem is the difference in sample size of the patient groups compared with controls. In a large sample, the threshold for significance of correlations is lower, i.e. relatively low correlation coefficients were significant in our control sample but not in patients. This may have skewed a fair comparison between the groups. We accounted for this by reporting all correlations above the threshold of rho ≥ 0.6. Second, a single FA and MD value was used for each WM tract. In long association fibers this may not be fully representative as it may obscure regional differences within the WM tract. This was partly forestalled by using the median WM measure rather than the mean. A further option would have been to parcellate these tracts into smaller sections. However, as we aimed to study coherence as defined by WM anatomy and its associated GM projections, we chose to look at anatomical connections as a whole rather than at subregions. Similarly, regional heterogeneity may have affected the large GM ROIs. For instance, GM within the occipital lobe was not similarly affected, with the right medial part showing GM volume loss whereas the right lateral part and left occipital ROI did not. Such heterogeneity within an ROI may result in inconsistent coherence patterns with associated WM microstructure.

In conclusion, we observed a disease-specific dissociation between structural degeneration and hypoperfusion. More importantly, we established a framework for assessing coherence between WM microstructure and GM volume and perfusion in AD and bvFTD. Within this framework we show that such coherence is mostly absent in healthy elderly controls, but present both in AD and bvFTD. Coherence is particularly strong in regions implicated in AD and bvFTD pathology, indicating concurrent degeneration in disease-specific networks. Moreover, the correlational methodology applied in this framework allows for the detection of incipient abnormalities that would go undetected in comparative group analyses. Our future research is aimed at further defining these relationships at different stages of aging and neurodegeneration.

REFERENCES

1. Koedam EL, Lauffer V, van der Vlies AE, van der Flier WM, Scheltens P, Pijnenburg YA. Early-versus late-onset Alzheimer's disease: more than age alone. J Alzheimers Dis. 2010;19: 1401-1408.
2. Zhang Y, Schuff N, Du AT, Rosen HJ, Kramer JH, Gorno-Tempini ML, et al. White matter damage in frontotemporal dementia and Alzheimer's disease measured by diffusion MRI. Brain. 2009;132: 2579-2592.
3. Mahoney CJ, Ridgway GR, Malone IB, Downey LE, Beck J, Kinnunen KM, et al. Profiles of white matter tract pathology in frontotemporal dementia. Hum Brain Mapp. 2014;35: 4163-4179.
4. Acosta-Cabronero J, Williams GB, Pengas G, Nestor PJ. Absolute diffusivities define the landscape of white matter degeneration in Alzheimer's disease. Brain. 2010;133: 529-539.
5. Rabinovici GD, Seeley WW, Kim EJ, Gorno-Tempini ML, Rascovsky K, Pagliaro TA, et al. Distinct MRI atrophy patterns in autopsy-proven Alzheimer's disease and frontotemporal lobar degeneration. Am J Alzheimers Dis Other Demen. 2007;22: 474-488.
6. Du AT, Jahng GH, Hayasaka S, Kramer JH, Rosen HJ, Gorno-Tempini ML, et al. Hypoperfusion in frontotemporal dementia and Alzheimer disease by arterial spin labeling MRI. Neurology. 2006;67: 1215-1220.
7. Hu WT, Wang Z, Lee VM, Trojanowski JQ, Detre JA, Grossman M. Distinct cerebral perfusion patterns in FTLD and AD. Neurology. 2010;75: 881-888.
8. Bron EE, Steketee RME, Houston GC, Oliver RA, Achterberg HC, Loog M, et al. Diagnostic classification of arterial spin labeling and structural MRI in presenile early stage dementia. Hum Brain Mapp. 2014;35: 4916-4931.
9. Wang Z, Das SR, Xie SX, Arnold SE, Detre JA, Wolk DA. Arterial spin labeled MRI in prodromal Alzheimer's disease: A multi-site study. Neuroimage: Clinical. 2013;2: 630-636.
10. Shimizu S, Zhang Y, Laxamana J, Miller BL, Kramer JH, Weiner MW, et al. Concordance and discordance between brain perfusion and atrophy in frontotemporal dementia. Brain Imaging Behav. 2010;4: 46-54.
11. Tosun D, Rosen H, Miller BL, Weiner MW, Schuff N. MRI patterns of atrophy and hypoperfusion associations across brain regions in frontotemporal dementia. Neuroimage. 2012;59: 2098-2109.
12. Benedictus MR, Binnewijzend MA, Kuijer JP, Steenwijk MD, Versteeg A, Vrenken H, et al. Brain volume and white matter hyperintensities as determinants of cerebral blood flow in Alzheimer's disease. Neurobiol Aging. 2014;35: 2665-2670.
13. Steketee RME, Bron EE, Meijboom R, Houston GC, Klein S, Mutsaerts HJ, et al. Early-stage differentiation between presenile Alzheimer's disease and frontotemporal dementia using arterial spin labeling MRI. Eur Radiol. 2015.
14. Mak HK, Chan Q, Zhang Z, Petersen ET, Qiu D, Zhang L, et al. Quantitative assessment of cerebral hemodynamic parameters by QUASAR arterial spin labeling in Alzheimer's disease and cognitively normal Elderly adults at 3-tesla. J Alzheimers Dis. 2012;31: 33-44.
15. Dashjamts T, Yoshiura T, Hiwatashi A, Yamashita K, Monji A, Ohyagi Y, et al. Simultaneous arterial spin labeling cerebral blood flow and morphological assessments for detection of Alzheimer's disease. Acad Radiol. 2011;18: 1492-1499.
16. Amlien IK, Fjell AM. Diffusion tensor imaging of white matter degeneration in Alzheimer's disease and mild cognitive impairment. Neuroscience. 2014;276: 206-215.
17. Agosta F, Pievani M, Sala S, Geroldi C, Galluzzi S, Frisoni GB, et al. White Matter Damage in Alzheimer Disease and Its Relationship to Gray Matter Atrophy. Radiology. 2011;258: 853-863.

18. Mielke MM, Okonkwo OC, Oishi K, Mori S, Tighe S, Miller MI, et al. Fornix integrity and hippocampal volume predict memory decline and progression to Alzheimer's disease. Alzheimers Dement. 2012;8: 105-113.
19. Lee DY, Fletcher E, Carmichael OT, Singh B, Mungas D, Reed B, et al. Sub-Regional Hippocampal Injury is Associated with Fornix Degeneration in Alzheimer's Disease. Front Aging Neurosci. 2012;4: 1.
20. Wang PN, Chou KH, Lirng JF, Lin KN, Chen WT, Lin CP. Multiple diffusivities define white matter degeneration in amnestic mild cognitive impairment and Alzheimer's disease. J Alzheimers Dis. 2012;30: 423-437.
21. Alves GS, O'Dwyer L, Jurcoane A, Oertel-Knochel V, Knochel C, Prvulovic D, et al. Different patterns of white matter degeneration using multiple diffusion indices and volumetric data in mild cognitive impairment and Alzheimer patients. PLoS One. 2012;7: e52859.
22. Whitwell JL, Avula R, Senjem ML, Kantarci K, Weigand SD, Samikoglu A, et al. Gray and white matter water diffusion in the syndromic variants of frontotemporal dementia. Neurology. 2010;74: 1279-1287.
23. Zhang Y, Tartaglia MC, Schuff N, Chiang GC, Ching C, Rosen HJ, et al. MRI signatures of brain macrostructural atrophy and microstructural degradation in frontotemporal lobar degeneration subtypes. J Alzheimers Dis. 2013;33: 431-444.
24. Avants BB, Cook PA, Ungar L, Gee JC, Grossman M. Dementia induces correlated reductions in white matter integrity and cortical thickness: a multivariate neuroimaging study with sparse canonical correlation analysis. Neuroimage. 2010;50: 1004-1016.
25. Zhang Y, Schuff N, Ching C, Tosun D, Zhan W, Nezamzadeh M, et al. Joint assessment of structural, perfusion, and diffusion MRI in Alzheimer's disease and frontotemporal dementia. Int J Alzheimers Dis. 2011;2011: 546871.
26. McKhann GM, Knopman DS, Chertkow H, Hyman BT, Jack CR,Jr, Kawas CH, et al. The diagnosis of dementia due to Alzheimer's disease: recommendations from the National Institute on Aging-Alzheimer's Association workgroups on diagnostic guidelines for Alzheimer's disease. Alzheimers Dement. 2011;7: 263-269.
27. Rascovsky K, Hodges JR, Knopman D, Mendez MF, Kramer JH, Neuhaus J, et al. Sensitivity of revised diagnostic criteria for the behavioural variant of frontotemporal dementia. Brain. 2011;134: 2456-2477.
28. Folstein MF, Folstein SE, McHugh PR. "Mini-mental state". A practical method for grading the cognitive state of patients for the clinician. J Psychiatr Res. 1975;12: 189-198.
29. Alsop DC, Detre JA, Golay X, Gunther M, Hendrikse J, Hernandez-Garcia L, et al. Recommended implementation of arterial spin-labeled perfusion MRI for clinical applications: A consensus of the ISMRM perfusion study group and the European consortium for ASL in dementia. Magn Reson Med. 2015;73: 102-116.
30. Jenkinson M, Beckmann CF, Behrens TE, Woolrich MW, Smith SM. Fsl. Neuroimage. 2012;62: 782-790.
31. Woolrich MW, Jbabdi S, Patenaude B, Chappell M, Makni S, Behrens T, et al. Bayesian analysis of neuroimaging data in FSL. Neuroimage. 2009;45: S173-86.
32. Smith SM, Jenkinson M, Woolrich MW, Beckmann CF, Behrens TE, Johansen-Berg H, et al. Advances in functional and structural MR image analysis and implementation as FSL. Neuroimage. 2004;23 Suppl 1: S208-19.
33. Smith SM. Fast robust automated brain extraction. Hum Brain Mapp. 2002;17: 143-155.
34. Behrens TE, Woolrich MW, Jenkinson M, Johansen-Berg H, Nunes RG, Clare S, et al. Characterization and propagation of uncertainty in diffusion-weighted MR imaging. Magn Reson Med. 2003;50: 1077-1088.

35. Smith SM, Jenkinson M, Johansen-Berg H, Rueckert D, Nichols TE, Mackay CE, et al. Tract-based spatial statistics: voxelwise analysis of multi-subject diffusion data. Neuroimage. 2006;31: 1487-1505.
36. Winkler AM, Ridgway GR, Webster MA, Smith SM, Nichols TE. Permutation inference for the general linear model. Neuroimage. 2014;92: 381-397.
37. Smith SM, Nichols TE. Threshold-free cluster enhancement: addressing problems of smoothing, threshold dependence and localisation in cluster inference. Neuroimage. 2009;44: 83-98.
38. Torso M, Serra L, Giulietti G, Spano B, Tuzzi E, Koch G, et al. Strategic lesions in the anterior thalamic radiation and apathy in early Alzheimer's disease. PLoS One. 2015;10: e0124998.
39. Duering M, Gonik M, Malik R, Zieren N, Reyes S, Jouvent E, et al. Identification of a strategic brain network underlying processing speed deficits in vascular cognitive impairment. Neuroimage. 2013;66: 177-183.
40. Tartaglia MC, Zhang Y, Racine C, Laluz V, Neuhaus J, Chao L, et al. Executive dysfunction in frontotemporal dementia is related to abnormalities in frontal white matter tracts. J Neurol. 2012;259: 1071-1080.
41. Staff RT, Murray AD, Deary IJ, Whalley LJ. Generality and specificity in cognitive aging: a volumetric brain analysis. Neuroimage. 2006;30: 1433-1440.
42. Hornberger M, Geng J, Hodges JR. Convergent grey and white matter evidence of orbitofrontal cortex changes related to disinhibition in behavioural variant frontotemporal dementia. Brain. 2011;134: 2502-2512.
43. Shollenbarger SG, Price J, Wieser J, Lisdahl K. Poorer frontolimbic white matter integrity is associated with chronic cannabis use, FAAH genotype, and increased depressive and apathy symptoms in adolescents and young adults. Neuroimage Clin. 2015;8: 117-125.
44. Gold BT, Johnson NF, Powell DK, Smith CD. White matter integrity and vulnerability to Alzheimer's disease: preliminary findings and future directions. Biochim Biophys Acta. 2012;1822: 416-422.
45. Mike A, Strammer E, Aradi M, Orsi G, Perlaki G, Hajnal A, et al. Disconnection mechanism and regional cortical atrophy contribute to impaired processing of facial expressions and theory of mind in multiple sclerosis: a structural MRI study. PLoS One. 2013;8: e82422.
46. Epstein KA, Cullen KR, Mueller BA, Robinson P, Lee S, Kumra S. White matter abnormalities and cognitive impairment in early-onset schizophrenia-spectrum disorders. J Am Acad Child Adolesc Psychiatry. 2014;53: 362-72.e1-2.
47. Sarubbo S, De Benedictis A, Merler S, Mandonnet E, Balbi S, Granieri E, et al. Towards a functional atlas of human white matter. Hum Brain Mapp. 2015;36: 3117-3136.
48. Borroni B, Brambati SM, Agosti C, Gipponi S, Bellelli G, Gasparotti R, et al. Evidence of white matter changes on diffusion tensor imaging in frontotemporal dementia. Arch Neurol. 2007;64: 246-251.
49. de Groot M, Vernooij MW, Klein S, Ikram MA, Vos FM, Smith SM, et al. Improving alignment in Tract-based spatial statistics: evaluation and optimization of image registration. Neuroimage. 2013;76: 400-411.
50. Ashburner J, Friston KJ. Unified segmentation. Neuroimage. 2005;26: 839-851.
51. Klein S, Staring M, Murphy K, Viergever MA, Pluim JP. Elastix: a Toolbox for Intensity-Based Medical Image Registration. IEEE Trans Med Imaging. 2010;29: 196-205.
52. Asllani I, Borogovac A, Brown TR. Regression algorithm correcting for partial volume effects in arterial spin labeling MRI. Magn Reson Med. 2008;60: 1362-1371.
53. Hammers A, Allom R, Koepp MJ, Free SL, Myers R, Lemieux L, et al. Three-dimensional maximum probability atlas of the human brain, with particular reference to the temporal lobe. Hum Brain Mapp. 2003;19: 224-247.

54. Gousias IS, Rueckert D, Heckemann RA, Dyet LE, Boardman JP, Edwards AD, et al. Automatic segmentation of brain MRIs of 2-year-olds into 83 regions of interest. Neuroimage. 2008;40: 672-684.
55. Tustison NJ, Avants BB, Cook PA, Zheng Y, Egan A, Yushkevich PA, et al. N4ITK: improved N3 bias correction. IEEE Trans Med Imaging. 2010;29: 1310-1320.
56. Heckemann RA, Hajnal JV, Aljabar P, Rueckert D, Hammers A. Automatic anatomical brain MRI segmentation combining label propagation and decision fusion. Neuroimage. 2006;33: 115-126.
57. Binnewijzend MA, Kuijer JP, Benedictus MR, van der Flier WM, Wink AM, Wattjes MP, et al. Cerebral blood flow measured with 3D pseudocontinuous arterial spin-labeling MR imaging in Alzheimer disease and mild cognitive impairment: a marker for disease severity. Radiology. 2013;267: 221-230.
58. Braak H, Braak E. Neuropathological stageing of Alzheimer-related changes. Acta Neuropathol. 1991;82: 239-259.
59. Sachdev PS, Zhuang L, Braidy N, Wen W. Is Alzheimer's a disease of the white matter? Curr Opin Psychiatry. 2013;26: 244-251.
60. Binnewijzend MA, Kuijer JP, van der Flier WM, Benedictus MR, Moller CM, Pijnenburg YA, et al. Distinct perfusion patterns in Alzheimer's disease, frontotemporal dementia and dementia with Lewy bodies. Eur Radiol. 2014;24: 2326-2333.
61. Seeley WW, Crawford R, Rascovsky K, Kramer JH, Weiner M, Miller BL, et al. Frontal paralimbic network atrophy in very mild behavioral variant frontotemporal dementia. Arch Neurol. 2008;65: 249-255.
62. Rosen HJ, Allison SC, Schauer GF, Gorno-Tempini ML, Weiner MW, Miller BL. Neuroanatomical correlates of behavioural disorders in dementia. Brain. 2005;128: 2612-2625.
63. Seelaar H, Rohrer JD, Pijnenburg YA, Fox NC, van Swieten JC. Clinical, genetic and pathological heterogeneity of frontotemporal dementia: a review. J Neurol Neurosurg Psychiatry. 2011;82: 476-486.
64. Zhou J, Greicius MD, Gennatas ED, Growdon ME, Jang JY, Rabinovici GD, et al. Divergent network connectivity changes in behavioural variant frontotemporal dementia and Alzheimer's disease. Brain. 2010:133; 1352-1367.
65. Du AT, Schuff N, Kramer JH, Rosen HJ, Gorno-Tempini ML, Rankin K, et al. Different regional patterns of cortical thinning in Alzheimer's disease and frontotemporal dementia. Brain. 2007;130: 1159-1166.
66. Rohrer JD, Ridgway GR, Modat M, Ourselin S, Mead S, Fox NC, et al. Distinct profiles of brain atrophy in frontotemporal lobar degeneration caused by progranulin and tau mutations. Neuroimage. 2010;53: 1070-1076.

SUPPLEMENTARY MATERIAL

Table 1. White matter tracts affected in Alzheimer's disease (AD) and/or behavioral variant frontotemporal dementia (bvFTD) based on the tract-based spatial statistics (TBSS) ($p<0.05$) analysis of fractional anisotropy (FA). Tractography tract thresholds based on De Groot et al. (2014), but multiplied with a factor of eight due to the resolution difference.

White matter tract	Tractography threshold
Anterior thalamic radiation (ATR)	0.016
Cingulum (cingulate gyrus)	0.08
Cingulum (parahippocampal region)	0.16
Forceps major (FMa)	0.04
Forceps minor (FMi)	0.08
Inferior fronto-occipital fasciculus (IFOF)	0.08
Inferior longitudinal fasciculus (ILF)	0.04
Superior longitudinal fasciculus (SLF)	0.008
Uncinate fasciculus (UF	0.08

Table 2. Gray matter regions of interest (ROIs) and their abbreviations.

Lobe	Gyrus	Abbr.	Consisting of:
Frontal	Superior frontal gyrus	SFG	Central superior frontal gyrus Anterior superior frontal gyrus
	Middle frontal gyrus	MFG	
	Inferior frontal gyrus	IFG	
	Straight gyrus		
	Orbitofrontal gyrus	OFG	Anterior orbital gyrus Medial orbital gyrus Lateral orbital gyrus Posterior orbital gyrus
	Subcallosal area		
	Anterior cingulate cortex	ACC	
	Insula		
	Precentral gyrus		

Temporal	Anterior temporal lobe	ATL	Medial anterior temporal lobe Lateral anterior temporal lobe
	Posterior temporal lobe	PTL	
	Amygdala		
	Hippocampal formation	HF	Hippocampus Parahippocampal gyrus
	Superior temporal gyrus	STG	
	Inferior temporal gyrus	ITG	
	Fusiform gyrus		
Parietal	Postcentral gyrus		
	Posterior cingulate cortex	PCC	
	Precuneus		
	Remainder of parietal lobe		
Occipital	Lingual gyrus		
	Cuneus		
	Lateral remainder of occipital lobe		
Subcortical	Thalamus		
	Putamen		
	Caudate		
	Nucleus accumbens		

Regions of interest (ROIs) assessed for gray matter volume and cerebral flood flow. Parcellated gyri (according to [53,54], right column) were combined (middle column) for analysis.

Table 3. Post-hoc two sample t-test for FA investigating AD < HC (n=29; $p_{corrected}$<0.05; k=50). k= voxel. L = left. R = right.

Cluster size (k)	White matter tracts within cluster
8687	L, R anterior thalamic radiation L, R body of the corpus callosum L, R cingulum L corticospinal tract L forceps major L, R forceps minor L, R genu of the corpus callosum L, R inferior fronto-occipital fasciculus L inferior longitudinal fasciculus L posterior corona radiata L splenium of the corpus callosum L, R superior corona radiata L, R superior longitudinal fasciculus L, R uncinate fasciculus
1691	R cingulum R corticospinal tract R forceps major R inferior fronto-occipital fasciculus R inferior longitudinal fasciculus R posterior corona radiata R splenium of the corpus callosum R superior longitudinal fasciculus
1469	R cingulum R forceps major R inferior fronto-occipital fasciculus R inferior longitudinal fasciculus
1313	L anterior thalamic radiation L cingulum L forceps major L inferior fronto-occipital fasciculus L inferior longitudinal fasciculus L splenium of the corpus callosum L superior longitudinal fasciculus
92	L forceps major L splenium of the corpus callosum
51	R superior longitudinal fasciculus

Table 4. Post-hoc two sample t-test for FA investigating bvFTD < HC (n=20; $p_{corrected}$<0.05; k=50). k= voxel. L = left. R = right.

Cluster size (k)	White matter tracts within cluster
55201	L, R anterior corona radiata L, R anterior thalamic radiation L, R body of the corpus callosum L, R cingulum L, R corticospinal tract L, R Genu of the corpus callosum L, R forceps major L, R forceps minor L, R inferior fronto-occipital fasciculus L, R inferior longitudinal fasciculus L, R splenium of the corpus callosum L, R superior corona radiata L, R superior longitudinal fasciculus
691	R anterior thalamic radiation R inferior fronto-occipital fasciculus
204	R anterior corona radiata
161	L superior longitudinal fasciculus
105	L forceps major L inferior fronto-occipital fasciculus L inferior longitudinal fasciculus
93	L forceps major L inferior fronto-occipital fasciculus L inferior longitudinal fasciculus
59	R inferior fronto-occipital fasciculus R inferior longitudinal fasciculus
55	R corticospinal tract
52	L forceps major L inferior fronto-occipital fasciculus L inferior longitudinal fasciculus

Table 5. Post-hoc two sample t-test for FA investigating bvFTD < AD (n=27; $p_{corrected}$<0.05; k=50). k= voxel. L = left. R = right.

Cluster size (k)	White matter tracts within cluster
36853	L, R anterior corona radiata L, R anterior thalamic radiation L, R body of the corpus callosum L, R cingulum L, R corticospinal tract L, R Genu of the corpus callosum R forceps major L, R forceps minor L, R inferior fronto-occipital fasciculus L, R inferior longitudinal fasciculus R splenium of the corpus callosum R superior corona radiata L, R superior longitudinal fasciculus L, R Uncinate fasciculus
1488	L cingulum L forceps major L posterior corona radiata L splenium of the corpus callosum
854	R cingulum R splenium of the corpus callosum
683	L superior longitudinal fasciculus
280	R corticospinal tract
146	L inferior longitudinal fasciculus
136	L posterior thalamic radiation L inferior longitudinal fasciculus
121	R anterior thalamic radiation
117	R cingulum R forceps major
102	L superior longitudinal fasciculus
100	L corticospinal tract
95	R cingulum
95	R superior longitudinal fasciculus
85	L superior longitudinal fasciculus
61	L superior longitudinal fasciculus
53	L superior longitudinal fasciculus

Table 6. ROIs that showed significant differences in GM volume between HC, bvFTD and AD patients. Shown are median nGM volume [% ICV] and 25th and 75th percentile (in parentheses).

Region of interest		Healthy controls		bvFTD		AD	
		Median (25th-75th %ile)	Mean rank	Median (25th-75th %ile)	Mean rank	Median (25th-75th %ile)	Mean rank
Supratentorial cortex		35.9 (34.6-38.2)	26	28.0 (26.3-32.1)	8[b]	33.1 (31.6-35.4)	17
L	Superior frontal gyrus	1.68 (1.59-1.78)	24	1.10 (0.95-1.47)	7[b]	1.60 (1.57-1.80)	22[c]
R	Superior frontal gyrus	1.65 (1.55-1.80)	25	1.15 (0.97-1.35)	8[b]	1.61 (1.44-1.74)	21[c]
L	Middle frontal gyrus	1.35 (1.23-1.42)	25	0.90 (0.76-1.17)	8[b]	1.21 (1.19-1.34)	20
R	Middle frontal gyrus	1.37 (1.23-1.47)	26	0.96 (0.69-1.13)	7[b]	1.24 (1.12-1.41)	20[c]
L	Inferior frontal gyrus	0.63 (0.58-0.69)	25	0.40 (0.38-0.56)	8[b]	0.59 (0.52-0.62)	19
R	Inferior frontal gyrus	0.59 (0.55-0.62)	24	0.42 (0.34-0.46)	7[b]	0.56 (0.45-0.63)	22[c]
L	Straight gyrus	0.17 (0.14-0.18)	26	0.10 (0.08-0.14)	9[b]	0.14 (0.13-0.16)	17
R	Straight gyrus	0.19 (0.16-0.20)	25	0.12 (0.090.13)	7[b]	0.17 (0.14-0.19)	20[c]
L	Orbitofrontal gyrus	0.81 (0.73-0.86)	25	0.46 (0.36-0.74)	10[b]	0.77 (0.70-0.80)	18
R	Orbitofrontal gyrus	0.82 (0.76-0.88)	24	0.49 (0.42-0.65)	8[b]	0.78 (0.70-0.84)	19
R	Anterior cingulate cortex	0.35 (0.31-0.39)	25	0.26 (0.20-0.29)	7[b]	0.32 (0.28-0.40)	21[c]
L	Insula	0.54 (0.52-0.56)	25	0.39 (0.35-0.50)	9[b]	0.50 (0.46-0.52)	18
R	Insula	0.50 (0.49-0.52)	26	0.37 (0.34-0.45)	9[b]	0.46 (0.45-0.49)	18
L	Precentral gyrus	0.94 (0.89-1.04)	24	0.87 (0.76-0.88)	10[b]	0.97 (0.85-1.01)	20
R	Precentral gyrus	0.93 (0.85-1.01)	23	0.82 (0.72-0.88)	11[b]	0.91 (0.78-1.00)	21
L	Anterior temporal lobe	0.47 (0.42-0.55)	26	0.35 (0.30-0.40)	9[b]	0.42 (0.35-0.47)	18
R	Anterior temporal lobe	0.49 (0.44-0.55)	25	0.34 (0.25-0.39)	7[b]	0.44 (0.43-0.49)	20[c]
L	Posterior temporal lobe	1.72 (1.64-1.88)	25	1.60 (1.46-1.68)	15	1.57 (1.47-1.58)	14[a]
L	Amygdala	0.09 (0.08-0.10)	26	0.08 (0.07-0.09)	14	0.08 (0.07-0.09)	14[a]
L	Hippocampal formation	0.39 (0.37-0.43)	27	0.32 (0.28-0.36)	11[b]	0.36 (0.29-0.38)	15[a]
R	Hippocampal formation	0.39 (0.36-0.42)	26	0.28 (0.27-0.37)	9[b]	0.37 (0.33-0.39)	18
L	Superior temporal gyrus	0.73 (0.69-0.77)	23	0.59 (0.55-0.68)	11[b]	0.72 (0.65-0.78)	21
R	Superior temporal gyrus	0.78 (0.70-0.82)	25	0.60 (0.50-0.69)	10[b]	0.70 (0.64-0.79)	18
L	Inferior temporal gyrus	0.71 (0.65-0.77)	26	0.58 (0.39-0.63)	10[b]	0.66 (0.50-0.70)	17
R	Inferior temporal gyrus	0.76 (0.67-0.82)	26	0.50 (0.38-0.58)	8[b]	0.64 (0.56-0.76)	18
L	Fusiform gyrus	0.22 (0.19-0.24)	25	0.17 (0.15-0.19)	9[b]	0.21 (0.17-0.24)	19
R	Fusiform gyrus	0.22 (0.18-0.23)	23	0.16 (0.12-0.19)	11[b]	0.22 (0.15-0.24)	21
R	Postcentral gyrus	0.78 (0.73-0.85)	25	0.67 (0.56-0.76)	12[b]	0.73 (0.66-0.78)	17
L	Posterior cingulate cortex	0.34 (0.30-0.35)	24	0.27 (0.24-0.32)	12[b]	0.31 (0.27-0.34)	18
R	Posterior cingulate cortex	0.34 (0.32-0.36)	26	0.27 (0.23-0.32)	12[b]	0.28 (0.27-0.31)	15[a]

L	Precuneus	1.27 (1.17-1.31)	26	1.06 (1.03-1.13)	10[b]	1.15 (1.05-1.20)	16[a]
R	Precuneus	1.28 (1.17-1.39)	27	1.01 (0.88-1.12)	9[b]	1.15 (0.99-1.19)	16[a]
L	Remainder of parietal lobe	1.35 (1.28-1.46)	27	1.10 (1.02-1.23)	11[b]	1.14 (1.09-1.26)	13[a]
R	Remainder of parietal lobe	1.33 (1.27-1.46)	26	1.14 (0.88-1.29)	13[b]	1.17 (0.98-1.30)	13[a]
R	Lingual gyrus	0.53 (0.51-0.57)	25	0.51 (0.47-0.51)	16	0.48 (0.45-0.52)	13[a]
R	Cuneus	0.38 (0.35-0.40)	24	0.34 (0.32-0.39)	18	0.31 (0.27-0.36)	12[a]
R	Lateral remainder of occipital lobe	1.54 (1.43-1.63)	24	1.38 (1.12-1.48)	14	1.38 (1.36-1.51)	17
R	Thalamus	0.17 (0.16-0.18)	25	0.14 (0.11-0.18)	15	0.15 (0.13-0.16)	14[a]
L	Caudate	0.20 (0.17-0.21)	23	0.15 (0.12-0.18)	11	0.18 (0.17-0.22)	21
R	Caudate	0.21 (0.18-0.23)	24	0.15 (0.13-0.19)	10[b]	0.19 (0.17-0.21)	19
L	Nucleus accumbens	0.02 (0.02-0.03)	27	0.02 (0.01-0.02)	11[b]	0.02 (0.02-0.02)	15[a]
L	Putamen	0.17 (0.17-0.20)	24	0.15 (0.11-0.17)	13[b]	0.15 (0.13-.19)	17
R	Putamen	0.15 (0.13-0.17)	24	0.12 (0.09-0.15)	12[b]	0.13 (0.12-.15)	19

Median nGM volumes and 25th and 75th percentile in ROIs for which post hoc pairwise comparisons showed significant different between healthy controls, bvFTD and AD patients. The mean ranks represent the group means of the rank-ordered nGM data in that particular ROI. These mean ranks were compared to assess differences between groups rather than the median because group distributions were not similarly shaped.
nGM = normalized gray matter; ICV = intracranial volume; ROIs = regions of interest; bvFTD = behavioral variant frontotemporal dementia; AD = Alzheimer's disease; HC = healthy controls; L = left; R = right.
[a] mean ranks HC>AD, $p<0.05$
[b] mean ranks HC>bvFTD, $p<0.05$
[c] mean ranks AD>bvFTD, $p<0.05$

Table 7. ROIs that showed significant differences in CBF corrected for nGM volume between HC, bvFTD and AD patients. Shown are median CBF and 25th and 75th percentile (in parentheses).

	Region of interest	Healthy controls		bvFTD		AD	
		Median (25th-75th %ile)	Mean rank	Median (25th-75th %ile)	Mean rank	Median (25th-75th %ile)	Mean rank
L	Orbitofrontal gyrus	6335 (5575-6853)	19	7069 (5926-8675)	26[b]	5111 (4634-6556)	12
R	Orbitofrontal gyrus	5911 (4927-6337)	19	6496 (5963-8057)	27[b]	5194 (4526-5925)	12
L	Posterior temporal lobe	2562 (2265-2711)	22	2602 (1839-2915)	21	1903 (1786-2298)	12[a]
R	Posterior temporal lobe	2491 (2083-2271)	23	2202 (1889-2620)	19	1888 (1779-2080)	12[a]
R	Hippocampal formation	9996 (9252-10839)	18	12089 (10475-13208)	28[b]	9173 (8714-10021)	12
L	Superior temporal gyrus	6699 (5998-7315)	22	7311 (5337-7998)	24[b]	5472 (4521-6631)	10[a]
R	Inferior temporal gyrus	6014 (5267-7131)	19	6984 (5975-8367)	26[b]	4833 (4591-7002)	13
R	Fusiform gyrus	16904 (13264-20749)	26	19132 (17180-19967)	20[b]	14351 (9710-16198)	11
L	Posterior cingulate cortex	18378 (15526-19054)	23	15551 (14189-18995)	19	14487 (12183-16075)	11[a]

L	Precuneus	3205 (2915-3838)	23	3062 (2461-4246)	20	2444 (1977-3118)	11[a]
R	Precuneus	3505 (3019-3773)	23	3370 (2471-4326)	21	2489 (2106-3039)	11[a]
R	Lateral remainder of occipital lobe	2770 (2176-2987)	23	2155 (1572-2925)	18	2105 (1312-2307)	12[a]

Median CBF and 25th and 75th percentile in ROIs for which post hoc pairwise comparisons showed significant different mean ranks between healthy controls, bvFTD and AD patients. The mean ranks represent the group means of the rank-ordered CBF data in that particular ROI. These mean ranks were compared to assess differences between groups rather than the median because group distributions were not similarly shaped.
CBF = cerebral blood flow; ROIs = regions of interest; bvFTD = behavioral variant frontotemporal dementia; AD = Alzheimer's disease; HC = healthy controls; L = left; R = right.
[a] mean ranks HC>AD, $p<0.05$
[b] mean ranks bvFTD>AD, $p<0.05$

Table 8. All within-group correlations between WM microstructure and GM volume or GM perfusion, exceeding rho≥0.6 for either AD, bvFTD or controls. Significant correlations are printed in bold.

WM tract	WM measure	GM region	GM measure	L/R	HC	BvFTD	AD
ATR	FA	HF	volume	R	0.150	0.142	**0.694**
ATR	MD	HF	volume	R	0.127	-0.335	**-0.607**
CGc	FA	ACC/subcallosal area	CBF	R	-0.077	0.283	**0.648**
CGc	FA	precuneus/PCC	CBF	R	0.257	**0.750**	0.527
CGc	MD	ACC/subcallosal area	volume	L	-0.006	**-0.683**	0.009
CGc	MD	precuneus/PCC	CBF	R	-0.178	**-0.867**	**-0.648**
CGh	FA	precuneus/PCC	CBF	R	-0.003	**0.933**	-0.382
CGh	MD	HF/ATL	volume	L	0.216	-0.517	**-0.645**
CGh	MD	HF/ATL	volume	R	-0.001	**-0.767**	-0.445
CGh	MD	precuneus/PCC	CBF	L	-0.394	-0.050	-0.600
CGh	MD	precuneus/PCC	CBF	R	0.323	-0.650	-0.091
FMa	FA	occipital	CBF	R	0.100	-0.617	-0.164
IFOF	FA	occipital	CBF	R	-0.104	0.400	**0.636**
IFOF	MD	occipital	CBF	L	0.023	-0.350	**-0.748**
IFOF	MD	occipital	CBF	R	-0.020	-0.600	-0.438
IFOF	MD	occipital	volume	R	**-0.765**	-0.200	-0.137

IFOF	MD	OFG/IFG	volume	L	-0.200	**-0.717**	-0.273
IFOF	MD	OFG/IFG	volume	R	**-0.546**	-0.517	**-0.761**
ILF	MD	occipital	volume	R	**-0.765**	-0.617	-0.318
ILF	MD	ITG/STG/ATL	volume	R	**-0.577**	**-0.767**	**-0.827**
SLF	MD	ITG/PTL	volume	R	-0.182	**-0.683**	-0.182
SLF	MD	precentral/IFG	volume	L	**-1.000**	**-1.000**	**-1.000**
SLF	MD	precentral/IFG	volume	R	-0.452	**-0.700**	-0.582
UF	MD	IFG/OFG	CBF	L	0.026	0.533	-0.624
UF	MD	IFG/OFG	volume	L	-0.189	**-0.733**	-0.027
UF	MD	STG/ATL	volume	L	-0.219	**-0.750**	-0.227

ATR = anterior thalamic radiation; CGc = cingulum (cingulate gyrus); CGh = cingulum (hippocampus); FMa = forceps major; IFOF = inferior fronto-occipital fasciculus; ILF = inferior longitudinal fasciculus; SLF = superior longitudinal fasciculus; UF = uncinate fasciculus; HF = hippocampal formation; = OFG = orbitofrontal gyrus; IFG = inferior frontal gyrus; ACC = anterior cingulate cortex; PCC = posterior cingulate cortex; ATL = anterior temporal lobe; ITG = inferior temporal gyrus; STG = superior temporal gyrus; PTL = posterior temporal lobe.

Chapter 3

Advanced MR neuroimaging in phenocopy FTD

Chapter 3.1

Structural and functional brain abnormalities place phenocopy frontotemporal dementia (FTD) in the FTD spectrum

Rebecca M.E. Steketee
Rozanna Meijboom
Esther E. Bron
Robert Jan Osse
Inge de Koning
Lize C. Jiskoot
Stefan Klein
Frank Jan de Jong
Aad van der Lugt
John C. van Swieten
Marion Smits

Submitted

ABSTRACT

Purpose 'Phenocopy' frontotemporal dementia (phFTD) patients may clinically mimic the behavioral variant of FTD (bvFTD), but do not show functional decline or abnormalities upon visual inspection of routine neuroimaging. We aimed to identify abnormalities in gray matter (GM) volume and perfusion in phFTD and to assess whether phFTD belongs to the FTD spectrum. We compared phFTD patients with both healthy controls and bvFTD patients.

Materials & methods Seven phFTD and 11 bvFTD patients, and 20 age-matched controls underwent structural T1-weighted magnetic resonance imaging (MRI) and 3D pseudo-continuous arterial spin labeling (pCASL) at 3T. Normalized GM (nGM) volumes and perfusion, corrected for partial volume effects, were quantified regionally as well as in the entire supratentorial cortex, and compared between groups taking into account potential confounding effects of gender and scanner.

Results PhFTD patients showed cortical atrophy, most prominently in the right temporal lobe. Regional GM volume was otherwise generally not different from either controls or from bvFTD, despite the fact that bvFTD showed extensive frontotemporal atrophy. Perfusion was increased in the left prefrontal cortex compared to bvFTD and to a lesser extent to controls.

Conclusion PhFTD and bvFTD show overlapping cortical structural abnormalities indicating a continuum of changes especially in the frontotemporal regions. Together with functional changes suggestive of a compensatory response to incipient pathology in the left prefrontal regions, these findings are the first to support a possible neuropathological etiology of phFTD and suggest that phFTD may be a neurodegenerative disease on the FTD spectrum.

INTRODUCTION

FTD is a presenile neurodegenerative disorder affecting the frontal and temporal lobes, with the behavioral variant (bvFTD) as its most common subtype. BvFTD is characterized by progressive deterioration in social and personal conduct [1]. Core clinical features are behavioral disinhibition, apathy, loss of empathy, and perseverative, stereotypical or compulsive behavior. In addition to these symptoms, the diagnosis of probable bvFTD requires frontotemporal changes on neuroimaging and a gradual decline in functional abilities [2]. A subset (reports range from 7% up to 37% [3,4]) of predominantly male patients presents with behavioral changes characteristic of bvFTD, but without abnormalities on structural magnetic resonance imaging (MRI) or fluorodeoxyglucose-positron emission tomography (FDG-PET) [5-8]. In addition, these patients have a more benign disease course [7] and do not show a decline in activities of daily living [9]. This clinical syndrome is referred to as 'phenocopy' FTD (phFTD) [10].

Because normal neuroimaging features and no cognitive decline over time are reported in these patients, a neurodegenerative etiology is disputed. Autopsy findings are sparse, but have not shown features of neurodegeneration [11,12], Very recently, repeat expansion in the C9ORF72 gene has been associated with very slowly progressive FTD, resembling phFTD. Some patients with this mutation have initially been diagnosed with phFTD [3,13], but currently, phFTD is still defined as a clinical syndrome. An alternative notion is that phFTD patients might have a pre-existent psychiatric disorder and decompensate during mid-life [14-16].

In the present study we used advanced quantitative MRI techniques and analyses to investigate both structural and functional abnormalities in phFTD in more detail, as the typical behavioral changes in phFTD imply neurophysiological changes which may be detected with these advanced methods [3]. We used arterial spin labeling (ASL)-MRI to quantify brain perfusion with higher spatial resolution than thus far achieved with PET [17]. Focal atrophy can be detected by regional quantification of gray matter volume on structural imaging. Gray matter volume and perfusion in phFTD patients were compared with both healthy controls and bvFTD patients in order to assess whether phFTD belongs to the FTD spectrum.

METHODS

Participant selection

PhFTD and bvFTD patients were recruited from the Alzheimer Center Southwest Netherlands at Erasmus MC, Rotterdam, The Netherlands, which is a tertiary referral center with special focus on FTD. Exclusion criteria for both phFTD and bvFTD patients were contraindications for MR imaging and lack of hetero-anamnestic information. In addition, phFTD patients were excluded when there was a diagnosis of dementia, or when other neurological or psychiatric disorders were suspected.

Of the fifteen patients that fulfilled the criteria for phFTD, i.e. behavioral features but no imaging findings consistent with bvFTD, and no progression for at least one year after initial diagnostic work-up, six patients declined to participate; one was excluded due to refusal of neuropsychological assessment; and one eventually showed progressive cognitive impairment at neuropsychological follow-up, resulting in the analysis of seven phFTD patients. One patient showing an asymptomatic cortical infarct in the right parietal lobe on MRI was retained in the analyses, as no residual clinical symptoms were reported and the infarct was not in a region of interest for FTD. Image processing results were visually checked and did not show any effect of the infarct on segmentation or registration procedures. All phFTD patients were screened for the presence of the repeat expansion of the C9ORF72 gene.

Twelve bvFTD patients with possible bvFTD [2] with an onset before 65 years and a Mini Mental State Examination (MMSE) score ≥ 20 were prospectively recruited as part of a larger ongoing study on advanced MR neuroimaging in the early stage of presenile dementia. If the diagnosis at the initial visit was uncertain, definitive diagnosis was confirmed after sufficient follow-up. One patient was excluded from analysis due to poor perfusion data quality, resulting in the analysis of 11 bvFTD patients.

Healthy age-matched controls were recruited through advertisement and from the patients' peers. They were matched for gender with the phFTD patients. Exclusion criteria were history of neurological or psychiatric disorders and contraindications for MRI. Of the twenty-three controls, two were excluded due to missing data and one because of below-average scores on neuropsychological assessment, resulting in the analysis of twenty healthy controls.

The study was approved by the medical ethics committee of Erasmus MC. All participants gave written informed consent.

Neuropsychological and psychiatric assessment

All participants underwent extensive neuropsychological examination as part of routine diagnostic work-up, assessing language and speech, attention and mental processing speed, executive functions, memory, and social cognition. PhFTD patients had an additional assessment to verify whether they fulfilled the criterion of no progression for at least one year. Additionally, they were assessed by an experienced psychiatrist to rule out major psychiatric disorders other than dementia. Psychiatric assessment was based on interviews with the patients and their caregivers, the Brief Psychiatric Rating Scale (BPRS [18]; Dutch translation [19]), and the psychiatrist's observations.

Image acquisition

Patients underwent MR imaging on two identical 3T scanners (Discovery MR750 system GE Healthcare, USA) with identical protocols. Seven healthy controls and all phFTD patients were scanned on one, and 13 healthy controls and all bvFTD patients on the other scanner.

Structural imaging

For gray matter volumetric assessment and anatomical reference, a high-resolution three-dimensional (3D) inversion recovery (IR) fast spoiled gradient-echo (FSPGR) T1-weighted (T1w) image was acquired (inversion time (TI) 450ms, echo time (TE) 3.06ms, repetition time (TR) 7.904s, flip angle 12°, ASSET factor 2, isotropic resolution 1mm^3 in a 240mm field of view (FOV), 176 sagittal slices, total acquisition time 4.41 min).

Perfusion imaging

Perfusion images were acquired using whole brain 3D pseudo-continuous ASL (p-CASL), currently the recommended sequence for clinical use [20] (interleaved fast spin-echo stack-of-spiral readout of 512 sampling points on 8 spirals, background suppressed, post labeling delay 1525 ms, labeling duration 1450 ms, TE 10.5 ms, TR 4632 ms, isotropic resolution 3.3 mm^3 in a 240 mm FOV, 36 axial slices, number of excitations (NEX) 3, total acquisition time 4.29 min). The labeling plane was positioned 9 cm below the anterior commissure – posterior commissure line.

Image data processing

We processed imaging data according to the methods described in detail by Bron et al., 2014 [21].

Tissue segmentation

Using the unified tissue segmentation method in SPM8 (Statistical Parametric Mapping, London, UK), we segmented T1w images into gray matter (GM), white matter and cerebrospinal fluid maps. The GM maps were subsequently used to derive GM volumes and cerebral blood flow (CBF).

ASL post-processing

The ASL data consisted of a difference image and a control image. GM maps were rigidly registered with the difference image (Elastix registration software [22]) and registrations were checked visually. Tissue maps were transformed to ASL image space to perform partial volume (PV) correction, and PV effects in ASL difference and control images were subsequently corrected using local linear regression within a 3D kernel based on tissue maps [23]. We quantified PV-corrected ASL images as CBF maps using the single-compartment model [20]. CBF maps were transformed to T1w image space for further analysis.

ROI labeling

We defined regions of interest (ROIs) for each participant using a multi-atlas approach. This involved registration of 30 labeled T1w images, each containing 83 cortical and subcortical ROIs [24,25], to the participants' T1w images. The labels of the 30 atlas images were fused by means of majority voting to obtain a final ROI labeling [26]. Rigid, affine, and non-rigid B-spline transformation models were applied successively for registration to the participants' nonuniformity-corrected T1w images [27]. Both the participants' and the labeled T1w images were masked for this registration using the Brain Extraction Tool [28].

ROI analysis

For all ROIs, we derived GM volumes and mean GM CBF values. The subcortical ROIs, cerebellum, brainstem, ventricles and white matter were excluded from analysis. ROIs that parcellated gyri in multiple sections were combined to constitute entire gyri (supplementary table 1). GM volumes and mean GM CBF values were subsequently obtained for the left and right hemisphere separately. Regional GM volumes were divided by the total intracranial volume to correct for head size and are referred to as normalized GM (nGM) volumes.

Data analysis

Using SPSS Statistics, version 20.0 (New York, USA) we first analyzed differences in gender and scanner across groups with Fisher's exact test. Both were significantly different between groups ($p<0.05$). To separate the confounding effect of gender and scanner differences from the actual effect of group differences, we used hierarchical regression to sequentially assess the effects of scanner, gender, and group on nGM and CBF. Only if the effects of scanner and gender were not significant and a significant effect of group was found, nGM and regional CBF ROIs were further tested for differences between groups. This was done using a nonparametric Kruskal-Wallis test with Dunn-Bonferroni correction for multiple comparisons (i.e. phFTD versus controls, phFTD versus bvFTD, bvFTD versus controls) as nGM, CBF, age and MMSE were not normally distributed across groups (Shapiro-Wilk test $p<0.05$). The findings were visually represented in boxplots of nGM and CBF for each of the brain lobes. Statistical thresholds were set at $p<0.05$.

RESULTS

Participant characteristics

Age was not different between groups ($H(2) = 1.129$, $p>.05$, Kruskal-Wallis test) (table 1). MMSE was significantly different between groups ($F(2) = 10.182$, $p<.05$, Kruskal-Wallis test): both phFTD and bvFTD patients had significantly lower MMSE scores than controls.

None of the phFTD patients had a C9ORF72 mutation, nor could their behavioral disturbances be attributed to an underlying psychiatric disorder. Neuropsychological assessment was normal in one and suggestive of FTD in six phFTD patients, but did not demonstrate progressive decline.

Median follow-up to establish definitive diagnosis of bvFTD was 1.4 years (range 1.7 months - 2.4 years).

Table 1: participant characteristics

	Controls	phFTD	bvFTD
N (male)	20 (20)	7 (7)	11 (5)
Median age in years (25th-75th %ile)	64 (62-66)	61 (60-70)	63 (57-66)
Median MMSE (25th-75th %ile)	28 (28-30)	27 (26-28)	27 (24-28)

bvFTD = behavioral variant frontotemporal dementia; IQR = interquartile range; MMSE = Mini Mental State Examination; phFTD = phenocopy frontotemporal dementia; SD = standard deviation

Gray matter volumetric changes

There were significant differences in nGM volume between groups mostly in frontal and temporal regions (Figure 1A, Table 2). PhFTD patients had lower supratentorial nGM volume than controls which was most pronounced in the right posterior temporal lobe, right superior temporal gyrus and bilateral fusiform gyrus. BvFTD showed extensive bilateral frontotemporal nGM volume loss compared to controls. Compared to phFTD, bvFTD showed lower nGM volume in the right hippocampal formation and the right amygdala. Other nGM volumes were not significantly different between bvFTD and phFTD. This spectrum of findings, with mean nGM volumes being highest in controls, lowest in bvFTD and in-between in phFTD, was particularly apparent in the frontal and temporal lobes (Figure 2A).

Perfusion changes in the gray matter

There were significant differences in CBF between groups in frontal regions (Figure 1B, Table 3). CBF in the bilateral subcallosal area was higher in phFTD than both in bvFTD and controls, as illustrated in Figure 2B. CBF in bvFTD was lower than in phFTD in the left superior and inferior frontal gyrus, the left orbitofrontal gyrus, and in the bilateral straight gyrus. bvFTD showed lower CBF than controls in the left inferior frontal and straight gyrus, and the left orbitofrontal gyrus.

Table 2: median nGM volume [% ICV] and 25th and 75th percentile (in parentheses) for healthy controls (HC), phFTD and bvFTD patients.

Region of interest		Healthy controls		PhFTD		BvFTD	
		Median (25th-75th %ile)	Mean rank	Median (25th-75th %ile)	Mean rank	Median (25th-75th %ile)	Mean rank
Supratentorial cortex		35.3 (33.3-36.1)	*26*	31.6 (30.0-33.6)	*13*[a]	29.1 (27.2-34.1)	*11*[c]
L	Superior frontal gyrus	1.62 (1.56-1.68)	*26*	1.50 (1.41-1.56)	*15*	1.21 (1.00-1.59)	*11*[c]
R	Superior frontal gyrus	1.62 (1.48-1.75)	*25*	1.55 (1.40-1.60)	*18*	1.17 (1.02-1.51)	*11*[c]
L	Middle frontal gyrus	1.29 (1.14-1.41)	*23*	1.20 (1.17-1.35)	*20*	0.95 (0.82-1.27)	*12*[c]
R	Middle frontal gyrus	1.27 (1.18-1.35)	*25*	1.17 (1.13-1.24)	*17*	0.98 (0.75-1.27)	*12*[c]
R	Inferior frontal gyrus	0.57 (0.54-0.62)	*24*	0.54 (0.50-0.59)	*19*	0.44 (0.40-0.52)	*11*[c]
L	Straight gyrus	0.15 (0.14-0.18)	*25*	0.15 (0.11-0.17)	*20*	0.10 (0.09-0.13)	*10*[c]
R	Straight gyrus	0.17 (0.15-0.19)	*26*	0.14 (0.12-0.19)	*18*	0.12 (0.09-0.13)	*9*[c]
L	Orbitofrontal gyrus	0.79 (0.73-0.84)	*25*	0.74 (0.60-0.76)	*15*	0.47 (0.39-0.76)	*12*[c]
R	Orbitofrontal gyrus	0.80 (0.76-0.85)	*25*	0.67 (0.64-0.78)	*14*	0.53 (0.44-0.77)	*12*[c]
R	Anterior cingulate gyrus	0.33 (0.29-0.39)	*25*	0.31 (0.28-0.32)	*18*	0.26 (0.20-0.29)	*11*[c]
L	Insula	0.54 (0.51-0.55)	*25*	0.51 (0.46-0.53)	*19*	0.39 (0.36-0.49)	*9*[c]
R	Insula	0.50 (0.49-0.53)	*26*	0.47 (0.46-0.50)	*19*	0.37 (0.34-0.42)	*8*[c]
L	Anterior temporal lobe	0.44 (0.41-0.49)	*25*	0.44 (0.38-0.46)	*21*	0.34 (0.27-0.37)	*9*[c]
R	Anterior temporal lobe	0.48 (0.44-0.52)	*26*	0.45 (0.39-0.49)	*19*	0.34 (0.26-0.38)	*9*[c]
L	Posterior temporal lobe	1.70 (1.66-1.74)	*24*	1.69 (1.50-1.74)	*18*	1.58 (1.43-1.65)	*12*[c]
R	Posterior temporal lobe	1.82 (1.75-1.89)	*26*	1.60 (1.53-1.63)	*11*[a]	1.57 (1.44-1.76)	*13*[c]
L	Hippocampal formation	0.39 (0.35-0.41)	*24*	0.37 (0.32-0.42)	*21*	0.29 (0.24-0.34)	*10*[c]
R	Hippocampal formation	0.38 (0.36-0.40)	*24*	0.37 (0.32-0.42)	*22*[b]	0.28 (0.26-0.37)	*9*[c]
L	Amygdala	0.09 (0.08-0.09)	*24*	0.09 (0.07-0.09)	*20*	0.07 (0.07-0.08)	*12*[c]
R	Amygdala	0.08 (0.07-0.08)	*22*	0.08 (0.07-0.09)	*26*[b]	0.07 (0.05-0.08)	*11*[c]
L	Superior temporal gyrus	0.71 (0.70-0.78)	*25*	0.63 (0.55-0.71)	*15*	0.59 (0.58-0.66)	*12*[c]
R	Superior temporal gyrus	0.72 (0.68-0.79)	*26*	0.65 (0.58-0.70)	*13*[a]	0.64 (0.51-0.71)	*12*[c]
L	Inferior temporal gyrus	0.70 (0.62-0.74)	*26*	0.66 (0.54-0.67)	*17*	0.50 (0.38-0.60)	*9*[c]
R	Inferior temporal gyrus	0.72 (0.62-0.76)	*26*	0.65 (0.54-0.67)	*18*	0.50 (0.35-0.59)	*9*[c]

L	Fusiform gyrus	0.22 (0.19-0.22)	*26*	0.16 (0.15-0.19)	*14*[a]	0.17 (0.11-0.18)	*11*[c]
R	Fusiform gyrus	0.21 (0.19-0.24)	*26*	0.16 (0.14-0.19)	*12*[a]	0.15 (0.13-0.18)	*11*[c]
L	Remainder of parietal lobe	1.33 (1.25-1.42)	*25*	1.24 (1.17-1.31)	*15*	1.16 (1.05-1.32)	*13*[c]

Median nGM volumes and 25th and 75th percentile in ROIs for which post hoc pairwise comparisons showed significant different mean ranks between healthy controls, phFTD and bvFTD patients. The mean ranks (italics) represent the group means of the rank-ordered nGM data in that particular ROI. The mean ranks rather than the medians of the nGM volume distributions were compared to assess differences between groups because group distributions were not similarly shaped. The shading indicates the relative order of mean ranks between groups, with light gray indicating the highest and dark gray indicating the lowest rank.
[a] phFTD < controls; $p \leq .05$.
[b] bvFTD < phFTD; $p \leq .05$.
[c] bvFTD < controls; $p \leq .05$.
nGM = normalized gray matter; ICV = intracranial volume; ROIs = regions of interest; PhFTD = phenocopy frontotemporal dementia; bvFTD = behavioral variant frontotemporal dementia; HC = healthy controls; L = left; R = right.

Table 3: Median CBF and 25th and 75th percentile (in parentheses) for healthy controls (HC), phFTD and bvFTD patients.

Region of interest		Healthy controls		PhFTD		BvFTD	
		Median (25th-75th %ile)	Mean rank	Median (25th-75th %ile)	Mean rank	Median (25th-75th %ile)	Mean rank
L	Superior frontal gyrus	38.1 (34.5-45.4)	*19*	46.0 (39.0-65.0)	*28*[b]	35.0 (29.6-43.8)	*15*
L	Inferior frontal gyrus	48.6 (40.5-51.1)	*22*	50.7 (43.8-60.7)	*27*[b,c]	38.1 (31.1-42.3)	*11*[b]
L	Straight gyrus	49.8 (44.6-54.3)	*22*	55.1 (46.4-63.7)	*27*[b,c]	38.1 (35.2-46.6)	*11*[b]
R	Straight gyrus	47.0 (43.6-50.1)	*21*	51.7 (44.0-62.6)	*28*[b]	38.7 (32.5-45.0)	*11*
L	Orbitofrontal gyrus	44.1 (40.3-48.8)	*23*	43.0 (38.5-62.6)	*25*[b,c]	35.9 (30.3-38.7)	*10*[b]
L	Subcallosal area	31.6 (25.3-42.4)	*19*	45.0 (40.1-50.8)	*32*[a,b]	23.8 (20.4-32.4)	*12*
R	Subcallosal area	27.8 (22.4-41.8)	*19*	42.8 (41.3-48.2)	*31*[a,b]	29.5 (17.9-34.6)	*13*

Median CBF and 25th and 75th percentile in ROIs for which post hoc pairwise comparisons showed significant different mean ranks between healthy controls, phFTD and bvFTD patients. The mean ranks (italics) represent the group means of the rank-ordered CBF data in that particular ROI. The mean ranks rather than the medians of the CBF value distributions were compared to assess differences between groups because group distributions were not similarly shaped. The shading indicates the relative order of mean ranks between groups, with light gray indicating the highest and dark gray indicating the lowest rank.
[a] phFTD > controls; $p \leq .05$.
[b] bvFTD < phFTD; $p \leq .05$.
[c] bvFTD < controls; $p \leq .05$.
CBF = cerebral blood flow; ROIs = regions of interest; phFTD = phenocopy frontotemporal dementia; bvFTD = behavioral variant frontotemporal dementia; HC = healthy controls; L = left; R = right.

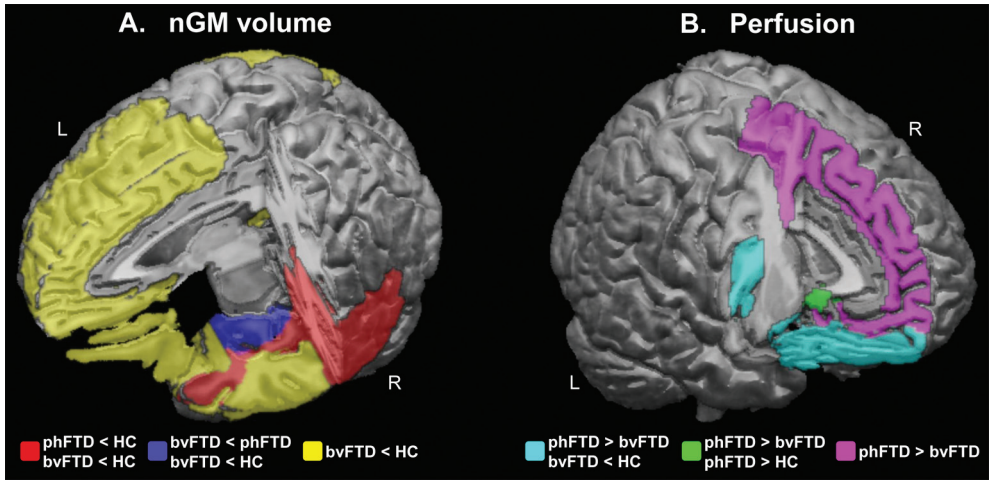

Figure 1: schematic overview of cortical regions showing (A) normalized GM volume and (B) perfusion abnormalities. Figure 1A shows in red regional nGM atrophy present in both phFTD and bvFTD; in blue regional nGM volume loss in bvFTD compared to both phFTD and controls; and in yellow regional nGM volume loss in in bvFTD when compared to controls, but not compared to phFTD. Figure 1B shows in cyan hyperperfusion in phFTD compared to bvFTD in regions that show hypoperfusion in bvFTD compared to controls; in green regional hyperperfusion in phFTD compared to both bvFTD and controls; and in violet regional hyperperfusion in phFTD compared to bvFTD.
HC = healthy controls; phFTD = phenocopy frontotemporal dementia; bvFTD = behavioral variant frontotemporal dementia; nGM = normalized gray matter.

DISCUSSION

To the best of our knowledge, our study is the first to show cortical brain abnormalities in phFTD. We found cortical atrophy in phFTD, most prominently in the right superior and posterior temporal lobe, and the fusiform gyrus bilaterally. Furthermore, we found left frontal hyperperfusion in phFTD compared to bvFTD and to a lesser extent to controls, which may reflect functional compensation for incipient pathology.

Regional right temporal atrophy was not only seen in phFTD but also present in bvFTD, suggesting similar underlying pathophysiology. Atrophy in right temporal regions has been linked to impaired emotion recognition and empathy in neurodegenerative disease [29,30], and more specifically to emotional blunting in bvFTD [31]. In addition, frontotemporal atrophy lateralized to the right hemisphere is more often associated with socially undesirable behavior in FTD than when lateralized to the left [32]. The fact that we found atrophy in this specific region may explain why symptoms in phFTD patients are mostly isolated to the behavioral domain, in contrast to bvFTD patients who show a more widespread frontotemporal atrophy and additional cognitive and functional decline.

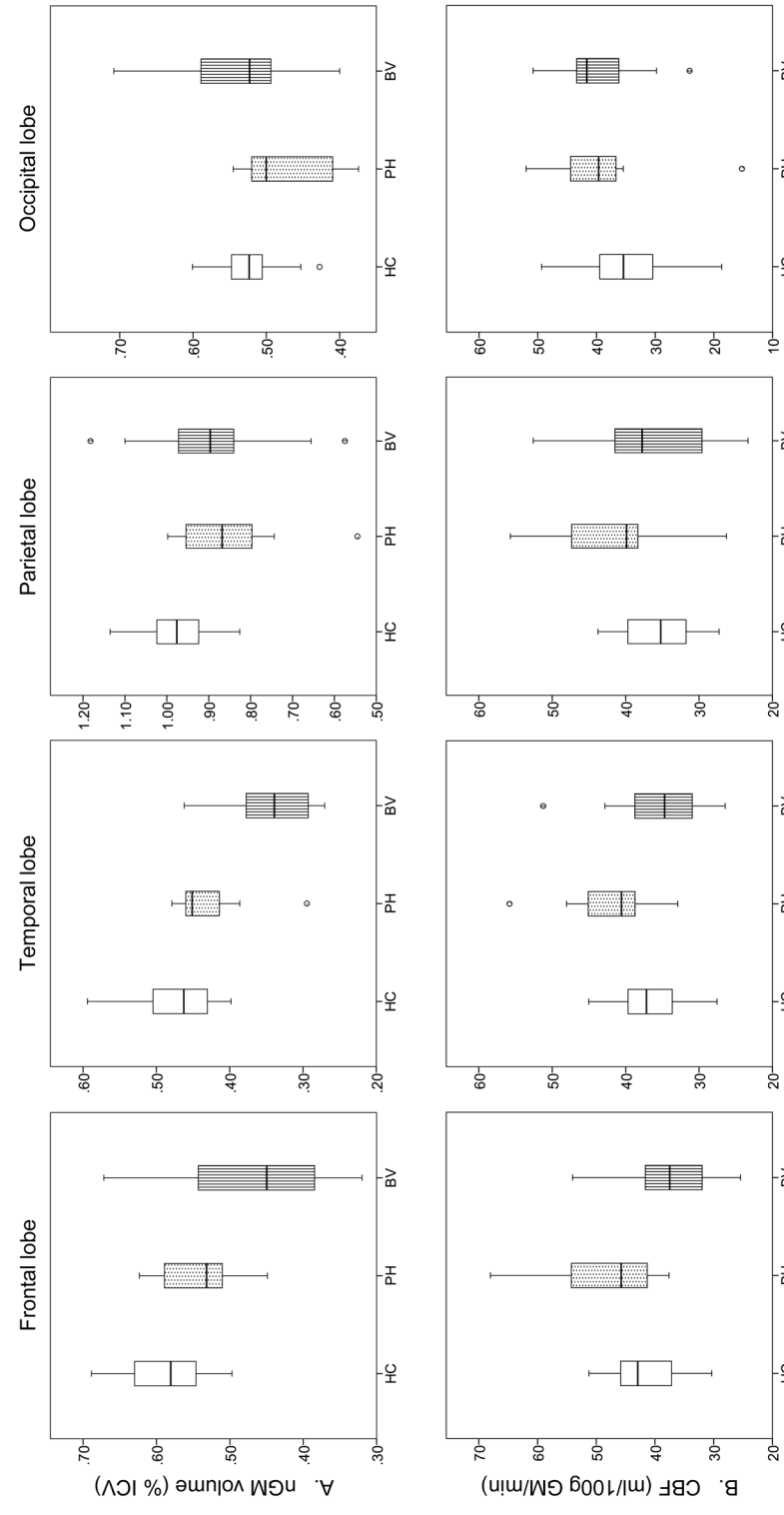

Figure 2: A) normalized GM (% ICV) and B) CBF (ml/100g GM/min) in the different lobes for healthy controls (HC), phFTD (PH) and bvFTD (BV) patients. The central box represents values from lower to upper quartile (25-75th percentile), the middle line represents the median, and vertical bars extend from minimum to maximum value. Spheres outside the bars indicate extreme values (value ≥ 1.5 x interquartile range). Note that GM volumes in phFTD are generally in-between those of HC and bvFTD, and that perfusion in phFTD is generally higher than in bvFTD and controls.
HC = healthy controls; phFTD = phenocopy frontotemporal dementia; bvFTD = behavioral variant frontotemporal dementia; nGM = normalized gray matter; ICV = intracranial volume; CBF = cerebral blood flow.

Our findings are in contrast to previous studies, in which no atrophy in phFTD was found using semi-quantitative ratings [7,33]. One possible explanation might be that such semiquantitative rating was not sufficiently sensitive. However, other studies using the potentially more sensitive VBM method did not show any abnormalities either [5,34], except for one case study reporting non-specific parieto-occipital, thalamic and subtle frontoinsular atrophy [3]. The discrepancy with the present study may lie in the fact that we used highly specific patient selection criteria, i.e. behavioral features consistent with bvFTD, without progression for at least one year, without psychiatric disorders and without C9ORF72 mutations. It may also be due to methodological differences between voxel-wise and ROI analyses. ROI analysis circumvents the problem of inter-individual anatomical variability, as well as subsequent corrections for such variability that may compromise resolution (such as smoothing). Additionally, statistical power of ROI analysis is hampered less by corrections for multiple comparisons than voxel-wise testing.

Apart from the focal right temporal atrophy, nGM volumes in phFTD were generally not different from neither bvFTD nor from controls. Only the right hippocampal formation and amygdala showed more atrophy in bvFTD compared with phFTD, suggesting preservation of those regions in phFTD, whereas these were severely affected in bvFTD [35]. Of note is that otherwise, nGM volumes were similar between phFTD and bvFTD, despite widespread GM loss in bvFTD compared to controls. These findings suggest that there is a continuum in nGM volumes ranging from normal on the one end to clearly abnormal in bvFTD on the other, with phFTD in-between. Together with the overlapping finding in both phFTD and bvFTD of right temporal lobe atrophy, this suggests that phFTD may be a disease on the FTD spectrum.

Our study was the first to use ASL-MRI in phFTD to assess perfusion. ASL is tightly coupled to brain metabolism and function as measured with FDG-PET, but previous PET studies failed to find any abnormalities in phFTD [5,8]. We found higher perfusion in phFTD in the bilateral straight gyus and left superior, inferior and orbital frontal gyrus compared to bvFTD, and to a lesser extent compared to controls. Some of these regions, i.e. in the left inferior frontal gyrus, correspond to those showing hypoperfusion in bvFTD compared to controls. Such hyperperfusion in phFTD relative to bvFTD may reflect a compensatory process of increased activity to compensate for incipient pathology in regions affected in bvFTD [36]. A similar pattern could be observed in the right straight gyrus, where perfusion was increased in phFTD compared to bvFTD, while there was a trend (p=0.06) towards hypoperfusion in bvFTD compared to controls. The other hyperperfused regions in phFTD relative to bvFTD, namely the superior frontal gyrus and subcallosal region, did not show hypoperfusion in bvFTD. Although not observed in our bvFTD sample, left superior frontal hypoperfusion has been found in FTD in previous ASL studies [37-39]. Similarly, PET studies have reported subcallosal hypometabolism in FTD [40-42]. Therefore, a compensatory process may still be hypothesized.

Taken together, our findings in phFTD suggest functional compensation as well as focal structural abnormalities overlapping with those found in bvFTD. Overlapping focal cortical atrophy was limited to the right temporal lobe, consistent with the

disease-specific prominent behavioral changes of phFTD, while cortical volumes in the remaining frontotemporal regions were in-between normal and those in bvFTD. These findings support the idea that phFTD is a disease of the FTD spectrum. One could even wonder whether phFTD is not simply an early manifestation of bvFTD. The notion of phFTD as a neurodegenerative disease is however still disputed due to the absence of disease progression in these patients. Psychiatric disorders have been proposed as an alternative or contributory etiology [14-16,43]. In support of this view, imaging findings show substantial overlap between FTD and disorders such as schizophrenia [44,45] and depression [46,47]. In addition, phFTD patients may carry a C9ORF72 mutation [3,13] which is not only associated with bvFTD, but also with psychotic symptoms [48]. Yet in our patients, alternative psychiatric diagnoses were ruled out, which renders interpretation in the context of neurodegenerative disease more likely. In addition, none of the phFTD patients had a mutation of the C9ORF72 gene. Therefore, as of yet, phFTD still seems to be described best as a clinical syndrome. As such, our phFTD population comprised patients with a distinct clinical profile: behavioral features consistent with bvFTD, without progression for at least one year, without psychiatric disorders and without the C9ORF72 mutation. This well-defined clinical profile may have enabled a first link between the typical behavioral changes in phFTD and potential neurophysiological changes as detected with imaging.

The present study has some limitations. Firstly, the sample size was small. This is inherent to phFTD being a rare disease, with only 17 documented cases in a large tertiary referral center as ours. Nevertheless, we studied a very well-defined phFTD sample, by strictly controlling for disease progression and alternative psychiatric etiology. One patient did have an asymptomatic cortical infarct in the right parietal lobe, but as this did not affect image processing results we expect it did not influence our findings. Secondly, groups were not fully gender-matched and were scanned on two - albeit identical - scanners. We tried to minimize potential confounding effects of gender and scanner by applying a very stringent analysis. Using hierarchical regression, we only investigated regions on which group had a significant effect but gender and scanner did not. Not only did this stringent analysis limit the number of regions that were eventually analyzed between groups, it even carries the risk of possible false negative results. However, our primary concern was to decrease the probability of false positives due to gender and scanner effects, and as such this stringent analysis strengthens the validity of our findings. Finally, despite a one year follow-up to ensure the absence of progression, longer follow-up in a longitudinal study will be even better suited to assess whether patients show no or very slow progression. Therefore, follow-up of our phFTD sample is currently ongoing. Ultimately, post-mortem examination is essential to determine whether neuropathology is present and if so, what type. Hence, studies investigating both neurodegenerative etiology and neuropsychiatric presentation of behavioral changes later in life [49] may further elucidate the relationship between behavior and neurophysiology.

In conclusion, in addition to overlapping focal right temporal lobe atrophy in phFTD and bvFTD, we found a continuum of frontotemporal cortical volumes ranging from normal on the one end to clearly abnormal in bvFTD on the other, with phFTD in-between. Furthermore, we observed left frontal hyperperfusion in

phFTD, suggestive of a compensatory process in response to incipient pathology in regions affected in FTD. To the best of our knowledge, our findings are the first evidence of a neuropathological substrate of phFTD and to possibly place it in an FTD spectrum. This may serve as the basis for further assessment in larger patient samples with longitudinal clinical and pathological follow-up.

REFERENCES

1. Neary D, Snowden JS, Gustafson L, Passant U, Stuss D, Black S, et al. Frontotemporal lobar degeneration: a consensus on clinical diagnostic criteria. Neurology. 1998;51: 1546-1554.
2. Rascovsky K, Hodges JR, Knopman D, Mendez MF, Kramer JH, Neuhaus J, et al. Sensitivity of revised diagnostic criteria for the behavioural variant of frontotemporal dementia. Brain. 2011;134: 2456-2477.
3. Khan BK, Yokoyama JS, Takada LT, Sha SJ, Rutherford NJ, Fong JC, et al. Atypical, slowly progressive behavioural variant frontotemporal dementia associated with C9ORF72 hexanucleotide expansion. J Neurol Neurosurg Psychiatry. 2012;83: 358-364.
4. Hornberger M, Shelley BP, Kipps CM, Piguet O, Hodges JR. Can progressive and non-progressive behavioural variant frontotemporal dementia be distinguished at presentation? J Neurol Neurosurg Psychiatr. 2009;80: 591-593.
5. Kipps CM, Hodges JR, Fryer TD, Nestor PJ. Combined magnetic resonance imaging and positron emission tomography brain imaging in behavioural variant frontotemporal degeneration: refining the clinical phenotype. Brain. 2009;132: 2566-2578.
6. Kipps CM, Davies RR, Mitchell J, Kril JJ, Halliday GM, Hodges JR. Clinical significance of lobar atrophy in frontotemporal dementia: application of an MRI visual rating scale. Dement Geriatr Cogn Disord. 2007;23: 334-342.
7. Davies RR, Kipps CM, Mitchell J, Kril JJ, Halliday GM, Hodges JR. Progression in frontotemporal dementia: identifying a benign behavioral variant by magnetic resonance imaging. Arch Neurol. 2006;63: 1627-1631.
8. Kerklaan BJ, Berckel BN, Herholz K, Dols A, Flier WM, Scheltens P, et al. The Added Value of 18-Fluorodeoxyglucose-Positron Emission Tomography in the Diagnosis of the Behavioral Variant of Frontotemporal Dementia. Am J Alzheimers Dis Other Demen. 2014.
9. Mioshi E, Hodges JR. Rate of change of functional abilities in frontotemporal dementia. Dement Geriatr Cogn Disord. 2009;28: 419-426.
10. Hornberger M, Piguet O, Kipps C, Hodges JR. Executive function in progressive and nonprogressive behavioral variant frontotemporal dementia. Neurology. 2008;71: 1481-1488.
11. Diehl-Schmid J, Grimmer T, Drzezga A, Bornschein S, Riemenschneider M, Forstl H, et al. Decline of cerebral glucose metabolism in frontotemporal dementia: a longitudinal 18F-FDG-PET-study. Neurobiol Aging. 2007;28: 42-50.
12. Kertesz A, McMonagle P, Blair M, Davidson W, Munoz DG. The evolution and pathology of frontotemporal dementia. Brain. 2005;128: 1996-2005.
13. Gomez-Tortosa E, Serrano S, de Toledo M, Perez-Perez J, Sainz MJ. Familial benign frontotemporal deterioration with C9ORF72 hexanucleotide expansion. Alzheimers Dement. 2014.
14. Kipps CM, Hodges JR, Hornberger M. Nonprogressive behavioural frontotemporal dementia: recent developments and clinical implications of the 'bvFTD phenocopy syndrome'. Curr Opin Neurol. 2010;23: 628-632.
15. Piguet O, Hornberger M, Mioshi E, Hodges JR. Behavioural-variant frontotemporal dementia: diagnosis, clinical staging, and management. Lancet Neurol. 2011;10: 162-172.
16. Manes F. Psychiatric conditions that can mimic early behavioral variant frontotemporal dementia: the importance of the new diagnostic criteria. Curr Psychiatry Rep. 2012;14: 450-452.
17. Wong EC, Buxton RB, Frank LR. Quantitative perfusion imaging using arterial spin labeling. Neuroimaging Clin N Am. 1999;9: 333-342.
18. Overall JE, Gorham DR. The brief psychiatric rating scale. Psychol Rep. 1962;10: 799-812.
19. Dingemans P. Vertaling en bewerking: Uitgebreide BPRS handleiding, Los Angeles Project. Amsterdam: Psychiatrisch Centrum AZUA; 1986.

20. Alsop DC, Detre JA, Golay X, Günther M, Hendrikse J, Hernandez-Garcia L, et al. Recommended implementation of arterial spin-labeled perfusion MRI for clinical applications: A consensus of the ISMRM perfusion study group and the European consortium for ASL in dementia. Magn Reson Med. 2015;73: 102-116.
21. Bron EE, Steketee RME, Houston GC, Oliver RA, Achterberg HC, Loog M, et al. Diagnostic classification of arterial spin labeling and structural MRI in presenile early stage dementia. Hum Brain Mapp. 2014;35: 4916-4931.
22. Klein S, Staring M, Murphy K, Viergever MA, Pluim JP. Elastix: a Toolbox for Intensity-Based Medical Image Registration. IEEE Trans Med Imaging. 2010;29: 196-205.
23. Asllani I, Borogovac A, Brown TR. Regression algorithm correcting for partial volume effects in arterial spin labeling MRI. Magn Reson Med. 2008;60: 1362-1371.
24. Hammers A, Allom R, Koepp MJ, Free SL, Myers R, Lemieux L, et al. Three-dimensional maximum probability atlas of the human brain, with particular reference to the temporal lobe. Hum Brain Mapp. 2003;19: 224-247.
25. Gousias IS, Rueckert D, Heckemann RA, Dyet LE, Boardman JP, Edwards AD, et al. Automatic segmentation of brain MRIs of 2-year-olds into 83 regions of interest. Neuroimage. 2008;40: 672-684.
26. Heckemann RA, Hajnal JV, Aljabar P, Rueckert D, Hammers A. Automatic anatomical brain MRI segmentation combining label propagation and decision fusion. Neuroimage. 2006;33: 115-126.
27. Tustison NJ, Avants BB, Cook PA, Zheng Y, Egan A, Yushkevich PA, et al. N4ITK: improved N3 bias correction. IEEE Trans Med Imaging. 2010;29: 1310-1320.
28. Smith SM. Fast robust automated brain extraction. Hum Brain Mapp. 2002;17: 143-155.
29. Rosen HJ, Wilson MR, Schauer GF, Allison S, Gorno-Tempini ML, Pace-Savitsky C, et al. Neuroanatomical correlates of impaired recognition of emotion in dementia. Neuropsychologia. 2006;44: 365-373.
30. Rankin KP, Gorno-Tempini ML, Allison SC, Stanley CM, Glenn S, Weiner MW, et al. Structural anatomy of empathy in neurodegenerative disease. Brain. 2006;129: 2945-2956.
31. Lee GJ, Lu PH, Mather MJ, Shapira J, Jimenez E, Leow AD, et al. Neuroanatomical correlates of emotional blunting in behavioral variant frontotemporal dementia and early-onset Alzheimer's disease. J Alzheimers Dis. 2014;41: 793-800.
32. Mychack P, Kramer JH, Boone KB, Miller BL. The influence of right frontotemporal dysfunction on social behavior in frontotemporal dementia. Neurology. 2001;56: S11-5.
33. Pennington C, Hodges JR, Hornberger M. Neural correlates of episodic memory in behavioral variant frontotemporal dementia. J Alzheimers Dis. 2011;24: 261-268.
34. Kipps CM, Nestor PJ, Acosta-Cabronero J, Arnold R, Hodges JR. Understanding social dysfunction in the behavioural variant of frontotemporal dementia: the role of emotion and sarcasm processing. Brain. 2009;132: 592-603.
35. Barnes J, Whitwell JL, Frost C, Josephs KA, Rossor M, Fox NC. Measurements of the amygdala and hippocampus in pathologically confirmed Alzheimer disease and frontotemporal lobar degeneration. Arch Neurol. 2006;63: 1434-1439.
36. Hu WT, Wang Z, Lee VM, Trojanowski JQ, Detre JA, Grossman M. Distinct cerebral perfusion patterns in FTLD and AD. Neurology. 2010;75: 881-888.
37. Tosun D, Rosen H, Miller BL, Weiner MW, Schuff N. MRI patterns of atrophy and hypoperfusion associations across brain regions in frontotemporal dementia. Neuroimage. 2012;59: 2098-2109.
38. Zhang Y, Schuff N, Ching C, Tosun D, Zhan W, Nezamzadeh M, et al. Joint assessment of structural, perfusion, and diffusion MRI in Alzheimer's disease and frontotemporal dementia. Int J Alzheimers Dis. 2011;2011: 546871.

39. Du AT, Jahng GH, Hayasaka S, Kramer JH, Rosen HJ, Gorno-Tempini ML, et al. Hypoperfusion in frontotemporal dementia and Alzheimer disease by arterial spin labeling MRI. Neurology. 2006;67: 1215-1220.
40. Salmon E, Garraux G, Delbeuck X, Collette F, Kalbe E, Zuendorf G, et al. Predominant ventromedial frontopolar metabolic impairment in frontotemporal dementia. Neuroimage. 2003;20: 435-440.
41. Schroeter ML, Raczka K, Neumann J, Yves von Cramon D. Towards a nosology for frontotemporal lobar degenerations-a meta-analysis involving 267 subjects. Neuroimage. 2007;36: 497-510.
42. Kanda T, Ishii K, Uemura T, Miyamoto N, Yoshikawa T, Kono AK, et al. Comparison of grey matter and metabolic reductions in frontotemporal dementia using FDG-PET and voxel-based morphometric MR studies. Eur J Nucl Med Mol Imaging. 2008;35: 2227-2234.
43. Gossink FT, Dols A, Kerssens CJ, Krudop WA, Kerklaan BJ, Scheltens P, et al. Psychiatric diagnoses underlying the phenocopy syndrome of behavioural variant frontotemporal dementia. J Neurol Neurosurg Psychiatry. 2015.
44. Andreasen NC, O'Leary DS, Flaum M, Nopoulos P, Watkins GL, Boles Ponto LL, et al. Hypofrontality in schizophrenia: distributed dysfunctional circuits in neuroleptic-naive patients. Lancet. 1997;349: 1730-1734.
45. Olabi B, Ellison-Wright I, McIntosh AM, Wood SJ, Bullmore E, Lawrie SM. Are there progressive brain changes in schizophrenia? A meta-analysis of structural magnetic resonance imaging studies. Biol Psychiatry. 2011;70: 88-96.
46. Drevets WC, Price JL, Simpson JR,Jr, Todd RD, Reich T, Vannier M, et al. Subgenual prefrontal cortex abnormalities in mood disorders. Nature. 1997;386: 824-827.
47. Dotson VM, Davatzikos C, Kraut MA, Resnick SM. Depressive symptoms and brain volumes in older adults: a longitudinal magnetic resonance imaging study. J Psychiatry Neurosci. 2009;34: 367-375.
48. Snowden JS, Rollinson S, Thompson JC, Harris JM, Stopford CL, Richardson AM, et al. Distinct clinical and pathological characteristics of frontotemporal dementia associated with C9ORF72 mutations. Brain. 2012;135: 693-708.
49. Krudop WA, Kerssens CJ, Dols A, Prins ND, Moller C, Schouws S, et al. Building a new paradigm for the early recognition of behavioral variant frontotemporal dementia: Late Onset Frontal Lobe Syndrome study. Am J Geriatr Psychiatry. 2014;22: 735-740.

SUPPLEMENTARY MATERIALS

Table 1: regions of interest (ROIs)

Lobe	Gyrus	Consisting of:
Frontal	Superior frontal gyrus	
	Middle frontal gyrus	
	Inferior frontal gyrus	
	Straight gyrus	
	Orbitofrontal gyrus	Anterior orbital gyrus Medial orbital gyrus Lateral orbital gyrus Posterior orbital gyrus
	Subcallosal area	
	Anterior cingulate gyrus	
	Insula	
	Precentral gyrus	
Temporal	Anterior temporal lobe	Medial anterior temporal lobe Lateral anterior temporal lobe
	Posterior temporal lobe	
	Amygdala	
	Hippocampal formation	Hippocampus Parahippocampal gyrus
	Superior temporal gyrus	
	Inferior temporal gyrus	
	Fusiform gyrus	
Parietal	Postcentral gyrus	
	Posterior cingulate gyrus	
	Precuneus	
	Remainder of parietal lobe	
Occipital	Lingual gyrus	
	Cuneus	
	Lateral remainder of occipital lobe	

Regions of interest (ROIs) assessed for gray matter volume and cerebral flood flow. Parcellated gyri (according to [24,25], right column) were combined (middle column) for analysis.

Chapter 3.2

Functional connectivity and microstructural white matter changes in phenocopy frontotemporal dementia

Rozanna Meijboom
Rebecca M.E. Steketee
Inge de Koning
Robert Jan Osse
Lize C. Jiskoot
Frank Jan de Jong
Aad van der Lugt
John C. van Swieten
Marion Smits

Submitted

ABSTRACT

Phenocopy frontotemporal dementia (phFTD) is a rare and poorly understood clinical syndrome. PhFTD presents with core behavioural variant FTD (bvFTD) symptoms (apathy, disinhibition, loss of insight), in the absence of associated cognitive deficits and brain abnormalities on conventional MRI, and without progression over time. In contrast with phFTD, brain abnormalities in functional connectivity and white matter microstructure have been observed in bvFTD. We hypothesise that phFTD belongs to the same disease spectrum as bvFTD, and investigated whether functional connectivity and microstructural white matter changes similar to bvFTD are also present in phFTD.

Seven phFTD patients (mean age 63.4y; 7 male) without disease progression and without alternative psychiatric diagnosis, twelve bvFTD patients (60.2y; 7male) and seventeen age-matched controls (64.1y; 17male) underwent resting state functional MRI (rs-fMRI) and diffusion tensor imaging (DTI). The default mode network (DMN), identified using independent component analysis (ICA), and DTI metrics (fractional anisotropy, mean diffusivity, radial diffusivity, axial diffusivity), calculated using tract-based spatial statistics (TBSS), were compared between all groups (FSL, Oxford, UK).

PhFTD patients compared with controls showed a subtle increase in DMN connectivity, and subtle microstructural changes in several white matter tracts, such as the cingulum, uncinate fasciculus and genu of the corpus callosum. BvFTD patients showed abnormalities in the same regions as phFTD patients, but had a lower increase in DMN connectivity, and more extensive microstructural white matter changes.

These findings can be interpreted as neuropathological changes, i.e. neuronal dysfunctioning and myelin damage, inducing functional compensation and reduced directional diffusion, and are in support of the hypothesis that phFTD belongs to the same disease spectrum as bvFTD. Advanced MRI techniques, such as rs-fMRI and DTI, would therefore be potentially suited to improve diagnosis of phFTD by objectively identifying brain abnormalities.

INTRODUCTION

Phenocopy (or nonprogressive) frontotemporal dementia (phFTD) is a rare and poorly understood syndrome, which was only recently described by Davies et al. (2006) [1] in a subgroup of behavioural variant FTD (bvFTD) patients who had a better prognosis than expected. PhFTD symptomatology is very similar to that of bvFTD, but some aspects of phFTD are essentially different. In phFTD, core bvFTD symptoms, such as apathy, behavioural disinhibition, and loss of insight [2], are generally not accompanied by cognitive and brain abnormalities as is the case in bvFTD. PhFTD patients show a cognitive profile that ranges from normal to suggesting FTD [3-8] and have a relatively intact performance of daily living activities (ADL) [2,7,9]. These clinical features in phFTD appear stable over time, whereas in bvFTD patients rapid progression of cognitive deficits is evident [1,7,10,11]. On conventional (structural) magnetic resonance imaging (MRI), phFTD patients show no or only borderline abnormalities [1,11] in the frontal and temporal regions that are typically affected in bvFTD [12,13]. Positron emission tomography (PET) does not show the frontal hypometabolism as observed in bvFTD [14]. As bvFTD patients may initially also present without structural MRI abnormalities, early-stage distinction between phFTD and bvFTD may be difficult.

A pathophysiological explanation for phFTD symptomatology is currently unavailable. Patients often remain undiagnosed or receive an alternative psychiatric diagnosis. Additionally, they are occasionally found to be C9orf72 mutation carriers [15]. It is therefore of importance to investigate the presence of possible brain abnormalities underlying their symptoms using more advanced MRI techniques such as resting state functional MRI (rs-fMRI) and diffusion tensor imaging (DTI). These techniques measure subtle brain changes so far left unexplored, by looking at functional connectivity and microstructural white matter. In bvFTD, parietal regions of the default mode network (DMN), one of the major functional networks, show increased connectivity [16-18]. Frontal DMN connectivity changes are found to be more ambiguously involved, either increased [19] or decreased [16,18]. Such functional changes are thought to precede grey matter atrophy appearing at the later stages of bvFTD [16,20]. White matter abnormalities in bvFTD are found mainly in frontal and temporal areas such as the uncinate fasciculus (UF), cingulum and the genu of the corpus callosum (CC) [21]. Similar regions are found to be already affected in asymptomatic-FTD mutation-carriers [20].

As phFTD patients present with behavioural symptoms similar to bvFTD, we hypothesise that phFTD belongs to the same disease spectrum. This study investigates whether phFTD patients have underlying brain abnormalities that are similar to those seen in bvFTD patients: functional brain abnormalities expressed as DMN connectivity changes and microstructural white matter abnormalities expressed as diffusion changes.

METHODS

Participants

All patients were recruited in the Alzheimer Centre Southwest Netherlands. PhFTD patient inclusion criteria were: age between 40 and 75 years; prominent behavioural changes interfering with social functioning, consisting of disinhibition and/or apathy and/or stereotypy; stability of patient's initial situation (i.e. no reported progression one year after initial routine diagnostic workup).

BvFTD patients were part of a larger ongoing study of advanced MR neuroimaging in early stage presenile dementia with the following inclusion criteria: age between 45 and 70 years; a suspected diagnosis of bvFTD [22]; a clinical dementia rating (CDR) scale score of ≤ 1; a Mini-Mental State Examination (MMSE) [23] score of ≥ 20.

Exclusion criteria for both patient groups were contraindications for MRI; inability to comprehend and/or execute fMRI tasks; other neurological disorders; past or current substance abuse; other psychiatric diagnosis. In addition, specific exclusion criteria for the phFTD patients were: diagnosis of dementia and missing heteroanamnesis. Specific exclusion criteria for bvFTD patients were: expected loss to follow up within one year and a different cause of dementia.

Healthy controls (aged 60 to 70 years), without neurological or psychiatric history, were recruited through advertisement. They were matched for gender with phFTD patients and for age with all patients.

The study was approved by the local medical ethics committee. All participants gave written informed consent.

Stimuli and apparatus

Psychiatric, neuropsychological and genetic mutation assessment

PhFTD patients underwent full psychiatric assessment as part of this study to exclude alternative diagnoses. Psychiatric assessment consisted of a psychiatric diagnostic interview by a senior psychiatrist with both the patient and the caregiver. Additionally, the Brief Psychiatric Rating Scale (BPRS) [24,25] was administered.

All participants underwent a full neuropsychological assessment consisting of a test battery of language, memory, attention and concentration, executive functioning, constructive and visuospatial skills, and social cognition. The assessment was conducted and evaluated by an experienced neuropsychologist at the Alzheimer Centre Southwest Netherlands.

MMSE [23] was assessed in phFTD patients during their psychiatric assessment, in bvFTD patients during their neuropsychological assessment, and in the healthy controls after the MRI scan by the researcher.

Additionally, DNA of phFTD patients was tested for the C9orf72 mutation.

Image acquisition

Scanning was performed on two 3T GE Discovery MR750 systems (GE Healthcare, Milwaukee, WI, US) with identical protocols. PhFTD patients and twelve healthy controls were scanned on one, and bvFTD patients and eight healthy controls on the other scanner.

A high-resolution three-dimensional (3D) inversion recovery (IR) fast spoiled gradient echo (FSPGR) T1-weighted (T1w) image was acquired for anatomical reference with a field of view (FOV) of 240mm, inversion time (TI) of 450ms, echo time (TE) of 3.06ms, repetition time (TR) of 7.904s, array spatial sensitivity encoding technique (ASSET) acceleration factor of 2, flip angle of 12°, acquisition matrix of 240x240, slice thickness of 1mm, resulting in isotropic voxel size of 1mm^3. 176 sagittal slices covering the entire brain were acquired in 4.41 minutes.

Functional scans with full coverage of the supratentorial brain were acquired using a gradient echo echo planar imaging (EPI) sequence with a TE/TR of 30/3000ms, ASSET acceleration factor of 2, flip angle of 90°, acquisition matrix of 96x96, slice thickness of 3mm, and FOV of 240mm. 200 volumes, each consisting of 44 axial slices, were acquired in 10 minutes. Additionally, five dummy scans were acquired which were not included in the analysis. Participants were instructed to focus on a fixation cross, to think of nothing in particular and to not fall asleep.

DTI scans with full coverage of the supratentorial brain were acquired with 25 non-collinear directions using a spin echo EPI sequence with a FOV of 240mm, TE/TR of 84.7/7.93ms, ASSET acceleration factor of 2, flip angle of 90°, acquisition matrix of 128x128, and slice thickness of 2.5mm. Maximum b-value was 1000 s/mm^2. Three volumes were acquired without diffusion weighting. In total 28 volumes, each consisting of 59 oblique slices, were acquired in 3.50 minutes.

Data analysis

Structural MRI

Grey matter volumes were calculated for all participants according to the methods described in Bron et al. (2014) [26]. First, grey matter maps were obtained from the T1w image using the unified tissue segmentation method of SPM8 (Statistical Parametric Mapping, London, UK). Second, intracranial volume (ICV) was calculated. Third, for each participant the grey matter volume was divided by ICV to correct for head size. Grey matter volume, expressed as % ICV, was compared between groups using a one-way ANOVA and post-hoc Bonferroni tests (IBM SPSS Statistics, version 21.0, New York, USA).

Rs-fMRI

Resting state data were analysed using FMRIB Software library (FSL4.1.9, Oxford, UK) [27-29]. T1w images were first reoriented to ensure the same orientation as

the standard template T1 images. The skull was stripped using the Brain Extraction Tool (BET) [30].

The Multivariate Exploratory Linear Optimized Decomposition into Independent Components (MELODIC) toolbox was used to preprocess the data and to perform independent component analysis (ICA). Preprocessing consisted of several steps. First the high pass filter was set to remove low-frequency drifts (cut-off 120s). Then MCFLIRT [31] motion correction was applied to correct for linear motion followed by spatial smoothing performed with a Gaussian kernel of 5mm FWHM. During registration, functional data were first linearly registered to the corresponding T1w images (full search, 7 degrees of freedom (DOF)). This was followed by both linear and nonlinear registration to a standard template brain (full search, 12 DOF) with a warp resolution of 10mm and a resampling resolution of 4mm. Resting state networks were identified by performing a multi-session temporal concatenation ICA. Component output was limited to 20. Dual regression [32] was used to identify the group components in the functional data of each participant. The component representing the DMN was identified. FSLcc was used to identify the component showing the highest correlation between a DMN template [33] and ICA output. The Randomize tool [34] was used to assess between-group differences in DMN network connectivity. The design was constructed using the general linear model (GLM) toolbox. A one-way ANOVA with three groups (phFTD≠bvFTD≠controls) was performed to assess which regions showed different connectivity between groups. Effects per group were investigated and six t-contrasts (phFTD>HC, HC>phFTD, bvFTD>HC, HC>bvFTD, phFTD>bvFTD, bvFTD>phFTD) were constructed to assess post-hoc between-group differences. Grey matter volume was added as covariate to account for grey matter atrophy. Threshold-free cluster enhancement (TFCE) [35] and nonparametric permutation testing with 5000 permutations was applied. Results were not family-wise error corrected for multiple comparisons on a voxel level. However, the f-test resulting from the one-way ANOVA and the group effects (phFTD, bvFTD, controls) were Bonferroni corrected for the number of contrasts, thus using an effective threshold of $p<0.0125$. Subsequent Bonferroni correction for the number of post hoc t-tests was considered unnecessary as their results were assessed within the constraints of the omnibus f-test, This was done by creating common binary masks to identify post-hoc t-tests results within the omnibus f-test positive connectivity regions. Using the Fslmaths tool, first binary masks were created for the f-test and for every t-test. Second, the binary mask of each t-test was multiplied with binary mask of the f-test, resulting in common binary masks for each t-test.

All t-test common binary masks ($p<0.05$, not corrected for multiple comparisons), the f-test and the three group effects ($p<0.05$, Bonferroni corrected for multiple contrasts) were evaluated using the Cluster tool to extract cluster size with a cluster threshold of $k\geq20$ voxels.

Results were visualised using FSLview. The Harvard-Oxford Cortical Structural Atlas and the Harvard-Oxford Subcortical Structural Atlas implemented in FSLView were used to anatomically identify the DMN regions.

DTI

Data were corrected for motion, eddy currents and EPI distortions using ExploreDTI [36]. Further analyses were performed with FSL (5.0.2.2, Oxford, UK) [27-29]. BET [30] was used to create skull-stripped binary-masks. Using DTIFIT, as implemented in FMRIB's Diffusion Toolbox (FDT) [37], the diffusion tensors were reconstructed. Then DTIFIT created subject images for fractional anisotropy (FA), mean diffusivity (MD), the first eigenvalue/axial diffusivity (AxD) and the second and third eigenvalues. Fslmaths was used to calculate subject radial diffusivity (RD) images by averaging the second and third eigenvalue images.

Registration of diffusivity measure images was executed by Tract-Based Spatial Statistics (TBSS) [38]. First, subject FA image outliers from DTIFIT were excluded by removing brain-end artefacts and end slices. Second, non-linear registration of all subject FA images to the FMRIB58 FA template was performed. Third, all subject FA images were normalised to the Montreal Neurological Institute (MNI) template. Then the mean of all normalised subject FA images was taken to create a mean FA skeleton. Fifth, the mean FA skeleton was binarised. Then each subject's FA image was projected onto this binary FA skeleton. TBSS was repeated for AxD, MD and RD images. FA nonlinear registration parameters were applied to subject AxD, MD and RD images creating nonlinearly registered images for each of them. For each measure all subject images were projected onto the FA skeleton, creating a new skeleton for each diffusivity measure.

Randomize [34] was run to test for between-group differences in all described diffusivity measures. TFCE [35] nonparametric permutation testing with 5000 permutations was applied. Results were family-wise error (FWE) corrected for multiple comparisons.

FA differences between phFTD, bvFTD and controls were assessed using the same design defined for the rs-fMRI analysis, but now only the f-test and subsequent post-hoc t-tests were investigated. As group effects were not investigated, additional Bonferroni correction for the number of contrast was unnecessary. Again, common binary masks were created to assess t-test results within the constraints of the omnibus f-test results by multiplying binary masks of each t-test with the binary mask of the f-test. All t-test common binary masks ($p<0.05$, FWE corrected for multiple comparisons) were evaluated using Cluster to extract cluster size with a cluster threshold of $k\geq20$.

Results were visualised using FSLView. The JHU White-Matter Tractography Atlas and the JHU ICBM-DTI-81 White-Matter labels implemented in FSLView were used to anatomically identify the white matter regions.

RESULTS

Participant and disease characteristics

Nine phFTD patients (all male), 12 bvFTD patients (7 male) and 20 healthy controls (all male) were included in the study. Two phFTD patients were excluded from the analysis: one refused neuropsychological testing and one showed disease progression on neuropsychological testing. One phFTD patient showed a cortical infarct in the right parietal lobe on the structural MRI scan, but reported no residual clinical symptoms and his neuropsychological profile was rated as normal; he was therefore retained in the analysis. Three controls were excluded from the analysis: one due to a below average score on a neuropsychological domain typically affected in FTD; the second due to an incidental scanner artefact observed in the MR images; the third because of missing DTI data. Three bvFTD patients had missing rs-fMRI data. Data of 7 phFTD patients, 12 bvFTD patients (9 for rs-fMRI analysis) and 17 controls were used for the current analyses (Table 1).

Age ($H(2) = 2{,}23$ $p>0.05$, Table 1) and MMSE score did not differ between groups ($H(2) = 5{,}93$, $p>0.05$, Table 1). Six of the seven included phFTD patients had a cognitive profile suggesting FTD, but showed no progression relative to previous neuropsychological testing consistent with the phFTD criteria. One phFTD patient had a normal cognitive profile. Mean interval between current and previous neuropsychological testing was 23 months (SD 14 months). All controls had a normal cognitive profile. None of the phFTD patients received an alternative psychiatric diagnosis that could explain their behavioural symptoms. Additionally, they were not carriers of the C9orf72 mutation.

Table 1. Demographic characteristics.

Group	N	Mean age	Mean MMSE
PhFTD	7 (all male)	63.4 (4.8)	26.6 (1.4)
BvFTD	12 (7 male)	60.2 (7.6)	26.6 (2.8)
Controls	17 (all male)	64.1 (3.3)	28.2 (1.5)

PhFTD = phenocopy FTD. BvFTD = behavioural FTD. N = sample size. Values given as Mean (SD). MMSE = Mini-Mental State Examination.

Structural MRI

The three groups showed a difference in grey matter volume corrected for ICV ($H(2) = 16.38$, $p<0.05$), with a mean of 0.32% (SD 0.02) for phFTD, 0.29% (SD 0.04) for bvFTD, and 0.35% (SD 0.02) for controls. Compared with controls, both phFTD patients ($p=0.013$) and bvFTD patients ($p<0.001$) had lower grey matter volume. Grey matter volume was not different between phFTD and bvFTD patients ($p=0.359$).

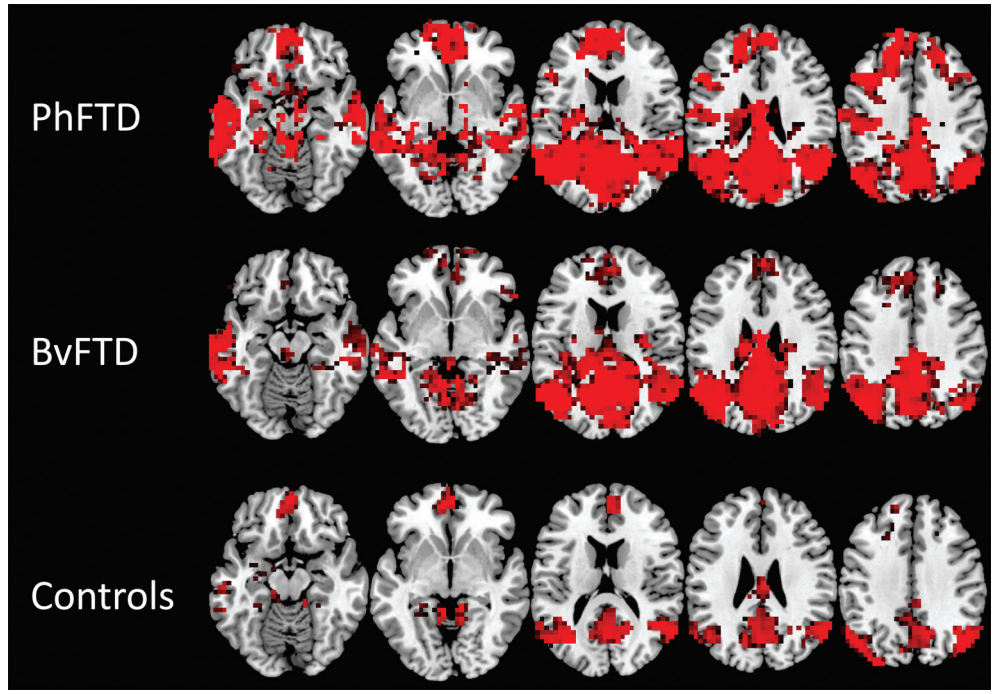

Figure 1. Group effects of default mode network (DMN) connectivity ($p<0.05$, not corrected for multiple comparisons, but Bonferroni corrected ($p<0.05$) for multiple contrasts; $k\geq20$) in phenocopy frontotemporal dementia (phFTD), behavioural variant FTD (bvFTD) and controls.

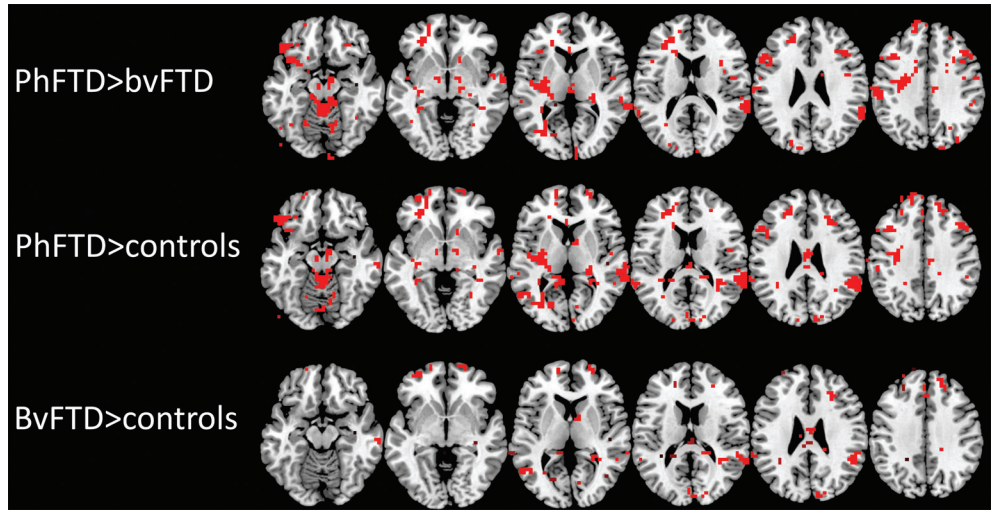

Figure 2. Post-hoc t-test comparisons (phFTD>bvFTD, phFTD>controls, bvFTD>controls) showing between-group DMN connectivity differences ($p<0.05$, not corrected for multiple comparisons, but within the constraints of the omnibus f-test ($p<0.05$, Bonferroni corrected for multiple contrasts); $k\geq20$).
DMN = default mode network, phFTD = phenocopy frontotemporal dementia, bvFTD = behavioural variant FTD.

Table 2A. Group effects (p<0.05, not corrected for multiple comparisons, but Bonferroni corrected (p<0.05) for multiple contrasts; k≥20) of DMN connectivity in phFTD, bvFTD and controls.
DMN = default mode network, phFTD = phenocopy frontotemporal dementia, bvFTD = behavioural variant frontotemporal dementia, HC = healthy controls, L = left, R = right.

Group effect	Number of DMN clusters	Total number of voxels	Number of voxels within largest DMN cluster	Anatomical regions within largest DMN cluster
phFTD	2	7,852	7,827	Medial prefrontal cortex L, R Lateral temporal cortex L, R Inferior parietal lobule L, R Precuneus/posterior cingulate cortex L, R
bvFTD	2	4,848	4,458	Lateral temporal cortex L, R Inferior parietal lobule L, R Precuneus/posterior cingulate cortex L, R
HC	5	1,635	1,015	Inferior parietal lobule R Precuneus/posterior cingulate cortex L, R

Table 2B. Post-hoc two sample t-tests (p<0.05, not corrected for multiple comparisons, but within the constraints of the omnibus f-test (p<0.05, Bonferroni corrected for multiple contrasts); k≥20) of group differences in DMN connectivity between phFTD, bvFTD and controls.
DMN = default mode network, phFTD = phenocopy frontotemporal dementia, bvFTD = behavioural variant frontotemporal dementia, HC = healthy controls, L = left, R = right.

T-stat	Number of DMN clusters	Total number of voxels	Number of voxels within largest DMN cluster	Anatomical regions within largest DMN cluster
phFTD>HC	7	635	162	Lateral temporal cortex R Inferior parietal lobule R
bvFTD>HC	3	104	43	Lateral temporal cortex R Inferior parietal lobule R
HC>bvFTD	1	44	44	Inferior parietal lobule R
phFTD>bvFTD	7	852	374	Lateral temporal cortex L Subcortical and cerebellar regions L

Functional connectivity

PhFTD and bvFTD patients (Figure 1, Table 2A) showed connectivity in all regions of the DMN. Controls showed connectivity in all DMN regions, except the right lateral temporal cortex (LTC) (Figure 1, Table 2A).

PhFTD patients compared with controls showed increased DMN connectivity in the bilateral medial prefrontal cortex (mPFC), LTC, and inferior parietal lobule (IPL), and in the left posterior cingulate cortex (PCC)/precuneus (Figure 2, Table 2B).

BvFTD patients compared with controls showed increased DMN connectivity in the bilateral mPFC, and right LTC and IPL, (Figure 2, Table 2B), and decreased DMN connectivity in the more posterior right IPL.

PhFTD patients compared with bvFTD patients showed increased DMN connectivity in the bilateral mPFC and LTC, and right IPL (Figure 2, Table 2B).

Microstructural white matter

PhFTD and bvFTD patients compared with controls showed decreased FA and increased RD and MD mainly in the frontal and temporoparietal white matter (Figure 3, Tables 3A-C), such as the cingulum (both cingulate and hippocampus portion), inferior fronto-occipital fasciculus (IFOF), superior longitudinal fasciculus (SLF), corpus callosum and uncinate fasciculus. In bvFTD patients in comparison with controls increased AxD was observed in these regions as well (Figure 3, Table 3D).

BvFTD patients compared with phFTD patients showed decreased FA and increased AxD in frontal white matter, and increased MD and RD in frontotemporal white matter, mainly in the cingulum (cingulate portion), IFOF, SLF, corpus callosum and uncinate fasciculus (Figure 4, Tables 3A-D).

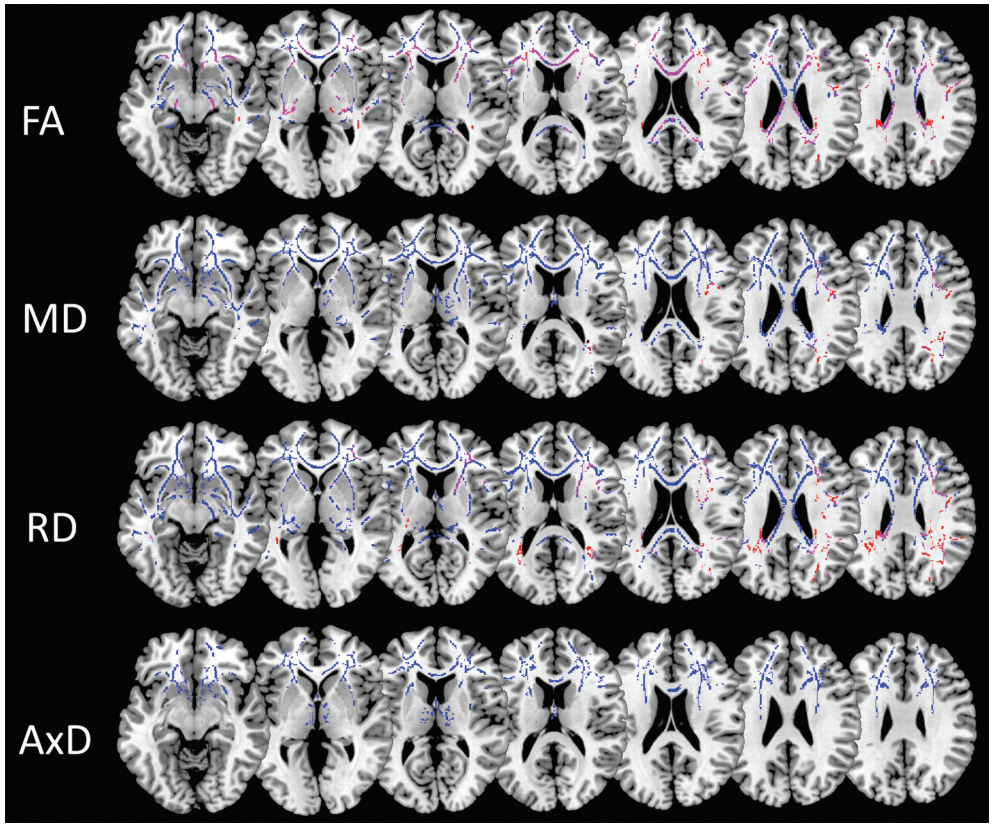

Figure 3. Post-hoc t-test of microstructural white matter changes for phFTD ($p_{corrected}$<0.05; k≥20) and bvFTD ($p_{corrected}$<0.05; k≥20) in comparison with controls. Lower FA and higher MD, RD and AxD in comparison with controls is shown in phFTD in red and in bvFTD in blue. WM regions showing overlapping abnormalities in phFTD and bvFTD are shown in pink.
PhFTD = phenocopy frontotemporal dementia, bvFTD = behavioural variant frontotemporal dementia, FA = fractional anisotropy, MD = mean diffusivity, RD = radial diffusivity, AxD = axial diffusivity.

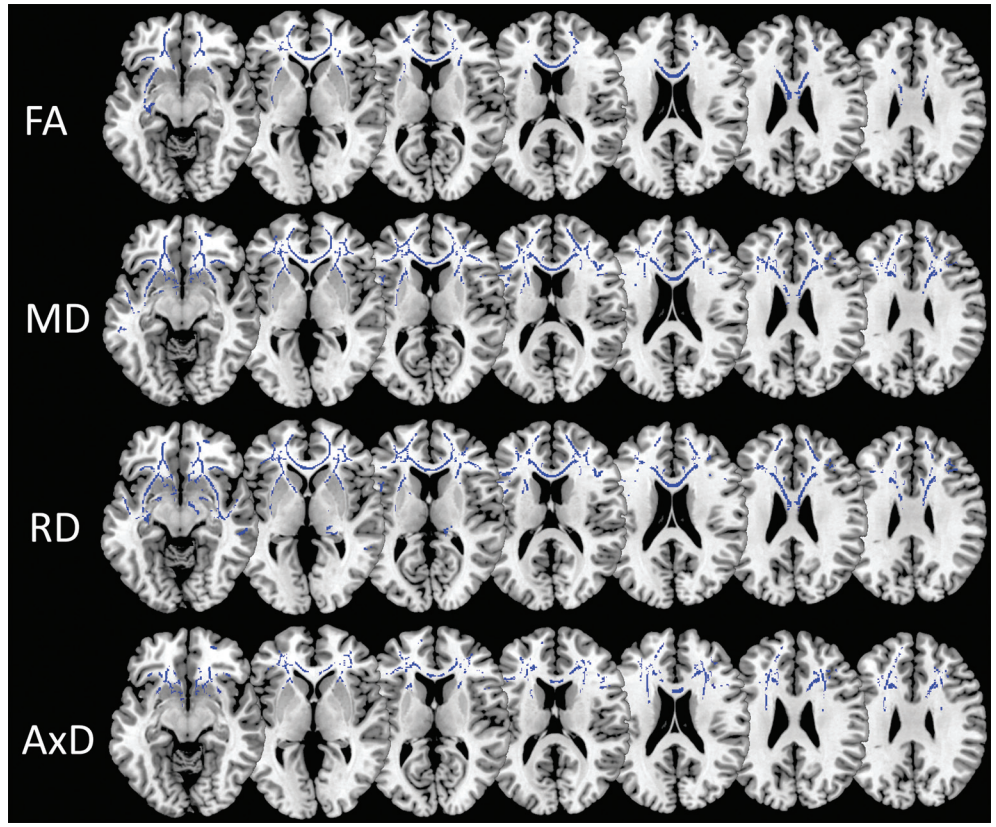

Figure 4. Post-hoc t-test microstructural white matter changes for bvFTD in comparison with phFTD ($p_{corrected}$<0.05; k≥20). Lower FA and higher MD, RD and AxD in bvFTD are shown in blue.
PhFTD = phenocopy frontotemporal dementia, bvFTD = behavioural variant FTD, FA = fractional anisotropy, MD = mean diffusivity, RD = radial diffusivity, AxD = axial diffusivity.

Table 3A. Post-hoc two sample t-tests ($p_{corrected}$<0.05; k≥20) of group differences in FA between phFTD, bvFTD and controls.
FA = fractional anisotropy, phFTD = phenocopy frontotemporal dementia, bvFTD = behavioural variant frontotemporal dementia, HC = healthy controls, L = left, R = right.

T-stat	Number of clusters	Total number of voxels	Number of voxels within largest cluster	Anatomical regions within largest cluster
phFTD<HC	28	14,084	4,644	Forceps minor Genu of the corpus callosum L, R Body of the corpus callosum L, R Inferior fronto-occipital fasciculus L, R Anterior thalamic radiation L, R Cingulum L, R Uncinate fasciculus L, R
bvFTD<HC	12	31,220	29,598	Forceps minor Forceps major Genu of the corpus callosum L, R Body of the corpus callosum L, R Splenium of the corpus callosum L, R Inferior fronto-occipital fasciculus L, R Anterior thalamic radiation L, R Cingulum L, R Uncinate fasciculus L, R Inferior longitudinal fasciculus L, R Superior longitudinal fasciculus L, R
bvFTD<phFTD	4	8,025	7,777	Forceps minor Genu of the corpus callosum L, R Body of the corpus callosum L, R Inferior fronto-occipital fasciculus L, R Anterior thalamic radiation L, R Cingulum L, R Uncinate fasciculus L, R

Table 3B. Post-hoc two sample t-tests ($p_{corrected}$<0.05; k≥20) of group differences in MD between phFTD, bvFTD and controls.
MD = mean diffusivity, phFTD = phenocopy frontotemporal dementia, bvFTD = behavioural variant frontotemporal dementia, HC = healthy controls, L = left, R = right.

T-stat	Number of clusters	Total number of voxels	Number of voxels within largest cluster	Anatomical regions within largest cluster
phFTD>HC	5	1,686	883	Anterior thalamic radiation L, R Inferio fronto-occipital fasciculus L, R Superior longitudinal fasciculus L, R
bvFTD>HC	14	39,036	37,066	Forceps minor Forceps major Genu of the corpus callosum L, R Body of the corpus callosum L, R Splenium of the corpus callosum L, R Inferior fronto-occipital fasciculus L, R Anterior thalamic radiation L, R Cingulum L, R Uncinate fasciculus L, R Inferior longitudinal fasciculus L, R Superior longitudinal fasciculus L, R
bvFTD>phFTD	4	19,769	19,586	Forceps minor Genu of the corpus callosum L, R Body of the corpus callosum L, R Inferior fronto-occipital fasciculus L, R Anterior thalamic radiation L, R Cingulum L, R Uncinate fasciculus L, R Inferior longitudinal fasciculus L Superior longitudinal fasciculus L, R

Table 3C. Post-hoc two sample t-tests ($p_{corrected}$<0.05; k≥20) of group differences in RD between phFTD, bvFTD and controls.
RD = radial diffusivity, phFTD = phenocopy frontotemporal dementia, bvFTD = behavioural variant frontotemporal dementia, HC = healthy controls, L = left, R = right.

T-stat	Number of clusters	Total number of voxels	Number of voxels within largest cluster	Anatomical regions within largest cluster
phFTD>HC	9	7,963	6,137	Forceps minor Forceps major Inferior fronto-occipital fasciculus R Anterior thalamic radiation R Cingulum R Uncinate fasciculus R Inferior longitudinal fasciculus R Superior longitudinal fasciculus R
bvFTD>HC	16	46,485	45,111	Forceps minor Forceps major Genu of the corpus callosum L, R Body of the corpus callosum L, R Splenium of the corpus callosum L, R Inferior fronto-occipital fasciculus L, R Anterior thalamic radiation L, R Cingulum L, R Uncinate fasciculus L, R Inferior longitudinal fasciculus L, R Superior longitudinal fasciculus L, R
bvFTD>phFTD	6	22,230	21,946	Forceps minor Genu of the corpus callosum L, R Body of the corpus callosum L, R Inferior fronto-occipital fasciculus L, R Anterior thalamic radiation L, R Cingulum L, R Uncinate fasciculus L, R Inferior longitudinal fasciculus L, R Superior longitudinal fasciculus L, R

Table 3D. Post-hoc two sample t-tests ($p_{corrected}$<0.05; k≥20) of group differences in AxD between phFTD, bvFTD and controls.
AxD = axial diffusivity, phFTD = phenocopy frontotemporal dementia, bvFTD = behavioural variant frontotemporal dementia, HC = healthy controls, L = left, R = right.

T-stat	Number of clusters	Total number of voxels	Number of voxels within largest cluster	Anatomical regions within largest cluster
phFTD>HC	0	n/a	n/a	n/a
bvFTD>HC	3	18,269	17,552	Forceps minor Genu of the corpus callosum L, R Body of the corpus callosum L, R Inferior fronto-occipital fasciculus L, R Anterior thalamic radiation L, R Cingulum L Uncinate fasciculus L, R Superior longitudinal fasciculus L, R
bvFTD>phFTD	8	11,202	10,396	Forceps minor Genu of the corpus callosum L, R Body of the corpus callosum L, R Inferior fronto-occipital fasciculus L, R Anterior thalamic radiation L, R Uncinate fasciculus L, R Superior longitudinal fasciculus L, R

DISCUSSION

To the best of our knowledge, this is the first study demonstrating functional connectivity changes and microstructural white matter abnormalities in phFTD. There was increased DMN connectivity in nearly all regions of the DMN, and abnormal microstructural white matter in frontal and temporoparietal lobes. These changes were similar to the changes observed in bvFTD, supporting our hypothesis that phFTD belongs to the same disease spectrum as bvFTD. Specifically, bvFTD also showed higher connectivity in DMN regions, but to a lesser extent than in phFTD, and microstructural white matter abnormalities in the frontal and temporoparietal lobes, but more pronounced than in phFTD.

DMN connectivity was increased, albeit to a moderate extent, in both phFTD and bvFTD. As there are overt behavioural symptoms in phFTD, as well as frequent neuropsychological abnormalities, it is not surprising to observe functional brain abnormalities. Increased functional connectivity reflects changes in neuronal activity becoming more congruent between regions. This may point to a brain mechanism compensating for early diminished neuronal functioning [39-41]. The degree of increased connectivity may reflect the brain's remaining ability of compensation, ultimately reversing to decreased connectivity as neuronal dysfunctioning progresses. This theory may explain why we observe higher connectivity in phFTD than in bvFTD. As pronounced cortical atrophy is evident in bvFTD but not in phFTD [1,11-13], neuronal dysfunctioning is likely much more prominent in bvFTD. This means that more relatively preserved neurons in phFTD may be able to provide a better functioning compensational mechanism than in bvFTD. The observation that the inferior parietal lobule showed both increased and decreased (depending on its subregion) functional connectivity in bvFTD in comparison with controls, is in line with this view. It is plausible that the various subregions of the inferior parietal lobule are not affected to the same extent in bvFTD, resulting in decreased functional connectivity in the more affected subregion and in increased functional connectivity in the less affected subregion.

Frontotemporal and parietal microstructural white matter abnormalities were observed in both phFTD and bvFTD. In phFTD, FA was decreased (i.e. there was less directional diffusion) and RD and MD were increased (i.e. there was more diffusion, particularly perpendicular to the tract's axis) in multiple white matter tracts, including the cingulum, UF, IFOF, genu of the CC and SLF. Damage to these white matter tracts has been linked to the various cognitive functions typically affected in bvFTD. Loss of behavioural control (e.g. disinhibition) has been related to diffusion changes in the UF, forceps minor and cingulum [42-44]. Additionally, abnormalities in executive functioning, visuo-spatial attention, working memory [45] and apathy have also been linked with diffusivity changes in the cingulum [45-47]. Interestingly, RD changes in these tracts were less pronounced than FA changes, which may be explained by FA being a composite measure of both RD and AxD (i.e. diffusion along the tract's main axis), and therefore more sensitive to subtle myelin and/or axonal changes, reflected by changes in RD [48] and AxD [49] respectively. In phFTD, AxD abnormalities were not observed, which may be explained by myelin damage only, without axonal injury. In bvFTD, white matter changes were more pronounced and widespread, with lower FA, and higher MD, RD and AxD than in phFTD. Hence, here we show an association in phFTD, similar to bvFTD, between symptomatology and damage to the frontotemporal and parietal white matter tracts. Additionally, we show differences possibly reflecting neuropathological changes between phFTD and bvFTD, with phFTD suggesting myelin damage only, and bvFTD showing more pronounced myelin and axonal damage.

Previous literature has shown a relationship between microstructural white matter changes and functional connectivity changes [50-53], and proposes that microstructural white matter predicts, or is reflected by, functional connectivity [50,52,53]. For example, the medial prefrontal cortex and posterior cingulate cortex, core regions of the DMN, are connected through the cingulum [52]. Cingulum abnormalities such as observed in this study may have – to a certain extent – disconnected these regions, reducing functional connectivity between anterior and posterior DMN regions. In support of this idea, there were more pronounced anterior white matter abnormalities in bvFTD that extended more posteriorly than in phFTD, and both frontal and parietal functional connectivity were seen to be correspondingly lower. A recent study by Weiler et al. (2014) [54] observed that higher RD in the cingulum and parahippocampal bundle (both connecting DMN regions) predicted reduced performance on measures related to DMN cognitive functions. We therefore postulate that more advanced abnormalities of white matter tracts of the DMN will eventually lead to a functional decrease in the associated DMN areas and result in reduced cognitive functioning.

Overall, phFTD showed functional connectivity and subtle white matter changes, whereas bvFTD showed fewer functional connectivity and more extensive white matter changes. These findings are indicative of incipient degeneration in phFTD. In order to investigate phFTD without the interference of an alternative diagnosis we ruled out alternative psychiatric disorders, neuropsychological progression and presence of the C9orf72 mutation. The observed incipient brain changes in this well-defined population are in favour of the controversial notion that phFTD and bvFTD belong to the same disease spectrum. PhFTD presents with behavioural, neuropsychological and, as shown here, also neurodegenerative changes that are all similar to those observed in bvFTD.

This study has some limitations. First, we were only able to investigate a small number of phFTD and bvFTD patients, limiting statistical power. As a result, rs-fMRI effects, expected to be subtle, were only detectable using a relatively lenient statistical threshold. The sample size is inherent to the rarity of the syndrome, together with the application of strict inclusion and exclusion criteria to avoid inadvertent inclusion of patients with bvFTD or alternative psychiatric disorders. Second, the bvFTD group was not fully matched for gender with the phFTD and control group. There is no conclusive evidence on gender differences in functional connectivity [55] or microstructural white matter. Both higher and lower FA was measured in the cingulum and in the white matter underlying the frontal cortex in men and in women compared with the opposite gender [56]. Given these findings it is not likely that the FA decreases observed in this study were driven by gender differences. Third, the bvFTD group and part of the control group were scanned on a different scanner, although of identical type and field strength, and

with identical protocols. While a scanner effect cannot be excluded, both rs-fMRI and DTI have been shown to be highly reproducible in terms of DMN functional connectivity and TBSS respectively, even across different scanner platforms and vendors (57, 58). Moreover, the fact that our findings in bvFTD are consistent with the previous literature suggest that the effect of scanner is likely to be minimal.

In conclusion, our findings are in support of the hypothesis that phFTD belongs to the same disease spectrum as bvFTD. In phFTD, there are changes in functional connectivity and microstructural white matter that are similar to those found in bvFTD. Advanced MRI techniques, such as rs-fMRI and DTI, would therefore be suited to improve diagnosis of phFTD by identifying such incipient changes. Our future efforts are aimed at shedding further light on the development of the observed brain changes using long-term follow-up of these patients.

REFERENCES

1. Davies RR, Kipps CM, Mitchell J, Kril JJ, Halliday GM, Hodges JR. Progression in frontotemporal dementia: identifying a benign behavioral variant by magnetic resonance imaging. Arch Neurol. 2006;63: 1627-1631.
2. Hornberger M, Shelley BP, Kipps CM, Piguet O, Hodges JR. Can progressive and non-progressive behavioural variant frontotemporal dementia be distinguished at presentation? J Neurol Neurosurg Psychiatr. 2009;80: 591-593.
3. Bertoux M, de Souza LC, Corlier F, Lamari F, Bottlaender M, Dubois B, et al. Two distinct amnesic profiles in behavioral variant frontotemporal dementia. Biol Psychiatry. 2014;75: 582-588.
4. Hornberger M, Piguet O, Graham AJ, Nestor PJ, Hodges JR. How preserved is episodic memory in behavioral variant frontotemporal dementia? Neurology. 2010;74: 472-479.
5. Hornberger M, Piguet O, Kipps C, Hodges JR. Executive function in progressive and nonprogressive behavioral variant frontotemporal dementia. Neurology. 2008;71: 1481-1488.
6. Irish M, Graham A, Graham KS, Hodges JR, Hornberger M. Differential impairment of source memory in progressive versus non-progressive behavioral variant frontotemporal dementia. Arch Clin Neuropsychol. 2012;27: 338-347.
7. Mioshi E, Hodges JR. Rate of change of functional abilities in frontotemporal dementia. Dement Geriatr Cogn Disord. 2009;28: 419-426.
8. Pennington C, Hodges JR, Hornberger M. Neural correlates of episodic memory in behavioral variant frontotemporal dementia. J Alzheimers Dis. 2011;24: 261-268.
9. Mioshi E, Kipps CM, Hodges JR. Activities of daily living in behavioral variant frontotemporal dementia: differences in caregiver and performance-based assessments. Alzheimer Dis Assoc Disord. 2009;23: 70-76.
10. Garcin B, Lillo P, Hornberger M, Piguet O, Dawson K, Nestor PJ, et al. Determinants of survival in behavioral variant frontotemporal dementia. Neurology. 2009;73: 1656-1661.
11. Kipps CM, Davies RR, Mitchell J, Kril JJ, Halliday GM, Hodges JR. Clinical significance of lobar atrophy in frontotemporal dementia: application of an MRI visual rating scale. Dement Geriatr Cogn Disord. 2007;23: 334-342.
12. Rosen HJ, Gorno-Tempini ML, Goldman WP, Perry RJ, Schuff N, Weiner M, et al. Patterns of brain atrophy in frontotemporal dementia and semantic dementia. Neurology. 2002;58: 198-208.
13. Seeley WW, Crawford R, Rascovsky K, Kramer JH, Weiner M, Miller BL, et al. Frontal paralimbic network atrophy in very mild behavioral variant frontotemporal dementia. Arch Neurol. 2008;65: 249-255.
14. Kipps CM, Hodges JR, Fryer TD, Nestor PJ. Combined magnetic resonance imaging and positron emission tomography brain imaging in behavioural variant frontotemporal degeneration: refining the clinical phenotype. Brain. 2009;132: 2566-2578.
15. Khan BK, Yokoyama JS, Takada LT, Sha SJ, Rutherford NJ, Fong JC, et al. Atypical, slowly progressive behavioural variant frontotemporal dementia associated with C9ORF72 hexanucleotide expansion. J Neurol Neurosurg Psychiatry. 2012;83: 358-364.
16. Whitwell JL, Josephs KA, Avula R, Tosakulwong N, Weigand SD, Senjem ML, et al. Altered functional connectivity in asymptomatic MAPT subjects: a comparison to bvFTD. Neurology. 2011;77: 866-874.
17. Zhou J, Greicius MD, Gennatas ED, Growdon ME, Jang JY, Rabinovici GD, et al. Divergent network connectivity changes in behavioural variant frontotemporal dementia and Alzheimer's disease. Brain. 2010;133: 1352-1367.
18. Trojsi F, Esposito F, de Stefano M, Buonanno D, Conforti FL, Corbo D, et al. Functional overlap and divergence between ALS and bvFTD. Neurobiol Aging. 2015;36: 413-423.

19. Rytty R, Nikkinen J, Paavola L, Abou Elseoud A, Moilanen V, Visuri A, et al. GroupICA dual regression analysis of resting state networks in a behavioral variant of frontotemporal dementia. Front Hum Neurosci. 2013;7: 461.
20. Dopper EG, Rombouts SA, Jiskoot LC, den Heijer T, de Graaf JR, de Koning I, et al. Structural and functional brain connectivity in presymptomatic familial frontotemporal dementia. Neurology. 2014;83: e19-26.
21. Mahoney CJ, Ridgway GR, Malone IB, Downey LE, Beck J, Kinnunen KM, et al. Profiles of white matter tract pathology in frontotemporal dementia. Hum Brain Mapp. 2014;35: 4163-4179.
22. Rascovsky K, Hodges JR, Knopman D, Mendez MF, Kramer JH, Neuhaus J, et al. Sensitivity of revised diagnostic criteria for the behavioural variant of frontotemporal dementia. Brain. 2011;134: 2456-2477.
23. Folstein MF, Folstein SE, McHugh PR. "Mini-mental state". A practical method for grading the cognitive state of patients for the clinician. J Psychiatr Res. 1975;12: 189-198.
24. Overall JE, Gorham DR. The brief psychiatric rating scale. Psychol Rep. 1962;10: 799-812.
25. Dingemans P. Vertaling en bewerking: Uitgebreide BPRS handleiding, Los Angeles Project. Amsterdam: Psychiatrisch Centrum AZUA; 1986.
26. Bron EE, Steketee RME, Houston GC, Oliver RA, Achterberg HC, Loog M, et al. Diagnostic classification of arterial spin labeling and structural MRI in presenile early stage dementia. Hum Brain Mapp. 2014;35: 4916-4931.
27. Jenkinson M, Beckmann CF, Behrens TE, Woolrich MW, Smith SM. Fsl. Neuroimage. 2012;62: 782-790.
28. Woolrich MW, Jbabdi S, Patenaude B, Chappell M, Makni S, Behrens T, et al. Bayesian analysis of neuroimaging data in FSL. Neuroimage. 2009;45: S173-86.
29. Smith SM, Jenkinson M, Woolrich MW, Beckmann CF, Behrens TE, Johansen-Berg H, et al. Advances in functional and structural MR image analysis and implementation as FSL. Neuroimage. 2004;23 Suppl 1: S208-19.
30. Smith SM. Fast robust automated brain extraction. Hum Brain Mapp. 2002;17: 143-155.
31. Jenkinson M, Bannister P, Brady M, Smith S. Improved optimization for the robust and accurate linear registration and motion correction of brain images. Neuroimage. 2002;17: 825-841.
32. Filippini N, MacIntosh BJ, Hough MG, Goodwin GM, Frisoni GB, Smith SM, et al. Distinct patterns of brain activity in young carriers of the APOE-epsilon4 allele. Proc Natl Acad Sci U S A. 2009;106: 7209-7214.
33. Beckmann CF, DeLuca M, Devlin JT, Smith SM. Investigations into resting-state connectivity using independent component analysis. Philos Trans R Soc Lond B Biol Sci. 2005;360: 1001-13.
34. Winkler AM, Ridgway GR, Webster MA, Smith SM, Nichols TE. Permutation inference for the general linear model. Neuroimage. 2014;92: 381-397.
35. Smith SM, Nichols TE. Threshold-free cluster enhancement: addressing problems of smoothing, threshold dependence and localisation in cluster inference. Neuroimage. 2009;44: 83-98.
36. Leemans A, Jeurissen B, Sijbers J, Jones D. ExploreDTI: a graphical toolbox for processing, analyzing, and visualizing diffusion MR data. Proceedings 17th Scientific Meeting, International Society for Magnetic Resonance in Medicine. 2009;17: 3537.
37. Behrens TE, Woolrich MW, Jenkinson M, Johansen-Berg H, Nunes RG, Clare S, et al. Characterization and propagation of uncertainty in diffusion-weighted MR imaging. Magn Reson Med. 2003;50: 1077-1088.
38. Smith SM, Jenkinson M, Johansen-Berg H, Rueckert D, Nichols TE, Mackay CE, et al. Tract-based spatial statistics: voxelwise analysis of multi-subject diffusion data. Neuroimage. 2006;31: 1487-1505.

39. Borroni B, Alberici A, Cercignani M, Premi E, Serra L, Cerini C, et al. Granulin mutation drives brain damage and reorganization from preclinical to symptomatic FTLD. Neurobiol Aging. 2012;33: 2506-2520.
40. Barkhof F, Haller S, Rombouts SA. Resting-state functional MR imaging: a new window to the brain. Radiology. 2014;272: 29-49.
41. Bookheimer SY, Strojwas MH, Cohen MS, Saunders AM, Pericak-Vance MA, Mazziotta JC, et al. Patterns of brain activation in people at risk for Alzheimer's disease. N Engl J Med. 2000;343: 450-456.
42. Hornberger M, Geng J, Hodges JR. Convergent grey and white matter evidence of orbitofrontal cortex changes related to disinhibition in behavioural variant frontotemporal dementia. Brain. 2011;134: 2502-2512.
43. Whitwell JL, Avula R, Senjem ML, Kantarci K, Weigand SD, Samikoglu A, et al. Gray and white matter water diffusion in the syndromic variants of frontotemporal dementia. Neurology. 2010;74: 1279-1287.
44. Agosta F, Scola E, Canu E, Marcone A, Magnani G, Sarro L, et al. White matter damage in frontotemporal lobar degeneration spectrum. Cereb Cortex. 2012;22: 2705-2714.
45. Tartaglia MC, Zhang Y, Racine C, Laluz V, Neuhaus J, Chao L, et al. Executive dysfunction in frontotemporal dementia is related to abnormalities in frontal white matter tracts. J Neurol. 2012;259: 1071-1080.
46. Tovar-Moll F, de Oliveira-Souza R, Bramati IE, Zahn R, Cavanagh A, Tierney M, et al. White matter tract damage in the behavioral variant of frontotemporal and corticobasal dementia syndromes. PLoS One. 2014;9: e102656.
47. Lu PH, Lee GJ, Shapira J, Jimenez E, Mather MJ, Thompson PM, et al. Regional differences in white matter breakdown between frontotemporal dementia and early-onset Alzheimer's disease. J Alzheimers Dis. 2014;39: 261-269.
48. Song SK, Sun SW, Ramsbottom MJ, Chang C, Russell J, Cross AH. Dysmyelination revealed through MRI as increased radial (but unchanged axial) diffusion of water. Neuroimage. 2002;17: 1429-1436.
49. Song SK, Sun SW, Ju WK, Lin SJ, Cross AH, Neufeld AH. Diffusion tensor imaging detects and differentiates axon and myelin degeneration in mouse optic nerve after retinal ischemia. Neuroimage. 2003;20: 1714-1722.
50. Schmidt R, Verstraete E, de Reus MA, Veldink JH, van den Berg LH, van den Heuvel MP. Correlation between structural and functional connectivity impairment in amyotrophic lateral sclerosis. Hum Brain Mapp. 2014;35: 4386-4395.
51. Damoiseaux JS, Greicius MD. Greater than the sum of its parts: a review of studies combining structural connectivity and resting-state functional connectivity. Brain Struct Funct. 2009;213: 525-533.
52. Greicius MD, Supekar K, Menon V, Dougherty RF. Resting-state functional connectivity reflects structural connectivity in the default mode network. Cereb Cortex. 2009;19: 72-78.
53. Honey CJ, Sporns O, Cammoun L, Gigandet X, Thiran JP, Meuli R, et al. Predicting human resting-state functional connectivity from structural connectivity. Proc Natl Acad Sci U S A. 2009;106: 2035-2040.
54. Weiler M, de Campos BM, Nogueira MH, Pereira Damasceno B, Cendes F, Balthazar ML. Structural connectivity of the default mode network and cognition in Alzheimers disease. Psychiatry Res. 2014;223: 15-22.
55. Weissman-Fogel I, Moayedi M, Taylor KS, Pope G, Davis KD. Cognitive and default-mode resting state networks: do male and female brains "rest" differently? Hum Brain Mapp. 2010;31: 1713-1726.

56. Gong G, He Y, Evans AC. Brain connectivity: gender makes a difference. Neuroscientist. 2011;17: 575-591.
57. Jovicich J, Minati L, Marizzoni M, Marchitelli R, Sala-Llonch R, Bartres-Faz D, et al. Longitudinal reproducibility of default-mode network connectivity in healthy elderly participants: A multicentric resting-state fMRI study. Neuroimage. 2015;124: 442-454.
58. Jovicich J, Marizzoni M, Bosch B, Bartres-Faz D, Arnold J, Benninghoff J, et al. Multisite longitudinal reliability of tract-based spatial statistics in diffusion tensor imaging of healthy elderly subjects. Neuroimage. 2014;101: 390-403.

Chapter 4

Vendor-specific features of arterial spin labeling MRI

Chapter 4.1

Inter-vendor reproducibility of pseudo-continuous arterial spin labeling at 3 Tesla

Henk Jan M.M. Mutsaerts
Rebecca M.E. Steketee
Dennis F.R.Heijtel
Joost P.A. Kuijer
Matthias J.P. van Osch
Charles B.L.M. Majoie
Marion Smits
Aart J. Nederveen

PLoS One. 2014;9:e104108

ABSTRACT

Purpose Prior to the implementation of arterial spin labeling (ASL) in clinical multi-center studies, it is important to establish its status quo inter-vendor reproducibility. This study evaluates and compares the intra- and inter-vendor reproducibility of pseudo-continuous ASL (pCASL) as clinically implemented by GE and Philips.

Material and Methods 22 healthy volunteers were scanned twice on both a 3T GE and a 3T Philips scanner. The main difference in implementation between the vendors was the readout module: spiral 3D fast spin echo vs. 2D gradient-echo echo-planar imaging respectively. Mean and variation of cerebral blood flow (CBF) were compared for the total gray matter (GM) and white matter (WM), and on a voxel-level.

Results Whereas the mean GM CBF of both vendors was almost equal (p=1.0), the mean WM CBF was significantly different (p<0.01). The inter-vendor GM variation did not differ from the intra-vendor GM variation (p=0.3 and p=0.5 for GE and Philips respectively). Spatial inter-vendor CBF and variation differences were observed in several GM regions and in the WM.

Conclusion These results show that total GM CBF-values can be exchanged between vendors. For the inter-vendor comparison of GM regions or WM, these results encourage further standardization of ASL implementation among vendors.

INTRODUCTION

Arterial spin labeling (ASL) is an emerging magnetic resonance imaging (MRI) perfusion modality that enables non-invasive cerebral perfusion measurements. Since ASL is virtually harmless, not hampered by the blood-brain barrier and enables absolute quantification of cerebral blood flow (CBF), it is an attractive tool compared to other perfusion imaging modalities [1,2]. Through several methodological advances, ASL perfusion MRI has matured to the point where it can provide high quality whole-brain perfusion images in only a few minutes of scanning [3]. Its reproducibility has been established and its CBF-maps are comparable with imaging methods based on exogenous tracers [4-7]. ASL is commercially available on all major MRI systems and clinical applications are under rapid development. ASL-based CBF measurements are of clinical value in a number of cerebral pathologies, such as brain tumors, cerebrovascular pathology, epilepsy and neurodegeneration [8,9]. Therefore, the initiation of large-scale multi-center ASL studies is a next step to extend our understanding of the pathophysiology of many common disorders.

However, it is essential to first establish the inter-vendor reproducibility of ASL [10,11]. One main obstacle that impedes multi-center studies, is that fundamental differences exist between ASL implementations of different vendors. Each MRI vendor has implemented a different labeling-readout combination, which may seriously hamper the comparison of multi-vendor ASL-data [12]. Since each labeling and readout strategy exhibits specific advantages and disadvantages, a substantial technical heterogeneity is introduced [13]. Therefore, it remains unclear to which degree ASL-based CBF-maps from centers with scanners of different vendors are comparable. The aim of the current study is to assess and compare the intra- and inter-vendor reproducibility of pseudo-continuous ASL (pCASL) CBF measurements as currently clinically implemented by two major vendors: i.e. GE and Philips.

MATERIALS AND METHODS

Subject recruitment and study design

Twenty-two healthy volunteers (9 men, 13 women, mean age 22.6 ± 2.1 (SD) years) were included. In addition to standard MRI exclusion criteria, subjects with history of brain or psychiatric disease or use of medication - except for oral contraceptives - were excluded. No consumption of vasomotor substances such as alcohol, cigarettes, coffee, licorice and tea was allowed on the scan days. On the day prior to the examination, alcohol and nicotine consumption was restricted to three units and cigarettes respectively.

All subjects were scanned twice at two academic medical centers in the Netherlands: Erasmus MC – University Medical Center Rotterdam (center 1) and Academic Medical Center Amsterdam (center 2). The inter-session time interval was kept at 1-4 weeks. MRI experiments were performed on a 3T GE scanner at cen-

ter 1 (Discovery MR750, GE Healthcare, Milwaukee, WI, US) and on a 3T Philips scanner at center 2 (Intera, Philips Healthcare, Best, the Netherlands), both equipped with an 8-channel head coil (InVivo, Gainesville, FL, US). Foam padding inside the head coil was used to restrict head motion during scanning [10]. Subjects were awake and had their eyes closed during all ASL scans. All subjects provided written informed consent and the study was approved by the ethical review boards of both centers.

Acquisition

Each scan session included a pCASL and 1 mm isotropic 3D T1-weighted scan for segmentation and registration purposes. For the acquisition of a single time-point CBF-map, pCASL has become the prefer.ed labeling strategy because of its relatively high signal-to-noise ratio (SNR) and wide availability across all platforms [3,14]. On both scanners we employed the clinically implemented pCASL protocols that are currently used in clinical studies [15,16]. Table 1 and Figure 1 summarize the protocol details and show the timing diagrams for both sequences respectively. The main difference between the GE and Philips implementations was the readout module: multi-shot spiral 3D fast spin-echo vs. single-shot 2D gradient-echo echo-planar imaging respectively.

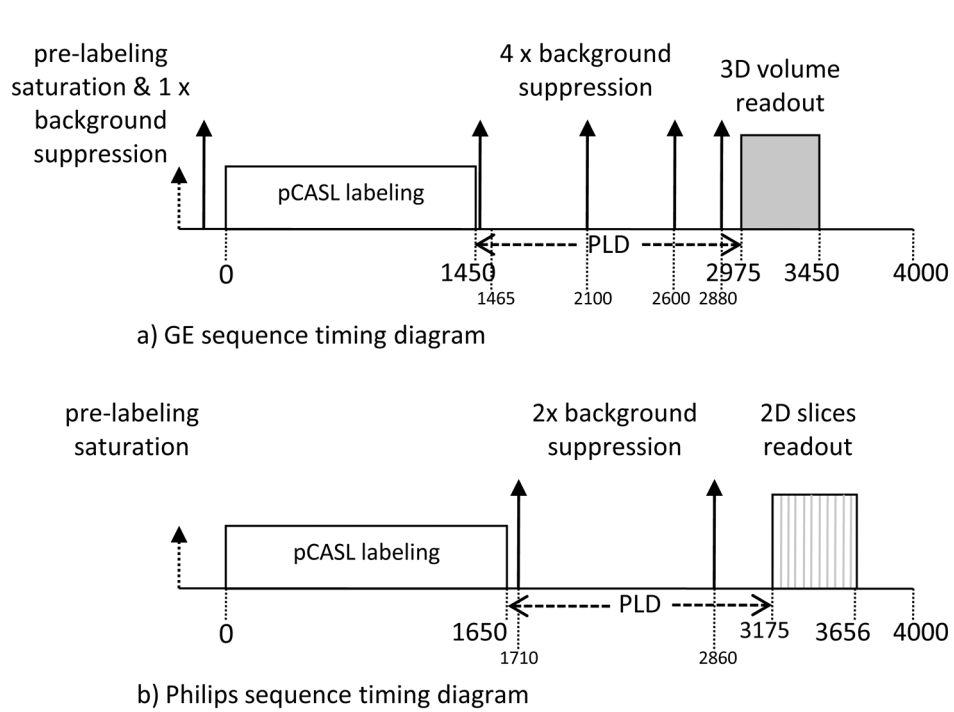

Figure 1. Sequence timing diagrams of a) General Electric (GE) and b) Philips, shown at the same time scale (ms). pCASL = pseudo-continuous arterial spin labeling, PLD = post-labeling delay.

Table 1. Acquisition protocols

	GE	Philips
Labeling module	pseudo-continuous	pseudo-continuous
Labeling pulse shape	Hanning	Hanning
Labeling pulse duration	0.5 ms	0.5 ms
Labeling pulse flip angle	23°	18°
Mean gradient strength	0.7 mT/m	0.6 mT/m
Maximal gradient strength	7 mT/m	6 mT/m
Labeling duration	1450 ms	1650 ms
Post-labeling delay (PLD) (initial)	1525 ms	1525 ms
PLD increase per slice	n.a.	28.3 ms
PLD (average)	1525 ms	1770 ms
Labeling plane planning	Fixed 22 mm below lower edge	89 mm below, parallel to AC-PC line
Labeling plane distance*	72 mm	89 mm
Readout module	3D fast spin-echo interleaved stack-of-spirals	2D gradient-echo single-shot echo-planar imaging
		SENSE 2.5, CLEAR
Acquisition matrix	8 spirals x 512 sampling points	80 x 80
Field of view	24 cm^3	24 cm^2
Number of slices	36	17

Slice thickness	4 mm	7 mm
Acquisition voxel size (volume)	3.8 x 3.8 x 4 mm (57.8 mm^3)	3.0 x 3.0 x 7.0 mm (63 mm^3)
Reconstruction voxel size	1.9 x 1.9 x 4.0 mm	3.0 x 3.0 x 7.0 mm
Slice gap	n.a.	0 mm
Echo time/repetition time	10.5/4600 ms	17/4000 ms
Number of signal averages	3	33
Readout planning	True axial, lower edge fixed at lower boundary pons	Parallel to AC-PC line
Background suppression (n pulses)	yes (5)	yes (2)
Vascular crushing	no	no
Acquisition duration	4:29 min	4:33 min

*Labeling plane distance represents distance from the anterior commissure-posterior commissure (ACPC) line in the head-feet direction [20]. n.a. = not applicable

Post-processing: quantification

Matlab 7.12.0 (MathWorks, MA, USA) and Statistical Parametric Mapping (SPM) 8 (Wellcome Trust Center for Neuroimaging, University College London, UK) were used for post-processing and statistical analyses. For the Philips data, label and control pCASL images were pair-wise subtracted and averaged to obtain perfusion-weighted images. For the GE data, the perfusion-weighted images as directly provided by the scanner were used. Since the images as provided by GE did not incorporate motion correction, this was not applied to the Philips data. The perfusion-weighted maps of both vendors were quantified into CBF maps using a single compartment model [3,17]:

$$CBF(mL/100g/\min) = \frac{6000\Delta M e^{PLD/T_{1a}}}{2\alpha\alpha_{inv}M_{0a}T_{1a}(1-e^{-\tau/T_{1a}})} \quad (1)$$

where ΔM represents the difference images between control and label and M_{0a} the equilibrium magnetization of arterial blood. In Philips, ΔM was corrected for the transversal magnetization decay time (T_2*) of arterial blood (48 ms) during the 17 ms echo time (TE) by $e^{TE/T2^*}$ [18]. PLD is the post-labeling delay (1.525 s), T_{1a} is the longitudinal relaxation time of arterial blood (1.650 s), α is the labeling efficiency (0.8), where α_{inv} corrects for the decrease in labeling efficiency due to the 5 and 2 background suppression pulses at GE (0.75) and Philips (0.83) respectively and τ represents the labeling duration (1.450 s and 1.650 s for GE and Philips respectively) [19-21]. The increase in label decay in the ascending acquired 2D slices in Philips-data was accounted for. GE has, but Philips has not, implemented a standard M_0-acquisition where proton density maps are obtained with a saturation recovery acquisition using readout parameters identical to the ASL readout. These maps were converted to M_{0a} by the following equation:

$$M_{0a} = \frac{PD}{\lambda_{GM}(1-e^{\frac{-t_{sat}}{T_{1GM}}})} \quad (2)$$

where t_{sat} is the saturation recovery time (2 s), T_{1GM} is the relaxation time of gray matter (GM) tissue (1.2 s) and λ_{GM} is the GM brain-blood water partition coefficient (0.9 mL/g) [15,22,23]. For the Philips data, a single M_{0a}-value was used for all subjects. This value was obtained in a previous study with the same center, scanner, head coil, pCASL protocol and a similar population (n=16, 56% M, age 20-24 years) [24]. In short, cerebrospinal fluid T1 recovery curves were fitted on the control images of multiple time-point pCASL measurements, with the same readout, without background suppression. The acquired M_0 was converted to M_{0a} by multiplication with the blood water partition coefficient (0.76) and the density of brain tissue (1.05 g/mL) [23,25]. No difference was made between the quantification of GM and WM CBF.

Post-processing: spatial normalization

A single 3D T1-weighted anatomical scan from each scanner for each subject (n=44) was segmented into GM and white matter (WM) tissue probability maps. All CBF maps were transformed into anatomical space by a rigid-body registration on the GM tissue probability maps. The tissue probability maps were spatially normalized using the Diffeomorphic Anatomical Registration analysis using Exponentiated Lie algebra (DARTEL) algorithm, and the resulting normalization fields were applied to the CBF maps as well [26]. Finally, all normalized images were spatially smoothed using an 8 x 8 x 8 mm full-width-half-maximum Gaussian kernel, to minimize registration and interpolation errors.

Data analysis

All intra-vendor reproducibility analyses were based on a comparison of session 1 with session 2 within each vendor (n=22). All inter-vendor reproducibility analyses were based on a comparison of GE session 1 with Philips session 2, and GE session 2 with Philips session 1 (n=44). In this way, the temporal physiological variation is expected to have an equal contribution to the intra- and inter-vendor reproducibility. All reproducibility analyses were based on the mean CBF of the two sessions, and on the mean and standard deviation of the paired inter-session CBF difference, denoted as ΔCBF and $SD_{\Delta CBF}$ respectively. The within-subject coefficient of variation (wsCV) - a normalized parameter of variation - was defined as the ratio of $SD_{\Delta CBF}$ to the mean CBF of both sessions:

$$wsCV = 100\% \frac{SD_{\Delta CBF}}{meanCBF} \quad (3)$$

Reproducibility was assessed on a total GM and WM level, and on a voxel-level.

Data analysis: total supratentorial GM and WM

Mean CBF-values of each session were obtained for the total supratentorial GM and WM. GM and WM masks were obtained by thresholding GM and WM probability maps at 70% and 95% tissue probabilities respectively. GM-WM CBF ratios were calculated individually. The significance of paired inter-session CBF differences (ΔCBF) was tested with a paired two-tailed Student's t-test. The Levene's test was used to test the significance of the difference between GE $SD_{\Delta CBF}$ and Philips $SD_{\Delta CBF}$, as well as between the inter-vendor $SD_{\Delta CBF}$ and both intra-vendor $SD_{\Delta CBF\ \{\{\}\}}$[27]. Limits of agreement - defining the range in which 95% of future measurements is expected to lie - were defined as ΔCBF ± 1.96 $SD_{\Delta CBF}$ [28].

Data analysis: voxel-level comparison

To assess spatial inter-vendor differences, CBF- and wsCV-values were computed for each voxel. For CBF, both sessions and all subjects were averaged. To test significant voxel-wise inter-vendor CBF differences, a Bonferroni-corrected paired two-tailed Student's t-test was performed (using both sessions, n=44). Individual histograms of CBF (25 bins, range 0-160 mL/100g/min) were averaged to generate a group-level histogram. A wsCV histogram (25 bins, range 5-45%) was generated from the wsCV-maps. Both CBF and wsCV histograms were generated for the total supratentorial GM and WM of each vendor. Statistical significance was set to $p<0.05$ for all tests.

RESULTS

Session timing

The number of days between intra-vendor sessions did not differ between vendors: 18.3 ± 6.5 and 19.7 ± 7.2 for GE and Philips respectively (independent sample Student's t-test, $p=0.5$). However, GE session 1 and session 2 took place earlier in the day compared to the Philips sessions (15h26 ± 4h00 and 15h55 ± 3h34 compared to 20h16 ± 2h06 and 19h47 ± 2h38 respectively, $p<0.01$).

Total GM and WM

The intra- and inter-vendor statistics are summarized in Table 2 and visualized by the Bland-Altman plots in Figure 2. GM CBF did not differ significantly between both vendors ($p=1.0$), but WM CBF did ($p<0.01$). Likewise, the intra-vendor GM variances of the paired CBF differences did not differ between the two vendors whereas the WM variances did ($p=0.6$ and $p=0.02$ respectively). The GM-WM CBF ratios of both vendors differed significantly, the 2D readout (Philips) GM-

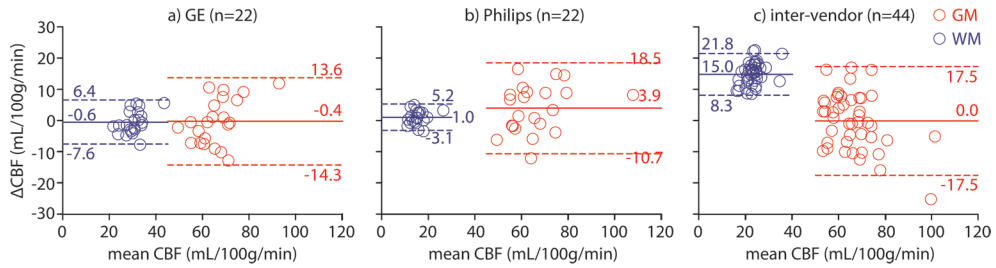

Figure 2. Bland-Altman plots. Intra-vendor a) GE (n=22) and b) Philips (n=22) and c) inter-vendor (n=44) GM (red) and WM (blue) CBF differences are plotted against mean CBF. Continuous and broken lines indicate mean difference and limits of agreement (mean difference ± 1.96 standard deviation of the paired difference) respectively. CBF= cerebral blood flow, GM=gray matter, WM=white matter.

Table 2. Inter-session statistics

	GE	CI (n=22)	Philips	CI (n=22)	inter-vendor	CI (n=44)
GM mean CBF (mL/100g/min)	65.9	48.4 ·· 83.4	65.9	42.0 ·· 89.8	65.9	45.4 ·· 86.4
GM ΔCBF	- 0.4	-3.5 ·· 2.8	3.9	0.6 ·· 7.2	0.0	-2.7 ·· 2.7
GM $SD_{\Delta CBF}$	7.1	4.8 ·· 9.4	7.5	5.1 ·· 9.8	8.9	7.0 ·· 10.9
GM lower LOA	-14.3	-18.2 ··-10.4	-10.7	-14.8 ·· -6.6	-17.5	-20.9 ·· -14.2
GM upper LOA	13.6	9.7 ·· 17.5	18.5	14.4 ·· 22.6	17.5	14.2 ·· 20.9
GM wsCV (%)	10.8	6.2 ··15.3	11.3	5.4 ·· 17.2	13.6	9.8 ·· 17.3
WM mean CBF (mL/100g/min)	30.5	22.0 ··39.0	15.4	9.1 ·· 21.7	22.9	15.6 ·· 30.3
WM ΔCBF	-0.6	-2.2 ·· 1.0	1.0	0.1 ·· 2.0	15.0	14.0 ·· 16.1
WM $SD_{\Delta CBF}$	3.6	2.4 ·· 4.7	2.1	1.4 ·· 2.8	3.5	2.7 ·· 4.2
WM lower LOA	-7.6	-9.6 ·· -5.7	-3.1	-4.3 ·· -2.0	8.3	7.0 ·· 9.6
WM upper LOA	6.4	4.4 ·· 8.3	5.2	4.1 ·· 6.4	21.8	20.5 ·· 23.1
WM wsCV (%)	11.7	9.5 ·· 13.9	13.8	12.2 ·· 15.4	15.0	13.7 ·· 16.4
GM-WM CBF ratio	2.2	1.9 ·· 2.5	4.3	3.4 ·· 5.2	2.9	2.4 ·· 3.4

Mean and ΔCBF represent the inter-session CBF mean and paired difference respectively.
The limits of agreement (LOA) represent ΔCBF ± 1.96 standard deviation of the paired difference ($SD_{\Delta CBF}$).
CI = confidence interval, CBF = cerebral blood flow, GE = General Electric, GM = gray matter,
WM = white matter, wsCV = within-subject coefficient of variation.

WM ratio being approximately twice as large as the ratio of the 3D readout (GE) (p<0.01). Both the GM and WM intra-vendor wsCVs were similar to the inter-vendor wsCVs (Table 2), which is confirmed by the Levene's test. The variance of GM inter-vendor CBF differences did not differ significantly from the variance of intra-vendor differences (p=0.3 and p=0.5 for GE and Philips respectively). For the WM, however, the variance of inter-vendor CBF differences did differ significantly from the Philips variance but not from the GE variance (p=0.02 and p=0.8 respectively).

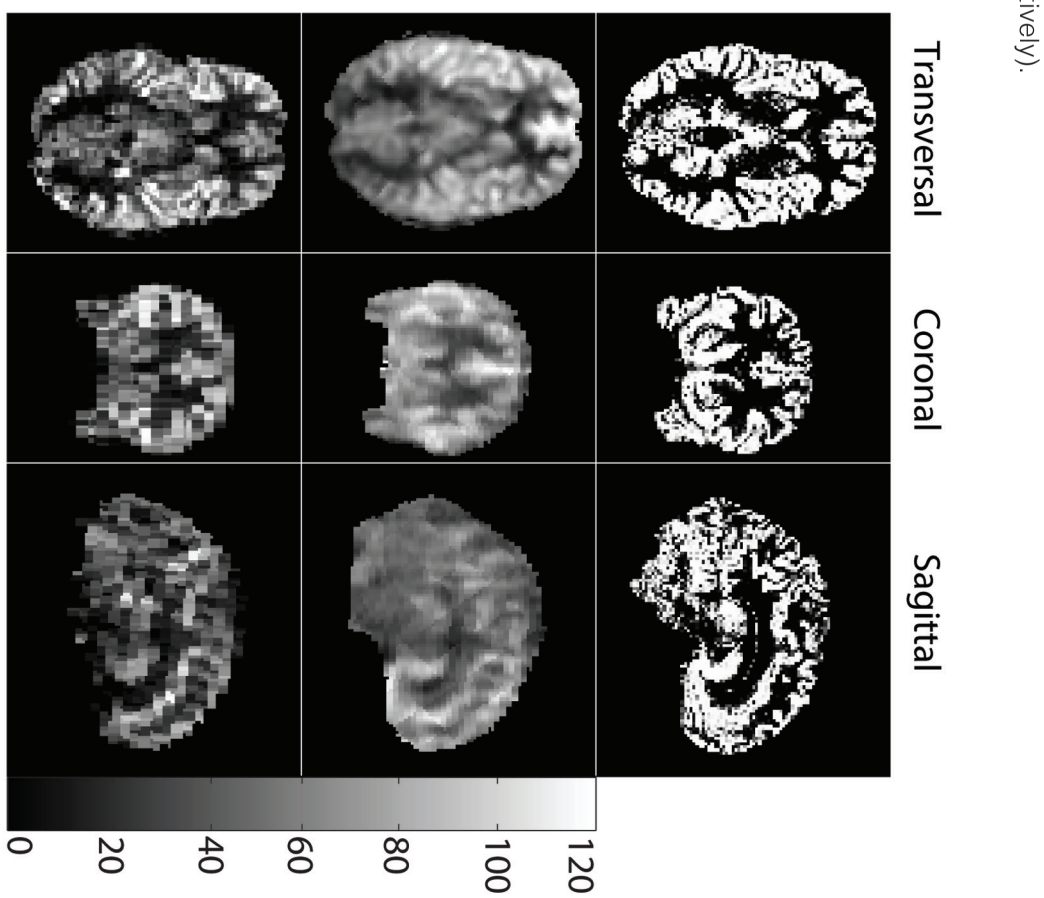

Figure 3. Cerebral blood flow maps of a representative subject of GE (b) and Philips (c), as compared to gray matter (GM) tissue probability map (a; for this example the GE 3D T1-weighted image was used). Maps are registered, re-sliced, skull-stripped and shown in native space.

Voxel-level comparison

Spatial CBF differences between GE and Philips are illustrated for a single subject and on group level in Figure 3 and 4 respectively. The spatial wsCV distribution is shown in Figure 5. In addition, Figure 6 provides an overview of spatial CBF differences between subjects, sessions and vendors for a single transversal slice. The main visual difference on all these maps was the homogeneity of GE compared to the heterogeneity of Philips, especially in the WM and in the z-direction. More specifically, the contrast between GM and WM was higher on the Philips CBF and wsCV-maps. Also within the GM, the CBF was more heterogeneous on the Philips maps compared to the GE maps. A CBF decrease and wsCV increase was observed in the posterior and superior regions on the GE maps and in the anterior-

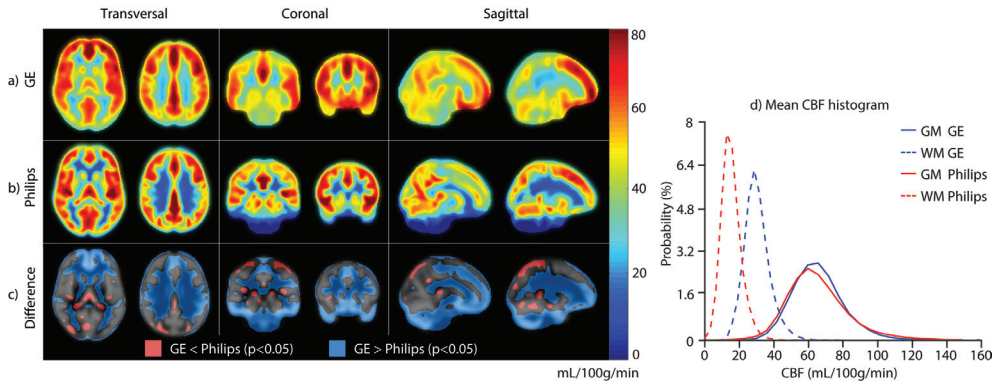

Figure 4. Mean cerebral blood flow (CBF) maps of all subjects (n=22) are shown for GE (a) and Philips (b), averaged for both sessions. Voxel-wise significant inter-vendor differences are visualized by a binary parametric map projected on the gray matter (GM) probability map (c). Red voxels represent where GE < Philips, blue voxels represent where GE > Philips (Bonferroni corrected p<0.05). On the right, mean CBF histograms are shown for the total GM and white matter (WM) (d).

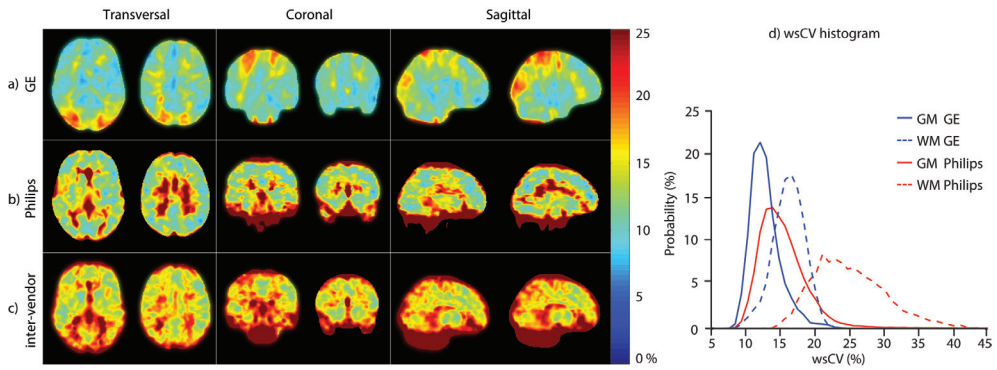

Figure 5. a) GE and b) Philips intra- and c) inter-vendor within-subject coefficient of variability (wsCV)-maps. d) wsCV histograms are shown on the right for the total gray matter (GM) and white matter (WM).

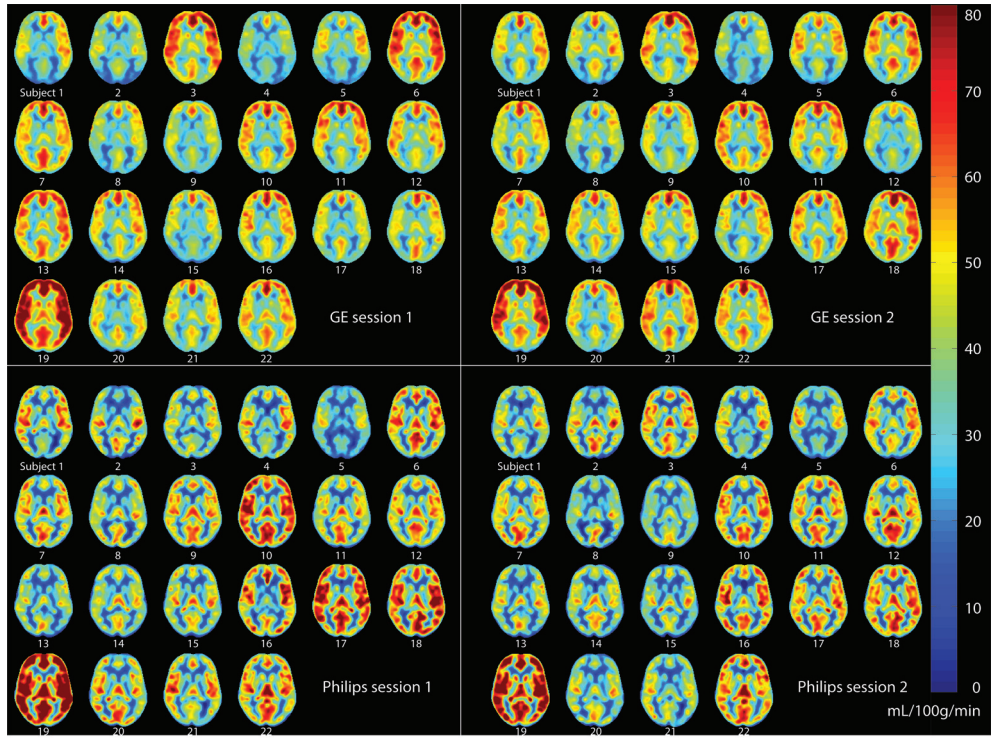

Figure 6. Single transversal cerebral blood flow slice of all subjects (n=22) for GE (upper quadrants) and Philips (lower quadrants), session 1 (left quadrants) and session 2 (right quadrants), after spatial normalization.

inferior and superior regions on the Philips maps. The GM CBF histograms were comparable between vendors (Figure 4d). The GE WM CBF histogram had a higher mean, but had the same shape as the Philips WM CBF histogram. The wsCV histograms, on the other hand, were less comparable (Figure 5d). The spatial GM wsCV distribution of Philips had a higher mean and was wider compared to GE. This difference in mean and spread was even larger for the WM.

DISCUSSION

The most important result of this study is that - despite several voxel-wise differences between vendors - there were no inter-vendor differences in mean CBF or wsCV on a total GM level. This can be explained by the fact that the variation between the sessions can for a large part be attributed to physiological factors, as was previously noted in single-vendor reproducibility studies [11,29-31]. For clinical studies that focus on the GM in total, it may therefore be more important to minimize and account for physiological variation than to account for inter-vendor differences in ASL implementation.

A different picture arises for smaller GM regions or for the total WM. We observed several spatial differences between vendors which can mainly be explained by differences in the readout module. The most visually striking inter-vendor difference on all CBF- and wsCV-maps was in the WM. The GM-WM CBF ratio of the 2D readout (Philips) was twice as large as the ratio of the 3D readout (GE), which is in agreement with a previous readout comparison on a single Siemens scanner [13]. This can be explained by the larger extent of spatial smoothing of a spiral 3D readout (GE) compared to the 2D readout (Philips), which leads to more contamination of the GM signal into the WM and vice versa. Therefore, a 2D readout seems most suitable when the goal is to acquire uncontaminated GM or WM CBF – although the ability of ASL to measure WM CBF is debatable due to the long transit time of WM [32].

This difference in spatial smoothing may also explain the homogeneous GM appearance of the mean CBF and wsCV maps acquired with GE as compared to the more heterogeneous appearance of those acquired with Philips. In addition, it may explain the significant inter-vendor CBF difference within the subcortical GM since this area is surrounded by WM and therefore suffers more from smoothing with WM signal in GE (Figure 4c). Another explanation for the smaller spatial variation of GE, is its higher SNR compared to Philips. The SNR at GE is most probably higher because of the intrinsically high SNR of a 3D readout and because background suppression is more efficient for a single-volume readout as compared to a multi-slice readout [13]. In addition, parallel imaging was not available in the GE sequence, but was turned on in the Philips sequence. To what extent the heterogeneous appearance of the Philips CBF maps has a physiological origin or is rather the result of a too low SNR, cannot be differentiated with these data.

In regions with long arrival times - i.e. the posterior vascular territory and posterior watershed area - lower CBF and higher wsCV was observed in GE but not in Philips (Figures 4 and 5) [6]. This inter-vendor difference can be explained by differences in the effective post-labeling delay (PLD) between the readouts, even though both acquisitions had the same initial PLD (1525 ms). Whereas the 3D readout obtains all ASL signal for the total 3D volume at a single time-point - i.e. after 1525 ms PLD - the 2D readout obtains signal from each slice sequentially. With this multi-slice acquisition, each slice exhibits a longer effective PLD compared to its previous slice. This inferior-superior PLD increase of the 2D readout (Philips) allows the labeled blood more time to reach the superior slices compared to the homogeneous PLD of the 3D readout (GE). Therefore, the PLD may have been too short for the label to reach the superior slices in 3D (GE), whereas the effective PLD for the superior slices in 2D (Philips) was sufficient. These inter-vendor CBF differences and higher wsCV for GE in superior regions with long transit times are probably resolved by selecting a longer PLD for the 3D readout, such as 2000 ms [3].

Other prominent spatial inter-vendor CBF (Figure 4) and wsCV (Figure 5) differences were observed on the brain edges. We observed higher CBF and lower wsCV in anterior and inferior regions in Philips but not in GE. The prominent inferior CBF and wsCV differences (Figure 4c and Figure 5c) are partly due to the fact that these slices were simply not acquired by the 2D readout (Philips). With

a 2D sequence, it is common practice to scan cerebral slices only as well as to optimize the PLD, T1 decay and background suppression for the cerebral slices. These issues do not apply for a 3D sequence, whose 3D slab usually has whole-brain coverage. The differences in the other areas can be explained by susceptibility artifacts from bone-air transitions at the paranasal sinuses and mastoid air cells present in the gradient-echo T2*-weighted readout implemented by Philips [33]. In addition, it is expected that the echo-planar imaging readout (Philips) exhibits geometric distortion in these regions [33]. The T2-weighted spin-echo readout employed by GE is much less sensitive to these artifacts, in comparison to the gradient-echo readout employed by Philips. For these reasons, a 3D readout is superior in regions such as the orbito-frontal lobe and cerebellum compared to a 2D readout. This especially favors the use of a 3D readout for clinical applications of ASL, since pathologies in these regions could remain undetected on a 2D readout [34-36].

A limitation of the current study is that we did not acquire spatial M_0-maps with the same readout in Philips. By employing a voxel-wise normalization of the ASL-signal, these maps would have opposed the T_2^* susceptibility effects, since these will be approximately equally large for the ΔM and M_0-map. Therefore, Philips spatial M_{0a}-maps could have improved quantification in regions of air-tissue transitions, which may have diminished the inter-vendor variation to a certain extent. However, the added value of spatial M_0-maps is limited since they cannot improve the lower SNR of the gradient-echo readout (Philips) near the air-tissue transitions. Therefore, the inter-vendor reproducibility in these regions is expected to remain low.

The current study may also be limited by the inter-vendor calibration of quantification parameters. These may remain arbitrary, mostly because they have been derived from simulations rather than measurements. One example is the inter-vendor differences in labeling efficiency due to a different number of background suppression pulses (5 and 2 for GE and Philips respectively) [21]. One way to deal with this is to scale to a phase-contrast MRI sequence of the main feeding arteries [20]. However, this would shift the inter-vendor CBF variation from the ASL-sequence towards the phase-contrast MRI measurements.

Inter-vendor CBF and wsCV differences were observed on a voxel-level but not on the total GM level. Apparently, the effects of the abovementioned readout differences do cancel out when sufficient GM voxels are averaged. There are several explanations for this observation. First, the higher SNR of the 3D module may be important on a voxel-level, but if sufficient GM voxels are averaged physiological variation seems to outnumber the SNR differences between the readout modules. Second, the smoothing of the GE 3D readout averages signal from multiple GM voxels which increases SNR and subsequently decreases the wsCV within a single voxel. This effect is similar to averaging signal from multiple GM voxels of the 2D readout in post-processing. Therefore, this difference of spatial signal averaging between both readouts becomes apparent on a voxel-level but is negligible when all GM voxels are averaged.

It should be acknowledged that this study evaluated healthy controls only. The abovementioned inter-vendor readout differences could become more or less im-

portant in patients, considering the different spatial CBF variation in patients compared to healthy controls. Furthermore, these inter-vendor differences should not be generalized to all MRI vendors. Visual readout differences between GE and Siemens, who both use a 3D approach, may be smaller than the readout differences in the current study [13].

In conclusion, the current study shows that pCASL results do not differ between vendors on a total GM level. Therefore, the reliability of averaged CBF-values for the total GM can be expected to be equal in single- and multi-vendor studies. However, the reliability of measurements in GM regions or in the WM, is impeded by differences between the readout modules of both vendors. Therefore, our results strongly encourage the standardization of ASL implementations among vendors, which was also advocated by the recent ASL consensus paper [3].

REFERENCES

1. Golay X, Hendrikse J, Lim TC. Perfusion imaging using arterial spin labeling. Top Magn Reson Imaging. 2004;15: 10-27.
2. Williams DS, Detre JA, Leigh JS, Koretsky AP. Magnetic resonance imaging of perfusion using spin inversion of arterial water. Proc Natl Acad Sci U S A. 1992;89: 212-216.
3. Alsop DC, Detre JA, Golay X, Günther M, Hendrikse J, Hernandez-Garcia L, et al. Recommended implementation of arterial spin-labeled perfusion MRI for clinical applications: A consensus of the ISMRM perfusion study group and the European consortium for ASL in dementia. Magn Reson Med. 2015;73: 102-116.
4. Chen Y, Wolk DA, Reddin JS, Korczykowski M, Martinez PM, Musiek ES, et al. Voxel-level comparison of arterial spin-labeled perfusion MRI and FDG-PET in Alzheimer disease. Neurology. 2011;77: 1977-1985.
5. Xu G, Rowley HA, Wu G, Alsop DC, Shankaranarayanan A, Dowling M, et al. Reliability and precision of pseudo-continuous arterial spin labeling perfusion MRI on 3.0 T and comparison with 15O-water PET in elderly subjects at risk for Alzheimer's disease. NMR Biomed. 2010;23: 286-293.
6. Petersen ET, Mouridsen K, Golay X, all named co-authors of the QUASAR test-retest study. The QUASAR reproducibility study, Part II: Results from a multi-center Arterial Spin Labeling test-retest study. Neuroimage. 2010;49: 104-113.
7. Jahng GH, Song E, Zhu XP, Matson GB, Weiner MW, Schuff N. Human brain: reliability and reproducibility of pulsed arterial spin-labeling perfusion MR imaging. Radiology. 2005;234: 909-916.
8. Detre JA, Rao H, Wang DJ, Chen YF, Wang Z. Applications of arterial spin labeled MRI in the brain. J Magn Reson Imaging. 2012;35: 1026-1037.
9. Hendrikse J, Petersen ET, Golay X. Vascular disorders: insights from arterial spin labeling. Neuroimaging Clin N Am. 2012;22: 259-69, x-xi.
10. Golay X. How to do an ASL multicenter neuroimaging study. Proc Intl Soc Mag Reson Med. 2009;17.
11. Liu T, Wierenga C, Mueller B, Wang J, Glover G, Voyvodic J, et al. Reliability and Reproducibility of Arterial Spin Labeling Perfusion Measures Assessed with a Multi-Center Study. Proc Intl Soc Mag Reson Med. 2008.
12. Kilroy E, Apostolova L, Liu C, Yan L, Ringman J, Wang DJ. Reliability of two-dimensional and three-dimensional pseudo-continuous arterial spin labeling perfusion MRI in elderly populations: comparison with 15O-water positron emission tomography. J Magn Reson Imaging. 2014;39: 931-939.
13. Vidorreta M, Wang Z, Rodriguez I, Pastor MA, Detre JA, Fernandez-Seara MA. Comparison of 2D and 3D single-shot ASL perfusion fMRI sequences. Neuroimage. 2012;66C: 662-671.
14. Chen Y, Wang DJ, Detre JA. Test-retest reliability of arterial spin labeling with common labeling strategies. J Magn Reson Imaging. 2011;33: 940-949.
15. Binnewijzend MA, Kuijer JP, Benedictus MR, van der Flier WM, Wink AM, Wattjes MP, et al. Cerebral blood flow measured with 3D pseudocontinuous arterial spin-labeling MR imaging in Alzheimer disease and mild cognitive impairment: a marker for disease severity. Radiology. 2013;267: 221-230.
16. Donahue MJ, Ayad M, Moore R, van Osch M, Singer R, Clemmons P, et al. Relationships between hypercarbic reactivity, cerebral blood flow, and arterial circulation times in patients with moyamoya disease. J Magn Reson Imaging. 2013;38: 1129-1139.
17. Alsop DC, Detre JA. Reduced transit-time sensitivity in noninvasive magnetic resonance imaging of human cerebral blood flow. J Cereb Blood Flow Metab. 1996;16: 1236-1249.

18. St Lawrence KS, Wang J. Effects of the apparent transverse relaxation time on cerebral blood flow measurements obtained by arterial spin labeling. Magn Reson Med. 2005;53: 425-433.
19. Lu H, Clingman C, Golay X, van Zijl PC. Determining the longitudinal relaxation time (T1) of blood at 3.0 Tesla. Magn Reson Med. 2004;52: 679-682.
20. Aslan S, Xu F, Wang PL, Uh J, Yezhuvath US, van Osch M, et al. Estimation of labeling efficiency in pseudocontinuous arterial spin labeling. Magn Reson Med. 2010;63: 765-771.
21. Garcia DM, Duhamel G, Alsop DC. Efficiency of inversion pulses for background suppressed arterial spin labeling. Magn Reson Med. 2005;54: 366-372.
22. Lu H, Nagae-Poetscher LM, Golay X, Lin D, Pomper M, van Zijl PC. Routine clinical brain MRI sequences for use at 3.0 Tesla. J Magn Reson Imaging. 2005;22: 13-22.
23. Herscovitch P, Raichle ME. What is the correct value for the brain--blood partition coefficient for water? J Cereb Blood Flow Metab. 1985;5: 65-69.
24. Heijtel DF, Mutsaerts HJ, Bakker E, Schober P, Stevens MF, Petersen ET, et al. Accuracy and precision of pseudo-continuous arterial spin labeling perfusion during baseline and hypercapnia: A head-to-head comparison with O HO positron emission tomography. Neuroimage. 2014;92C: 182-192.
25. Chalela JA, Alsop DC, Gonzalez-Atavales JB, Maldjian JA, Kasner SE, Detre JA. Magnetic resonance perfusion imaging in acute ischemic stroke using continuous arterial spin labeling. Stroke. 2000;31: 680-687.
26. Ashburner J. A fast diffeomorphic image registration algorithm. Neuroimage. 2007;38: 95-113.
27. Levene H. Robust tests for equality of variances. In: Olkin I, Ghurye SG, Hoeffding W, Madow WG, Mann HB, editors. Contributions to probability and statistics: essays in honor of Harold Hotelling. Stanford, CA: Stanford University Press; 1960. pp. 278.
28. Bland JM, Altman DG. Measuring agreement in method comparison studies. Stat Methods Med Res. 1999;8: 135-160.
29. Floyd TF, Ratcliffe SJ, Wang J, Resch B, Detre JA. Precision of the CASL-perfusion MRI technique for the measurement of cerebral blood flow in whole brain and vascular territories. J Magn Reson Imaging. 2003;18: 649-655.
30. Parkes LM, Rashid W, Chard DT, Tofts PS. Normal cerebral perfusion measurements using arterial spin labeling: reproducibility, stability, and age and gender effects. Magn Reson Med. 2004;51: 736-743.
31. Gevers S, van Osch MJ, Bokkers RP, Kies DA, Teeuwisse WM, Majoie CB, et al. Intra- and multicenter reproducibility of pulsed, continuous and pseudo-continuous arterial spin labeling methods for measuring cerebral perfusion. J Cereb Blood Flow Metab. 2011;31: 1706-1715.
32. van Gelderen P, de Zwart JA, Duyn JH. Pittfalls of MRI measurement of white matter perfusion based on arterial spin labeling. Magn Reson Med. 2008;59: 788-795.
33. Deichmann R, Josephs O, Hutton C, Corfield DR, Turner R. Compensation of susceptibility-induced BOLD sensitivity losses in echo-planar fMRI imaging. Neuroimage. 2002;15: 120-135.
34. Timmann D, Konczak J, Ilg W, Donchin O, Hermsdorfer J, Gizewski ER, et al. Current advances in lesion-symptom mapping of the human cerebellum. Neuroscience. 2009;162: 836-851.
35. Wolf RC, Thomann PA, Sambataro F, Vasic N, Schmid M, Wolf ND. Orbitofrontal cortex and impulsivity in borderline personality disorder: an MRI study of baseline brain perfusion. Eur Arch Psychiatry Clin Neurosci. 2012;262: 677-685.
36. Walther S, Federspiel A, Horn H, Razavi N, Wiest R, Dierks T, et al. Resting state cerebral blood flow and objective motor activity reveal basal ganglia dysfunction in schizophrenia. Psychiatry Res. 2011;192: 117-124.

Chapter 4.2

Quantitative functional arterial spin labeling (fASL) MRI – sensitivity and reproducibility of regional CBF changes using pseudo-continuous ASL product sequences

Rebecca M.E. Steketee
Henk Jan M.M. Mutsaerts
Esther E. Bron
Matthias J.P. van Osch
Charles B.L.M. Majoie
Aad van der Lugt
Aart J. Nederveen
Marion Smits

PLoS ONE. 2015;10:e0132929

ABSTRACT

Arterial spin labeling (ASL) magnetic resonance imaging is increasingly used to quantify task-related brain activation. This study assessed functional ASL (fASL) using pseudo-continuous ASL (pCASL) product sequences from two vendors. By scanning healthy participants twice with each sequence while they performed a motor task, this study assessed functional ASL for 1) its sensitivity to detect task-related cerebral blood flow (CBF) changes, and 2) its reproducibility of resting CBF and absolute CBF changes (delta CBF) in the motor cortex. Whole-brain voxel-wise analyses showed that sensitivity for motor activation was sufficient with each sequence, and comparable between sequences. Reproducibility was assessed with within-subject coefficients of variation (wsCV) and intraclass correlation coefficients (ICC). Reproducibility of resting CBF was reasonably good within (wsCV: 14.1-15.7%; ICC: 0.69-0.77) and between sequences (wsCV: 15.1%; ICC: 0.69). Reproducibility of delta CBF was relatively low, both within (wsCV: 182-297%; ICC: 0.04-0.32) and between sequences (wsCV: 185%; ICC: 0.45), while inter-session variation was low. This may be due to delta CBF's small mean effect (0.77-1.32 mL/100g gray matter/min). In conclusion, fASL seems sufficiently sensitive to detect task-related changes on a group level, with acceptable inter-sequence differences. Resting CBF may provide a consistent baseline to compare task-related activation to, but absolute regional CBF changes are more variable, and should be interpreted cautiously when acquired with two pCASL product sequences.

INTRODUCTION

Arterial spin labeling (ASL) perfusion magnetic resonance imaging (MRI) is being increasingly used for imaging of task-related brain activation. Such functional ASL (fASL) has been used to study the neural correlates of a multitude of cognitive domains, including attention [1], memory [2], language [3], visual [4] and sensorimotor processing [5], and is increasingly considered as an alternative to blood oxygen level-dependent (BOLD) functional MRI (fMRI), which has been predominantly used as a marker for neural activation during the last two decades.

ASL has several advantages over BOLD imaging with respect to acquisition and interpretation. First, ASL has better sensitivity in low frequency paradigms. The BOLD signal has been shown to be confounded by slow 'drift' effects in baseline signal, which are reduced in ASL imaging as a result of the pairwise subtraction of labeled and unlabeled images [5]. Second, despite the intrinsically low signal-to-noise ratio (SNR) of ASL, spatial localization of neuronal activity seems more accurate when measured with ASL than with BOLD. The BOLD signal is affected by macrovascular venous effects [6] whereas ASL is more sensitive to the microvasculature [7]. The interpretation of the BOLD signal is more complex as it reflects a combination of cerebral blood flow (CBF), cerebral blood volume (CBV) and cerebral metabolic rate of oxygen consumption (CMRO2) [8,9], whereas ASL provides a measure of CBF that is relatively less sensitive to other hemodynamic parameters. Furthermore, ASL provides an in principle quantitative measure of CBF, whereas the BOLD signal is relative. These advantages favor the application of fASL over fMRI BOLD for task-related brain imaging.

The quantitative aspect of ASL in particular could facilitate the comparison and exchange of CBF values across multiple sites and enable multicenter studies, for instance, to pool data. However, before fASL can be used as such, its variability needs to determined, not only within sessions and scanners, but also between product sequences of different vendors, as each vendor provides its own particular ASL implementation. Reproducibility of ASL in general is affected by intrinsic properties, such as low SNR and relative sensitivity to hemodynamics such as arterial transit time (ATT) [10]. In addition, although within-sequence reproducibility is sufficient for the commonly available labeling schemes [11-22], pseudo-continuous arterial spin labeling (pCASL) has been shown to be best reproducible within session, scanner, and vendor, being more stable and less variable than continuous ASL (CASL) and pulsed ASL (PASL) [23,24].

Nevertheless, not every user is aware of the potential impact of these factors and may assume that any ASL implementation will provide the same information, as can be expected from a quantitative technique. This may seem particularly appealing for the quantification of brain activation in functional imaging studies. The extent to which different vendor implementations affect these data is not known. We will therefore compare two pCASL product sequences as implemented by two different vendors, while limiting adjustment of sequence parameters to within the constraints imposed by the vendor-specific implementation.

Baseline or resting CBF values have been found to be well reproducible within sessions, within scanners, and between scanners of the same vendor on a whole-brain level, whereas on a regional level reproducibility was lower [23,24].. We previously assessed the reproducibility of whole-brain resting CBF within and between pCASL product sequences at 3T scanners of two different vendors [25]. Mean global CBF did not differ between product sequences, but voxel-by-voxel assessment revealed regional differences. Regional variability presents a challenge for fASL, where local effects are of particular interest. In addition to the variability in regional CBF changes, the variability in the detection of such CBF changes needs to be assessed. Sufficient and similar sensitivity to detect local task-induced CBF changes is a prerequisite for multicenter fASL implementations, and essential to good reproducibility.

As of yet, variability of quantitative fASL and variation of sensitivity for task-induced CBF changes between product sequences of different vendors have not been studied. Not only is this information essential for exchanging and comparing fASL data, but results generated by one product sequence can only be generalized to another if variability between them is known. The aim of the present study was to assess quantitative fASL by 1) assessing sensitivity to detect regional CBF changes in a voxel-wise whole-brain analysis, and 2) by investigating regional reproducibility of both resting CBF and task-induced CBF changes in the primary motor cortex, within and between pCASL product sequences from two major vendors. We investigated this by means of paced finger tapping, a simple behavioral paradigm that is known to elicit robust and consistent regional activation in the primary motor cortex in a multitude of activation studies using BOLD as well as fASL (e.g [5-7]). We employed this paradigm in healthy volunteers using product sequences from two different vendors.

METHODS

Participants

Twenty-two healthy volunteers, aged 18-40 years, were recruited as part of a larger study on ASL reproducibility [25]. Participants were recruited through advertisement at the University of Amsterdam. Only participants with no history of neurological or psychiatric disease were included. Participants that used medication other than contraceptives, or had contraindications for MRI were excluded.

Participants were asked to limit their consumption of alcohol, nicotine and caffeine to a maximum of three units 12-24 hours prior to scanning, and to refrain from consuming alcohol, nicotine and caffeine 12 hours prior to scanning. The study was approved by the local medical research ethics committees of both sites: the Erasmus MC – University Medical Center Rotterdam and the Academic Medical Center, Amsterdam and was conducted according to the Declaration of Helsinki. All participants gave written informed consent and received financial compensation for participation.

Image acquisition

Imaging was performed on a 3T Intera (Philips Healthcare, Best, the Netherlands) and a 3T Discovery MR750 (GE Healthcare, WI, USA) scanner, using an 8 channel receive head coil. Participants were scanned twice on both scanners, i.e. four sessions in total, in no specific order (Figure 1A). Scanning sessions were separated by at least one week, but no more than four weeks.

Table 1: Vendor-specific parameters of the pCASL product sequences

	GE	**Philips**
Readout sequence	3D FSE stack-of-spirals	2D gradient-echo single-shot EPI
Acquisition matrix	8 arms with 512 sampling points	80 * 80
Parallel imaging	No	SENSE factor = 2.5
Voxel size	3.75 * 3.75 * 4 mm^3	3 * 3 * 7 mm^3
Field of view (FOV)	24 * 24 cm^2	24 * 24 cm^2
Number of slices	36	17
Echo time	10.5 ms	17 ms
Repetition time	4 600 ms	4 000 ms
Flip angle	111°	90°
Labeling duration	1 450 ms	1 650 ms
Post-labeling delay	1 525 ms	1 525 ms
Labeling plane (distance from AC-PC line[a] in head-feet direction)	89 mm	72 mm
Background suppression	Yes	Yes
Vascular crushers	No	No
Total scanning time	2:01 min	2:08 min
NEX (no. of excitations) GE; NSA (no. of repetitions) Philips	1	16

[a] anterior commissure – posterior commissure line

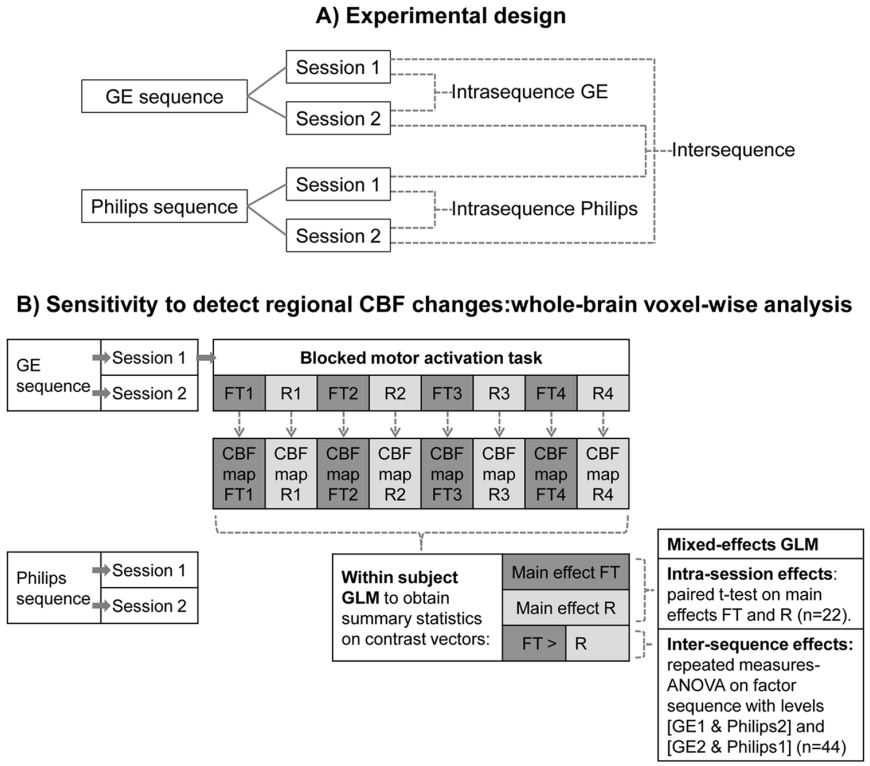

Figure 1: design and analyses. Schematic overview of A) experimental design and analyses of B) whole-brain voxel-wise activation sensitivity and of C) reproducibility of regional resting CBF and regional task-induced CBF changes

A high resolution 3D T1-weighted (T1w) scan for anatomical reference was acquired during one of the two sessions on each scanner. Perfusion data were acquired using pCASL product sequences that were provided by the vendor of each scanner. As we aimed to assess the reproducibility of the currently implemented (i.e. product) sequences, we chose to employ vendor-supplied sequences rather than to reprogram the sequences to make them match completely. Hence, parameters were only adjusted within the given limits of the clinical scanning sequences. Imaging data of the two sites were acquired by two different researchers. Strict agreements were made about the complete process of instructing and positioning participants in order to minimize differences between researchers and subsequently between sequences. Details of both pCASL sequences are listed in Table 1. Note that on the GE scanner a segmented 3D readout was employed, whereas on the Philips scanner single-shot multi-slice 2D imaging was combined with averaging to obtain a temporal resolution similar to the GE-sequence. Another difference between sequences was that on the GE scanner perfusion data are averaged during acquisition, whereas for Philips data is averaged after acquisition, after pair-wise subtraction of label and control images during post-processing. As the GE sequence only provides three fixed post-labeling delays (1 025, 1 525 and 2 025 ms for respectively children, adults, and older adults or adults with cerebrovascular disease), a delay of 1 525 ms, considered most suitable for the current population, was selected for all ASL imaging.

Motor activation paradigm

Eight ASL scans were acquired, during which participants performed a blocked motor activation task (Figure 1). Block length was equal to acquisition time of one scan, i.e. 2 minutes. Participants were instructed to tap the fingers of both hands to the thumbs in random order (finger tapping, FT) during the odd scans and to keep their hands still (rest) during even scans. FT was auditorily paced at a frequency of 1 Hz.

Data processing

The imaging data were processed according to the methods described in full in Bron *et al.*, 2014 [26].

Tissue segmentation

The unified tissue segmentation method [27] of SPM8 (Statistical Parametric Mapping 8, Wellcome Trust Centre for Neuroimaging, University College London, UK) was used to obtain gray matter (GM), white matter (WM) and cerebrospinal fluid (CSF) probability maps from the T1w image.

ASL post-processing

For Philips data, label and control pCASL images were pair-wise subtracted (without motion correction) and averaged to obtain perfusion weighted images. For GE

data, the perfusion-weighted images, as provided by the scanner, were used. For each participant, the perfusion-weighted image and the GM probability map were rigidly registered (Elastix registration software [28]). The results of the registration were visually inspected and showed good correspondence.

Quantification

To quantify the perfusion-weighted maps of both pCASL sequences as cerebral blood flow (CBF) maps, a single-compartment model was used [10]:

$$CBF(mL/100g/\min) = \frac{6000\lambda\Delta M e^{PLD/T_{1a}}}{2\alpha\ T_{1a} M_{0a}\ (1-\ e^{-\tau/T_{1a}})}$$

Parameters used in this model and their values are summarized in Table 2. Differences in effective post-labeling delay for different slices resulting from the 2D multi-slice readout were accounted for in the Philips data (Table 2).

Table 2: variables of the single-compartment model used for quantification (based on Alsop et al., 2015 [10])

Symbol	Variable	Value
λ	blood-brain partition coefficient for gray matter	0.9 mL/g
ΔM	perfusion-weighted image	Philips: corrected for transversal magnetization decay time (T_2*) of arterial blood (50 ms) during the 17 ms echo time (TE) by $e^{TE/T2*}$ {{242 Hammers,A. 2003; 243 Gousias,I.S. 2008}}
M_{oa}	equilibrium magnetization of arterial blood	GE: obtained by individual proton density maps, adjusted for T1 decay time of gray matter tissue ($T1_{GM}$, 1.2 s) during saturation recovery time (t_{sat}, 2 s) by $1 - e^{-tsat/T1GM}$; Philips: scanner average ($3.7*10^6$ a.u.) from previous study [29]
PLD	post-labeling delay	1 525 ms
T_{1a}	longitudinal relaxation time of arterial blood	1 650 ms [30]
α	labeling efficiency	0.8 [31]. In order to correct for background suppression pulses [32]: for GE α* 0.75; for Philips: α* 0.83
τ	labeling duration	GE: 1 450 ms; Philips: 1 650 ms

Whole-brain voxel-wise preprocessing and activation sensitivity analysis

Registered T1w images and CBF maps were transformed to a common template space based on the T1w images of all participants [26]; CBF maps were smoothed using an isotropic 8 mm full width at half maximum (FWHM) kernel.

Voxel-wise differences within and between sequences in relation to finger tapping (Figure 1B) were assessed using SPM8. Averaged CBF maps per block of finger tapping (FT) and rest were convolved with the hemodynamic response function and modeled on an individual level using a General Linear Model (GLM), yielding parameter estimates for the main effects of FT and rest and the contrast [FT > rest] which were subsequently used in group analyses (Figure 1B). Task-induced changes were assessed per session per sequence by pair-wise comparison of main effects of FT and rest for each participant during each session. As participants were scanned in a random order, we chose to assess inter-sequence differences by means of a repeated measures ANOVA on the contrast [FT > rest] for GE (session) 1 compared to Philips 2 and GE 2 to Philips 1 (n=44). By comparing sessions this way, we can assume that temporal physiological variation affected intra-sequence and inter-sequence reproducibility to a similar extent. All voxel-wise results were thresholded at p<0.001 without correction for multiple comparisons, to be maximally sensitive to intra- and inter-sequence differences in the detection of CBF changes.

ROI preprocessing and regional reproducibility analysis

ROI labeling and selection

Individual CBF maps were transformed to individual T1w image space for region of interest (ROI) analysis. ROIs for each participant were defined using a multi-atlas approach by registering thirty labeled T1w images, each containing 83 ROIs [33,34], to the participants' T1w images, using a rigid, affine, and non-rigid model consecutively. For the current study, we focused on the bilateral primary motor cortex, i.e. the superior aspect of the precentral gyri, containing the hand-motor area [35]. The hand motor area was identified in all thirty T1w atlas images and followed down to the level of the cingulum, which was used as the inferior cut off of the precentral gyrus. Analysis of CBF in the primary motor cortex was performed in GM only.

CBF post-processing in the primary motor cortex

For every pCASL scan, mean GM CBF values were obtained from the left and right superior precentral gyrus (primary motor cortex). CBF values were averaged per session over the four FT blocks and over the four rest blocks, and then over the primary motor cortex bilaterally, such that for every session we obtained one mean GM CBF value in the bilateral primary motor cortex for the FT condition (CBF_{FT}) and one for the rest condition (CBF_{rest}, Figure 1C).

Task-induced regional CBF changes within sessions

To assess task-induced CBF changes in the primary motor cortex, CBF_{FT} and CBF_{rest} within sessions were compared with paired t-tests ($p<.05$). Absolute CBF changes as a result of finger tapping are referred to as delta CBF: [CBF_{FT} – CBF_{rest}] (Figure 1C).

Reproducibility of regional resting CBF and regional task-induced CBF changes

Intra- and inter-sequence reproducibility were assessed by the following measures (Figure 1C):

1. Within-subject coefficients of variation (wsCV) were calculated as the ratio of the standard deviation of the CBF difference (SD_{diff}) between sessions to the mean CBF value of those sessions: wsCV = 100% (SD_{diff}/mean value). The SD_{diff} , rather than the SD of the mean, was used to reflect the extent of variability in differences in relation to the mean.Mean CBF values over sessions, mean CBF differences between sessions, SD_{diff}, and wsCVs and their 95% confidence intervals (CIs) are reported for CBF_{rest}, CBF_{FT}, and delta CBF.

   Intra-sequence measures were calculated between the two sessions per sequence. Inter-sequence measures were calculated by comparing GE (session) 1 to Philips 2 and GE 2 to Philips 1 (n=44).

2. Intraclass correlation coefficients (ICC) and 95% CIs were calculated for CBF_{rest}, CBF_{FT}, and delta CBF. A two way-random model and absolute agreement were employed to allow for generalization of the results and to take into account systematic variability between sequences, respectively. ICCs were defined as function of ANOVA mean squares using the following formula [36]:

$$\frac{BMS - EMS}{BMS + (K - 1)\,EMS + k / n\,(JMS - EMS)}$$

   in which BMS refers to the between-targets mean square (i.e. variance between participants), JMS refers to the between-judges mean square (i.e. variance between intra- or inter-sequence sessions) and EMS to the residual mean square (i.e. residual sources of variance), in a two-way ANOVA with n = 22 (intra-sequence) or 44 (inter-sequence) targets and k = 2 judges.

   Inter-sequence ICCs were calculated between the two sessions per sequence by comparing GE (session) 1 to Philips 2 and GE 2 to Philips 1 (n=44).

3. Bland-Altman plots and 95% limits of agreement (mean difference ± 1.96 SD_{diff}) were created for CBF_{rest} and delta CBF to visualize agreement within and between sequences.

Statistical analyses were carried out in IBM SPSS Statistics, version 20.0 (New York, USA).

RESULTS

Participant characteristics

Nine male and 13 female volunteers with a mean age of 22.1 ± 2.1 years (range: 19-27 years) participated in the study. It should be noted that one participant had CBF values that were 2 – 3 standard deviations higher than the group mean, but this participant was retained in the analysis as data were normally distributed (Kolmogorov-Smirnov tests did not detect significant deviations from normality in any session, $p>.05$). The two sessions scanned using the GE sequence were separated by 2.8 ± 1.0 weeks and those using the Philips sequence by 2.6 ± 0.9 weeks (not significant (n.s.)). Inter-sequence sessions were separated by 3.1 ± 1.1 weeks (GE 1 – Philips 2) and 2.6 ± 1.9 weeks (GE 2 – Philips 1), n.s.. Both sessions scanned with the GE sequence took place at an earlier time of day than those scanned with the Philips sequence: 3:26pm ± 4h00min and 3:55pm ± 3h34min versus 8:16pm ± 2h06min and 7h47pm ± 2h38min respectively, $p<.05$.

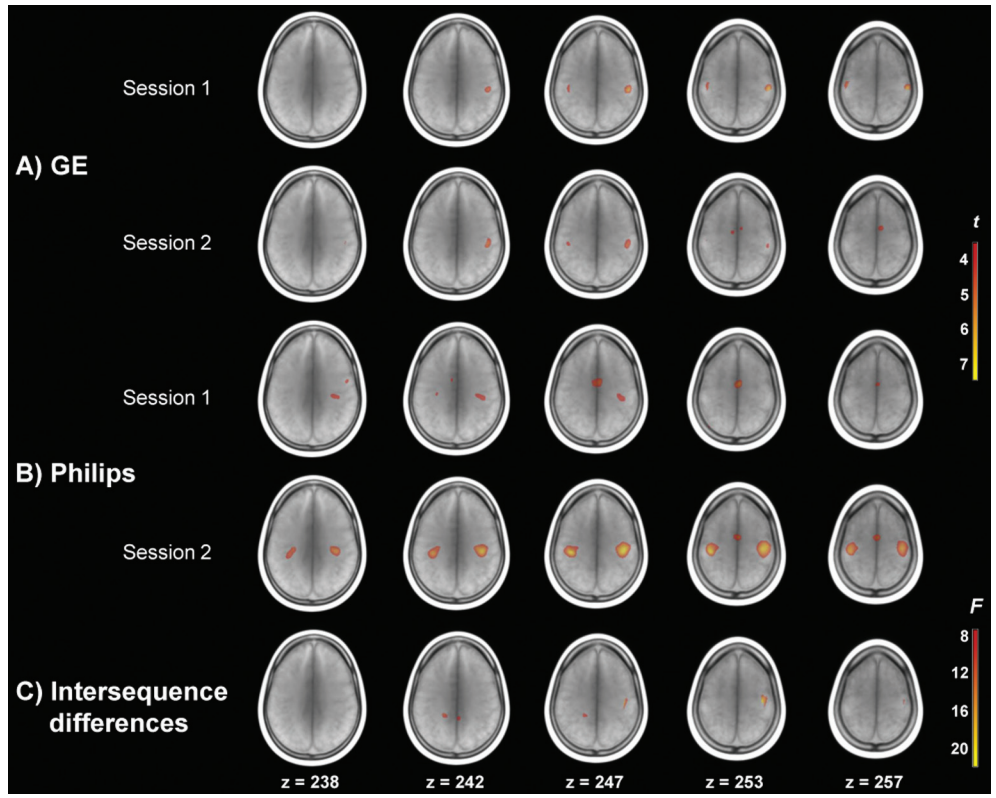

Figure 2: whole-brain voxel-wise CBF differences associated with finger tapping compared to rest.
Activation maps are overlaid on a mean T1w scan. T-maps for the two sessions of A) GE and B) Philips sequences are thresholded at t=3.52, $p<.001$ (uncorrected). C) shows the F-map depicting differences in activation between pCASL sequences, thresholded at $F(2,63) = 7.7$, $p<.001$ (uncorrected).

Whole-brain voxel-wise activation sensitivity of pCASL sequences

Voxel-wise CBF changes in relation to FT are illustrated with t-statistic maps in Fig. 2. Both with GE (Fig. 2A) and Philips (Fig. 2B) CBF increases were observed in the bilateral primary motor cortex in both sessions. Additional activation was observed in the supplementary motor area and the left cerebellum in GE session 2; and in the thalamus, and supplementary motor area in both Philips sessions. As can be appreciated visually, Philips (Figure 2B) seems to be more sensitive to detect activation than GE (Figure 2A). Upon formal assessment with repeated measures ANOVA (Figure 2C), differences between pCASL sequences were found in the right primary motor cortex, left precuneus, right posterior cingulate, and in the bilateral thalamus.

Task-induced regional CBF changes within sessions

Absolute CBF values differed systematically between pCASL sequences, with mean CBF_{rest} values being 4.1 mL/100g GM/min lower as measured with GE than with Philips. The increase in CBF in the motor cortex as a result of FT was significant for both GE sessions and the second Philips session (Table 3). The increase in CBF due to FT relative to CBF_{rest} was larger for the two GE sessions (6.13 and 4.27%) than for the two Philips sessions (2.27 and 3.53%).

Table 3: mean CBF and standard deviations (mL/100g GM/min) in the motor cortex during finger tapping and rest, and respective p-values; and relative CBF increase expressed as a percentage of resting CBF, per sequence per session.

	GE				Philips			
	Session 1		Session 2		Session 1		Session 2	
	FT	R	FT	R	FT	R	FT	R
Mean	65.8	62.0	66.2	63.5	69.6	68.1	67.8	65.5
SD	11.49	14.11	9.50	10.60	13.10	13.39	11.65	14.45
p-value	.005		.010		.078		.020	
Relative CBF increase (%)	6.13%		4.27%		2.27%		3.53%	

CBF: cerebral blood flow, SD: standard deviation, FT: finger tapping, R: rest.

Table 4: Mean CBF measurements and reproducibility estimates between sessions and sequences for resting CBF (CBF_{rest}), finger tapping CBF (CBF_{FT}) and delta CBF in the primary motor cortex.

		GE	95% CI	Philips	95% CI	Inter-sequence	95% CI
CBF_{rest}	Mean CBF	62.7	57.6 – 67.8	66.8	61.0 – 72.6	64.8	61.1 – 68.5
	Mean CBF difference	-1.51	-5.87 – 2.85	2.58	-1.59 – 6.76	-4.08	-7.07 – -1.09
	SD difference	9.83	6.67 – 13.0	9.42	6.40 – 12.4	9.81	7.67 – 11.9
	wsCV (%)	15.7	9.68 – 21.7	14.1	7.55 – 20.7	15.1	10.9 – 19.4
	ICC	0.69	0.40 – 0.86	0.77	0.52 – 0.90	0.69	0.47 – 0.82
CBF_{FT}	Mean CBF	66.0	61.7 – 70.2	68.7	63.6 – 73.9	67.4	64.2 – 70.5
	Mean CBF difference	-0.42	-4.32 – 3.47	1.81	-2.05 – 5.68	-2.76	-5.77 – 0.26
	SD difference	8.78	5.96 – 11.6	8.71	5.91 – 11.5	9.90	7.74 – 12.1
	wsCV (%)	13.3	8.20 – 18.4	12.7	6.81 – 18.5	14.7	10.9 – 18.5
	ICC	0.66	0.34 – 0.85	0.75	0.50 – 0.89	0.61	0.39 – 0.77
Delta CBF	Mean CBF	3.25	1.42 – 5.09	1.93	0.61 – 3.24	2.59	1.39 – 3.79
	Mean CBF difference	1.09	-1.54 – 3.72	-0.77	-3.30 – 1.77	1.32	-0.13 – 2.78
	SD difference	5.93	4.02 – 7.83	5.72	3.88 – 7.55	4.79	3.75 – 5.83
	wsCV (%)	182	180 – 185	297	294 – 299	185	183 – 186
	ICC	0.32	-0.10 – 0.65	0.04	-0.40 – 0.45	0.45	0.18 – 0.65

CBF: cerebral blood flow, SD: standard deviation, wsCV: within subject coefficient of variation, ICC: intraclass correlation coefficient, CI: confidence interval.

Reproducibility of regional resting CBF and regional task-induced CBF changes

WsCV, SD_{diff}, mean CBF values and ICCs and 95% CIs are reported for CBF_{rest}, CBF_{FT}, and delta CBF in Table 4. WsCVs were comparable within and between pCASL sequences for CBF_{rest} and CBF_{FT}.

Reproducibility of CBF_{rest} and CBF_{FT} in terms of ICCs was moderate to good for both sequences, with ICCs of .69 and .66 for GE and .77 and .75 for Philips, respectively (Figure 3). Reproducibility of absolute delta CBF was poor for both sequences with ICCs of .32 (GE) and .04 (Philips), and CIs being 1.5 – 2.3 times larger than for CBF_{rest} and CBF_{FT}. Between sequences, reproducibility was reasonable for CBF_{rest} (.69) and CBF_{FT} (.61) and fair for absolute delta CBF (ICC: .45). Inter-sequence CIs for delta CBF were approximately 1.3 times larger than for CBF_{rest} and CBF_{FT}.

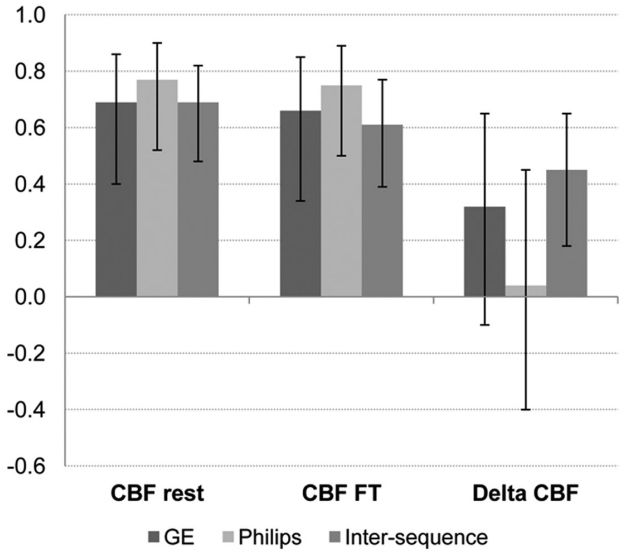

Figure 3: intra- and intersequence intraclass correlation coefficients for CBF_{rest}, CBF_{FT} and delta CBF in the motor cortex.
Error bars denote 95% confidence intervals.

Figs. 4-I and II show the agreement within and between sequences for CBF_{rest} and absolute delta CBF respectively. For both CBF_{rest} and delta CBF, differences within sequences were somewhat larger for measurements performed with GE (Figs. 4A-I and II) than with Philips (Figs. 4B-I and II). The low intra-sequence reproducibility of delta CBF with Philips in particular (Figure 4B-II) is illustrated by the variability relative to the mean effect being higher for delta CBF than for CBF_{rest} (Figure 4B-I). Both CBF_{rest} and delta CBF show a comparable spread in differences within and between sequences. Figure 4C-I and II show the agreement between sequences for CBF_{rest} and delta CBF respectively, and illustrate that al-

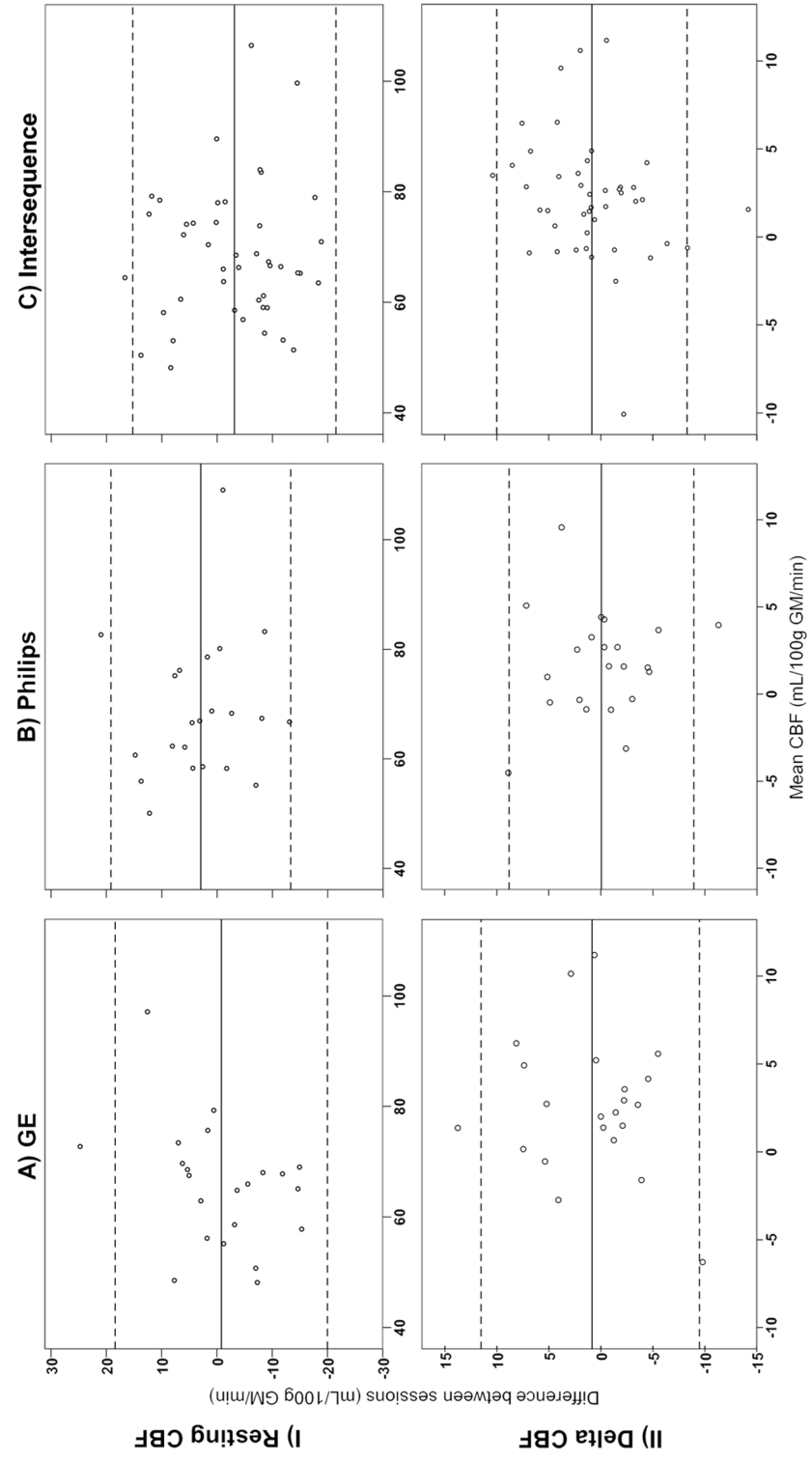

Figure 4: agreement within and between pCASL sequences for resting CBF and delta CBF.Bland Altman plots of agreement between the two sessions per sequence (A, B) and between sequences (C) for resting CBF (I) and delta CBF (II) in the primary motor cortex. The solid line indicates the mean difference between sessions, dotted lines the 95% limits of agreement.

though the spread in differences is higher for CBF_{rest} (Figure 4C-I), the variability relative to the mean effect is 1.5 times as large for delta CBF (Figure 4C-II).

DISCUSSION

Using pCASL product sequences as supplied by two MR vendors, we found that sensitivity to detect primary motor cortex activation was sufficient and comparable for both sequences. Secondly, we found intra- and intersequence reproducibility of resting CBF in the motor cortex to be reasonably good, as was reproducibility of CBF during finger tapping. More important in the context of fASL however, we found absolute CBF changes to be only moderately reproducible, both within and between sequences, despite a more or less consistent task-induced CBF increase within sessions at the group level.

This study adopted a pragmatic and clinically applicable approach in employing pCASL product sequences as supplied by the vendors. Parameters were adjusted to match each other as much as possible, but within the constraints of the provided sequence. This reflects the de facto situation of commercially supplied sequences in which parameters can only be adjusted to a certain extent. As CBF measured with ASL is claimed to be and promoted as a quantitative measure, one would assume that measurements are independent of sequence parameters. Here we show to what extent standard implementation of the sequences gives rise to substantial differences and thus limited reproducibility for functional ASL.

The increase in CBF in the motor cortex during finger tapping is in line with previous cross-sectional fASL studies employing finger tapping paradigms [5,7,37,38]. Our results replicate these findings within both sequences, except in one of the Philips sessions. Although we found the extent and spatial patterns of activation to differ between sequences, they both detected activation in the primary motor cortex as a result of finger tapping, and formal comparison of activation patterns between sequences demonstrated only minor differences in motor areas. This supports the notion that on the group level, fASL is sufficiently sensitive to detect activation in the primary motor cortex, and that differences in sensitivity between pCASL product sequences are acceptable. The magnitude of CBF changes was, however, surprisingly modest in our study compared to previous studies, which may – at least partially – be due to methodological differences. For instance, our ROI comprised the entire superior precentral gyrus, which may have resulted in only a modest increase since CBF is averaged over this entire ROI. Previous studies quantified CBF in ROIs more spatially specific to activation, such as the 'precentral hand knob' or activated volumes [5,39].

We found reproducibility of resting CBF in the motor cortex to be reasonably good within and good between pCASL sequences. Our intra-sequence results are in line with previous whole-brain resting CBF studies that have shown reasonable to good reproducibility within and between sessions on the same scanner [23], as well as between scanners of the same vendor [16,24]. We recently compared resting gray matter CBF between two different pCASL sequences and also found

it to be well reproducible on the global level [25]. The current study focused on regional resting gray matter CBF and showed that, when compared to global CBF, reproducibility was slightly lower. Previous studies found that smaller regions are subject to higher variability and thus may yield lower reproducibility estimates [11,23]. In addition, regional reproducibility has been found to be lower for CBF measured at an interval of 2-4 weeks than for measurements within one day, implying that temporal physiological differences dominate between-weeks reproducibility [23,40]. Other sources of physiological variation may also be present, such as the one participant with CBF values that were consistently higher than the group mean. This physiological variation could have been accounted for by adding global CBF as a covariate, but as we aimed to demonstrate the variability in *absolute* regional CBF changes, scaling the signal would have defeated the objective of the current study.

Apart from temporal dynamics in physiology, regional variability could also be affected by the difference in effective post-labeling delay (PLD) between pCASL sequences. In order for labeled blood to reach the relatively superiorly located motor cortex, arterial transit time (ATT) is longer than for inferior regions, because of the larger distance between the labeling plane and the target tissue. This was previously demonstrated by Gonzalez-At *et al.* [41], who measured ATT to the visual region (5.1 cm from the labeling plane) to be 514 ms and to the motor region (11.5 cm from the labeling plane) 906 ms. Although in the current study the same initial PLD (1 525 ms) was applied for both sequences, the 2D multi-slice acquisition employed by Philips may have allowed labeled blood more time to reach superior slices, including regions with longer arrival times, than did the single time-point 3D acquisition employed by GE. This difference in effective PLD between sequences may have contributed to decreased reproducibility between their respective measurements. Moreover, the level of reproducibility of different regions seems to vary with PLD [16], with a PLD of 2 500 ms yielding better reproducibility than a PLD of 1 500 ms when using a 3D single time-point sequence. Therefore, effective PLD differences may have affected our results, as the precentral gyrus is located at the superior aspect of the brain, and therefore exhibits longer transit delays. This may have led to an underestimation of CBF values due to incomplete inflow of label, and to higher variability due to difference in arterial arrival times. Note that this is not resolved by merely prolonging the PLD, because although this may be a benefit for optimal bolus delivery, it also compromises signal due to label decay.

Differences between sequences may not only affect resting CBF measures, but also those of motor activation. Studies that compared fASL data obtained with 2D and 3D sequences found that activated clusters are generally larger when using 3D sequences, while 2D sequences yield larger effect sizes in terms of relative CBF changes [42,43]. Our results on the other hand showed larger activated clusters with the 2D sequence, and larger relative CBF changes with the 3D sequence. The larger effective PLD of Philips may have allowed more labeled blood to reach the primary motor cortex during finger tapping than GE, yielding larger activation clusters. In addition, the 3D sequence is more susceptible to spatial blurring, which obscures the gray matter to white matter contrast [42], and may attenuate signal from the gray matter. The larger relative signal change measured

with GE on the other hand may be explained by decreasing ATT as a result of finger tapping [41]. Although (pseudo-) continuous ASL techniques are not very sensitive to changes (especially decreases) in ATT [44], it is likely that the known decreased ATT during neuronal activation [45] also leads to faster extravasation of the label into the tissue compartment, leading to faster decay of the label as the longitudinal relaxation time of tissue is shorter than that of blood. This would lead to an underestimation of CBF during activation. Additionally, because of its shorter effective PLD, particularly in the superior regions, such shorter ATT after finger tapping may have caused the relative signal change as measured by GE to be higher than by Philips.

The reproducibility of delta CBF, i.e. the CBF difference observed between finger tapping and rest, is less straightforward to interpret. Despite the smaller inter-session variation of delta CBF differences (as indicated by smaller standard deviations of differences) when compared to that of resting CBF and finger tapping CBF, wsCVs are extremely high. The relatively small effect of delta CBF is more likely to be susceptible to high variability than resting and finger tapping CBF, which may affect its reproducibility to a larger extent than the other CBF measures. This is in fact reflected by the ICCs indicating poor intra-sequence reproducibility. Previous fASL studies reported wsCVs of 10-11% [39,46], and ICCs up to 0.74 [47], between sessions that were a week apart. However, these studies assessed the reproducibility of relative CBF changes, instead of absolute CBF changes. It has been suggested that relative CBF changes are more accurate and robust than absolute CBF changes, as they may reduce potential effects of basal perfusion variations on measures of neuronal activation [47]. Relative CBF changes may therefore generate higher ICCs than absolute CBF changes. Nevertheless, as mentioned earlier, as absolute quantification is a specific advantage of fASL, it seems more appropriate to investigate the reproducibility of absolute CBF changes.

Slight variation in signal change as a result of finger tapping has been observed, but shown to be similar between sessions that took place on the same day or on different days [46]. Raoult *et al*. [47] found similar levels of variation using a finger flexion-extension paradigm. Moreover, they found task-induced CBF to be higher, albeit not significantly, with shorter sequence lengths, and concluded that a motor paradigm with 4 blocks of 30s on/off activation is optimal for clinical practice [39]. Longer sequence durations are considered to induce habituation and thus decreased activation. Our paradigm consisted of 2 minute blocks of on/off activation because of the limited temporal resolution of the GE sequence. These relatively long blocks thus may have attenuated activation, and thus the effect of finger tapping as compared to other studies, which may have reduced reproducibility.

On the other hand, one of the major reasons to use ASL for functional imaging is its suitability for low frequency designs, as it is much less sensitive to drift effects over time than BOLD fMRI [48]. Wang *et al.* [5] even demonstrated that fASL shows constant sensitivity across different task frequencies corresponding to blocks lengths ranging from 0.5 – 5 minutes, with ASL outperforming BOLD contrast at a block length of 4 minutes. Some higher cognitive functions, such

as sustained attention [1], depend on an experimental design with even longer blocks to detect slow, low-frequeny signal changes of interest, for which fASL is particularly well suited. Despite ASL's appropriateness for such cognitive paradigms, we purposely chose a simple behavioral paradigm known to elicit robust and consistent regional activation, before moving on to more complex processes and paradigms. We find that even this simple motor activation paradigm gives rise to substantial variability, which warrants caution with respect to more complex and less robust designs.

To our knowledge, no studies exist on the reproducibility of task-induced CBF changes using pCASL product sequences from two different vendors. In the current study, we found reproducibility of task-induced CBF to be comparable within and between sequences, both in terms of wsCV and ICC. Nevertheless, the findings indicate that absolute CBF changes in the motor cortex still vary considerably, and this variation needs to be taken into account when comparing regional quantitative CBF changes, particularly between sequences. Therefore, absolute fASL data should not be simply pooled between product sequences.

This study has some limitations. First, we quantified CBF using a model that simplifies the actual *in vivo* situation, which would have required measurement of many variables that are difficult to obtain on an individual basis. This is illustrated by the discrepancy between the results of the voxel-wise group analysis and region-wise analysis: whereas the qualitative voxel-wise analysis showed acceptable inter-sequence differences, results from region-wise quantitative analysis are far less similar. Nevertheless, this lends support to our conclusion that current standard implementation of ASL and recommended analysis of ASL are not – yet – suited for quantitative functional ASL experiments. Second, we did not collect information on motor behavior. Although variations in frequency were avoided by externally pacing the finger tapping, we may have missed individual variations in tapping, which may have added to the variability. Next, as time of acquisition differed between sequences, with GE data collected earlier on the day, diurnal fluctuations in CBF may have added to variability between sequences. This potentially affected reproducibility of resting CBF more than that of delta CBF, as the latter is based on a subtractive measure. Still, inter-sequence reproducibility of resting CBF was found to be reasonably good. Furthermore, subsequent analysis of the Philips data was performed in a similar manner to maximize comparability with the GE data, i.e. by averaging over rest and activation periods, whereas one would normally choose to exploit the higher temporal resolution in a more formal manner within the design matrix. Finally, due to practical constraints we studied the product sequences of only two out of the three major vendors on the market. Although assessment of variability between the three vendors would have been more comprehensive, the current study was conducted as a proof-of principle, and demonstrated as such that substantial variability is already evident when product sequences of two vendors are compared. Future work should be directed at optimizing ASL sequences for functional imaging, and at assessing sensitivity and reproducibility of fASL in single-subject designs, as longitudinal studies and clinical application of fASL will eventually need to be aimed at repeated measurements within individuals.

In conclusion, in a voxel-wise whole-brain analysis, fASL shows sufficient sensitivity to detect regional CBF changes on a group level, both within and between pCASL product sequences of two different vendors. The between sequence reproducibility of fASL is comparable with within sequence reproducibility, although inter-sequence differences in readout should be taken into account. Although reproducibility of regional resting CBF is affected by differences in sequence implementation, particularly in the readout, resting CBF in the motor cortex may provide a reasonably consistent baseline to compare task-induced CBF to. The relatively low reproducibility of task-induced CBF changes in the primary motor cortex, however, should be taken into consideration when comparing fASL data between sessions and particularly between pCASL product sequences as implemented by different vendors. Its interpretation should be performed with caution in repeated measurements and multicenter designs, as current vendor-specific implementations do not allow for simple pooling of functional ASL data.

REFERENCES

1. Demeter E, Hernandez-Garcia L, Sarter M, Lustig C. Challenges to attention: a continuous arterial spin labeling (ASL) study of the effects of distraction on sustained attention. Neuroimage. 2011;54: 1518-1529.
2. Fernandez-Seara MA, Wang J, Wang Z, Korczykowski M, Guenther M, Feinberg DA, et al. Imaging mesial temporal lobe activation during scene encoding: comparison of fMRI using BOLD and arterial spin labeling. Hum Brain Mapp. 2007;28: 1391-1400.
3. Kemeny S, Ye FQ, Birn R, Braun AR. Comparison of continuous overt speech fMRI using BOLD and arterial spin labeling. Hum Brain Mapp. 2005;24: 173-183.
4. Cavusoglu M, Bartels A, Yesilyurt B, Uludag K. Retinotopic maps and hemodynamic delays in the human visual cortex measured using arterial spin labeling. Neuroimage. 2012;59: 4044-4054.
5. Wang J, Aguirre GK, Kimberg DY, Roc AC, Li L, Detre JA. Arterial spin labeling perfusion fMRI with very low task frequency. Magn Reson Med. 2003;49: 796-802.
6. Gaxiola-Valdez I, Goodyear BG. Origins of intersubject variability of blood oxygenation level dependent and arterial spin labeling fMRI: implications for quantification of brain activity. Magn Reson Imaging. 2012;30: 1394-1400.
7. Pimentel MA, Vilela P, Sousa I, Figueiredo P. Localization of the hand motor area by arterial spin labeling and blood oxygen level-dependent functional magnetic resonance imaging. Hum Brain Mapp. 2013;34: 96-108.
8. Ogawa S, Menon RS, Tank DW, Kim SG, Merkle H, Ellermann JM, et al. Functional brain mapping by blood oxygenation level-dependent contrast magnetic resonance imaging. A comparison of signal characteristics with a biophysical model. Biophys J. 1993;64: 803-812.
9. Obata T, Liu TT, Miller KL, Luh WM, Wong EC, Frank LR, et al. Discrepancies between BOLD and flow dynamics in primary and supplementary motor areas: application of the balloon model to the interpretation of BOLD transients. Neuroimage. 2004;21: 144-153.
10. Alsop DC, Detre JA, Golay X, Günther M, Hendrikse J, Hernandez-Garcia L, et al. Recommended implementation of arterial spin-labeled perfusion MRI for clinical applications: A consensus of the ISMRM perfusion study group and the European consortium for ASL in dementia. Magn Reson Med. 2015;73: 102-116.
11. Wang Y, Saykin AJ, Pfeuffer J, Lin C, Mosier KM, Shen L, et al. Regional reproducibility of pulsed arterial spin labeling perfusion imaging at 3T. Neuroimage. 2011;54: 1188-1195.
12. Parkes LM, Rashid W, Chard DT, Tofts PS. Normal cerebral perfusion measurements using arterial spin labeling: reproducibility, stability, and age and gender effects. Magn Reson Med. 2004;51: 736-743.
13. Hermes M, Hagemann D, Britz P, Lieser S, Rock J, Naumann E, et al. Reproducibility of continuous arterial spin labeling perfusion MRI after 7 weeks. MAGMA. 2007;20: 103-115.
14. Pfefferbaum A, Chanraud S, Pitel AL, Shankaranarayanan A, Alsop DC, Rohlfing T, et al. Volumetric cerebral perfusion imaging in healthy adults: regional distribution, laterality, and repeatability of pulsed continuous arterial spin labeling (PCASL). Psychiatry Res. 2010;182: 266-73.
15. Xu G, Rowley HA, Wu G, Alsop DC, Shankaranarayanan A, Dowling M, et al. Reliability and precision of pseudo-continuous arterial spin labeling perfusion MRI on 3.0 T and comparison with 15O-water PET in elderly subjects at risk for Alzheimer's disease. NMR Biomed. 2010;23: 286-293.
16. Wu B, Lou X, Wu X, Ma L. Intra- and interscanner reliability and reproducibility of 3D whole-brain pseudo-continuous arterial spin-labeling MR perfusion at 3T. J Magn Reson Imaging. 2014;39: 402-409.

17. Yen YF, Field AS, Martin EM, Ari N, Burdette JH, Moody DM, et al. Test-retest reproducibility of quantitative CBF measurements using FAIR perfusion MRI and acetazolamide challenge. Magn Reson Med. 2002;47: 921-928.
18. Jahng GH, Song E, Zhu XP, Matson GB, Weiner MW, Schuff N. Human brain: reliability and reproducibility of pulsed arterial spin-labeling perfusion MR imaging. Radiology. 2005;234: 909-916.
19. Petersen ET, Mouridsen K, Golay X, all named co-authors of the QUASAR test-retest study. The QUASAR reproducibility study, Part II: Results from a multi-center Arterial Spin Labeling test-retest study. Neuroimage. 2010;49: 104-113.
20. Floyd TF, Ratcliffe SJ, Wang J, Resch B, Detre JA. Precision of the CASL-perfusion MRI technique for the measurement of cerebral blood flow in whole brain and vascular territories. J Magn Reson Imaging. 2003;18: 649-655.
21. Gevers S, Majoie CB, van den Tweel XW, Lavini C, Nederveen AJ. Acquisition time and reproducibility of continuous arterial spin-labeling perfusion imaging at 3T. AJNR Am J Neuroradiol. 2009;30: 968-971.
22. Wu WC, Jiang SF, Yang SC, Lien SH. Pseudocontinuous arterial spin labeling perfusion magnetic resonance imaging--a normative study of reproducibility in the human brain. Neuroimage. 2011;56: 1244-1250.
23. Chen Y, Wang DJ, Detre JA. Test-retest reliability of arterial spin labeling with common labeling strategies. J Magn Reson Imaging. 2011;33: 940-949.
24. Gevers S, van Osch MJ, Bokkers RP, Kies DA, Teeuwisse WM, Majoie CB, et al. Intra- and multicenter reproducibility of pulsed, continuous and pseudo-continuous arterial spin labeling methods for measuring cerebral perfusion. J Cereb Blood Flow Metab. 2011;31: 1706-1715.
25. Mutsaerts HJ, Steketee RME, Heijtel DF, Kuijer JP, van Osch MJ, Majoie CB, et al. Inter-vendor reproducibility of pseudo-continuous arterial spin labeling at 3 tesla. PLoS One. 2014;9: e104108.
26. Bron EE, Steketee RME, Houston GC, Oliver RA, Achterberg HC, Loog M, et al. Diagnostic classification of arterial spin labeling and structural MRI in presenile early stage dementia. Hum Brain Mapp. 2014;35: 4916-4931.
27. Ashburner J, Friston KJ. Unified segmentation. Neuroimage. 2005;26: 839-851.
28. Klein S, Staring M, Murphy K, Viergever MA, Pluim JP. Elastix: a Toolbox for Intensity-Based Medical Image Registration. IEEE Trans Med Imaging. 2010;29: 196-205.
29. Heijtel DF, Mutsaerts HJ, Bakker E, Schober P, Stevens MF, Petersen ET, et al. Accuracy and precision of pseudo-continuous arterial spin labeling perfusion during baseline and hypercapnia: A head-to-head comparison with O HO positron emission tomography. Neuroimage. 2014;92C: 182-192.
30. Lu H, Clingman C, Golay X, van Zijl PC. Determining the longitudinal relaxation time (T1) of blood at 3.0 Tesla. Magn Reson Med. 2004;52: 679-682.
31. Aslan S, Xu F, Wang PL, Uh J, Yezhuvath US, van Osch M, et al. Estimation of labeling efficiency in pseudocontinuous arterial spin labeling. Magn Reson Med. 2010;63: 765-771.
32. Garcia DM, Duhamel G, Alsop DC. Efficiency of inversion pulses for background suppressed arterial spin labeling. Magn Reson Med. 2005;54: 366-372.
33. Hammers A, Allom R, Koepp MJ, Free SL, Myers R, Lemieux L, et al. Three-dimensional maximum probability atlas of the human brain, with particular reference to the temporal lobe. Hum Brain Mapp. 2003;19: 224-247.
34. Gousias IS, Rueckert D, Heckemann RA, Dyet LE, Boardman JP, Edwards AD, et al. Automatic segmentation of brain MRIs of 2-year-olds into 83 regions of interest. Neuroimage. 2008;40: 672-684.

35. Yousry TA, Schmid UD, Alkadhi H, Schmidt D, Peraud A, Buettner A, et al. Localization of the motor hand area to a knob on the precentral gyrus. A new landmark. Brain. 1997;120 (Pt 1): 141-157.
36. Shrout PE, Fleiss JL. Intraclass correlations: uses in assessing rater reliability. Psychol Bull. 1979;86: 420-428.
37. Mildner T, Trampel R, Moller HE, Schafer A, Wiggins CJ, Norris DG. Functional perfusion imaging using continuous arterial spin labeling with separate labeling and imaging coils at 3 T. Magn Reson Med. 2003;49: 791-795.
38. Ye FQ, Yang Y, Duyn J, Mattay VS, Frank JA, Weinberger DR, et al. Quantitation of regional cerebral blood flow increases during motor activation: A multislice, steady-state, arterial spin tagging study. Magn Reson Med. 1999;42: 404-407.
39. Raoult H, Ferre JC, Petr J, Bannier E, Stamm A, Barillot C, et al. Functional arterial spin labeling: Optimal sequence duration for motor activation mapping in clinical practice. J Magn Reson Imaging. 2012;36: 1435-1444.
40. Klomp A, Caan MW, Denys D, Nederveen AJ, Reneman L. Feasibility of ASL-based phMRI with a single dose of oral citalopram for repeated assessment of serotonin function. Neuroimage. 2012;63: 1695-1700.
41. Gonzalez-At JB, Alsop DC, Detre JA. Cerebral perfusion and arterial transit time changes during task activation determined with continuous arterial spin labeling. Magn Reson Med. 2000;43: 739-746.
42. Vidorreta M, Wang Z, Rodriguez I, Pastor MA, Detre JA, Fernandez-Seara MA. Comparison of 2D and 3D single-shot ASL perfusion fMRI sequences. Neuroimage. 2012;66C: 662-671.
43. Hu Y, Glover GH. Three-dimensional spiral technique for high-resolution functional MRI. Magn Reson Med. 2007;58: 947-951.
44. Alsop DC, Detre JA. Reduced transit-time sensitivity in noninvasive magnetic resonance imaging of human cerebral blood flow. J Cereb Blood Flow Metab. 1996;16: 1236-1249.
45. van Osch MJ, Hendrikse J, van der Grond J. Sensitivity comparison of multiple vs. single inversion time pulsed arterial spin labeling fMRI. J Magn Reson Imaging. 2007;25: 215-221.
46. Tjandra T, Brooks JC, Figueiredo P, Wise R, Matthews PM, Tracey I. Quantitative assessment of the reproducibility of functional activation measured with BOLD and MR perfusion imaging: implications for clinical trial design. Neuroimage. 2005;27: 393-401.
47. Raoult H, Petr J, Bannier E, Stamm A, Gauvrit JY, Barillot C, et al. Arterial spin labeling for motor activation mapping at 3T with a 32-channel coil: reproducibility and spatial accuracy in comparison with BOLD fMRI. Neuroimage. 2011;58: 157-167.
48. Aguirre GK, Detre JA, Zarahn E, Alsop DC. Experimental design and the relative sensitivity of BOLD and perfusion fMRI. Neuroimage. 2002;15: 488-500.

Chapter 4.3

Reproducibility of pharmacological ASL using sequences from different vendors: implications for multi-center drug studies

Henk Jan M.M. Mutsaerts
Rebecca M.E. Steketee
Dennis F.R. Heijtel
Joost P.A. Kuijer
Matthias J.P. van Osch
Charles B.L.M. Majoie
Marion Smits
Aart J. Nederveen

MAGMA. 2015;28:427-36.

ABSTRACT

Objective The current study assesses the multi-center feasibility of pharmacological arterial spin labeling (ASL) by comparing a caffeine-induced relative cerebral blood flow decrease (%CBF↓) measured with two pseudo-continuous ASL sequences as provided by two major vendors.

Material and Methods Twenty-two healthy volunteers were scanned twice with both a 3D spiral (GE) and a 2D EPI (Philips) sequence. The inter-session reproducibility was evaluated by comparisons of the mean and within-subject coefficient of variability (wsCV) of the %CBF↓, both for the total cerebral gray matter and on a voxel level.

Results The %CBF↓ was larger when measured with the 3D spiral sequence (23.9% ± 5.9%) than when measured with the 2D EPI sequence (19.2% ± 5.6%) on a total gray matter level (p=0.02), and on a voxel level in the posterior watershed area (p<0.001). There was no difference between the gray matter wsCV of the 3D spiral (57.3%) and 2D EPI sequence (66.7%, p=0.3), whereas on a voxel level the wsCV was visibly different between the sequences.

Conclusion The observed differences between ASL sequences of both vendors can be explained by differences in the employed readout modules. These differences may seriously hamper multi-center pharmacological ASL, which strongly encourages standardization of ASL implementations.

INTRODUCTION

Pharmacological magnetic resonance imaging (phMRI) is increasingly used as a tool to study hemodynamic changes in response to a pharmaceutical substance [1]. Cerebral blood flow (CBF) as a marker of drug effects has potential use at various stages of human drug research and may even enable to monitor or predict therapeutic efficacy [2,3].

Arterial spin labeling (ASL) is an attractive MRI perfusion modality that exhibits several advantages compared to modalities that have previously been used to study pharmacological effects on the brain [4]. The use of blood as an endogenous perfusion tracer renders ASL non-invasive, making it preferable to modalities based on exogenous tracers such as positron emission tomography (PET) [5]. Because ASL is based on a subtraction method, scanner signal drift is cancelled out, which renders ASL preferable to blood-oxygen-level-dependent (BOLD) pharmacological MRI for the study of longitudinal changes [4]. Moreover, ASL enables absolute CBF quantification as compared to the complex contrast provided by BOLD. This exact quantification is a key advantage of ASL for the assessment of drug effects on CBF during both resting and task activation states [4].

Through several methodological advances, ASL perfusion MRI has matured to the point where it can provide whole brain perfusion images in only a few minutes of scanning [6]. The reproducibility of baseline measurements has been thoroughly assessed and initial pharmacological ASL (phASL) results are promising [7-10]. Therefore, the initiation of large-scale multi-center pharmacological ASL (phASL) trials is the next step to extend our understanding of the effects of drugs on cerebral hemodynamics [4].

One main obstacle that may impede multi-center studies, is that fundamental differences exist between ASL implementations of different vendors [11-13]. It is currently unknown to what extent these differences limit the interpretation and/or power of phASL. Therefore, we performed a multi-vendor reproducibility study in which we employed caffeine as a pharmacological challenge, of which the baseline results have been reported elsewhere [13].

Caffeine is an adenosine antagonist that not only acts as a neuro-stimulant (adenosine A1) but is also a strong vasoconstrictor (adenosine A2), reducing CBF by 13–30% [14,15]. Furthermore, caffeine is one of the most socially accepted and widely consumed neuro-stimulants in the world, which facilitates its use in explorative studies in healthy volunteers [16,17]. For these reasons, caffeine has been the research topic in many pharmacological MRI studies and can be considered a first choice challenge to gain knowledge and experience with phASL [4].

The current study assesses the inter-session reproducibility of a caffeine-induced CBF decrease as measured with pseudo-continuous ASL (pCASL) and compares this reproducibility between the different pCASL sequences of two MRI vendors. The mean and variation of the CBF decrease are compared on a total GM level and on a voxel level, to compare the reproducibility of phASL between the sequences on a global and on a spatial level. In addition, the obtained reproducibil-

ity measures are employed in a sample size calculation to illustrate their implications for future phASL studies.

MATERIALS AND METHODS

Subject recruitment

Twenty-two healthy volunteers (9 men, 13 women, mean age 22.6 ± 2.1 years standard deviation (SD)) were included. All subjects provided written informed consent and the study was approved by the institutional review boards of both centers. In addition to standard MRI exclusion criteria, subjects with a history of neurologic or psychiatric disease or the use of prescription medication (except for oral contraceptives) were excluded. No consumption of vasoactive substances such as alcohol, cigarettes, coffee, licorice and tea was allowed on the scan days. On the day prior to the examination, alcohol and nicotine consumption was restricted to three units and cigarettes respectively.

Study design

Figure 1 provides a schematic overview of the study design. All subjects were scanned twice at two academic medical centers in the Netherlands. MRI experiments were performed at center 1 on a 3T GE scanner (Discovery MR750, GE Healthcare, Milwaukee, WI, US) and at center 2 on a 3T Philips scanner (Intera, Philips Healthcare, Best, the Netherlands), both equipped with an 8–channel head coil (InVivo, Gainesville, Fl, US), in random order to avoid order effects. The inter-session time interval was kept at 1–4 weeks. pCASL scans were performed before and 30 minutes after the oral intake of four 50 mg caffeine tablets , from a

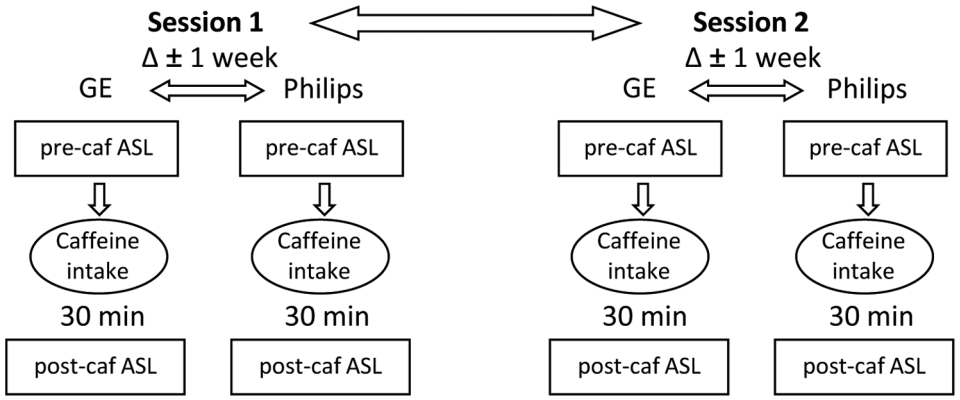

Figure 1. A schematic view of the study design. ASL = arterial spin labeling, caf = caffeine, Δ = inter-session time difference.

single preparation batch from a single supplier (Fagron, Capelle aan den IJssel, The Netherlands). This resulted in an average administrated dose of 2.9 ± 0.4 mg/kg at an average subject weight of 69.2 ± 9.6 kg. For the intake of caffeine, subjects were removed from the scanner gantry, remained seated on the scanner couch and were returned in the scanner gantry after which localizer and reference scans were repeated. Care was taken to keep the head position in relation to the coil as identical as possible. Foam padding was used to restrict head motion during scanning.

Acquisition

Each scan session included a pCASL and a 1 mm^3 isotropic 3D T1-weighted scan for segmentation, registration and normalization purposes. On both scanners we employed the standard clinical pCASL protocols as provided by the vendors, which are currently used in clinical research [18,19]. Table 1 summarizes the similarities and differences between the two pCASL protocols. The main difference between the pCASL sequences implemented by GE and Philips is the readout module: multi-shot spiral 3D fast spin-echo versus single-shot 2D gradient-echo echo-planar imaging (EPI) respectively.

Table 1. Acquisition protocols

	3D spiral sequence	2D EPI sequence
Labeling module	pseudo-continuous	pseudo-continuous
Labeling pulse shape	Hanning	Hanning
Labeling pulse duration	0.5 ms	0.5 ms
Labeling pulse flip angle	23°	18°
Mean gradient strength	0.7 mT/m	0.6 mT/m
Maximal gradient strength	7 mT/m	6 mT/m
Labeling duration	1450 ms	1650 ms
Post-labeling delay (PLD) (initial)	1525 ms	1525 ms
PLD increase per slice	n.a.	28.3 ms
PLD (average)	1525 ms	1770 ms
Labeling plane planning	Fixed 22 mm below lower edge	89 mm below, parallel to AC-PC line
Labeling plane distance*	72 mm	89 mm

Readout module	3D fast spin-echo interleaved stack-of-spirals	2D gradient-echo single-shot echo-planar imaging
		SENSE 2.5, CLEAR
Acquisition matrix	8 spirals x 512 sampling points	80 x 80
Field of view	24 cm^3	24 cm^2
Number of slices	36	17
Slice thickness	4 mm	7 mm
Acquisition voxel size (volume)	3.8 x 3.8 x 4 mm (57.8 mm^3)	3.0 x 3.0 x 7.0 mm (63 mm^3)
Reconstruction voxel size	1.9 x 1.9 x 4.0 mm	3.0 x 3.0 x 7.0 mm
Slice gap	n.a.	0 mm
Echo time/repetition time	10.5/4600 ms	17/4000 ms
Number of signal averages	3	33
Readout planning	True axial, lower edge fixed at lower boundary pons	Parallel to AC-PC line
Background suppression (n pulses)	yes (5)	yes (2)
Vascular crushing	no	no
Acquisition duration	4:29 min	4:33 min

*Labeling plane distance represents distance from the anterior commissure-posterior commissure (ACPC) line in the head-feet direction [21]. n.a. = not applicable

CBF quantification

Matlab 7.12.0 (MathWorks, MA, USA) and Statistical Parametric Mapping (SPM) 8 (Wellcome Trust Center for Neuroimaging, University College London, UK) were used for post-processing and statistical analyses. For the 2D EPI data, label and control pCASL images were pair-wise subtracted and averaged to obtain perfusion-weighted images. For the 3D spiral data, the perfusion-weighted images as directly provided by the scanner were used. Since the 3D spiral data did not incorporate motion correction, this was also not applied to the 2D EPI data. The quantification of CBF from the acquired perfusion-weighted scans was based on a single compartment model [6]:

$$CBF(mL/100g/\min) = \frac{6000\Delta M e^{PLD/T_{1a}}}{2\alpha\alpha_{inv}M_{0a}T_{1a}(1-e^{-\tau/T_{1a}})} \quad [1]$$

where ΔM represents the difference images between control and label and M_{0a} the equilibrium magnetization of arterial blood. PLD is the post-label delay (1.525 s), T_{1a} is the longitudinal relaxation time of arterial blood (1.650 s), α is the labeling efficiency (0.8), where α_{inv} corrects for the decrease in labeling efficiency due to the 5 and 2 background suppression pulses for the 3D spiral (0.75) and the 2D EPI sequence (0.83) respectively and τ represents the labeling duration (1.450 s and 1.650 s for 3D spiral and 2D EPI respectively) [20-22]. The inferior-superior increase in post-label delay in the 2D EPI multi-slice data was accounted for. GE has, but Philips has not, implemented a standard M_0-acquisition where proton density (PD) maps are obtained with a saturation recovery acquisition using read-out parameters identical to the ASL readout. These maps were converted to M_{0a} by the following equation:

$$M_{0a} = \frac{PD}{\lambda_{GM}(1-e^{\frac{-t_{sat}}{T_{1GM}}})} \quad [2]$$

where t_{sat} is the saturation recovery time (2 s), T_{1GM} is the relaxation time of gray matter (GM) tissue (1.2 s) and λ_{GM} is the GM brain-blood water partition coefficient (0.9 mL/g) [23,24]. For the 2D EPI data, a single

M_{0a}-value was used for all subjects. This value was obtained in a previous study within the same center, with the same scanner, head coil, pCASL protocol and a similar population (n=16, 56% M, age 20–24 years), by fitting cerebrospinal fluid T1 recovery curves on the control images of multiple time-point pCASL measurements [25]. M_0 was converted to M_{0a} by multiplication with the blood water partition coefficient (0.76), the density of brain tissue (1.05 g/mL) and by correction for the transversal magnetization decay time (T_2*) of arterial blood (48 ms) during the 17 ms echo time (TE) by $e^{TE/T2^*}$ [24,26,27].

Spatial normalization

A single 3D T1-weighted anatomical scan from each scanner for each subject (n=44) was segmented into GM and white matter tissue probability maps. All CBF maps were transformed into anatomical space by a rigid-body registration to the GM tissue probability maps. The tissue probability maps were spatially normalized using the Diffeomorphic Anatomical Registration analysis using Exponentiated Lie algebra (DARTEL) algorithm [28]. The resulting normalization fields were then applied to the CBF maps as well.

Statistics

Reproducibility parameters

The inter-session intra-vendor reproducibility was evaluated by a comparison of the relative CBF decrease (%CBF↓) of session 1 with %CBF↓ of session 2 (n=22). %CBF↓ was defined as:

$$\%CBF\downarrow = 100\% \frac{CBF_{pre} - CBF_{post}}{CBF_{pre}} \quad [3]$$

where CBF_{pre} and CBF_{post} represent the CBF maps acquired before and 30 minutes after caffeine intake respectively. Reproducibility analyses were based on the mean %CBF↓ of the sessions (i.e. the measured phASL effect), and on the standard deviation (SD) of the inter-session difference ($\Delta_{\%CBF\downarrow}$) in %CBF↓ ($SD\Delta_{\%CBF\downarrow}$, i.e. the variation of the phASL effect). The within-subject coefficient of variability (wsCV), a normalized parameter of variation, was defined as the ratio of $SD\Delta_{\%CBF\downarrow}$ to the mean %CBF↓ of both sessions.

Total cerebral GM

To assess global differences in the phASL effect between both sequences, mean %CBF↓ was calculated for the total cerebral GM (tissue probability thresholded >70%), for each single session separately and for both sessions averaged. The %CBF↓ of each session and the differences between sessions ($\Delta_{\%CBF\downarrow}$) were tested for normality using the Shapiro-Wilk test. A paired two-tailed Student's t-test was used to test whether the %CBF↓ (both sessions pooled, n=44) and whether the intra-session $\Delta_{\%CBF\downarrow}$ (n=22) differed between the sequences. The Levene's test was used to test whether there was an inter-sequence difference in $SD\Delta_{\%CBF\downarrow}$. Limits of agreement were defined as $\Delta_{\%CBF\downarrow} \pm 1.96\ SD\Delta_{\%CBF\downarrow}$ [29]. To compare results with previous ASL reproducibility studies, the absolute cerebral GM CBF decrease was calculated as well.

Spatial comparison

To assess spatial phASL differences between both sequences, both %CBF↓- and wsCV-values were computed for each cerebral GM voxel. To test in which voxels the %CBF↓ was different from 0, a two-tailed t-test was performed on the %CBF↓ maps of each session. To test in which voxels the %CBF↓ differed between the sequences, a two-tailed t-test was performed for both sessions pooled per vendor (n=44). To be sensitive for subtle differences between sequences, statistical significance was not defined strictly (p<0.001, not corrected for multiple comparisons). Individual histograms of the %CBF↓ maps (50 bins, range -30–60%) were averaged to generate a group-level histogram of each session. Histograms were generated from the wsCV-maps (40 bins, range 0–150%). Both %CBF↓ and wsCV histograms were generated for the total cerebral GM. To investigate the effect of differences in data smoothness between the 3D spiral and 2D EPI sequences, the 2D EPI data were smoothed with an anisotropic Gaussian kernel to achieve the same smoothness as the 3D spiral data. Data smoothness was estimated with SPM according to a previously described method [30]. %CBF↓ and wsCV maps and histograms were also generated from these smoothed 2D EPI data.

Sample size calculation for future studies

The cerebral GM $SD\Delta_{\%CBF\downarrow}$ from the data of both vendors were used to calculate the required sample size (n) for future phASL studies. Calculations were performed for a within-subject cross-over experimental design with a desired effect size of 15%. This effect size was chosen in a previous study that determined the sample size for ASL baseline studies [31]. Two sample sizes were calculated, to detect 1) a 15% CBF decrease caused by caffeine and 2) a 15% change in the caffeine-induced %CBF↓. A study design example where the second calculation would be applicable, is to test whether a caffeine-induced %CBF↓ changes if the measurement is repeated with a different condition (e.g. with a different drug dose). For a one-tailed t-test in which we have a hypothesis about the direction of the CBF change (CBF is expected to decrease with caffeine) the following equation applies:

$$n = (Z_{1-\alpha/2} + Z_{1-\beta})^2 \left(\frac{SD\Delta_{\%CBF\downarrow}}{effect\_size}\right)^2 \quad [4]$$

where $Z_{1-\alpha/2}$ is the Z-value related to the significance level (p<0.05), $Z_{1-\beta}$ the Z-value corresponding to the detection power (80%) and $SD\Delta_{\%CBF\downarrow}$ is used for the SD in the sample size calculation of a within-subject design [31]. 15% of the mean baseline CBF and 15% of the mean %CBF↓ from both vendors were used as effect size for the first and second sample size calculation respectively.

RESULTS

Total GM

The inter-session statistics are summarized in Table 2 and visualized in Bland-Altman plots in Figure 2. For both vendors, the %CBF↓ of both sessions and the

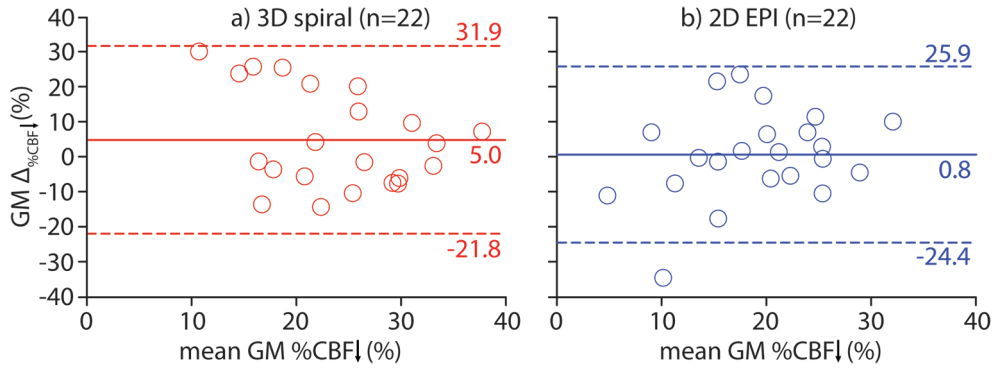

Figure 2. a–b Bland Altman plots of inter-session statistics, as summarized in Table 2. Total cerebral gray matter (GM) inter-session differences in relative cerebral blood flow decrease ($\Delta_{\%CBF\downarrow}$) are plotted against the mean GM %CBF↓ for the a) 3D spiral (n=22) and b) 2D EPI sequence (n=22). Dotted lines indicate limits of agreement (mean difference ± 1.96 standard deviation).

Table 2. Inter-session statistics

	3D spiral	CI (n=22)		2D EPI	CI (n=22)	
%CBF↓ session 1 (%)	* 21.4	-0.8	43.6	18.8	3.4	34.2
%CBF↓ session 2 (%)	* 26.4	11.1	41.8	19.6	-1.0	40.2
Mean %CBF↓ (%)	* 23.9	10.3	37.5	19.2	6.0	32.4
$\Delta_{\%CBF\downarrow}$ (%)	5.0	-1.1	11.1	0.8	-4.9	6.4
$SD\Delta_{\%CBF\downarrow}$ (%)	13.7	9.3	18.1	12.8	8.7	16.9
Lower LOA (%)	-21.8	-29.3	-14.3	- 24.4	-31.4	-17.3
Upper LOA (%)	31.9	24.4	39.4	25.9	18.9	32.9
wsCV (%)	57.3	51.9	62.7	66.7	61.7	71.8

Inter-session statistics for the total cerebral gray matter, as illustrated in the Bland-Altman plots in Figure 2. Values represent mean and difference of mean %CBF↓ of both sessions respectively. %CBF↓= relative cerebral blood flow decrease, wsCV = within-subject coefficient of variability. Asterisk (*) denotes significant (p<0.05) difference between sequences. The limits of agreement (LOA) represent $\Delta_{\%CBF\downarrow}$ ±1.96 standard deviation of the paired inter-session difference ($SD\Delta_{\%CBF\downarrow}$).

inter-session $\Delta_{\%CBF\downarrow}$ were normally distributed according to the Shapiro-Wilk test. The mean %CBF↓ measured with 3D spiral was larger than the mean %CBF↓ measured with 2D EPI (p=0.02). The $\Delta_{\%CBF\downarrow}$ (p=0.3) and $SD\Delta_{\%CBF\downarrow}$ (p=0.3) did not differ between both vendors, resulting in similar wsCVs (57.3% and 66.7% for 3D spiral and 2D EPI respectively).

The mean absolute CBF decrease was 15.9 ± 5.1 and 13.1 ± 6.5 mL/100g/min for the 3D spiral and 2D EPI data respectively. The SD of the inter-session difference of the absolute CBF decrease was 9.5 and 8.7 mL/100g/min for the 3D spiral and 2D EPI data respectively.

Spatial comparison

Figures 3 and 4 illustrate the spatial distribution of the caffeine-induced statistically significant %CBF↓ and wsCV respectively. The significant caffeine-induced %CBF↓ was higher for the 3D spiral sequence than for the 2D EPI sequence on visual comparison, especially in the posterior watershed region (Figure 3a and 3d). The wsCV-maps showed a homogeneous distribution for the 3D spiral data but heterogeneous for the 2D EPI data, which approached the homogeneity of the 3D spiral data after additional smoothing. The shapes of the %CBF↓ histograms of 3D spiral session 1 and both 2D EPI sessions were similar, although 3D spiral session 1 had a higher peak location (Figure 3e). The peak location of the histogram

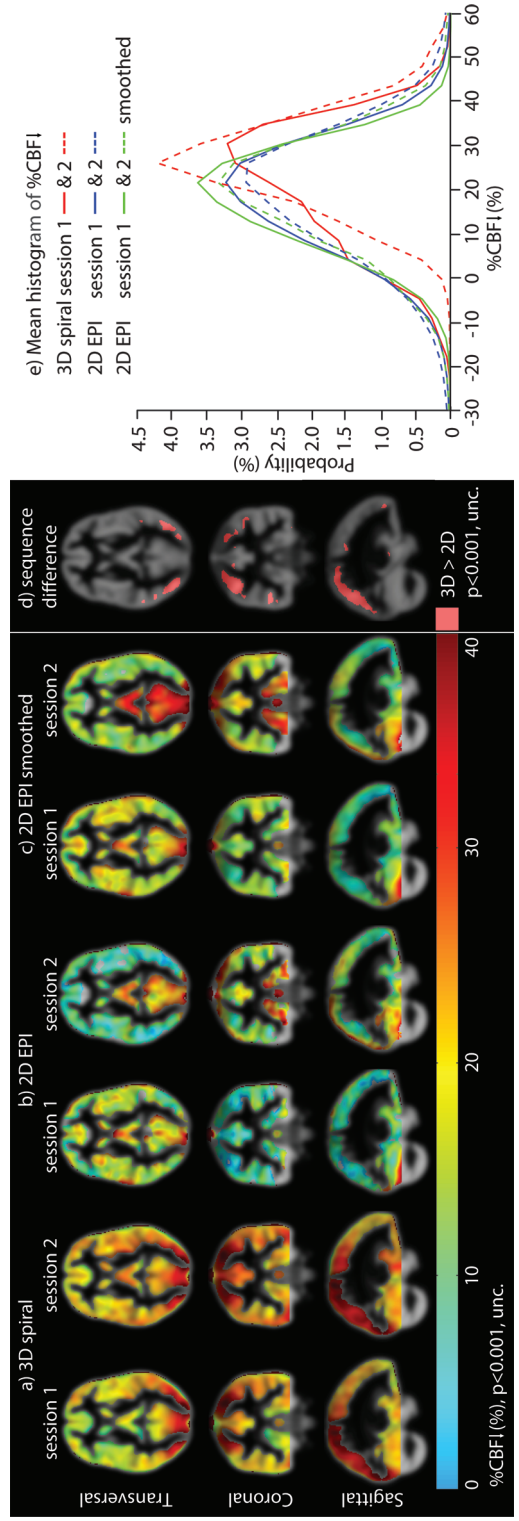

Figure 3 Parametric maps showing voxels with significant cerebral blood flow (CBF) decrease (%CBF↓, p<0.001 uncorrected) for the 3D spiral (a) and 2D EPI sequences (b), as well as for the additionally smoothed 2D EPI data (c). There were no voxels showing a significant CBF increase. d) Parametric maps depicting voxels with significant inter-sequence %CBF↓ differences (p<0.001 uncorrected). All maps are projected on gray matter probability maps. On the right (e), mean individual histograms of the %CBF↓ are shown for all sessions.

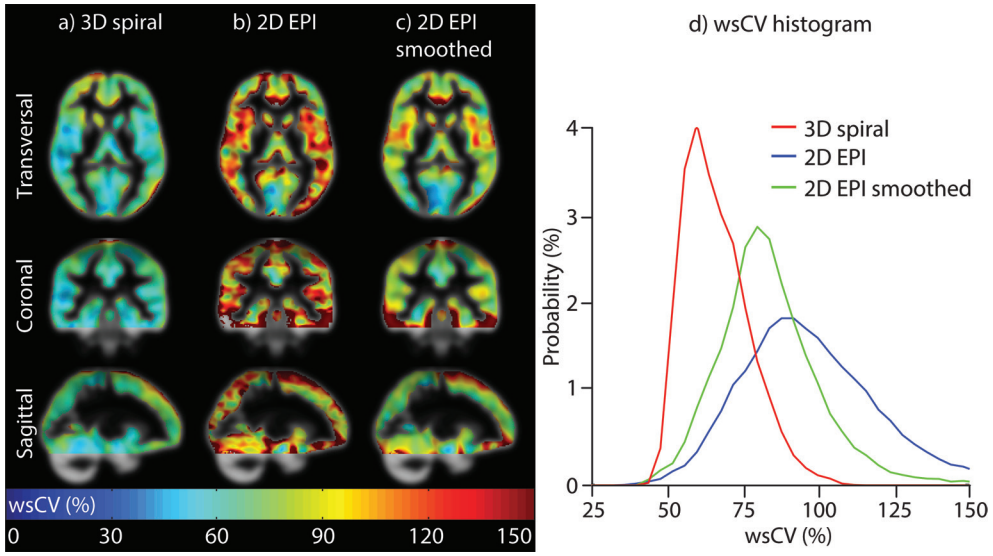

Figure 4 Within-subject coefficient of variation (wsCV)-maps of a) 3D spiral and b) 2D EPI sequences. c) Here, the same 2D EPI wsCV maps are shown after smoothing them to the smoothness of the 3D spiral maps. d) wsCV histograms are shown on the right.

of 3D spiral session 2 was comparable to 3D spiral session 1, but the distribution was narrower. The wsCV histogram of 3D spiral had a lower peak location and a narrower distribution compared to the 2D EPI wsCV histogram (Figure 4d). After additional smoothing, the 2D EPI wsCV histogram approached the 3D spiral wsCV histogram.

Sample size calculation for future studies

To detect a caffeine-induced 15% GM decrease in CBF – equivalent to 9.9 mL/100g/min for both vendors – the calculated sample sizes were n=7 and n=6 for 3D spiral and 2D EPI measurements respectively [13]. To detect a 15% change of caffeine-induced GM %CBF↓ (15% * 23.9% = 3.6% (3D spiral) and 15% * 19.2% = 2.9% (2D EPI)) the calculated sample sizes were n=115 and n=155 for 3D spiral and 2D EPI respectively.

DISCUSSION

The main results of this study were threefold: 1) the mean but not the variation of the global %CBF↓ differed between the pCASL sequences of both vendors, 2) both the mean and variation of %CBF↓ spatially differed between the sequences, and 3) the sample size for future studies was much larger to detect a *change* in the caffeine effect than to detect whether there *is* a caffeine effect.

It has previously been suggested that the inter-session variation of ASL measurements is dominated by the physiological variability of baseline CBF [32]. For the measurement of caffeine-induced %CBF↓, different or additional sources of physiological variability can be expected, including those related to the absorption of caffeine from the gastrointestinal tract, as well as the pharmaco-kinetics and cardiovascular effects of caffeine [16,33,34]. Nevertheless, the inter-session variation of the caffeine-induced CBF change was not much larger than the previously reported baseline CBF variation of the current study, or than baseline CBF variation from previous studies [13,35,36]. This can be attributed to the presence of co-variance between baseline and post-caffeine CBF measurements, which may have decreased the influence of baseline CBF variability on the %CBF↓ variation. In addition, the normalization of the absolute CBF difference by the baseline CBF (equation 3) may have reduced the contribution of baseline CBF variability to the %CBF↓ variation even further.

Whereas the baseline reproducibility of ASL has been thoroughly investigated, only one previous study has reported on the inter-session reproducibility of ASL for the measurement of a pharmaceutically induced CBF change [36]. This study assessed the reproducibility of perfusion changes induced by an oral 16 mg citalopram administration as measured with pulsed ASL. Whereas the inter-session variation was similar (SD 10.1 versus 9.5 [3D spiral] or 8.7 mL/100g/min [2D EPI]), the effect size of citalopram was roughly 3 times as small as caffeine (mean absolute CBF change 4.4 versus 15.9 [3D spiral] or 13.1 mL/100g/min [2D EPI]). As a result, the reproducibility of CBF changes induced by citalopram (expressed by wsCV) can be expected to be roughly 3 times as low as the reproducibility of caffeine-induced CBF changes. This comparison shows that pharmaceuticals with a specific affinity, such as citalopram, have a lower effect size but not necessarily a lower inter-session variation than less specific pharmaceuticals, such as caffeine. This again points to the fact that the variation of phASL is dominated by physiological CBF fluctuations. The recently reported inter-session reproducibility of ASL for a CO_2 inhalation challenge supports this point, since the baseline and hypercapnia wsCV were equal (12.8% versus 12.7% respectively) [25].

Surprisingly, we found a significant difference in total GM effect size between sequences, whereas our previous baseline results showed perfect agreement [13]. One explanation for this difference in the phASL effect size could be the confounding effect of transit times on the measurement of CBF. A caffeine-induced vaso-constriction is not only expected to result in a decrease in CBF, but also in an increase in arterial transit time [37]. Therefore, the post-caffeine transit time can be expected to be longer than the pre-caffeine transit time, which could have led to a post-caffeine CBF underestimation and subsequently a %CBF↓ overestimation. This confounding effect will be larger for a shorter PLD and will be most pronounced in the brain region with the longest transit times, which is the posterior watershed area [38].

Although the same initial PLD was applied for both sequences (1525 ms), the effective PLD is longer for superior slices in the 2D EPI readout. The sequential multi-slice 2D EPI readout results in an infero-superior increase of the effective PLD as compared to the homogeneous PLD of a single time-point 3D spiral read-

out. Therefore, with the same initial PLD applied, the 2D EPI readout will be less sensitive to the confounding effect of prolonged transit times on the measurement of %CBF↓. This can explain the inter-sequence difference in effect size, both globally as well as in the posterior watershed area. In addition, the higher sensitivity of the 3D spiral readout for transit times may have increased the variation of the 3D spiral data. This is not supported by the homogeneous 3D spiral wsCV-maps. However, any larger variation in the superior regions could be masked by the high degree of smoothing in the Z-direction of the 3D spiral readout. These sequence differences in CBF and in wsCV in superior regions with long transit times are probably resolved by selecting a longer PLD for the 3D spiral readout, such as 2000 ms [6].

There was a large difference between the calculated sample sizes to either 1) detect the effect of phASL or to 2) detect a change in the effect of phASL. Whereas the first was comparable with baseline sample size recommendations to detect a 15% GM CBF change (n=4), the second was much larger [31]. It is worth noting that the sample size calculation is quadratically dependent on the ratio of the variation to the effect size (equation 4). For the first sample size, the inter-session variation of caffeine-induced CBF changes was not much larger than baseline, and the effect size is the same as for baseline sample size calculations – i.e. 15% of the mean baseline CBF. For the second sample size, however, the inter-session variation is the same but the effect size is one fifth of baseline sample size calculations – i.e. 15% of the %CBF↓. This shows that the number of subjects required to detect the effect of a pharmaceutical on CBF, does not necessarily have to be large. However, to detect changes of the phASL effect size, statistical power seems mainly limited by a relatively small effect size of phASL. One important example in which changes of phASL effect size are of interest, is the investigation of a drug dose response [39].

It should be acknowledged that our study design choice - comparing two different ASL product sequences on two different vendors - is both a major strength and major weakness of this study. The major strength is that it represents the current status of multi-center phASL: each center will most likely use the ASL product sequence with its optimal settings as implemented on their MRI system. However, this design choice limits the ability to differentiate to what extent the observed differences were caused by differences in ASL readout and the corresponding sequence parameters, by MRI hardware or site effects. Fortunately, we were able to compare our results with previous studies that isolated the effects of different labeling or readout strategies on a single vendor [11,32].

The observation that the variation of phASL was comparable between sequences on a total GM level but not on a voxel level is in agreement with our baseline results [13]. However, when identical sequences are implemented, the voxel level variation of ASL is comparable between vendors [12]. This strongly suggests that the spatial phASL variability differences between vendors can be mainly explained by sequence differences and much less by hardware or site effects. A 3D spiral readout has a higher SNR and a higher degree of spatial smoothing than a 2D EPI readout [11]. Both are expected to have decreased the spatial variation as observed in the 3D spiral data. This is supported by Figure 3 and 4, showing that

it is possible to approach the voxel level effect size and variability of 3D spiral by additionally smoothing the 2D EPI data.

One previous study compared voxel-wise group-level activation after a sensory-motor task between a 3D spiral and 2D EPI readout on a single scanner, with and without the addition of background suppression to the 3D spiral sequence [11]. With background suppression, the 3D spiral readout showed much larger areas of activation compared to the 2D EPI readout, which is in agreement with our results. Without background suppression, however, the performance of both readouts was not very different. This suggests that the residual differences between the wsCV histograms of the 3D spiral and smoothed 2D EPI data can be mainly explained by differences in background suppression efficiency between the 3D and 2D readout [22]. Another factor that may have contributed to the smaller variation of the 3D spiral data compared to the 2D EPI data is the higher SNR resulting from the shorter TE of the 3D spiral sequence compared to the 2D EPI sequence.

The positioning of the label plane differed between both sequences (Table 1). Whereas it is common practice for the Philips 2D EPI sequence to plan the labeling plane parallel to, and 9 cm lower than, the anterior commissure-posterior commissure-line (ACPC), the GE 3D spiral sequence has a fixed labeling plane, which is closer to the brain. This may have decreased the transit times for the 3D spiral sequence, although it has been previously shown that signal intensity differences are small when the labeling plane distance is varied between 74-94 mm [21]. Another difference between the standard implementation of both sequences was the labeling duration (1450 ms versus 1650 ms at 3D spiral and 2D EPI respectively). This 13% longer bolus may have added SNR for the 2D EPI sequence, which may have slightly counterbalanced the large SNR difference due to the intrinsic SNR difference between 2D and 3D and the higher efficiency of background suppression for the 3D spiral sequence.

The differences in M_0 acquisitions between the vendors could potentially have a effect on the quantification of CBF. However, any M_0 quantification differences between sequences will most likely be similar for the pre- and post-caffeine scans and will not contribute to the differences in %CBF↓ between the 3D spiral and 2D EPI sequences.

Conclusion

Using the current clinical ASL product sequences, only the inter-session variation of the phASL total GM effect size can be compared. The mean total GM effect size, as well as the spatial mean and variation of the phASL effect size differed between the sequences. This may seriously impede multi-center phASL studies, especially in cases with locally restricted effects. These sequence differences strongly encourage the standardization of ASL implementations.

REFERENCES

1. Donahue MJ, Jezzard P. MR perfusion imaging in neuroscience. In: Barker PB, Golay X, Zaharchuk G, editors. Clinical Perfusion MRI: techniques and applications. New York: Cambridge University Press; 2013. pp. 114-117.
2. George E, Becerra L, Upadhyay J, Schmidt U, Borsook D. Evaluation of novel drugs using fMRI in early-phase clinical trials: safety monitoring. Drug Discov Today. 2010;15: 684-689.
3. Handley R, Zelaya FO, Reinders AA, Marques TR, Mehta MA, O'Gorman R, et al. Acute effects of single-dose aripiprazole and haloperidol on resting cerebral blood flow (rCBF) in the human brain. Hum Brain Mapp. 2013;34: 272-282.
4. Wang DJ, Chen Y, Fernandez-Seara MA, Detre JA. Potentials and challenges for arterial spin labeling in pharmacological magnetic resonance imaging. J Pharmacol Exp Ther. 2011;337: 359-366.
5. Golay X. How to do an ASL multicenter neuroimaging study. Proc Intl Soc Mag Reson Med. 2009;17.
6. Alsop DC, Detre JA, Golay X, Günther M, Hendrikse J, Hernandez-Garcia L, et al. Recommended implementation of arterial spin-labeled perfusion MRI for clinical applications: A consensus of the ISMRM perfusion study group and the European consortium for ASL in dementia. Magn Reson Med. 2015;73: 102-116.
7. Petersen ET, Mouridsen K, Golay X, all named co-authors of the QUASAR test-retest study. The QUASAR reproducibility study, Part II: Results from a multi-center Arterial Spin Labeling test-retest study. Neuroimage. 2010;49: 104-113.
8. Zelaya FO, Zois E, Muller-Pollard C, Lythgoe DJ, Lee S, Andrews C, et al. The response to rapid infusion of fentanyl in the human brain measured using pulsed arterial spin labelling. MAGMA. 2012;25: 163-175.
9. Khalili-Mahani N, van Osch MJ, Baerends E, Soeter RP, de Kam M, Zoethout RW, et al. Pseudocontinuous arterial spin labeling reveals dissociable effects of morphine and alcohol on regional cerebral blood flow. J Cereb Blood Flow Metab. 2011;31: 1321-1333.
10. Chen Y, Wan HI, O'Reardon JP, Wang DJ, Wang Z, Korczykowski M, et al. Quantification of cerebral blood flow as biomarker of drug effect: arterial spin labeling phMRI after a single dose of oral citalopram. Clin Pharmacol Ther. 2011;89: 251-258.
11. Vidorreta M, Wang Z, Rodriguez I, Pastor MA, Detre JA, Fernandez-Seara MA. Comparison of 2D and 3D single-shot ASL perfusion fMRI sequences. Neuroimage. 2012;66C: 662-671.
12. Mutsaerts HJMM, Van Osch MJP, Zelaya FO, Wang DJJ, Nordhoy W, Wang Y, et al. Multi-vendor comparison of arterial spin labeling with same labeling and readout modules. International Society for Magnetic Resonance in Medicine. 2014;22: 4569.
13. Mutsaerts HJ, Steketee RME, Heijtel DF, Kuijer JP, van Osch MJ, Majoie CB, et al. Inter-vendor reproducibility of pseudo-continuous arterial spin labeling at 3 tesla. PLoS One. 2014;9: e104108.
14. Mulderink TA, Gitelman DR, Mesulam MM, Parrish TB. On the use of caffeine as a contrast booster for BOLD fMRI studies. Neuroimage. 2002;15: 37-44.
15. Vidyasagar R, Greyling A, Draijer R, Corfield DR, Parkes LM. The effect of black tea and caffeine on regional cerebral blood flow measured with arterial spin labeling. J Cereb Blood Flow Metab. 2013;33: 963-968.
16. Fredholm BB, Battig K, Holmen J, Nehlig A, Zvartau EE. Actions of caffeine in the brain with special reference to factors that contribute to its widespread use. Pharmacol Rev. 1999;51: 83-133.
17. Field AS, Laurienti PJ, Yen YF, Burdette JH, Moody DM. Dietary caffeine consumption and withdrawal: confounding variables in quantitative cerebral perfusion studies? Radiology. 2003;227: 129-135.
18. Binnewijzend MA, Kuijer JP, Benedictus MR, van der Flier WM, Wink AM, Wattjes MP, et al. Cerebral blood flow measured with 3D pseudocontinuous arterial spin-labeling MR imaging in Alzheimer disease and mild cognitive impairment: a marker for disease severity. Radiology. 2013;267: 221-230.
19. Donahue MJ, Ayad M, Moore R, van Osch M, Singer R, Clemmons P, et al. Relationships between hypercarbic reactivity, cerebral blood flow, and arterial circulation times in patients with moyamoya disease. J Magn Reson Imaging. 2013;38: 1129-1139.
20. Lu H, Clingman C, Golay X, van Zijl PC. Determining the longitudinal relaxation time (T1) of blood at 3.0 Tesla. Magn Reson Med. 2004;52: 679-682.
21. Aslan S, Xu F, Wang PL, Uh J, Yezhuvath US, van Osch M, et al. Estimation of labeling efficiency in pseudocontinuous arterial spin labeling. Magn Reson Med. 2010;63: 765-771.
22. Garcia DM, Duhamel G, Alsop DC. Efficiency of inversion pulses for background suppressed arterial spin labeling. Magn Reson Med. 2005;54: 366-372.
23. Lu H, Nagae-Poetscher LM, Golay X, Lin D, Pomper M, van Zijl PC. Routine clinical brain MRI sequences for use at 3.0 Tesla. J Magn Reson Imaging. 2005;22: 13-22.
24. Herscovitch P, Raichle ME. What is the correct value for the brain--blood partition coefficient for water? J Cereb Blood Flow Metab. 1985;5: 65-69.
25. Heijtel DF, Mutsaerts HJ, Bakker E, Schober P, Stevens MF, Petersen ET, et al. Accuracy and precision of pseudo-continuous arterial spin labeling perfusion during baseline and hypercapnia: A head-to-head comparison with O HO positron emission tomography. Neuroimage. 2014;92C: 182-192.
26. St Lawrence KS, Wang J. Effects of the apparent transverse relaxation time on cerebral blood flow measurements obtained by arterial spin labeling. Magn Reson Med. 2005;53: 425-433.
27. Chalela JA, Alsop DC, Gonzalez-Atavales JB, Maldjian JA, Kasner SE, Detre JA. Magnetic resonance perfusion imaging in acute ischemic stroke using continuous arterial spin labeling. Stroke. 2000;31: 680-687.
28. Ashburner J. A fast diffeomorphic image registration algorithm. Neuroimage. 2007;38: 95-113.
29. Bland JM, Altman DG. Measuring agreement in method comparison studies. Stat Methods Med Res. 1999;8: 135-160.
30. Worsley KJ, Marrett S, Neelin P, Vandal AC, Friston KJ, Evans AC. A unified statistical approach for determining significant signals in images of cerebral activation. Hum Brain Mapp. 1996;4: 58-73.
31. Murphy K, Harris AD, Diukova A, Evans CJ, Lythgoe DJ, Zelaya F, et al. Pulsed arterial spin labeling perfusion imaging at 3 T: estimating the number of subjects required in common designs of clinical trials. Magn Reson Imaging. 2011;29: 1382-1389.
32. Chen Y, Wang DJ, Detre JA. Test-retest reliability of arterial spin labeling with common labeling strategies. J Magn Reson Imaging. 2011;33: 940-949.
33. Arnaud MJ. The pharmacology of caffeine. Prog Drug Res. 1987;31: 273-313.
34. Blanchard J, Sawers SJ. The absolute bioavailability of caffeine in man. Eur J Clin Pharmacol. 1983;24: 93-98.
35. Gevers S, van Osch MJ, Bokkers RP, Kies DA, Teeuwisse WM, Majoie CB, et al. Intra- and multicenter reproducibility of pulsed, continuous and pseudo-continuous arterial spin labeling methods for measuring cerebral perfusion. J Cereb Blood Flow Metab. 2011;31: 1706-1715.
36. Klomp A, Caan MW, Denys D, Nederveen AJ, Reneman L. Feasibility of ASL-based phMRI with a single dose of oral citalopram for repeated assessment of serotonin function. Neuroimage. 2012;63: 1695-1700.

37. MacIntosh BJ, Pattinson KT, Gallichan D, Ahmad I, Miller KL, Feinberg DA, et al. Measuring the effects of remifentanil on cerebral blood flow and arterial arrival time using 3D GRASE MRI with pulsed arterial spin labelling. J Cereb Blood Flow Metab. 2008;28: 1514-1522.
38. Hendrikse J, Petersen ET, van Laar PJ, Golay X. Cerebral border zones between distal end branches of intracranial arteries: MR imaging. Radiology. 2008;246: 572-580.
39. Chen Y, Parrish TB. Caffeine dose effect on activation-induced BOLD and CBF responses. Neuroimage. 2009;46: 577-583.

Chapter 5

General Discussion

In this thesis, I investigated whether advanced MR neuroimaging techniques, namely arterial spin labeling (ASL), diffusion tensor imaging (DTI) and resting state fMRI (rs-fMRI), could provide markers of neuropathology in the early stage of presenile dementia.

(Pathophysiological) assessment

We have shown that advanced MR neuroimaging can provide valuable information about the disease process in the brain based on its sensitivity to subtle structual and functional changes. This might be beneficial for several reasons. First, detecting subtle changes that precede macrostructural changes contributes to earlier diagnosis of both Alzheimer's disease (AD) and frontotemporal dementia (FTD) as well as related disorders without changes on conventional MRI, such as phenocopy frontotemporal dementia (phFTD). Second, these subtle MRI changes may provide more detailed insight into pathophysiological processes of neurodegeneration.

Possible neuropathological etiology of phenocopy FTD

The sensitivity of advanced MR techniques to previously undetected changes is exemplified by our study of phFTD, which is characterized by behavioral changes similar to behavioral variant FTD (bvFTD), such as disinhibition, apathy, loss of empathy, and perseverative, stereotypical or compulsive behavior [1]. Neither structural magnetic resonance imaging (MRI) nor fluorodeoxyglucose-positron emission tomography (FDG-PET) [2-5] shows abnormalities in this clinical entity, and there is no decline in activities of daily living. As this condition has a more benign course than bvFTD [4] without cognitive or functional decline over time [6] and normal neuroimaging, a neurodegenerative etiology is disputed. By using ASL, DTI and rs-fMRI in phFTD patients, we detected structural and functional abnormalities which partly overlapped with those found in bvFTD (**Chapter 3.1 and 3.2**). Our findings of right temporal cortical atrophy, white matter damage in the frontal and tempoparietal lobes and increased default mode network (DMN) connectivity in phFTD compared to controls were all consistent with neuropathological changes in bvFTD and with the specific behavioral symptomatology in phFTD. Additionally, we found increased perfusion in bilateral medial and left lateral frontal regions which, together with the increased functional connectivity, may indicate a functional compensation mechanism for incipient abnormalities in regions affected in bvFTD. Hence, using ASL, DTI and rs-fMRI we showed for the first time changes in this clinical entity that can be linked to the neurodegenerative process of bvFTD.

Regional relationships between incipient white and gray matter abnormalities in AD and bvFTD

We also explored the more fundamental contribution of advanced MRI techniques to characterize AD and bvFTD. Both diseases are characterized by distinct white matter (WM) and gray matter (GM) changes, but it is still largely unclear whether and how WM and GM abnormalities are related. One hypothesis is that WM and GM changes develop in a Wallerian-like degenerative manner, in which GM cell death leads to degeneration of WM tracts that connect affected GM regions. Another possible mechanism is that WM microstructural changes occur independently from GM volume loss and/or hypoperfusion [7]. As both diseases are characterized by specific WM and GM abnormalities, it is conceivable that these do no occur in isolation, but that they co-occur in the context of a common disease process. Regional coherence would indicate that abnormalities in local WM and GM occur to a similar degree, and thus reflect regionally concurrent degeneration. Therefore we investigated the regional coherence between regional abnormalities in WM microstructure and GM volume and perfusion in both AD and bvFTD. We first assessed WM microstructure and GM volume and perfusion abnormalities separately and subsequently correlated WM microstructural measures with associated GM volume and perfusion values in GM regions connected by the WM tract. We showed that measures of WM microstructure and GM volume and perfusion were more coherent in regions implicated in AD and bvFTD, suggesting concurrent degeneration in disease-specific networks. As this study investigated subtle incipient pathological changes, the results provided insight in the regional relationships between WM and GM changes in the early stage of neurodegeneration. This may contribute to the more fundamental understanding of the neuropathological processes in AD and bvFTD.

Overcoming small sample sizes: towards multicenter assessment

The techniques used in these studies enabled us to detect subtle changes despite relatively small patient sample sizes. This was probably conterbalanced by a well-defined group of patients, avoiding heterogeneity within the cohort. Still, small sample size limits statistical power by increasing the chance of Type II errors and thus false negatives. This is exacerbated by the need to correct to for multiple comparisons when assessing differences between groups, in order to control for Type I error (false positives). Although false positive results should obviously be avoided, (too) strict control of Type I error reduces the power or sensitivity to detect actual group differences, particularly with small samples. Therefore statistical analysis in small samples, such as the patient groups in this thesis, often involves a compromise between controlling for false positives while at the same time maintaining sufficient sensitivity or power to detect differences. This is reflected by the different approaches taken in this thesis to correct for multiple comparisons, as different considerations apply not only to the sample that is studied but also to the different techniques used.

With ASL, we found differences between AD and FTD patients versus controls in features used to classify them, without correcting for multiple comparisons. However, as this was done using permuation testing, which is known to have a low false positive detection rate, type I error was still sufficiently controlled for (**Chapter 2.1**). This apparent sensivity of ASL to pathophysiological processes, even when false positives are controlled for, was also illustrated by the detection of group differences while correcting for multiple comparisons between AD and FTD (**Chapter 2.2**), AD and bvFTD (**Chapter 2.3**), and phFTD and bvFTD (**Chap-**

ter 3.1), despite the small sample sizes. DTI proved to be robust as well, detecting differences between AD and bvFTD (**Chapter 2.3**) and between phFTD and bvFTD (**Chapter 3.2**) with correction for multiple comparisons applied. Although DTI and ASL by themselves showed to be sensitive to early pathophysiological changes, the correlations between these respective measures were studied both with and without correction for multiple comparisons, as the small patient groups apparently reduced power to such an extent that only a few significant differences in correlations could be detected (**Chapter 2.3**). This could also be due to the subtlety of the process studied, as the correlational methodology appeared to be sensitive to incipient abnormalities that were not (yet) evident as differences between groups. Nevertheless, the uncorrected correlations should be interpreted with caution and have to be confirmed in larger samples.

Functional connectivity as studied with rs-fMRI seemed to have less sensitivity for detecting abnormalities associated with phFTD than ASL and DTI (**Chapter 3.2**), as voxelwise differences between groups were only detectable when correction for multiple comparison was not applied. Due to this relatively lenient statistical threshold, the results thus carry the risk of being false positive. Although an attempt to reduce this risk was made by considering only those clusters that were also significantly different in the overall comparison between groups – which was corrected for the number of contrasts used – rs-fMRI effects may be more subtle than those assessed with ASL and DTI, and relatively more susceptible to limited power due to small sample size.

A related issue due to small patient samples, is the compromise of pooling data from different scanners, which may introduce effects due to scanner that may obscure effects truly due to group. We compared data of phFTD patients acquired on one scanner to data of bvFTD patients acquired on another scanner, and compared both patient groups to control data acquired on both scanners. Scanners were identical in terms of field strength and protocol, and although we explicitly and strictly corrected for an effect of scanner on the ASL data (**Chapter 3.1**) and have strong reasons to believe the use of different scanners will not have a detrimental effect on DTI and rs-fMRI data (**Chapter 3.2**), a potential effect of scanner cannot be fully ruled out. Nevertheless, concessions with respect to data acquisition and analysis are unfortunately commonly inherent to the study of relatively rare patient populations and thus small samples as described in this thesis.

Unfortunately, small sample size is a common limitation in many clinical neuroimaging studies. Future efforts should be aimed at expanding sample sizes to increase power and thus sensitivity of (clinical) imaging studies. Studies should therefore be conducted in the context of multicenter designs, in which patient recruitment as well as data acquisition are highly standardized. Standardized patient recruitment across multiple sites will result in a relatively homogeneous population. Standardized MRI acquisition is essential as qualitative and semi-quantitative imaging techniques are gradually replaced by quantitative imaging. Such quantitative imaging needs to be standardized in order to provide reference data for optimal individual clinical assessment, but also for pooling (research) data. Potential variability in quantitative imaging data should be minimized before comparing patients within and especially between imaging sites.

Standardization: a prerequisite for multicenter applications

The need for standardization is illustrated by our studies on the reproducibility of similar ASL sequences as implemented by different vendors. Fundamental differences exist between ASL implementations of different vendors in terms of labeling and readout [8], each with their specific advantages and disadvantages, which introduces substantial technical heterogeneity [9]. Knowing the variability between different vendor implementations is essential for exchanging and comparing ASL data. Therefore we assessed the reproducibility of vendor-supplied ASL sequences, by comparing two product sequences as implemented by two different vendors. Adjustment of sequence parameters was limited within the constraints imposed by the vendor-specific implementation, reflecting the de facto situation of commercially supplied sequences. As cerebral blood flow (CBF) measured with ASL is promoted as a quantitative measure, one would assume that measurements are independent of sequence implementation and parameters. We showed however that although baseline CBF on a total GM level was not different between vendors, regional CBF showed substantial variability (**Chapter 4.1 and 4.2**). On a total GM level, baseline CBF was mainly affected by physiological variability, but this averaged out between sequences, resulting in perfect agreement. Regional differences in baseline CBF however were caused by the different readouts (2D multi slice versus 3D single shot) employed by the different vendors. Such regional variability may dilute focal CBF changes, which are of interest in a clinical context, but also in detecting task-related changes in specific brain areas with functional ASL (fASL). Additionally, in the context of pharmacological ASL (phASL) one may want to assess locally restricted effects of a pharmaceutical agent (**Chapter 4.3**).

I conclude from our reproducibility studies that we can only benefit fully from the quantitative information provided by ASL if implementation is standardized. Therefore, future efforts should be directed at standardized acquisition and processing between vendors. This means employing identical sequences in terms of labeling scheme, but also in terms of readout, as outlined above. Additionally, acquisition parameters should be identical. In terms of image processing, there should be a consensus about the quantification model and its underlying assumptions. Recently, an attempt was made to realize such a standardized approach by publishing recommended implementations of ASL for clinical applications [10]. Such initiatives are essential for the clinical implementation of ASL, but also for setting up meaningful (multicenter) clinical trials. Thus, only by standardization, the gain of advanced quantitative MRI techniques for clinical practice and large scale multicenter research settings can be brought to maximum.

Clinical potential: the individual patient level

Advanced MR neuroimaging should ultimately benefit the diagnostic process in individual patients. As in many clinical imaging studies, the findings described in this thesis are based on group studies rather than the individual patient level. Group results cannot be generalized to every individual patient. Although patients are classified by means of best available clinical evidence, a certain degree of

uncertainty always remains, which only decreases as the disease progresses. Future studies should therefore focus on translation of group results to the individual patient level, to maximize the potential of these techniques to aid individual diagnosis. Although the studies described in this thesis report group results, those on ASL MRI in presenile early stage dementia (**Chapters 2.1 and 2.2**) carry implications for the individual patient too.

Contribution to early diagnosis of and differentiation between presenile AD and FTD

Presenile dementia (age of onset ≤65 years) comprises a substantial subset of dementia patients [11]. It more often has an atypical presentation and a more progressive disease course compared to late-onset dementia. Early diagnosis of presenile dementia remains difficult as different etiologies are hard to distinguish. Presenile AD more often has a non-amnestic presentation than late-onset AD [12]. Additionally, non-neurological causes of cognitive dysfunction are more prevalent in younger patients and may mimic neurodegenerative disorders, particularly complicating differentiation between psychiatric disease and FTD [13]. A considerable number of patients with presenile onset presents with primary progressive aphasia (PPA), in which the underlying pathology – AD or FTD – is often unclear [14]. Unfortunately, routine MR imaging in clinical practice shows structural abnormalities only in the later stages of AD and FTD [15]. Therefore, early diagnosis requires imaging techniques visualizing early brain changes such as FDG-PET, with distinct patterns of hypometabolism in AD compared to FTD [16]. However, FDG-PET has limited availability and relatively high costs [17], and therefore ASL has been proposed as an alternative as it is noninvasive and easily added to routine diagnostic MRI protocols. As hypoperfusion measured with ASL is consistent with PET in advanced AD and FTD [18,19] and the use of ASL in the earliest stages of dementia is being increasingly studied [20,21], we investigated the value of ASL in the early stage of presenile dementia.

To study whether ASL contributes to early differential diagnosis of AD and FTD, we compared CBF between AD patients, FTD patients, and controls (**Chapter 2.2**), and found lower CBF in the posterior cingulate cortex (PCC) in AD than in FTD. Diagnostic performance of PCC hypoperfusion to differentiate AD from FTD was 74%. Additionally, focal hypoperfusion in the ACC in FTD and more extensive hypoperfusion in AD, which was most prominent in the precuneus, discriminated patients from controls with diagnostic performances of 78% and 85% respectively. As GM volume was not different between patient groups, this indicates that the distinction between AD and FTD at this stage could be based on regional CBF only, as measured with ASL.

Future potential: computer aided diagnosis

We collected ASL data at a time point in the disease process when diagnosis was not yet definitive. Thus, we show that using ASL the diagnosis can be made at an earlier time point in the disease process than with routine clinical criteria, even at the individual patient level. By quantitative measurement of CBF in the PCC, ACC and precuneus, the clinician can distinguish presenile AD and FTD in the early stage in the individual patient. This may be further facilitated by the implementation of computer aided diagnosis (**Chapter 2.1**), by applying machine learning to classify a group of healthy controls and a group of patients with early stage AD or FTD. We showed that classification based on CBF performed equally well as structural data. However, CBF markers did not show added value over structural markers. This may be the result of the patient sample comprising both AD and FTD patients. However, ASL does provide added value over structural imaging in classifying AD and FTD when comparing separate samples of AD patients and FTD patients to each other, as in **Chapter 2.2**. Taken together, our findings suggest that automated computer classification may facilitate diagnosis of dementia which we can expect even more benefit from when classifiers are trained on better defined patient samples (e.g genetically confirmed diagnosis). Future efforts should therefore be directed at optimizing specificity of machine learning techniques by applying them to well defined samples. Eventually, computer aided diagnosis may be able to provide for each individual patient a probability distribution for underlying pathology to help clinicians reach a diagnostic decision.

CONCLUSION

In conclusion, advanced MR neuroimaging contributes to early and differential diagnosis of presenile early stage dementia, and its clinical implementation may be augmented by means of computer automated classification of each individual patient. In addition to added clinical value, techniques such as ASL, DTI and rs-fMRI add to the more fundamental understanding of neurodegenerative diseases by revealing subtle and incipient pathophysiological changes. Full benefit of these techniques for clinical practice as well as large scale multicenter research settings should be realized by standardization of patient recruitment, data acquisition and processing.

REFERENCES

1. Neary D, Snowden JS, Gustafson L, Passant U, Stuss D, Black S, et al. Frontotemporal lobar degeneration: a consensus on clinical diagnostic criteria. Neurology. 1998;51: 1546-1554.
2. Kipps CM, Hodges JR, Fryer TD, Nestor PJ. Combined magnetic resonance imaging and positron emission tomography brain imaging in behavioural variant frontotemporal degeneration: refining the clinical phenotype. Brain. 2009;132: 2566-2578.
3. Kipps CM, Davies RR, Mitchell J, Kril JJ, Halliday GM, Hodges JR. Clinical significance of lobar atrophy in frontotemporal dementia: application of an MRI visual rating scale. Dement Geriatr Cogn Disord. 2007;23: 334-342.
4. Davies RR, Kipps CM, Mitchell J, Kril JJ, Halliday GM, Hodges JR. Progression in frontotemporal dementia: identifying a benign behavioral variant by magnetic resonance imaging. Arch Neurol. 2006;63: 1627-1631.
5. Kerklaan BJ, Berckel BN, Herholz K, Dols A, Flier WM, Scheltens P, et al. The Added Value of 18-Fluorodeoxyglucose-Positron Emission Tomography in the Diagnosis of the Behavioral Variant of Frontotemporal Dementia. Am J Alzheimers Dis Other Demen. 2014.
6. Mioshi E, Hodges JR. Rate of change of functional abilities in frontotemporal dementia. Dement Geriatr Cogn Disord. 2009;28: 419-426.
7. Amlien IK, Fjell AM. Diffusion tensor imaging of white matter degeneration in Alzheimer's disease and mild cognitive impairment. Neuroscience. 2014;276: 206-215.
8. Kilroy E, Apostolova L, Liu C, Yan L, Ringman J, Wang DJ. Reliability of two-dimensional and three-dimensional pseudo-continuous arterial spin labeling perfusion MRI in elderly populations: comparison with 15O-water positron emission tomography. J Magn Reson Imaging. 2014;39: 931-939.
9. Vidorreta M, Wang Z, Rodriguez I, Pastor MA, Detre JA, Fernandez-Seara MA. Comparison of 2D and 3D single-shot ASL perfusion fMRI sequences. Neuroimage. 2012;66C: 662-671.
10. Alsop DC, Detre JA, Golay X, Gunther M, Hendrikse J, Hernandez-Garcia L, et al. Recommended implementation of arterial spin-labeled perfusion MRI for clinical applications: A consensus of the ISMRM perfusion study group and the European consortium for ASL in dementia. Magn Reson Med. 2015;73: 102-116.
11. van der Flier, W. M., Scheltens P. Epidemiology and risk factors of dementia. J Neurol Neurosurg Psychiatr. 2005;76 Suppl 5: v2-7.
12. Koedam EL, Lauffer V, van der Vlies AE, van der Flier WM, Scheltens P, Pijnenburg YA. Early-versus late-onset Alzheimer's disease: more than age alone. J Alzheimers Dis. 2010;19: 1401-1408.
13. Rossor MN, Fox NC, Mummery CJ, Schott JM, Warren JD. The diagnosis of young-onset dementia. Lancet Neurol. 2010;9: 793-806.
14. Gorno-Tempini ML, Hillis AE, Weintraub S, Kertesz A, Mendez M, Cappa SF, et al. Classification of primary progressive aphasia and its variants. Neurology. 2011;76: 1006-1014.
15. Frisoni GB, Fox NC, Jack CR,Jr, Scheltens P, Thompson PM. The clinical use of structural MRI in Alzheimer disease. Nat Rev Neurol. 2010;6: 67-77.
16. Ishii K. PET approaches for diagnosis of dementia. AJNR Am J Neuroradiol. 2014;35: 2030-2038.
17. McMahon PM, Araki SS, Sandberg EA, Neumann PJ, Gazelle GS. Cost-effectiveness of PET in the diagnosis of Alzheimer disease. Radiology. 2003;228: 515-522.
18. Hu WT, Wang Z, Lee VM, Trojanowski JQ, Detre JA, Grossman M. Distinct cerebral perfusion patterns in FTLD and AD. Neurology. 2010;75: 881-888.
19. Du AT, Jahng GH, Hayasaka S, Kramer JH, Rosen HJ, Gorno-Tempini ML, et al. Hypoperfusion in frontotemporal dementia and Alzheimer disease by arterial spin labeling MRI. Neurology. 2006;67: 1215-1220.
20. Wang Z. Characterizing early Alzheimer's disease and disease progression using hippocampal volume and arterial spin labeling perfusion MRI. J Alzheimers Dis. 2014;42 Suppl 4: S495-502.
21. Wierenga CE, Hays CC, Zlatar ZZ. Cerebral blood flow measured by arterial spin labeling MRI as a preclinical marker of Alzheimer's disease. J Alzheimers Dis. 2014;42 Suppl 4: S411-9.

Chapter 6

Summary
Samenvatting

SUMMARY

Dementia is a syndrome affecting cognitive functions and behavior, with an overwhelming impact on both patients and caregivers. An estimated number of 35.6 million patients suffers from dementia, with a subset affected before the age of 65 years, i.e. presenile dementia [1]. Alzheimer's disease (AD) is the most common underlying cause of dementia, both at older and younger age. Frontotemporal dementia (FTD) is a rare cause of dementia at old age, but relatively prevalent among the younger population [2]. Establishing the underlying cause of presenile dementia in the early stage proves to be difficult as younger dementia patients often initially present with atypical symptoms. Additionally, cognitive dysfunction in younger patients may also have a non-neurological cause, nevertheless resembling a neurodegenerative disorder [3]. Diagnosis in patients presenting with language dysfunction as its primary clinical feature (primary progressive aphasia, PPA) is particularly difficult, as the underlying pathology can either be AD or FTD [4]. Morphological brain changes associated with the early stage of dementia are often absent or unspecific on routine clinical magnetic resonance imaging (MRI). Advanced MR neuroimaging techniques may be more sensitive to early neurodegenerative processes [5] as they can capture functional and microstructural brain changes that precede (macro)structural damage, as discussed in the introductory **Chapter 1**.

The advanced techniques used to study presenile dementia in this thesis are resting state functional MRI (rs-fMRI), arterial spin labeling (ASL), and diffusion tensor imaging (DTI). Rs-fMRI measures spontaneous fluctuations of brain activation. By assessing which brain regions are simultaneously active, it allows us to map functional connections in the brain. Such functional networks show alterations as a result of neurodegeneration before atrophy occurs. Another way to image synaptic dysfunction is by using ASL-MRI, which quantifies brain perfusion. As well as changes in brain function, microstructural changes in the white matter (WM) of the brain precede (macro)structural damage. These changes can be detected with DTI which can be used to reconstruct WM trajectories, visualizing structural connectivity. In this thesis, I investigated whether rs-fMRI, ASL and DTI could serve as early neuropathological markers of presenile dementia.

Section 2 describes the early brain changes found in presenile AD and FTD using ASL and DTI. In **Chapter 2.1**, the added value of ASL relative to structural MRI was investigated for the computer aided classification of presenile dementia patients with AD or FTD versus controls. Patients and controls were classified based on cerebral blood flow (CBF) as perfusion marker, gray matter (GM) volume as structural atrophy marker, and their combination using a voxel-wise and region of interest (ROI)-wise approach. We found that the voxel-wise approach achieved more accurate results. When used as a separate measure, CBF was a good diagnostic marker for dementia. However, combining ASL with structural MRI had only little added diagnostic value, as it did not significantly improve accuracy of using structural MRI by itself.

In **Chapter 2.2** we extended these findings by investigating ASL for the differentiation between AD and FTD. We compared CBF between AD and FTD patients and controls, and found lower CBF in the posterior cingulate cortex (PCC) in AD than in FTD, differentiating both disorders with a diagnostic performance of 74%. Additionally, focal hypoperfusion in the anterior cingulate cortex (ACC) in FTD and more extensive hypoperfusion in AD mainly in the precuneus, discriminated patients from controls with diagnostic performances of 78% and 85% respectively. GM volume did not differ between patient groups, indicating that differential diagnosis of AD and FTD at this stage could only be based on regional CBF.

In **Chapter 2.3** we studied regional associations between GM and WM measures in AD and behavioral variant FTD (bvFTD) using structural imaging, ASL and DTI. Compared with controls, WM and GM measures correlated more strongly between the cingulum and frontotemporal GM in AD, and temporoparietal GM in bvFTD. Additionally, in AD compared with controls, inferior fronto-occipital fasciculus microstructure correlated more strongly with occipital GM perfusion. The finding that correlations are particularly strong in regions implicated in AD and bvFTD suggests that WM and GM abnormalities co-occur as a common disease process. Moreover, this methodology allowed for the detection of incipient pathology that would have gone undetected in comparative group analyses.

Summarizing our findings on early brain changes in presenile AD and FTD, I conclude that advanced MR neuroimaging techniques are sensitive to subtle incipient changes. This facilitates early diagnosis and differentiation of AD and FTD, and contributes to their respective characterization in a more fundamental way.

Section 3 focused on phenocopy FTD (phFTD) patients, who present with the characteristic behavioral features of bvFTD but without cognitive or functional decline or abnormalities on routine structural imaging. Using advanced techniques, we show that there are structural and perfusion changes (**Chapter 3.1**) as well as changes in functional networks and white matter microstructure (**Chapter 3.2**) in these patients. We found that phFTD patients showed cortical atrophy, most prominently in the right temporal lobe. Regional GM volume was otherwise generally different from neither controls nor from bvFTD, even though bvFTD showed extensive frontotemporal atrophy. We also found hyperperfusion in the left prefrontal cortex compared to bvFTD and to a lesser extent to controls. Additionally, compared with controls phFTD patients showed a subtle increase in default mode network (DMN) functional connectivity, as well as subtle microstructural changes mainly in the cingulum, uncinate fasciculus and genu of the corpus callosum. BvFTD had a lower increase of DMN connectivity, and more extensive microstructural white matter changes. These findings in phFTD were all consistent with neuropathological changes in bvFTD and with the specific behavioral symptomatology in phFTD. Additionally, the increased perfusion and increased functional connectivity may indicate a functional compensation mechanism for incipient pathology in regions affected in bvFTD.

In summary, using ASL, DTI and rs-fMRI we showed for the first time changes in this clinical entity that can be linked to the neurodegenerative process of bvFTD.

As Section 2 and 3 illustrate the value of ASL as a clinical imaging tool, exploring its wider application – including but not limited to dementia – is of potential inter-

est. However, despite being a quantitative technique, there is extensive variability between ASL data acquired on MR scanners of different vendors, as each vendor provides their own particular ASL implementation. In **Section 4** we reported to which extent the implementation of similar sequences by two different vendors affect ASL perfusion data in several experimental designs in healthy young controls. In **Chapter 4.1**, we assessed whether baseline CBF measurements were reproducible when acquired with sequences from different vendors. We found that on a total GM level, mean CBF was almost equal between sequences, and that variation between sequences was not different from variation within the same sequence. On a regional GM level however, mean CBF and variation was different between sequences, most likely as a result of the different readouts (2D multi slice versus 3D single shot) employed by the different vendors.

Such regional variability may dilute focal CBF changes, which are of interest in detecting task-related changes in specific brain areas with functional ASL (fASL). This was the focus of **Chapter 4.2.** We investigated the sensitivity of both sequences to detect task-related brain activation, as well as their reproducibility in quantifying such activation. We showed that sensitivity for motor activation was sufficient with each sequence, and comparable between sequences. Reproducibility of CBF in the motor cortex was reasonably good for resting CBF, within as well as between sequences, whereas that of absolute CBF changes was relatively low. This suggests that resting CBF may provide a consistent baseline to compare task-related activation to, but that absolute regional CBF changes are more variable, and should be interpreted cautiously when acquired with two pCASL product sequences.

The variability of absolute CBF changes was further demonstrated in **Chapter 4.3**, where we assessed reproducibility of pharmacological ASL (phASL) by comparing caffeine induced perfusion decrease between sequences. Normalizing absolute CBF decreases to baseline CBF reduced the effect of physiological variability of baseline CBF, which resulted in mean CBF decrease variation to be comparable between vendors. Nevertheless, the mean CBF decrease itself remained different between vendors after normalization. Additionally, on a regional level there were still differences between sequences in both mean CBF decrease and variation in CBF decrease.

I conclude from our reproducibility studies that we can only compare and exchange quantitative CBF data if ASL implementation is standardized.

In **Section 5** the main findings, their clinical implication and methodological considerations are discussed. In conclusion, advanced MR neuroimaging contributes to early and differential diagnosis of presenile early stage dementia. In addition to added clinical value, advanced techniques aid the more fundamental understanding of neurodegenerative diseases by revealing subtle and incipient pathophysiological changes. Full benefit of these techniques for clinical practice as well as large scale multicenter research settings should be realized by standardization of patient recruitment, data acquisition and processing.

REFERENCES

1. Prince M, Bryce R, Albanese E, Wimo A, Ribeiro W, Ferri CP. The global prevalence of dementia: a systematic review and metaanalysis. Alzheimers Dement. 2013;9: 63-75.e2.
2. van der Flier, W. M., Scheltens P. Epidemiology and risk factors of dementia. J Neurol Neurosurg Psychiatr. 2005;76 Suppl 5: v2-7.
3. Rossor MN, Fox NC, Mummery CJ, Schott JM, Warren JD. The diagnosis of young-onset dementia. Lancet Neurol. 2010;9: 793-806.
4. Gorno-Tempini ML, Hillis AE, Weintraub S, Kertesz A, Mendez M, Cappa SF, et al. Classification of primary progressive aphasia and its variants. Neurology. 2011;76: 1006-1014.
5. Sperling RA, Aisen PS, Beckett LA, Bennett DA, Craft S, Fagan AM, et al. Toward defining the preclinical stages of Alzheimer's disease: recommendations from the National Institute on Aging-Alzheimer's Association workgroups on diagnostic guidelines for Alzheimer's disease. Alzheimers Dement. 2011;7: 280-292.

SAMENVATTING

Dementie is een syndroom dat gekenmerkt wordt door achteruitgang van cognitieve functies en problemen in het dagelijks functioneren. Tevens kunnen er gedragsveranderingen optreden. Wereldwijd lijden er naar schatting 35.6 miljoen mensen aan dementie. Bij een gedeelte van hen treedt de ziekte op voor het 65e levensjaar, zogenaamde preseniele dementie. Net zoals bij dementie op oudere leeftijd is Alzheimer dementie (AD) meest voorkomende oorzaak van dementie op jongere leeftijd, gevolgd door frontotemporale dementie (FTD). Tot op heden is het vaststellen van de onderliggende oorzaak van preseniele dementie in het vroege stadium van de ziekte lastig. Bij jongere patiënten is de presentatie vaak niet typisch voor de onderliggende vorm van dementie. Bovendien hebben cognitieve problemen bij jongere patiënten vaker een niet-neurologische oorzaak, zoals bijvoorbeeld een depressie, ondanks dat het klinisch beeld wel sterke gelijkenissen vertoont met een neurodegeneratieve aandoening. Daarnaast is er een groep jongere patiënten die zich voornamelijk presenteert met taalproblemen, zgn. primair progressieve afasie (PPA). Het diagnosticeren van de onderliggende oorzaak van PPA is in het bijzonder moeilijk, aangezien hier zowel AD als FTD aan ten grondslag kan liggen.

Vaak kan de vermoedelijke onderliggende oorzaak van dementie bevestigd of ondersteund worden door structurele magnetische resonantie (MR) beelden van de hersenen. Helaas zijn in een vroeg stadium structurele veranderingen vaak nog niet of amper zichtbaar op standaard klinische MR beelden. Er wordt echter verondersteld dat veranderingen in de (macro)structuur van de hersenen voorafgegaan worden door subtielere veranderingen in o.a. hersenfunctie en microstructuur. Deze subtiele veranderingen zijn te detecteren met nieuwe geavanceerde MR technieken, die als dusdanig sensitiever zouden zijn voor vroege neurodegeneratieve processen dan standaard klinische MR beeldvorming.

In dit proefschrift heb ik onderzocht of metingen met geavanceerde MR technieken kunnen dienen als neuropathologische markers voor het vroege stadium van preseniele dementie. De daarvoor gebruikte technieken zijn *resting state functionele magnetic resonance imaging* (rs-fMRI), *arterial spin labeling* (ASL), en *diffusion tensor imaging* (DTI) zoals geïntroduceerd in **hoofdstuk 1**. Rs-fMRI visualiseert de spontane activiteit van de hersenen. Door te analyseren welke hersengebieden tegelijkertijd actief zijn, kunnen we functionele netwerken in het brein in kaart brengen. De activiteit binnen deze netwerken kan veranderen als gevolg van een neurodegeneratief proces. Met rs-fMRI kunnen we deze afwijkingen in functionele connectiviteit detecteren, nog voor structurele schade optreedt. Een tweede marker voor functie is de doorbloeding van de hersenen. Afwijkingen daarin kunnen we meten en kwantificeren met ASL. Naast functionele veranderingen wordt (macro)structurele schade voorgegaan door microstructurele veranderingen van de witte stof in het brein. Deze kunnen worden opgespoord met behulp van DTI.

In **sectie 2** beschrijf ik de vroege veranderingen in het brein van patiënten met preseniele AD en FTD gemeten met ASL en DTI. In **hoofdstuk 2.1** onderzochten we de toegevoegde waarde van ASL ten opzichte van structurele MRI voor computer-gestuurde diagnose. Patiënten met AD of FTD en gezonde controles

werden automatisch geclassificeerd op basis van doorbloeding gemeten met ASL, volume van de grijze stof gemeten met structurele MRI, en een combinatie van beide. ASL op zichzelf bleek een goede techniek voor het identificeren van patiënten met dementie, maar had slechts geringe toegevoegde diagnostische waarde ten opzichte van de meer gangbare structurele MRI.

Deze bevindingen hebben we in **hoofdstuk 2.2** uitgebreid door te onderzoeken of ASL onderscheid kan maken tussen patiënten met AD en FTD. Hiervoor vergeleken we ASL data van patiënten met AD, patiënten met FTD en gezonde controles. De doorbloeding van het posterieure cingulum was lager bij AD patiënten dan FTD patiënten, en kon de patiënten onderscheiden met een diagnostisch vermogen van 74%. Daarnaast kon enerzijds de regionale afname in doorbloeding van het anterieure cingulum bij FTD en anderzijds de meer wijdverbreide afname bij AD onderscheid maken tussen patiënten en controles met een diagnostisch vermogen van respectievelijk 78 en 85%. Noemenswaardig is dat het volume van de grijze stof niet verschilde tussen de patiënten. Dit impliceert dat in dit stadium het onderscheid tussen AD en FTD dus alleen gemaakt kan worden op basis van regionale verschillen in doorbloeding gemeten met ASL.

In **hoofdstuk 2.3** bestudeerden we regionale samenhang tussen verschillende hersenmaten bij AD en FTD. We gebruikten hiervoor structurele MRI, ASL en DTI data van patiënten met AD en met de gedragsvariant van FTD (*behavioral variant FTD*, bvFTD). Ten opzichte van controles vonden we bij AD patiënten een sterkere correlatie tussen de microstructuur van het cingulum en de frontotemporale grijze stof, en bij FTD patiënten tussen het cingulum en de temporopariëtale grijze stof. Daarnaast lieten AD patiënten een sterkere correlatie zien tussen de microstructuur van de inferieure fronto-occipitale fasciculus en de occipitale grijze stof. De bevinding dat correlaties voornamelijk sterk zijn in gebieden die betrokken zijn bij AD dan wel bvFTD suggereert dat afwijkingen van de witte en grijze stof samen optreden, wellicht in het kader van een gemeenschappelijk ziekteproces. Bovendien toont deze correlationele methodologie beginnende pathologie aan die in reguliere (groeps)analyses niet aan het licht komt.

Samenvattend laten we zien dat geavanceerde MR technieken gevoelig zijn voor subtiele beginnende veranderingen in het vroege stadium van AD en FTD. Dit bevordert de vroegere diagnose van en onderscheid tussen AD en FTD. Ook draagt het op een meer fundamentele wijze bij aan de pathofysiologische kennis van beide aandoeningen.

In **sectie 3** beschrijf ik bevindingen bij patiënten met *phenocopy* FTD (phFTD). Deze patiënten presenteren zich met de typische gedragskenmerken van bvFTD, maar vertonen geen achteruitgang in cognitie of dagelijks functioneren, noch hebben zij afwijkingen op standaard MR beeldvorming. Met behulp van geavanceerde MR technieken hebben wij aangetoond dat er bij deze patiënten wel degelijk sprake is van afwijkingen in het brein. PhFTD patiënten lieten corticaal volumeverlies zien, voornamelijk in de rechter temporaalkwab. Verder verschilden de regionale grijze stof volumes van phFTD patiënten doorgaans niet van bvFTD patiënten, terwijl er bij deze laatste groep sprake was van uitgesproken frontotemporaal volumeverlies. Daarnaast was de doorbloeding van de linker prefron-

tale cortex bij phFTD patiënten hoger dan bij bvFTD patiënten, en in mindere mate ook hoger dan in controles (**hoofdstuk 3.1**). Ook was er bij phFTD patiënten een toename in de functionele connectiviteit van het *default mode network* (DMN) in vergelijking met controles, evenals subtiele afwijkingen in de microstructuur van de witte stof. Bij bvFTD patiënten was de toename van functionele connectiviteit binnen het DMN kleiner en was de microstructurele schade aanzienlijker (**hoofdstuk 3.2**). Deze (micro)structurele bevindingen in de grijze en witte stof bij phFTD zijn in overeenstemming met pathofysiologische veranderingen zoals die worden gezien bij bvFTD, en zouden de karakteristieke gedragsmatige symptomen bij phFTD kunnen verklaren. De toename in zowel doorbloeding als functionele connectiviteit van gebieden betrokken bij bvFTD zou daarnaast kunnen duiden op een functioneel compensatiemechanisme in reactie op beginnende pathologie bij phFTD.

Samenvattend hebben we bij phFTD – een tot nu toe klinisch gedefinieerd syndroom – veranderingen van het brein aangetoond met behulp van ASL, DTI en rs-fMRI, die tevens gerelateerd lijken te zijn aan het neurodegeneratieve proces zoals gezien bij bvFTD.

Uit bovenstaande bevindingen blijkt duidelijk de klinische waarde van ASL en de potentiële relevantie van een bredere toepassing van ASL. Een voorbehoud hierbij is dat ondanks dat ASL in beginsel een kwantitatieve techniek is, er aanzienlijke variabiliteit bestaat tussen ASL data afkomstig van verschillende MR scanners. Dit is met name het geval bij scanners van verschillende fabrikanten, aangezien elke fabrikant een eigen specifieke implementatie heeft. In **sectie 4** onderzoek ik in welke mate de implementatie door verschillende fabrikanten invloed heeft op kwantitatieve ASL data. We scanden daarvoor gezonde jonge controles met een vergelijkbare ASL sequentie op verschillende scanners. In **hoofdstuk 4.1** onderzochten we in welke mate metingen van de doorbloeding tijdens rust de reproduceerbaar waren. We vonden dat hoewel de gemiddelde doorbloeding in de totale grijze stof vrijwel gelijk was, regionale doorbloeding niet gelijk was tussen de verschillende scanners. Dit is hoogstwaarschijnlijk het gevolg van verschillende *read-outs* gebruikt door de fabrikanten (*2D multislice* ten opzichte van *3D single shot)*. Regionale variabiliteit kan de detectie van lokale veranderingen in doorbloeding vertroebelen, terwijl deze juist van belang zijn – niet alleen in klinische context, maar bijvoorbeeld ook in het kader van taakgerelateerde hersenactiviteit. Daarom bestudeerden we in **hoofdstuk 4.2** voor beide sequenties de sensitiviteit voor het detecteren van taakgerelateerde hersenactiviteit. Ook onderzochten we in welke mate de kwantificatie van de taakgerelateerde verandering in doorbloeding reproduceerbaar was. Beide sequenties bleken voldoende en vergelijkbaar sensitief voor het detecteren van regionale activiteit. Regionale doorbloeding tijdens rust was redelijk reproduceerbaar, maar de reproduceerbaarheid van absolute veranderingen in doorbloeding was relatief laag. Ook de absolute afname van doorbloeding als gevolg van cafeïne-inname (zgn. farmacologische ASL) zoals beschreven in **hoofdstuk 4.3** was slecht reproduceerbaar tussen sequenties, zelfs met inachtneming van fysiologische variabiliteit.

Op basis van ons onderzoek naar reproduceerbaarheid kunnen we concluderen dat kwantitatieve ASL data alleen vergeleken en uitgewisseld kan worden tussen scanners van verschillende fabrikanten als de implementatie van de sequentie volledig wordt gestandaardiseerd.

In **sectie 5** worden tenslotte de algemene bevindingen en daaruit volgende klinische implicaties besproken, evenals methodologische overwegingen. De conclusie luidt dat geavanceerde MR beeldvorming van de hersenen bijdraagt aan de diagnose van en differentiatie tussen verschillende vormen van preseniele dementie in het vroege stadium. Naast een toegevoegde waarde voor de klinische praktijk brengen deze geavanceerde technieken subtiele en beginnende pathofysiologische veranderingen aan het licht, die bijdragen aan de meer fundamentele kennis van neurodegeneratieve aandoeningen. De volledige potentie van deze technieken voor de klinische praktijk moet gerealiseerd en benut worden door standaardisatie van zowel patiëntenpopulaties als van dataverzameling en –verwerking.

Chapter 7

Dankwoord
List of publications
PhD Portfolio
About the author

Dankwoord

Mijns inziens is een promotietraject alleen mogelijk met de commitment van zoveel andere mensen dan alleen de onderzoeker zelf, en daarom wil ik graag mijn dank uitspreken aan iedereen die op welke manier dan ook een bijdrage heeft geleverd hieraan!

Ten eerste mijn grote dank aan alle deelnemers aan de Iris, Iris+ en VESPA studie. Zonder jullie vrijwillige en belangeloze inzet zou onderzoek niet mogelijk zijn. Ik heb zeer veel bewondering en waardering voor jullie betrokkenheid bij dit onderzoek.

Mijn promotoren, prof. dr. Aad van der Lugt en prof. dr. John van Swieten, heel veel dank voor al jullie begeleiding, vooral tijdens de cruciale eindfase. Beste Aad, bedankt voor het vertrouwen, dat je samen met Marion mij als 'onbekende' neuroscience student uit Utrecht de kans gaf dit project te mogen uitvoeren. Bedankt ook voor alle mogelijkheden buiten het onderzoek zelf, ik heb zo veel opgestoken van alle cursussen en congressen die ik heb mogen bijwonen. Tenslotte was geen paper compleet zonder jouw laatste kritische blik. Bedankt voor alles! Beste John, ik waardeer het heel erg dat ik als onderzoeker van de Radiologie ook deel uit mocht maken van de Neurologie en het Alzheimercentrum. Bedankt voor je betrokkenheid bij de studies, met name je moeite voor de inclusie en het meedenken hoe we deze konden verbeteren. Ook wil ik graag je begeleiding bij het schrijven noemen, ik heb veel geleerd van jouw kritische manier van lezen. Veel dank voor alle inspanningen!

Mijn co-promotor, dr. Marion Smits: ik ben je enorm dankbaar voor je nauwe betrokkenheid al die jaren bij elke stap van elke studie. Dat jij altijd tijd maakte voor de projecten en voor mij als persoon heb ik echt als een voorrecht ervaren. Bedankt voor de ontzettend fijne begeleiding en samenwerking.

Dank ook aan de leden van de promotiecommissie voor het willen plaatsnemen hierin en voor het kritisch beoordelen van het proefschrift: prof. dr. Wiesje van der Flier, prof. dr. Serge Rombouts, prof. dr. Maarten Frens, prof. dr. Wiro Niessen, dr. Meike Vernooij en dr. Francesco Mattace Raso.

Dear Carolina, partner in crime, if it wasn't for you this book wouldn't have been there. I wouldn't have known about this PhD project if you would not have looked out for me as you have done since we met doing our neuroscience internship together in the UMC. Thank you for everything we shared, and still do, despite the distance. I feel privileged to have you look out for me on the day of my defense as well.

Lieve Rozanna, van 'geachte mevrouw Steketee' in 2011 tot aan mijn zijde staan als paranimf op D-day. Die afgelopen jaren heb jij je niet alleen ontpopt tot een super collega, maar ook en vooral tot een enorm dierbare vriendin. Bedankt voor je eeuwige betrokkenheid, die jij zelf zo vanzelfsprekend lijkt te vinden, maar waar ik me nog regelmatig gelukkig over prijs. R-team FTW ;).

Er komt heel wat kijken bij het opzetten en uitvoeren van een klinische (f)MRI studie, zonder de bijdrage van de volgende mensen was dit niet gelukt. Inge de Koning, jouw input voor de fMRI paradigma's voor de Iris studie is zeer waardevol geweest. Ook jouw inzet voor de Iris+ studie wil ik noemen, bedankt voor het nagaan en het benaderen van alle deelnemers! Robert Jan Osse, ook aan jou veel dank dat we mochten leunen op jouw expertise voor de Iris+ studie. Hanneke Muharam, dank voor de moeite onderzoek te accomoderen op de klinische scanners. Sylvia Bruininks, bedankt voor mij de fijne kneepjes van het scannen bijbrengen en Bob Visser voor alle hulp met de fMRI set up. Jan Linnebank ben ik zeer erkentelijk voor zijn hulp met het programmeren van de fMRI taken. Mart Rentmeester, wat te doen zonder jou en je hulp met (fMRI) computers, software, en PACS! Voor alle ondersteuning wil ik graag het trialbureau bedanken, vooral Laurens Groenendijk en Caroline van Bavel voor hun hulp met de METC aanvragen. Ook veel dank iedereen van het research office en het secretariaat, met name Fania Jarmohamed, Nora el Issati en Diane van Meurs. Jolanda Meijer, fijn dat ik voor zo ongeveer elke OO&O kwestie en nog 100 andere dingen bij jou terecht kon. Ton Everaers, veel dank voor de hulp met de opmaak van dit proefschrift!

Dear Gavin, finally I get the chance to thank you without you not wanting to listen ;). There were so many times I have been 'worried' due to some scanner issue, and you always tried to fix it, even if I was scanning during weekends. Without you, much of the data in this thesis would not have been there. Thank you!

Esther, bedankt voor de fijne samenwerking! Ik ben heel blij met alle resultaten die we samen uit de Iris studie hebben gekregen. Stefan, ook veel dank aan jou voor de betrokkenheid bij het project. Henk Jan, ook al was VESPA een enigszins hectische ervaring, we hebben er mooie resultaten mee geboekt! Ik ben onder de indruk van je ontembare enthousiasme, zelfs een pilot scannen om 3u 's nachts in het AMC ging jou niet te ver. Aart Nederveen, bedankt voor de fijne samenwerking tussen Amsterdam en Rotterdam, en Thijs van Osch veel dank dat we op jouw ASL expertise mochten leunen.

Dank ook aan alle mensen van wie ik door de jaren heen veel heb mogen opsteken in de fMRI/AMBER/BKAA meetings: Freddy van der Veen, Jos van der Geest, Tonya White, Ryan Muetzel, Gerbrich van den Bosch, Hanan El Marroun, Reshmi Marhe, Ivo van den Berg, Gabry Mies, Karen Schuil, en Margriet Veldhorst.

Dr. Sjel, volgens mij moest jij even wennen aan mij als kamergenoot, maar ik miste jou wel hoor toen je de kliniek in ging! Bedankt voor de gezelligheid op de kamer en het gedogen van het kippenhok dat er af en toe ontstond door mijn aanwezigheid. Mijn 'room13' kamergenootjes in het Na-gebouw: Carolina, Rozanna, Anouk, Renske, Taihra, Rinske en Marjolein: een nog groter kippenhok maar een oh zo fijne basis. Vooral dankzij jou Anouk, dank je wel voor je eeuwig luisterende oor en alle gezelligheid tijdens de vele koffiepauzes en wandelingetjes door het Museumpark. Thanks to all other people that make the 25th/26th floor and beyond a colorful environment: Pierre, Valerio, Gennady, Jean Marie, Esther, Carolyn, Joost, Gaby, Sandra, Marcel, Marius, Hakim, Ewoud, Gokhan, Ghassan, Piotr, Jasper, and Daniel. Jory, bedankt voor alle therapeutische koffiepauzes. Sophie Ooms en Rick Zuur, bedankt voor al het werk wat jullie voor de Iris studie hebben verricht tijdens jullie keuze-onderzoek.

Maartje, fMRI buddy van het eerste uur! Wat was het fijn om met jou fMRI meetings te organiseren, aan fMRI opstellingen te prutsen, te SPMen, zelfs jouw paranimf te mogen zijn, en zoveel meer. Ik heb heel veel van je geleerd en dat doe ik nog steeds: ik heb zo veel bewondering voor jou als wetenschapper! Dank je wel voor al je support en betrokkenheid, zelfs nu je 'helemaal' in Nijmegen zit.

Dank aan alle mensen van de neuro, ten eerste natuurlijk Janne! Life is like a long weekend met jou, zelfs op werk! Heb genoten van onze cursussen, congressen, meetings, werksessies in het café, en zo veel meer. En dat terwijl je ook nog eens zo veel en zulk goed werk verzet. You're one of a kind! Frank Jan, bedankt voor al je hulp met het benaderen van patiënten. Harro, Wan, Elise, ik ben heel blij met jullie inzet voor het includeren van de patiënten, fijn dat jullie altijd mee wilden denken! Lize, dank voor alle NPOs die je hebt afgenomen in het kader van de studies. Ook Meike Huiskens wil ik daarvoor bedanken, evenals de stagiaires van de neuropsychologie. Lieke en Tsz, zonder jullie waren er geen genetica resultaten geweest in de Iris+ studie. Bedankt voor jullie moeite! Last but not least alle andere mensen die de neurologie/het Alzheimercentrum een boeiende werkplek maken: Leonie, Jeroen, Jessica, Sophie, Sanne, Janneke.

Lieve Judy, jij weet als niemand anders hoeveel details er wel niet zijn om je druk over te maken gedurende een promotietraject (OCPD olé olé! :) Ik ben dankbaar dat ik die allemaal met je heb mogen delen.

Alle vriendinnen die ik heb overgehouden aan psychologie: lieve Gaby, heerlijk om jou als buurvrouw te hebben en gewoon even binnen te lopen voor een kop koffie (of een glas, ehh, fles wijn ;). Dank je wel voor je eeuwig luisterend oor! Ik ben trots op al je ontwikkelingen binnen de fotografie, en nog trotser dat jouw werk de voorkant van dit proefschrift siert! Ik kijk uit naar ons volgende weekendje weg, natuurlijk samen met Ike en Marleen! Nieke, bedankt voor alle jaren trouwe vriendschap waar geen promotie, eigen zaak, baby of verhuizing tussen komt! Dieuwertje, we zien elkaar dan wel niet zo vaak als we eigenlijk zouden willen, hopelijk komt daar verandering in nu ik klaar ben met mijn 'roman' ;).

Mijn liefste neuroscience nerds, Do en Mitzy! Hoe heerlijk om met jullie tijdens onze zeldzame maar oh zo fijne DoReMi sessies onder het genot van mimosa's te filosoferen over het neurowetenschappelijke wereldje. Dank jullie wel voor alle support!

Ingrid, Aline, Finneke, jullie zijn de beste coachende mede-wijndrinkers die ik me kan wensen. Dank voor al die therapeutische wijnmarathons!

Van naast elkaar zitten in de brugklas tot allebei promoveren op het gebied van hersenen, en alles daar tussenin: lieve Marlies, dank je wel voor alle gezelligheid, steun en betrokkenheid al die jaren.

Nathalie en Annemijn, wat een voorrecht om dit alles en meer met jullie te mogen delen. Liefste Nali, het is nog steeds zo ontzettend fijn om al mijn dagelijkse sores met jou te bespreken. Vaak ging dat over mijn promotie. Bedankt voor alle momenten dat je me helpt geholpen te relativeren, die zijn onbeschrijflijk waardevol geweest, zoals jouw vriendschap dat überhaupt is! Liefste Anneman, ik heb zoveel bewondering voor hoe jij als je aan de andere kant van wereld zit nog steeds dichtbij kan zijn. Ik koester het enorm dat ik één van de mensen mag zijn die je altijd dichtbij je hebt. Dank jullie wel voor alles m'n liefste vriendinnetjes! Jurre, ik denk dat je één van de weinige mensen bent die daadwerkelijk geprobeerd heeft mijn papers te lezen, zo onvoorstelbaar lief! Dank je wel voor je betrokkenheid.

Mijn familie, met name tante Janny en tante Jo, Caroline, Johan, Karin, Corina, Nancy en Sandra, dank voor jullie eeuwige belangstelling in de voortgang van mijn onderzoek! Nu kunnen we dit agendapunt schrappen voor de toekomstige kerstdiners en high tea's. Veel dank aan tante Ineke voor het helpen werven van gezonde vrijwilligers en aan oom Piet voor pilot-proefpersoon zijn, ook al mocht hij de afronding van het daadwerkelijke onderzoek helaas niet meer meemaken.

Ook mijn schoonfamilie, Martijn en Sandra, Floris en Greini, Pieter en Marieke, bedankt voor jullie interesse in mijn onderzoek en vooral het begrip als dat onderzoek weer eens de prioriteit had. Speciale dank aan mijn schoonouders, Joost en Gerda, jullie betrokkenheid gaat zelfs zo ver dat jullie als gezonde vrijwilligers hebben deelgenomen aan het onderzoek. Ik ben jullie heel dankbaar voor alles!

David en Kimberley, Esther en Ben, dank voor jullie betrokkenheid bij het wel en wee van het onderzoek van jullie kleine (schoon)zusje! Fijn ook dat we onze schrijffrustraties hebben kunnen delen Dadie ;) Speciale dank aan Esther voor je aandacht voor mijn onderzoek, zelfs terwijl jij dagelijks met het onderwerp wordt geconfronteerd. Lieve Bram en Karlijn, dank jullie wel voor jullie onbezorgde gezelligheid!

Liefste pappa en mamma, ik had dit niet zonder jullie gekund. Jullie willen altijd het beste voor mij en daarom heb ik het geluk op deze manier opgegroeid en opgeleid te mogen zijn. Dank voor jullie onvoorwaardelijke steun en liefde. Mam, speciale dank aan jou voor alles wat je voor het onderzoek hebt gedaan, van gezonde vrijwilliger zijn, tot Iris-bollen regelen als presentje voor de deelnemers, tot medewerking aan de voorkant van dit proefschrift. Je bent een kanjer.

Live Wouter Naber, zoals alles wat we doen hebben we deze promotie ook bijna samen gedaan: dank je wel voor al je steun en ervoor zorgen dat ik ook stil stond bij (kleine) successen, maar ook voor het tekenen van logo's, pilot proefpersoon zijn, het luisteren naar mijn presentaties, en nog honderden zaken meer, maar ik ben je vooral dankbaar voor altijd en overal achter me staan. Woorden kunnen niet beschrijven hoe dankbaar en gelukkig ik ben dat ik mijn leven met jou mag delen!

List of publications

Mutsaerts HJMM, **Steketee RME**, Heijtel DFR, Kuijer JPA, Van Osch MJP, Majoie CBLM, Smits M, Nederveen AJ. Inter-vendor reproducibility of pseudo-continuous arterial spin labeling at 3 Tesla. PLoS One. 2014;9:e104108.

Bron EE, **Steketee RME**, Houston GC, Oliver RA, Achterberg HC, Loog M, Van Swieten JC, Hammers A, Niessen WJ, Smits M, Klein S. Diagnostic classification of arterial spin labeling and structural MRI in presenile early stage dementia. Hum Brain Mapp. 2014;35:4916-31.

Steketee RME, Mutsaerts HJMM, Bron EE, Van Osch MJP, Majoie CBLM, Van der Lugt A, Nederveen AJ, Smits M. Quantitative functional arterial spin labeling (fASL)-MRI – sensitivity and reproducibility of regional CBF changes using pseudo-continuous ASL product sequences. PLoS ONE. 2015;10:e0132929.

Bron EE, Smits M, van der Flier WM, Vrenken H, Barkhof F, Scheltens P, Papma JM, **Steketee RME**, Méndez Orellana C, Meijboom R, Pinto M, Meireles JR, Garrett C, Bastos-Leite AJ, Abdulkadir A, Ronneberger O, Amoroso N, Bellotti R, Cárdenas-Peña D, Álvarez-Meza AM, Dolph CV, Iftekharuddin KM, Eskildsen SF, Coupé P, Fonov VS, Franke K, Gaser C, Ledig C, Guerrero R, Tong T, Gray KR, Moradi E, Tohka J, Routier A, Durrleman S, Sarica A, Di Fatta G, Sensi F, Chincarini A, Smith GM, Stoyanov ZV, Sørensen L, Nielsen M, Tangaro S, Inglese P, Wachinger C, Reuter M, van Swieten JC, Niessen WJ, Klein S; Alzheimer's Disease Neuroimaging Initiative. Standardized evaluation of algorithms for computer-aided diagnosis of dementia based on structural MRI: the CADDementia challenge. Neuroimage. 2015;111:562-79.

Mutsaerts HJMM, **Steketee RME**, Heijtel DFR, Kuijer JPA, Van Osch MJP, Majoie CBLM, Smits M, Nederveen AJ. Reproducibility of pharmacological ASL using scanners from different vendors: implications for multi-center drug studies. MAGMA. 2015;28:427-36.

Steketee RME, Bron EE, Meijboom R, Houston GC, Klein S, Mutsaerts HJMM, Mendez Orellana CP, De Jong FJ, Van Swieten JC, Van der Lugt A, Smits M. Early-stage differentiation between presenile Alzheimer's disease and frontotemporal dementia using arterial spin labeling MRI. Eur Radiol. 2016:26;244-53.

Steketee RME, Meijboom R, Bron EE, Osse RJ, De Koning I, Jiskoot LC, Klein S, De Jong FJ, Van der Lugt A, Van Swieten JC, Smits M. Structural and functional brain abnormalities place phenocopy frontotemporal dementia (FTD) in the FTD spectrum. Submitted.

Steketee RME*, Meijboom R*, De Groot M, Bron EE, De Jong FJ, Van der Lugt A, Van Swieten JC, Smits M. Concurrent white and gray matter degeneration of disease-specific networks in early-stage Alzheimer's disease and behavioral variant frontotemporal dementia. Submitted.

* These authors contributed equally to this work

Meijboom R, **Steketee RME**, De Koning I, Osse RJ, Jiskoot LC, Klein S, De Jong FJ, Van der Lugt A, Van Swieten JC, Smits M. Functional connectivity and microstructural white matter changes in phenocopy frontotemporal dementia. Submitted.

Méndez Orellana CP, Visch-Brink E, Weterings A, **Steketee RME**, Koudstaal P, Van der Lugt A, Smits M. Differential involvement of the left inferior frontal gyrus during auditory phonological and semantic processing in older healthy adults. Submitted.

Weyts K, Vernooij MW, **Steketee RME**, Valkema R, Smits M. ASL perfusion MRI versus FDG PET-CT in patients suspected of an early dementia syndrome. In preparation.

PhD Portfolio

Name PhD Student: Rebecca M.E. Steketee
Erasmus MC department: Radiology
Research School: Graduate School Neurosciences Amsterdam Rotterdam (ONWAR)

1. PhD training		Year	ECTS
General courses			
Introduction to Data Analysis (NIHES, Rotterdam/NL)	2010		1,0
Regression Analysis (NIHES, Rotterdam/NL)		2010	1,9
Basiscursus Regelgeving Klinisch Onderzoek (Erasmus MC, Rotterdam/NL)		2011	1,0
Biomedical English Writing and Communication (Erasmus MC, Rotterdam/NL)		2012	4,0
Specific courses			
Statistical Parametric Mapping for fMRI (UCL Wellcome Trust Centre for Neuroimaging, London/UK)		2010	0,9
Functional Neuroanatomy (ONWAR, Amsterdam/NL)		2011	1,4
Functional Magnetic Resonance Imaging: From Neurophysiology to Cognitive Neuroscience (ESMRMB, Maastricht/NL)		2011	1,0
Neurodegeneration of the nervous system (ONWAR, Amsterdam/NL)		2012	1,4
Resting State fMRI - Analysis and Interpretation (ESMRMB, Magdenburg/DE)		2012	0,8
Neuropsychopharmacology (ONWAR, Amsterdam/NL)		2012	2,0
Neuroradiology and Funtional Neuroanatomy (UCL Institute of Neurology, London/UK)		2012	1,2
ISMRM Scientific Workshop on Perfusion MRI (ISMRM, Amsterdam/NL)		2012	1,2
Grant writing (ONWAR, Amsterdam/NL)		2013	1,8
Arterial Spin Labeling training school (COST ASL Initiative in Dementia, Verona/IT)		2013	1,0

(Inter)national conferences and presentations

Alzheimer's Association International Conference, Paris/FR	2011	1,0
Annual meeting of the European Society for Magnetic Resonance in Medicine and Biology, Leipzig/DE. Oral presentation	2011	1,5
European Congress of Radiology, Vienna/AT. Oral presentation	2012	1,5
Meeting of the Organization for Human Brain Mapping, Beijing/CN. Poster presentation	2012	1,5
Radiologendagen, Den Bosch/NL. Oral presentation	2012	1,0
Annual meeting of the International Society for Magnetic Resonance in Medicine Benelux, Rotterdam/NL. Poster presentation	2013	1,0
European Congress of Radiology, Vienna/AT. Oral presentation	2013	1,5
Annual meeting of the American Society of Neuroradiology, San Diego/US. Invited oral presentation	2013	2,0
Annual meeting of the European Society for Magnetic Resonance in Medicine and Biology, Toulouse/FR. Oral presentation	2013	1,5

Other

ONWAR Annual meetings	2010-2013	3,0
COST ASL Initiative in Dementia meetings	2012-2013	0,5
Alzheimer Nederland Mix & Match research meetings	2012, 2014	0,5

2. Teaching	Year	ECTS
Lecturing		
Laborantenonderwijs afdeling Radiologie, Erasmus MC Rotterdam	2011	0,5
Lecture for Student Society of Biology, Biomedical sciences and Psychobiology, University of Amsterdam		0,5

Supervising Master's theses		
Supervision research projects 4th year medical students	2011, 2013	2,0
Supervision master thesis neuropsychology student	2012	1,0
Other		
Coordinator weekly meetings fMRI research group	2011-2013	3,0
Participation in creating the 'Alzheimer Kompas', a databank for the International Alzheimer Research Foundation (ISAO)	2014	1,0
TOTAL		45,1

About the author

Rebecca Martinetta Elisabeth Steketee was born on February 17, 1985 in Leiden, the Netherlands. In 2003, she completed bilingual secondary school at the Rijnlands Lyceum Oegstgeest and started studying Psychology at Utrecht University. In 2007 she obtained her master's degree in Neuropsychology and started her research master degree in Neuroscience and Cognition at Utrecht University. As part of the research master's program, she carried out one of her internships at the Department of Radiology at Erasmus MC Rotterdam in 2009. The project was supervised by dr. M. Smits and prof. dr. Aad van der Lugt and focused on optimizing functional MRI paradigms to test memory and emotion recognition in presenile dementia. After obtaining her degree in Cognitive Neuroscience, she started her PhD research at Erasmus MC in 2010 under supervision of dr. Smits and prof. dr. van der Lugt as well as prof. dr. John van Swieten. She set up and conducted the Iris and Iris+ study on advanced MR neuroimaging in early stage presenile dementia, as well as the VESPA study on multicenter reproducibility of arterial spin labeling MRI. The results of these studies are described in this thesis. Rebecca currently lives in Rotterdam with her partner Wouter and continues working at Erasmus MC as a postdoctoral researcher at the Department of Radiology.